

# Deterministic and Stochastic Modelling of Ocean Surface Waves

DETERMINISTISCH EN STOCHASTISCH MODELLEREN VAN OCEANISCHE  
OPPERVLAKTEGOLVEN



# Deterministic and Stochastic Modelling of Ocean Surface Waves

## Proefschrift

ter verkrijging van de graad van doctor  
aan de Technische Universiteit Delft,  
op gezag van de Rector Magnificus prof. ir. K. C. A. M. Luyben,  
voorzitter van het College voor Promoties,  
in het openbaar te verdedigen op vrijdag 6 juni 2014 om 12:30 uur

door

**Pieter Bart SMIT**

civiel ingenieur  
geboren te Zoetermeer.

Dit proefschrift is goedgekeurd door de promotor:

Prof. dr. ir. G. S. Stelling

Samenstelling promotiecommissie:

Rector Magnificus,	voorzitter
Prof. dr. ir. G. S. Stelling,	Technische Universiteit Delft, promotor
Prof. dr. ir. A. J. H. M. Reniers,	Technische Universiteit Delft
Prof. dr. ir. R. H. M. Huijsmans,	Technische Universiteit Delft
Prof. dr. ir. D. Roelvink,	Unesco-IHE institute for water education
Prof. dr. A. E. P. Veldman,	Rijksuniversiteit Groningen
Dr. ir. T. T. Janssen,	Theiss Research
Dr. ir. M. Zijlema,	Technische Universiteit Delft
Prof. dr. ir. A. Mynett,	Technische Universiteit Delft, reservelid



*Published by:* VSSD, Delft, the Netherlands

*Front & Back:* Based on a photograph by E. Dupont.

Copyright © 2014 by P.B. Smit

ISBN 978-90-6562-354-6

An electronic version of this dissertation is available at  
<http://repository.tudelft.nl/>.

# Abstract

## DETERMINISTIC AND STOCHASTIC MODELLING OF OCEAN SURFACE WAVES

Predicting the mean wave statistics in the nearshore, for instance the significant wave height, has predominantly been the domain of operational stochastic wave models based on the radiative transport (or energy balance) equation. Although reasonably successful in the nearshore, these models were originally developed for oceanic scales, and necessarily neglect or parametrise processes that are only significant in shallow water, such as the linear processes of interference and diffraction, or the nonlinear triad wave-wave interactions and dissipation due to wave breaking. In this dissertation we investigate the possibility of predicting the wave statistics on small scales in strongly non-linear conditions, such as found in the surfzone, using the recently developed Surface WAVes till SHore (SWASH) model, whereas on larger scales we pursue a generalisation of existing stochastic models by incorporating coherent effects, hereby extending these models to include interference and diffractive effects.

First we determine whether non-hydrostatic models, and the SWASH model in particular, can be used to predict the wave statistics, such as the mean wave height and period, in the surfzone. Specifically, we consider how to incorporate dissipation due to wave breaking in non-hydrostatic models in an efficient and accurate way. Here we strive not only to capture the bulk statistics as encompassed by the mean wave height and period, but also the spectral evolution, and the development of the higher order nonlinear statistics in a dissipative surfzone. Hereto the so-called Hydrostatic Front Approximation is proposed, which enforces a hydrostatic pressure distribution in the water column below the front of a breaking wave so that, based on the analogy between a hydraulic jump and a turbulent bore, energy dissipation can be accounted for by ensuring conservation of mass and momentum using shock capturing numerics.

The model is verified with observations of the mean wave heights and periods for irregular, unidirectional waves in wave flumes, and with observations of such bulk statistics for short-crested wave propagation in a wave basin. The results demonstrate that the model can accurately predict the bulk parameters as well as wave-driven horizontal circulations. Moreover, our results show that, without specific calibration, the model accurately predicts not only the second-order bulk statistics, but also the details of the spectral evolution, as well as the higher-order statistics (skewness and asymmetry) of the waves. Monte Carlo simulations show that the model can capture the principal features of the wave probability density function in the surfzone, and that the spectral distribution of dissipation in SWASH is proportional to the frequency squared, which is consistent with observations reported by earlier studies. These results show that relatively efficient non-hydrostatic models such as SWASH can be successfully used to parametrise surfzone wave processes.

Outside the surfzone the wave motion is often weakly influenced by nonlinear processes and is therefore to a good approximation linear. This allows for a closed stochastic description of the wave motion that can be applied on large scales. How-

ever, conventional third generation stochastic wave-models based on the Radiative Transport Equation (RTE) are based on the premise that waves propagating at mutual angles are independent, and linear processes such as interference (e.g. standing waves) and diffraction are therefore not accounted for. The second part of this thesis therefore focuses on the derivation and verification of a new stochastic wave model that, unlike traditional models based on the RTE, can account for fast-scale variations in the wave statistics that occur in these focal zones by including coherent interference that occurs between crossing waves.

Hereto, on the premise of dispersive wave motion over slowly varying topography, a deterministic equation that governs the linear wave motion is derived. Based on this deterministic equation, we subsequently derive an evolution equation for the second-order statistics in terms the Wigner – or Coupled Mode – spectrum that governs the evolution of the complete second-order statistics, including coherent interference. The resulting Quasi-Coherent (QC) approximation reduces to the RTE in case of quasi-homogeneous statistics, and therefore embodies a natural generalisation of quasi-homogeneous theory to include effects of coherent interference.

The model is verified through comparison to analytic solutions, and laboratory and field observations. We discuss the differences with the radiative transfer equation and the limitations of our approximation, and illustrate the model’s ability to resolve coherent interference structures in wave fields such as those typically found in refractive focal zones and around obstacles. Moreover, we demonstrate that a robust numerical implementation of the QC approximation takes the form of the RTE including an additional scattering source term that accounts for the coherent interference in the field. Consequently, the QC-approximation derived in the present thesis can be incorporated into existing stochastic wave models based on the RTE.

In conclusion: in the present study we considered prediction of nearshore wave statistics by further development of deterministic and stochastic wave models. The resulting deterministic model SWASH, with proper treatment of wave breaking, is suited for application in the surfzone, whereas the stochastic QC model bridges the gap between traditional stochastic models, valid for oceanic scales, and deterministic models. Both models are validated with empirical data, confirming that they form a robust and complementary set of models for the prediction of wave statistics in the nearshore.

# Samenvatting

DETERMINISTISCH EN STOCHASTISCH MODELLEREN VAN OCEANISCHE OPPERVLAKTEGOLVEN.

Tot op heden is het voorspellen van de golf statistiek nabij de kust, bijvoorbeeld de significante golfhoogte, voornamelijk het domein van stochastische golfmodellen gebaseerd op de stralingstranport (ook wel energie balans) vergelijking. Alhoewel deze modellen met succes zijn toegepast in het kustgebied, zijn deze modellen van origine ontwikkeld voor grootschalige toepassingen op de open oceaan, en dientengevolge verwaarlozen of parametriseren ze processen die alleen significant zijn in ondiep water, zoals de lineaire processen van interferentie en diffractie, of de niet-lineaire drie-golf wisselwerkingen en dissipatie door golfbreken. In dit proefschrift onderzoeken we de mogelijkheid om de golfstatistiek voor kleinschalige maar sterk niet lineaire situaties, zoals in de brandingszone, te voorspellen met behulp van het recent ontwikkelde “Oppervlakte golven tot de kust” (SWASH<sup>1</sup>) model, terwijl we voor grootschaliger toepassingen een generalisatie van de bestaande stochastische aanpak nastreven, zodat deze rekening houdt met diffractie en interferentie effecten.

Allereerst wordt onderzocht of een niet-hydrostatische model, en in het bijzonder het SWASH model, toepasbaar is om de golfstatistiek, zoals de gemiddelde golfhoogte en golfperiode, te voorspellen in de brandingszone. In het bijzonder kijken we hoe de dissipatie die naar aanleiding van golfbreken optreedt efficiënt en accuraat kan worden meegenomen. Om dit te bereiken wordt de Hydrostatische Front Approximatie (HFA) voorgesteld waarin de drukverdeling in de water kolom onder een brekende golf hydrostatisch wordt verondersteld en, gebaseerd op de analogie tussen een brekende golf en een watersprong, golfenergie gedissipeerd wordt door te vereisen dat massa en impuls in het numerieke model behouden blijven over de resulterende schokgolf. Dit met als doel niet alleen een accurate weergave van de bulkstatistiek, maar ook een natuurgetrouwe weergave van de evolutie van het golfspectrum en de hogere orde statistiek in een dissipatieve brandingszone.

Het ontwikkelde model is geverifieerd met observaties van de gemiddelde golfhoogte en golfperiode voor onregelmatige, uni-directionele golven in golfgoten, en met observaties van deze parameters voor kortkammige golven in een golfbasin. Uit deze verificatie blijkt dat het resulterende model zowel de bulk parameters als de golfgedreven stroming accuraat kan voorspellen. Bovendien laat deze studie zien dat het model zonder verdere kalibratie naast de bulk tweede orde statistiek ook de spectrale evolutie van het variantie spectrum nauwgezet beschrijft (inclusief niet lineaire contributies), alsmede de hogere orde statistiek (asymmetrie en scheefheid) van de golven. Monte-Carlo simulaties laten zien dat het model ook de karakteristieke eigenschappen van de kansdichtheid functie reproduceert behorende bij het vrije oppervlak in de brandingszone. Daarnaast blijkt dat de resulterende spectrale

---

<sup>1</sup>Afgeleid van de Engelse vertaling: “Surface WAVes till SHore”

verdeling van de dissipatie door golfbreken proportioneel is met de frequentie in het kwadraat, consistent met eerdere observaties in de literatuur. Deze resultaten bevestigen dat een niet-hydrostatisch model zoals SWASH de effecten van de dominante golf processen in de brandingszone met grote nauwkeurigheid kan reproduceren.

Buiten de brandingszone wordt de golfbeweging zwak beïnvloed door niet-lineaire processen en is daarom bij benadering lineair. Dit maakt een gesloten stochastische benadering die grootschalig toepasbaar is mogelijk. Echter, conventionele derde generatie stochastische modellen gebaseerd op de stralingstransport vergelijking (RTE<sup>2</sup>) veronderstellen daarnaast ook dat golven die in verschillende richtingen propageren statistisch onafhankelijk zijn. Dientengevolge worden ook lineaire processen zoals interferentie (e.g. staande golven) en diffractie – van belang in convergentiezones – verwaarloosbaar geacht. Het tweede deel van dit proefschrift is daarom gewijd aan de afleiding en verificatie van een nieuw stochastisch model dat, in tegenstelling tot modellen gebaseerd op de RTE, rekening houdt met coherente interferentie, en dus rekening houdt met de snelle variatie in de golfstatistiek die kan optreden in convergentiezones.

Het model is afgeleid onder de aanname van dispersieve golfbeweging over langzaam variërende topografie, van waaruit een deterministische vergelijking die de lineaire golfbeweging beschrijft is opgesteld. Uit deze deterministische beschrijving is een vergelijking voor de evolutie van het Wigner – of “coupled mode” – spectrum afgeleid, die de evolutie van de complete tweede orde statistiek beschrijft, inclusief coherente interferentie. De resulterende Quasi-Coherente (QC) benadering reduceert tot de conventionele RTE wanneer de golfstatistiek quasi-homogeen is, en vormt dus als zodanig een natuurlijke generalisatie van de bestaande quasi-homogene theorie om deze uit te breiden met de effecten van coherente interferentie.

Verificatie van het model wordt bereikt door middel van een vergelijking met analytische oplossingen, en met laboratorium en veld observaties. We bediscussiëren de verschillen met de stralingstransport vergelijking, de limitaties van de huidige aanpak en demonstreren dat deze coherente interferentie structuren kan beschrijven zoals optreden in convergentiezones en rondom obstakels. Bovendien demonstreren we dat een robuuste numerieke implementatie van de QC benadering de vorm heeft van de RTE aangevuld met een verstrooiingsterm die rekening houdt met de coherente interferentie in het golfveld. Dientengevolge kan de QC benadering afgeleid in dit proefschrift toegevoegd worden aan bestaande derde generatie golfmodellen gebaseerd op de RTE.

Concluderend: in de huidige studie beschouwen we de voorspelling van de golfstatistiek in de kustzone door een verdere ontwikkeling van deterministische en stochastische golf modellen. Het resulterende deterministische model SWASH, aangevuld met HFA, is toepasbaar in de brandingszone, terwijl het stochastische QC model het gat tussen conventionele stochastische modellen – geschikt voor applicaties op de open oceaan – en deterministische modellen overbrugt. De verificatie van beide modellen met empirische data bevestigt dat ze een robuuste en complementaire set van modellen vormen om de golf statistiek in de kustzone te voorspellen.

---

<sup>2</sup>Afgeleid van de Engelse vertaling: “Radiative Transport Equation”

# Contents

<b>Abstract</b>	<b>v</b>
<b>Samenvatting</b>	<b>vii</b>
<b>1 Introduction</b>	<b>1</b>
1.1 Objective and Outline . . . . .	4
<b>2 Deterministic and stochastic wave models</b>	<b>5</b>
2.1 Deterministic wave models in intermediate and shallow waters . . . . .	6
2.2 Stochastic wave models in shallow waters . . . . .	11
<b>3 Wave breaking in a non-hydrostatic wave model</b>	<b>17</b>
3.1 Introduction. . . . .	17
3.2 Non-hydrostatic modelling . . . . .	19
3.3 Wave breaking approximations. . . . .	22
3.4 Monochromatic wave breaking over a sloping beach . . . . .	26
3.5 Random waves breaking over barred topography . . . . .	30
3.6 Short-crested waves over 2D topography . . . . .	35
3.7 Discussion . . . . .	39
3.8 Conclusions . . . . .	41
<b>Appendices</b>	<b>43</b>
3.A Turbulent stress approximations. . . . .	43
3.B Wave generating boundary conditions. . . . .	43
3.C Wave breaking initiation criterion . . . . .	44
<b>4 Non-hydrostatic modelling of surfzone wave dynamics</b>	<b>47</b>
4.1 Introduction. . . . .	47
4.2 Model description. . . . .	49
4.3 Experiment and model setup. . . . .	52
4.4 Results . . . . .	56
4.5 Discussion . . . . .	67
4.6 Conclusions . . . . .	70
<b>Appendix</b>	<b>73</b>
4.A Frequency dispersion in SWASH. . . . .	73
<b>5 The evolution of inhomogeneous wave statistics</b>	<b>75</b>
5.1 Introduction. . . . .	76
5.2 Evolution of correlators . . . . .	77
5.3 Evolution of coherent wave structures. . . . .	81
5.4 Discussion . . . . .	89

5.5	Conclusions . . . . .	95
	<b>Appendices</b>	<b>97</b>
5.A	Operator definition . . . . .	97
5.B	Relation to geometric optics . . . . .	99
5.C	Boundary condition for wide-angle diffraction . . . . .	100
<b>6</b>	<b>Narrow-band wave statistics over nearshore topography</b>	<b>101</b>
6.1	Introduction. . . . .	101
6.2	Evolution of inhomogeneous wave fields . . . . .	103
6.3	Wave deformation by an elliptical shoal . . . . .	107
6.4	Swell over submarine canyons . . . . .	111
6.5	Discussion and conclusions . . . . .	118
	<b>Appendices</b>	<b>121</b>
6.A	Fourier transform operators . . . . .	121
6.B	Discrete model . . . . .	121
<b>7</b>	<b>Conclusions and outlook</b>	<b>127</b>
7.1	Conclusions . . . . .	127
7.2	Outlook . . . . .	132
	<b>References</b>	<b>135</b>
	<b>List of figures</b>	<b>147</b>
	<b>Acknowledgements</b>	<b>151</b>
	<b>List of publications</b>	<b>153</b>
	<b>Curriculum vitae</b>	<b>155</b>

# 1

## Introduction

The sight – and sound – of ocean waves violently breaking on the shore during a severe storm is impressive. The wild, chaotic and unpredictable appearance of the ocean is built of a superposition of many waves, each with its own characteristic height, length and period. These waves are generated by wind and they travel the ocean basins propagating freely, nearly frictionless, under the influence of gravity. With periods of approximately one until twenty seconds, heights in the order of centimetres to (tens of) metres, and horizontal scales of several to hundreds of metres, these are known as wind-generated surface gravity waves, often referred to more simply – as done here – as ocean waves.

The necessity of nearshore wave prediction became urgent during World War II, when knowledge of wave conditions at the landing beaches was a matter of life and death (see Parker, 2010). Besides military applications, wave prediction in shallow water was – and is – of economic interest (e.g. wave conditions at the port entrance), relevant for engineering (e.g. design wave conditions) and important for scientific research (e.g. understanding nearshore processes). Sometimes detailed (phase-resolved) information of the wave evolution is needed (e.g. impact forces on a structure Gomez-Gesteira and Dalrymple, 2004), but for many applications statistical information on the wave field suffices, represented for instance by mean wave height or period, or a wave spectrum (e.g. Wise Group, 2007).

Conceptually, there are two different – but related – techniques to predict the wave statistics. The starting point is the same: a simplified description of the dynamics of a fluid with a free-surface in terms of a set of partial differential equations, the solution of which depends on boundary and initial conditions, and on the environmental parameters such as e.g. wind, bathymetry, ambient currents, and variations therein. Given the initial and boundary conditions, and medium variations, the prediction of a wave variable – say the surface elevation  $\eta(\mathbf{x}_0, t_0)$  at a certain location  $\mathbf{x}_0$  and time  $t_0$  – then reduces to the (often formidable) task of solving the equations by mathematical or numerical means.

This deterministic approach can also be used to calculate wave statistics. By

considering  $N$  different realizations of the model input (drawn from their respective statistical distributions) and successively solving the equations for each input, an ensemble of observations can be generated, from which the statistics of e.g. the free-surface elevation (mean, variance etc.) can be discerned. This technique, often referred to as Monte-Carlo analysis, is straightforward to apply, but requires either large ensembles, or (assuming ergodicity) a single simulation with a long duration. Its major advantage is that the physical processes which are included in the underlying model are also encapsulated in the statistical results, which in particular for strongly nonlinear waves prevents the need for additional statistical closure approximations. The downside is that certain processes (most notably wave generation by wind) are difficult to include, and accurate representation of small-scale motion (e.g. turbulence), is not feasible in large domains due to computational constraints. Hence, the more advanced nearshore models, such as the well established Boussinesq models (e.g. Madsen *et al.*, 1991; Nwogu, 1993; Wei *et al.*, 1995; Madsen *et al.*, 2006; Klopman *et al.*, 2010) or the more recently developed non-hydrostatic models (e.g. Stelling and Zijlema, 2003; Yamazaki *et al.*, 2009; Zijlema *et al.*, 2011b; Ma *et al.*, 2012; Cui, 2013), necessarily parametrise some processes such as turbulence, bed-friction and most importantly depth-induced wave breaking. Generally, prediction of bulk statistical parameters is reasonable in these models. However, describing the evolution of higher-order statistics, as encompassed by e.g. the wave-spectrum or third-order moments (e.g. skewness or asymmetry), is more elusive, as this critically depends on the interplay between breaking-induced dissipation and nonlinear processes (e.g. Chen *et al.*, 1997). In this regard, correctly accounting for the rate of wave energy dissipation in breaking waves is critical.

Alternatively, the deterministic equations can be used to derive stochastic evolution equations for the second-order moments of the free surface, usually expressed in terms of the variance density spectrum (e.g. Hasselmann, 1962; Willebrand, 1975; Komen *et al.*, 1994). In this way, there is no need to generate an ensemble, or predict long time series to obtain wave statistics. Moreover, because the wave statistics often change on slow scales, such models can be applied efficiently on spatial scales ranging from ocean basins to coastal regions. Prediction of bulk statistics, such as mean wave heights and – to a lesser extent – periods, are often reasonable (Wise Group, 2007), and over extended regions including locally generated waves, stochastic models are the only feasible alternative. However, the downside of a stochastic approach is that it is restricted to near-Gaussian and quasi-homogeneous statistics, which in particular in shallow water might be overly restrictive. In such regions, not only do waves develop non-Gaussian statistics, but - through interaction with the topography - inhomogeneous effects can become important as well. For instance, the statistics of coherent interference patterns found in wave focal zones resulting in locally enhanced sea states and caustics can only be accurately represented when accounting for strongly inhomogeneous effects in wave statistics. However, such effects are completely ignored in state-of-the-art (operational) wave models, which are invariably based on some form of an energy balance equation, implying quasi-homogeneous statistics (Janssen *et al.*, 2008).

In the present work, developments are considered in both the deterministic and

---

stochastic approach, with a particular focus on wave modelling in the nearshore, including the surfzone. We continue development and verification of the recently introduced non-hydrostatic models, which form a promising alternative to the Boussinesq wave models for simulating nonlinear wave dynamics and statistics in the surfzone. In particular, we consider depth-induced wave breaking in the non-hydrostatic wave model Simulating Waves till SHore<sup>1</sup>, or SWASH (Zijlema *et al.*, 2011b), and consider whether a relatively simple and efficient parameterisation of wave breaking, which locally reduces the equations to the Nonlinear Shallow Water Equations (NSWE) and represents the bore as a shock wave, can not only reproduce bulk parameters, but also capture the details of the surfzone energy balance.

The other focus of this work is to develop a generalized stochastic modelling framework that allows the evolution of cross-correlation information radiated into the region or developed while propagating through a variable medium. This framework is applied to develop a more general form of the radiative transfer equation that incorporates inhomogeneous and diffraction effects and which is referred to as the Quasi Coherent (QC) approximation. Since the resulting QC model is a generalization of the widely used energy balance equation, the model equation is compatible with existing operational models. However, with the inclusion of coherent interference effects (and diffraction) it is more accurate in predicting evolution of swell wave statistics in coastal regions with strong medium variations. Moreover, and in contrast to traditional models based on the radiative transfer equation, this approach can resolve the fine structure of alongshore standing waves in focal zones, which affects the wave-induced flows, and thus transport processes.

---

<sup>1</sup>In which the author has been involved in its development.

## 1.1. OBJECTIVE AND OUTLINE

The overarching objective of the present study is to advance the predictive capability and understanding of wave dynamics - and in particular the evolution of wave statistics - in shallow water, through (a) further development and verification of the non-hydrostatic modelling framework, and (b) the development of a new stochastic wave model that accounts for wave coherence and is applicable to wave propagation over extended 2D topography.

The base of this thesis is formed by a set of journal papers<sup>2</sup> that resulted from these efforts. The articles are included almost verbatim (with minor updates to correct for small errors) as four separate chapters, each of which can be read independently. This necessarily entails that information from the introductory chapters (1 and 2), and between the main chapters, is repeated to retain individual legibility. The outline of this work is therefore as follows. Following the introduction (this chapter), and to sketch the context of the developments within the present work, we shall discuss developments in both deterministic and stochastic wave models, with a focus on nearshore wave modelling (Chapter 2).

The next two chapters (3 and 4) concern the further development and verification of the deterministic SWASH model. The introduction of a new wave breaking parametrisation, which locally reduces the governing equations to the nonlinear shallow water equations, is the subject of Chapter 3. Through comparison with flume experiments, we demonstrate that this approach reproduces observed wave heights well, while allowing for a much reduced vertical resolution, thus improving efficiency. Moreover observations of short-crested waves in a wave basin, including wave heights, wave spectra, and wave-driven currents, are also reproduced well. Next, we consider the model representation of the detailed nonlinear wave dynamics and statistics in a dissipative surfzone (Chapter 4).

Subsequently, we shall develop and discuss a generalization of spectral wave models that includes the effects of coherent interferences on wave statistics (Chapter 5). Using multiple scales, we approximate the transport equation for the (complete) second-order wave correlation matrix. The resulting model, which accounts for the generation and propagation of coherent interferences in a variable medium (e.g. in wave focal zones), is validated through comparison with analytic solutions and laboratory observations. In addition, we discuss the differences with the radiative transfer equation and the limitations of our approximation. Chapter 6 concerns further development of the model, with a particular focus on implementation and verification by means of a field data set of swell waves incident on submarine canyons.

Lastly, discussions and conclusions on individual developments concerning the stochastic and deterministic models are provided separately at the end of each chapter. Discussions and conclusions of the overall thesis, including an outlook to future developments, are presented in Chapter 7.

---

<sup>2</sup>Three of which have been published, and one will be submitted later in 2014.

# 2

## Deterministic and stochastic wave models

In the early days of wave research, near the end of the 19<sup>th</sup> century, attention was primarily focused on investigating analytical descriptions of waves of constant form propagating through a uniform medium, with important contributions due to Stokes, Airy, Cauchy, Korteweg and de Vries and others (see Craik, 2004, for a historical overview). These studies remain invaluable today as their principal results, e.g. the linear approximation introduced by Airy, or the seminal work by Stokes on nonlinear waves, advanced our understanding of wave motion greatly, and in one form or another still influence our physical interpretation thereof. However, the extension of their methods to nonlinear irregular wave motion, propagating through an inhomogeneous medium, invariably results in a set of coupled partial (or ordinary) differential equations which (most likely) cannot be solved by analytical means. Therefore, with the introduction of widespread computing facilities during the latter half of the 20<sup>th</sup> century, focus shifted to solving (approximate) equations governing water wave dynamics using numerical approximations.

Nevertheless, computational limitations prevented – as they still do – using the basic primitive equations, the (Reynolds-averaged) Navier-Stokes equations, to resolve all scales of motion (up to turbulence) on spatial and temporal scales of interest<sup>1</sup>. Instead, often a considerable simplification is pursued in describing the free-surface as a single-valued function of the horizontal coordinates, and neglecting friction (leading to the Euler equations), or parametrising the effects of turbulence by a suitable closure assumption. Wave models often reduce the problem further by considering irrotational flow governed by the potential equations (i.e. the Laplace and Bernoulli equations combined with the dynamic and kinematic boundary conditions, see e.g. Mei *et al.*, 2005; Dingemans, 1997).

---

<sup>1</sup>Although Volume Of Fluid (VOF) methods or Smoothed Particle Hydrodynamics (SPH) models can now be feasibly applied on a 1D surfzone on scales of several wave lengths and periods (e.g. Dalrymple and Rogers, 2006; Torres-Freyermuth *et al.*, 2007).

If the vertical excursion of the free surface remains small (compared with local depth and wave length), and the topography changes slowly (compared with the wave length), this gives rise to linear wave theory, which has proven to be remarkably successful (even within the highly nonlinear surfzone). For instance, the linear approximation to energy propagation (see e.g. Dingemans, 1997; Mei *et al.*, 2005) is the foundation of stochastic operational wave models. For complex situations, e.g. with steep topography, or for strongly nonlinear waves, linear models have been augmented with a myriad of more involved (non)linear models (deterministic and stochastic), each with its own region of applicability (e.g. deep or shallow water) depending on underlying assumptions on the relative importance of the relative slope, wave nonlinearity and wave dispersion.

In what follows we will discuss deterministic and stochastic models applicable to (non)linear waves in intermediate to shallow waters. This results in a discussion of the relation to and the advantages of non-hydrostatic models such as SWASH when compared with other deterministic models in Section 2.1, with the purpose of sketching the context of the work presented in Chapters 3 and 4 of this thesis. Analogously, we discuss stochastic models, and the context of the improvements that are pursued thereon in section 2.2.

## 2.1. DETERMINISTIC WAVE MODELS IN INTERMEDIATE AND SHALLOW WATERS

In shallow water, the depth over wavelength ratio ( $\mu$ ) reduces significantly ( $\mu \rightarrow 0$ ) and water wave motion becomes weakly dispersive, with small vertical variations in the horizontal particle velocities, and a near linear variation in the vertical velocities. In this regime, nonlinear effects, expressed in terms of the amplitude to depth ratio ( $\delta$ ), become comparable with dispersive effects. The problem of wave evolution in the nearshore is then usually approached under the assumption that nonlinear effects dominate (resulting in the NSWE), or that they are of similar importance. The latter limit, setting  $\delta = O(\mu^2)$ , gave rise to first models suitable for wave propagation over uneven topography, the so-called Boussinesq models (Peregrine, 1967). In their classic form these types of models consider a series solution to eliminate the vertical cross-space in lieu of the appearance of additional corrections to the nonlinear shallow water equations to account for dispersion.

Since their inception, these models, and somewhat comparable models<sup>2</sup> based on Serre (1953) or Green and Naghdi (1976), have undergone rapid developments, with research focusing on extending dispersive properties of such models (e.g. Witting, 1984; Madsen *et al.*, 1991), deriving so called fully nonlinear models<sup>3</sup> (e.g. Wei *et al.*, 1995), wave-current interaction (e.g. Chen *et al.*, 1999), wave breaking (e.g. Kennedy *et al.*, 2000; Schäffer *et al.*, 1993; Tonelli and Petti, 2010; Tissier *et al.*, 2012) and wave run-up (e.g. Fuhrman and Madsen, 2008). However, in intermediate to deep

<sup>2</sup>In the remainder of this section we will, for brevity, include these models under the umbrella of Boussinesq models.

<sup>3</sup>Such models make no a-priori assumption on the ordering of  $\mu$  and  $\delta$ , although  $\mu$  is still assumed to be small, see Kirby (1996).

water, the classic Boussinesq approach becomes less attractive, as one has to consider increasingly complex equations containing higher-order (cross-) derivatives in time and space<sup>4</sup>. This not only affects model complexity, but can also introduce inherent unstable behaviour into the equations (i.e. the wave energy grows without bounds, Løvholt and Pedersen, 2009), although recasting the Boussinesq equations into different form can alleviate such problems (e.g. the Hamiltonian model by Klopman *et al.*, 2010, ensures conservation of energy). Good introductions into Boussinesq models are found in Kirby (1996), Madsen and Schäffer (1999) and a recent overview of the state of the art in Brocchini (2013).

Arguably, direct numerical evaluation of the Boussinesq, potential, or Euler equations, ignores that there are typically multiple scales of motion, one (or more) slow scales related to e.g. changes in the medium (ambient currents and bathymetry) or nonlinearity, and one fast scale related to the wave motion proper (resolving the phases of the individual waves). The existence of such scales can be exploited through a perturbation type solution of the wave variables (e.g. free-surface, velocity potential). For instance, the free surface elevation can be expressed a Fourier sum with free-surface modes of the form  $a_n(\mathbf{x}, t) \exp[i\omega_n t - i\phi(\mathbf{x})]$ , where  $a_n(\mathbf{x})$  denotes a slowly varying amplitude (incorporating the effects on slower scales),  $\omega_n$  is the modal frequency,  $\phi$  the wave function and  $\nabla_x \Phi = \mathbf{k}_n$  is the modal wavenumber. Assuming that angles are restricted to small angles with respect to a reference direction (e.g the coast-normal), directional waves can be included by utilizing an angular spectrum expansion for each mode (e.g. Dalrymple and Kirby, 1988; Janssen *et al.*, 2006), or a parabolization of the governing equations (e.g. Kaihatu and Kirby, 1995). Substitution of the assumed form into the governing equations then results in a linear problem for the fast scale motion (often formalized using multiple scale analysis) that can often be solved explicitly, and a set of coupled (due to nonlinearity) ordinary differential equations for the modal amplitudes that – as long as medium variations and nonlinearity remain weak – can be integrated over the slow scales of variation.

For instance, evolution equations based on the lowest-order Boussinesq theory (Peregrine, 1967) were used by e.g. Freilich and Guza (1984), to model unidirectional nonlinear wave shoaling on laterally uniform topography, and Herbers and Burton (1997), for short-crested wave propagation. Advances have since then focussed on inclusion of full linear dispersion (e.g. Kaihatu and Kirby, 1995; Bredmose *et al.*, 2005; Janssen *et al.*, 2006), improved nonlinear behavior (e.g. inclusion of arbitrary resonance mismatch Bredmose *et al.*, 2005; Janssen *et al.*, 2006), and inclusion of (weakly) two-dimensional topography (e.g. Kaihatu and Kirby, 1995; Janssen *et al.*, 2006). In intermediate to deep water (if cubic interactions are included, Janssen *et al.*, 2006) these amplitude evolution models are more accurate, and more efficient than time-domain models. Moreover, they form a suitable framework for deriving stochastic models, to which we shall return later. However, in regions where such a multiple scale approach breaks down, for instance where medium variations are rapid or is nonlinearity strong, the validity of these multiple-scale (or WKB-like) models is obviously limited. A model based on a direct numerical evolution of the

---

<sup>4</sup>This can be seen for instance by comparing the governing equations derived by Peregrine (1967) to the model presented by Madsen *et al.* (2006).

primitive equations does not have such restrictions, and is thus more accurate in regions where the WKB approximations break down (e.g. wave reflection, wave runup, steep bathymetry).

For shallow-water waves, in which the vertical structure of the flow is fairly uniform, an obvious alternative to the Boussinesq approach would be to evaluate the Euler equations with a coarse vertical grid resolution. Extension to deep water (adding dispersion effects) would then merely require an increase in vertical grid resolution. However, common numerical solution techniques (central differences and a staggered layout between pressure points and velocity components) would render this approach very inefficient. For instance, resolving the phase celerity with a relative error of 5% (compared with linear theory) for  $kd \approx 1$  requires  $O(10)$  points in the vertical, which is an order of magnitude more demanding than Boussinesq models of similar accuracy (at comparable horizontal resolution).

However, due to two recent developments this approach is not only feasible, but in fact shows great potential. First, a pressure decomposition into a hydrostatic and a dynamic (non-hydrostatic) contribution allows for an efficient fractional-step integration, where the velocity field is first predicted using the shallow water equations, and subsequently, by solving a discrete Poisson equation for the dynamic pressure, corrected to ensure that the velocity field is divergence-free (Casulli and Stelling, 1998). Second, discretization of the vertical pressure gradients by means of a Hermitian method such as the Keller-box or Preissmann Scheme (e.g. Lam and Simpson, 1976) allows to make use of the smooth vertical pressure profile by effectively using a finite series of spline functions as approximations. Combining these two approximations, Stelling and Zijlema (2003) achieves good dispersive properties for a non-hydrostatic model with a small number of vertical pressure points (1–3), and a computational effort comparable to Boussinesq models. Compared to the Boussinesq approach in general<sup>5</sup>, this makes the non-hydrostatic approach an attractive alternative because: (i) it can handle rotational flows (important for wave-current interaction); (ii) the governing equations are very similar to the basic primitive equations (facilitating physical interpretation); (iii) the model contains at most second-order derivatives thus simplifying the numerical implementation; (iv) extension to deeper water requires merely an increase of the vertical resolution (which provides flexibility); and (v) the method is easily incorporated to an existing shallow-water solver.

Since its initial inception, the non-hydrostatic approach<sup>6</sup> has rapidly gained traction, culminating in the release of codes ready for general use (e.g. SWASH and NHWave, Zijlema *et al.*, 2011b; Ma *et al.*, 2012), and inclusion into existing shallow-water models (e.g. H2Ocean, XBeach<sup>7</sup> and NEOWAVE<sup>8</sup>, Cui *et al.*, 2012; Smit *et al.*, 2009; Yamazaki *et al.*, 2009). Recent developments include implementation on unstructured grids (Cui *et al.*, 2012; Wei and Jia, 2014) and improvement of the dispersive properties (Cui, 2013). Yet, within the present context, the most important development has been their extension to include dissipative surfzone waves, which

<sup>5</sup>Noting that this also depends on the particular formulation one is comparing with.

<sup>6</sup>From now on, unless stated otherwise, when referring to non-hydrostatic models, we specifically refer to those based on the framework presented in Stelling and Zijlema (2003).

<sup>7</sup>eXtreme Beach behavior.

<sup>8</sup>Non-hydrostatic Evolution of Ocean WAVE.

requires the inclusion of the dominant and arguably most poorly understood process in the surfzone: depth-induced breaking.

### EXTENSION OF NON-HYDROSTATIC MODELS TO THE SURFZONE

When solving the Navier-Stokes equations directly, wave breaking is an emerging property of the equations and thus intrinsically included. However, adopting a single-valued representation of the free-surface – as done by non-hydrostatic models – implies that processes such as overturning, air entrainment, and wave-generated turbulence are no longer resolved. Instead, the dissipation of organized wave energy through turbulence into heat must be considered as an unresolved sub-grid process, the integral properties of which (i.e. the dissipation rate) are to be captured by model approximations.

By observing that both spilling and plunging breakers eventually evolve into a quasi-steady bore, in which the entire front-face of the wave is turbulent (Peregrine, 1983), breaking wave dynamics becomes somewhat analogous to a hydraulic jump (e.g. Lamb, 1932). Consequently, its integral properties (rate of energy dissipation, jump height) are reasonably well estimated by regarding the breaking wave as a discontinuity in the flow variables (free surface, velocities). If the underlying model equations permit the development of such bores (or shock waves), proper numerical treatment of such a discontinuity (conservation of mass and momentum) can be used to determine the energy dissipation of waves in the surfzone. For example, Hibberd and Peregrine (e.g. 1978) used the (non-dispersive) NSW to investigate the runup on a beach. Until relatively recently, this approach has not been pursued in nearshore wave models, because dispersive terms in the Boussinesq equations preclude the formation of shocks; nonlinear amplitude dispersion effects (responsible for wave steepening) are balanced by linear dispersive effects thus stabilizing the wave profile (Schäffer *et al.*, 1993). In addition, the dispersive terms cannot be expressed in conservative form, which prohibits the application of standard shock capturing numerical methods. Consequently, Boussinesq models often parametrise wave breaking by including locally enhanced horizontal diffusion of momentum (thus dissipating energy e.g. Kennedy *et al.*, 2000), or by including the effect of a surface roller (e.g. Schäffer *et al.*, 1993).

The similarity with shallow-water models suggests that for non-hydrostatic models the bore analogy combined with a shock-capturing method can be used to simulate surfzone waves. Zijlema and Stelling (2008) used the shock-capturing method of Stelling and Duinmeijer (2003) and demonstrated, by comparison to flume observations, that this is indeed feasible. Moreover, the resulting model reproduces the runup of waves (also by virtue of Stelling and Duinmeijer, 2003), such as the maximum runup of solitary waves on a plane beach (Synolakis, 1986), as demonstrated in Smit (2008). Subsequently, numerous researchers have used non-hydrostatic formulations – albeit with different underlying numerical implementations – to describe not only surfzone waves (e.g. Ma *et al.*, 2012; Yamazaki *et al.*, 2009), but also tsunami propagation, generation, and the resulting inundation (Yamazaki *et al.*, 2011; Tehranirad *et al.*, 2012; Cui, 2013).

The most attractive feature of the bore approach is that no model parameters are

required to predict the onset or dissipation rate of wave breaking. From a physical viewpoint, disadvantages are that all breaking waves transition into a sawtooth shape, resulting in exaggerated wave asymmetry compared to observations, and that the turbulent energy generated in the breaking process is not accounted for. A further practical disadvantage is that correctly predicting the location of incipient breaking requires disproportionately high vertical resolution (10–20 points) when compared to vertical mesh requirements outside the surfzone (2–3 points). The high resolution is required because the characteristic vertical length scale of the wave motion is no longer the wave length  $L$ , as in intermediate to deep water, but the wave height  $H$ . Since  $H/L \sim O(10^{-1})$ , this generally poses a higher restriction on the vertical resolution. When using lower resolutions, the waves do still break in the model, but because particle velocities near the surface are underestimated (see Chapter 3), the kinematic instability that initiates breaking (particle velocity exceeds wave celerity) is shifted shoreward, and the onset of dissipation is delayed towards shallower water. These stringent mesh requirements pose a severe constraint on the feasibility of the bore concept in engineering practice, as a comparatively small region prohibits the use of an otherwise acceptable coarse vertical resolution.

Hence, for efficiency reasons, dissipation based on an enhanced eddy viscosity were reintroduced in non-hydrostatic models, either using the Smagorinsky subgrid model (Smagorinsky, 1963; Jacobs, 2010; Ma *et al.*, 2012), or a mixing-length hypothesis (Zijlema *et al.*, 2011b) to estimate the eddy viscosity. Although effective in the surfzone, these formulations must be calibrated, and are too dissipative outside the surfzone for short waves in the tail of the spectrum (which possess relatively high curvature). Therefore – as in Boussinesq models – not only additional dissipation is required, it must also be localized (or ‘triggered’) in the surfzone; in other words, inclusion or adaption of one of the existing breaker models. Yet, the fact that in the approximation of the nonlinear shallow-water (NSW) equations, by lack of a stabilizing dispersive mechanism, all waves develop into breakers, suggests that in the vicinity of the breaking wave front, we can simplify the governing equations to the NSW equations. In this work we investigate the effect of an enforced hydrostatic pressure distribution near the wave front and how it can be used to force the transition into a bore. Similar developments have been tried in Boussinesq models, where - by disabling the dispersive terms over the extent of the wave profile once the wave is deemed breaking - the NSW equations are used to model the transition into a bore (e.g. Tonelli and Petti, 2010). The primary advantage of this general approach is that without any calibration the dissipation rate in the breaking wave is ensured to agree with that of a hydraulic jump. However, the location of incipient wave breaking does need to be parametrised.

It is not unreasonable to assume (and results within Chapter 3 corroborate this) that for long-crested waves this approach will give a reasonable approximation of mean dissipation rates and consequently bulk wave parameters (characteristic wave height, mean period). After all, using the bore analogy to derive (stochastic) dissipation rates due to depth induced breaking – including a hydrostatic pressure assumption near the bore front – has been successfully used in phase-averaged models since the work by Battjes and Janssen (1978) and later Thornton and Guza (1983). To

achieve this, the only required step is to locally enforce hydrostatic pressure under a breaking wave. Whether or not this approach is equally successful in predicting bulk parameters for a short-crested wave field is not clear, primarily since the notion of a 'breaking wave', and thus the determination of where to enforce hydrostatic pressure, is not obvious. Naturally, doing this consistently is important, not only for estimating wave dissipation, but subsequently also for driving of mean flows (through radiation stress gradients) and transport processes. Additionally, accurately resolving breaking wave dynamics in the surfzone is important for understanding of the spectral evolution (harmonic generation and driving of infragravity waves) and higher-order statistical quantities such as skewness and asymmetry. These aspects critically depend on the interplay between breaking-induced dissipation, and nonlinear processes (e.g. Chen *et al.*, 1997). Since it is not clear whether such detailed information is resolved in non-hydrostatic models, we investigate the detailed representation of wave dissipation, nonlinearity, and the subsequent spectral evolution in a dissipative surfzone, in this new class of models.

## 2.2. STOCHASTIC WAVE MODELS IN SHALLOW WATERS

Stochastic wave models stand at the heart of modern operational global wave prediction systems. Examples include WAM<sup>9</sup> model (The WAMDI Group, 1988), or WaveWatch (Tolman, 1991), which are routinely used for global and regional-scale wave predictions. These models are fundamentally based on the premise that the wave field (say the free-surface elevation  $\zeta(\mathbf{x}, t)$ ) as a function of space  $\mathbf{x}$  and time  $t$ , can be represented as a zero-mean, quasi-homogeneous and quasi-stationary Gaussian process, which can be fully described by its slowly varying (compared with a typical wave length and period) variance density spectrum  $E(f, \theta, \mathbf{x}, t)$  (Komen *et al.*, 1994). It essentially describes the distribution of variance  $\langle \zeta^2 \rangle$  (where  $\langle \dots \rangle$  denotes the ensemble average), over its spectral components with frequency  $f$  and direction  $\theta$ .

The evolution of the wave spectrum is then obtained by considering a balance equation for the mean wave energy. Such a balance merely states that the change in energy is due to the net energy transported into the area, and the generation and dissipation of energy in that same area. Augmented with transport among spectral components (due to refraction and currents), and formulated in wave number space  $\mathbf{k}$ , it can be written in the form of the Radiative Transport Equation (RTE, Willebrand, 1975; Komen *et al.*, 1994)

$$\partial_t E + \mathbf{c}_x \cdot \nabla_{\mathbf{x}} E + \mathbf{c}_k \cdot \nabla_{\mathbf{k}} E = S, \quad (2.1)$$

with transport velocities  $\mathbf{c}_x(\mathbf{k}, \mathbf{x})$ , and  $\mathbf{c}_k(\mathbf{k}, \mathbf{x})$  in, respectively, geographic  $\mathbf{x}$ -space and spectral  $\mathbf{k}$ -space, and where  $S$  denotes the various source terms. Since its initial inception, much of the development has gone into the improvement of the source terms on the right side of equation (2.1), but the left side of (2.1), the energy balance, has remained unchanged. In deep water, the source terms on the right side of (2.1) include wind generation (Phillips, 1957; Miles, 1957; Cavaleri and Rizzoli,

---

<sup>9</sup>WAve Modelling.

1981; Snyder and Elliott, 1981; Komen *et al.*, 1984), dissipation due to white capping (Hasselmann, 1974; Komen *et al.*, 1994), and four-wave nonlinearity (Philips, 1960; Hasselmann, 1962). The nonlinear term, and the introduction of (economic) approximations thereof (Hasselmann and Hasselmann, 1985), is a cornerstone to the successful development and rapid evolution of this class of so-called third generation models.

Following the success of these models on oceanic scales, a push was made to extend the applicability of stochastic models to the coastal zone. This involves accounting for shallow water processes such as depth-induced breaking (e.g., Salmon *et al.*, 2014b, for an overview), bottom friction (Hasselmann *et al.*, 1973), and the effects of triad interactions (Eldeberky, 1996; Becq-Girard *et al.*, 1999), resulting in the development of the shallow-water stochastic wave models such as SWAN<sup>10</sup> (Booij *et al.*, 1999) and TOMAWAC<sup>11</sup> (Benoit *et al.*, 1996). In general, this approach has been quite successful in predicting bulk statistics of the wave field (Wise Group, 2007), but further improvement of these models in shallow water has primarily focussed on development of the source terms, whereas the underlying premise that the wavefield has near-Gaussian and homogeneous statistics has remained unchanged.

In the deep ocean, where the wave field principally evolves under the action of wind, white-capping and quadruplet interactions, the effects of dispersion and a fairly homogeneous medium, ensures that the conditions of Gaussianity and homogeneity are often reasonable. However, in shallow water, the effects of medium variations and transition to weakly dispersive wave motion, can create spatial coherency (e.g. Janssen *et al.*, 2008), and the representation of nonlinear effects requires higher-order (three-wave) correlations (e.g. Agnon and Sheremet, 1997; Herbers and Burton, 1997; Eldeberky and Madsen, 1999; Herbers *et al.*, 2003). To capture such coherent structures in the wave field, be it introduced through medium variations or nonlinearity, requires the evaluation of additional correlators, and cannot be described by the evolution of auto-covariance contributions alone.

Efforts have been made to describe the evolution of non-Gaussian statistics for special cases, such as the evolution of nonlinear statistics of forward propagating waves over one-dimensional topography (e.g. Agnon and Sheremet, 1997; Herbers and Burton, 1997; Eldeberky and Madsen, 1999; Herbers *et al.*, 2003; Janssen *et al.*, 2008), and inhomogeneous effects in narrow-band waves in deep water (e.g. Alber, 1978; Janssen, 1983; Stiassnie *et al.*, 2008). Invariably, the evolution of non-Gaussian statistics involves accounting for the transport of third-order cross-correlations, i.e. the bispectrum, combined with an (often heuristic) closure assumption. Through additional assumptions (e.g. bandwidth, direction, 1D topography) such models are limited to special cases, and equations describing the 2D (isotropic) evolution of the bispectrum over topography are at present not available, which fundamentally hampers the inclusion of nonlinear effects in shallow water. Instead, spectral evolution is approximated by sometimes rather crude approximations (Eldeberky, 1996; Becq-Girard *et al.*, 1999; Booij *et al.*, 2009; Toledo and Agnon, 2012) to capture the principal nonlinear evolution, but without accounting for the evolution of third-order

---

<sup>10</sup>Simulating WAVes Nearshore.

<sup>11</sup>TELEMAC-based Operational Model Addressing Wave Action Computation.

correlations.

## EVOLUTION OF INHOMOGENEOUS STATISTICS OVER TOPOGRAPHY

Although it is clear that in regions of strong medium variations, which are common in coastal areas, the wave field can develop inhomogeneity, the classic quasi-homogeneous radiative transport approximation does not account for this, and despite many efforts to extend wave modelling to coastal areas, this has received very little attention thus far. To date (to our knowledge), the only stochastic model to include linear interference (diffraction) is based on an angular spectrum decomposition (Janssen, 2006; Janssen *et al.*, 2008), and is therefore restricted to forward wave propagation over weakly two-dimensional topography. A principal issue in the development of an isotropic description which includes heterogeneous effects is that there appears to be no general conservation principle for the complete second-order wave correlation matrix. The energy balance implied by the radiative transfer equation only applies to the energy carrying (variance) components of the correlation matrix, but the inhomogeneous effects associated with the evolution of wave cross-correlations cannot be accounted for in this manner.

The issue can be illustrated by considering the classic case of a narrow-band wave train in intermediate to shallow water ( $kd < 1$ , with  $k$  and  $d$  a characteristic wave number and depth, respectively), propagating over a submerged shoal (see Fig. 2.1) in an otherwise flat region. The effect of the shoal, reminiscent of a lens refracting light, is to focus the waves in the convergence zone down-wave of the shoal. In the region up-wave of the shoal, the wave field can be characterized by its complex amplitude  $a_0$ , and wavenumber  $\mathbf{k}_0$ , so that the spectrum  $E(\mathbf{k}, \mathbf{x})$  takes the form of a single peak near  $\mathbf{k}_0$ , representing the variance  $\langle \frac{1}{2} a_0 a_0^* \rangle$  (where  $*$  denotes the complex conjugate). If we consider the directional wave spectrum in a point behind the shoal, say in a point P along the central ray (see Fig. 2.1), we expect three separate contributions ( $\mathbf{k}_m$ , with  $m = 1 \dots 3$ ), one peak (or wave component) associated with each wave ray. However, since the three rays originate from the same coherent wave front, and are not independent, additional information is needed to fully characterize the second-order statistics of the waves. In addition to the variance (or auto-correlations) denoted as  $\langle \frac{1}{2} a_m a_n^* \rangle$  with  $m = n$ , the cross-variance contributions ( $m \neq n$ ) are required also. In this case, it is obvious that such cross-correlations emerge through the interaction with the topography, but it is not clear how to represent their generation and propagation in a statistical sense.

In the present thesis (Chapter 5) we set out to derive a consistent extension of the radiative transport equation to include such cross-variance contributions, where we follow analogous developments in the context of quantum mechanics and optics (e.g. Bremmer, 1972; Torre, 2005). Essentially, the radiative transfer equation (RTE) represents a particle-like description of the wave field, where each 'wave-energy particle' evolves along its own characteristic path, and is not affected by the presence of the other 'particles' in the field (at least in the linear approximation). The effects of nonlinearity (i.e. quadruplet wave-wave interactions) are included through a particle 'collision' analogy, and although this allows for particle interaction, their behavior is still strictly particle-like. In essence, by deriving transport equations for

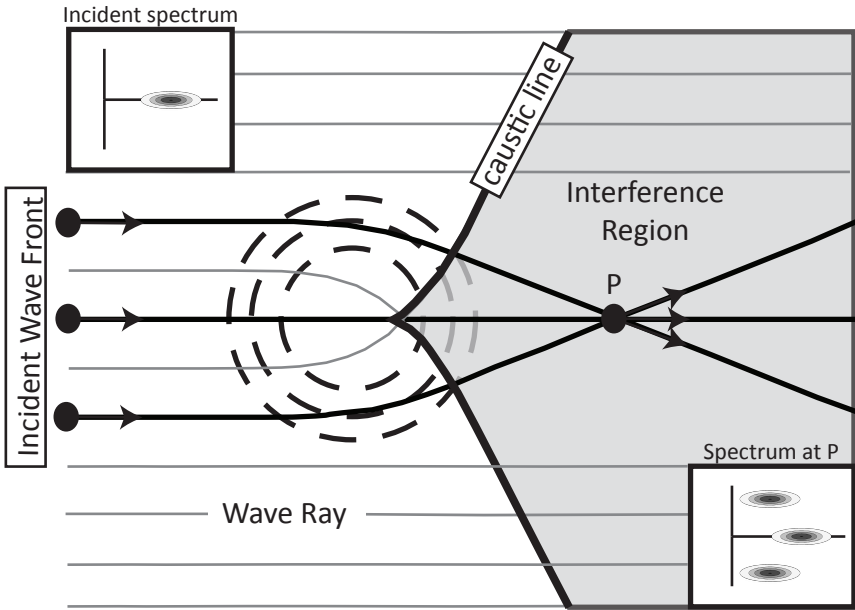


Figure 2.1: Sketch of a possible ray pattern induced by the refraction of a monochromatic, unidirectional wave impinging on a submerged shoal (dashed lines). The shoal focuses the waves so that on the leeward side, across the caustic line, an interference pattern occurs. Radiative transport models correctly predict a singly peaked spectrum in the region before the shoal, but fail to account for the interference that occurs between the peaks in the interference region behind the shoal.

the cross-variances in the wave field, and thus resolving coherent structures in the wave field, wave-like behavior is re-introduced. As a consequence, the total variance at any given location is no longer simply the sum of the variances associated with the individual particles, but depends on constructive and/or destructive coherent interference (wave-like behavior). By including wave-like features to the statistical evolution, the evolution model can account for coherent interference effects and diffraction on the wave statistics.

Principally, if the underlying deterministic equation for the random wave variable, such as the complex-valued free-surface  $\zeta$  (so that  $\eta = \text{Re}\{\zeta\}$ ), can be written in the form

$$\partial_t \zeta(\mathbf{x}, t) = -i\Omega(i\nabla_{\mathbf{x}}, \mathbf{x})\zeta(\mathbf{x}, t), \quad (2.2)$$

where  $\Omega$  is a linear (pseudo-differential) operator, the evolution for the complete second-order statistics can be obtained by multiplication of (2.2) evaluated at  $\mathbf{x}_1$  with  $\zeta^*$  evaluated at  $\mathbf{x}_2$ , adding the conjugate equation evaluated at  $\mathbf{x}_2$  multiplied with  $\zeta_1 = \zeta(\mathbf{x}_1, t)$ , and ensemble averaging the result, which gives

$$\partial_t \langle \zeta_1 \zeta_2^* \rangle = -i [\Omega(i\nabla_{\mathbf{x}_1}, \mathbf{x}_1) - \Omega^*(i\nabla_{\mathbf{x}_2}, \mathbf{x}_2)] \langle \zeta_1 \zeta_2^* \rangle. \quad (2.3)$$

This equation captures the evolution of the full second-order statistics of the field, including cross-correlations – as governed by the deterministic Eq. (2.2). However, the cross-correlator is expected to oscillate rapidly as a function of the spatial co-

ordinates, which makes solving (2.3) directly untenable. Instead, introducing a coordinate transformation, and exchanging a spatial coordinate for a wavenumber coordinate through a Fourier transformation<sup>12</sup> (see Chapter 5 for details), Eq. (2.3) can be transformed into an evolution equation for a distribution function referred to as the Wigner distribution (Wigner, 1932), denoted as  $\mathcal{E}(\mathbf{k}, \mathbf{x}, t)$ . This distribution represents an intermediate form between a spectral, and a spatial description of the second-order statistics, effectively assigning (cross-) variance contributions a definite position and wavenumber, much like the wave packets of the variance density spectrum. Furthermore, under quasi-homogeneous conditions, it becomes a slowly varying function in space and reduces to the variance (or energy) density spectrum. Moreover, irrespective of the spatial variability of the statistics, the marginal distribution (i.e.  $\int \mathcal{E} d\mathbf{k}$ ) always represents the variance (or average potential energy density) of the wave field.

However, for heterogeneous wave fields  $\mathcal{E}$  does not represent an energy density function, nor does the resulting evolution equation reduce to a radiative transfer equation. After all, the cross-variance components in the wave field are not strictly conserved, and can generally fluctuate between positive (constructive interference) and negative (destructive interference) values. For example, in a node of the interference pattern behind the shoal in Fig. 2.1, where due to destructive interference the surface is stationary, three additional interference peaks occur that are of equal magnitude, but opposite sign to those predicted by Quasi-Homogeneous theory; conversely, at point P these same peaks contribute constructively, reflecting the enhanced sea state at the focal point.

Naturally, if such formalism is to be useful, it requires a diligent definition of the operator  $\Omega(i\nabla_{\mathbf{x}}, \mathbf{x})$ , so that (2.2) represents progressive wave motion over topography. For linear wave motion in a uniform medium (constant depth and currents),  $\Omega$  can be expressed as an integral (or alternatively pseudo-differential) operator derived from the dispersion relation. The extension to variable topography is not trivial (see also, e.g. Van Groesen and Andonowati, 2011), and in the present work this is obtained by an appropriate operator association argument (see Chapter 5). Defined in this way the model reproduces classic geometric optics for wave evolution over slowly varying topography, and the resulting equation for  $\mathcal{E}$  reduces to the RTE under quasi-homogeneous conditions (see Chapter 5).

The result is thus what appears to be a natural extension of the radiative transfer equation for regions where the statistics undergo potentially rapid (intra-wave scales) variations due to the presence of inhomogeneities (coherent wave interference) in the wave field, and reduces to quasi-homogeneous theory when the statistics change slowly (infra-wave scales). In the present work we explore the potential of a stochastic wave model derived with this formalism, discuss the implications of the underlying assumptions, and investigate the potential for the use in operational wave models.

---

<sup>12</sup>Specifically:  $\mathcal{E}(\mathbf{k}, \mathbf{x}, t) = (2\pi)^{-2} \int \Gamma(\boldsymbol{\xi}, \mathbf{x}, t) \exp[-i\mathbf{k} \cdot \boldsymbol{\xi}] d\boldsymbol{\xi}$  where  $\Gamma$  denotes the covariance function that is defined as  $\Gamma(\boldsymbol{\xi}, \mathbf{x}, t) = \langle \zeta(\mathbf{x} + \boldsymbol{\xi}/2, t) \zeta^*(\mathbf{x} - \boldsymbol{\xi}/2, t) \rangle$ .



# 3

## Depth-induced wave breaking in a non-hydrostatic, nearshore wave model

The energy dissipation in the surfzone due to wave breaking is inherently accounted for in shock-capturing non-hydrostatic wave models, but this requires high vertical resolutions. To allow coarse vertical resolutions a hydrostatic front approximation is suggested. It assumes a hydrostatic pressure distribution at the front of a breaking wave which ensures that the wave front develops a vertical face. Based on the analogy between a hydraulic jump and a turbulent bore, energy dissipation is accounted for by ensuring conservation of mass and momentum. Results are compared with observations of random, unidirectional waves in wave flumes, and to observations of short-crested waves in a wave basin. These demonstrate that the resulting model can resolve the relevant nearshore wave processes in a short-crested wave-field, including wave breaking and wave-driven horizontal circulations.

### 3.1. INTRODUCTION

Of all the physical processes active in the nearshore, wave breaking often dominates the hydrodynamics in the surfzone. It controls wave setup (e.g. Longuet-Higgins and Stewart, 1964), drives long-shore currents, rip-currents and undertow (e.g. Longuet-Higgins and Stewart, 1964; Longuet-Higgins, 1970; Svendsen, 1984; MacMahan *et al.*, 2006) and is involved in the generation (or release) of infra-gravity waves (e.g. Symonds *et al.*, 1982; Battjes *et al.*, 2004). It is therefore of paramount importance to accurately include the macro-scale effects of wave breaking into coastal wave models describing nearshore hydrodynamics.

---

This chapter has been published as: SMIT, P.B., ZIJLEMA, M. and STELLING, G.S., 2013 Depth-induced breaking in a non-hydrostatic nearshore wave model. *Coast. Eng.*, 76, 1–16.

At present, nearshore, nonlinear wave models of a phase-resolving nature, are usually based on either a Boussinesq-type formulation or a non-hydrostatic approach. Boussinesq models are well established (e.g. Madsen *et al.*, 1991; Nwogu, 1993; Wei *et al.*, 1995) and have been very successful in applications in nearshore regions. However, to increase accuracy, these models have grown quite involved, thereby complicating the numerical implementation. The non-hydrostatic approach is more recent (e.g. Stelling and Zijlema, 2003; Yamazaki *et al.*, 2009; Ma *et al.*, 2012) and uses an implementation of the basic 3D mass and momentum balance equations for a water body with a free surface. The resulting Euler equations can be supplemented with second-order shear-stress terms when required (resulting in the Navier-Stokes equations). The basic difference with conventional Navier-Stokes models is that the free-surface is described using a single-valued function of the horizontal plane. When compared to more involved methods (e.g. Volume of Fluid or Smoothed Particle Hydrodynamics Hirt and Nichols, 1981; Dalrymple and Rogers, 2006), this allows non-hydrostatic models to efficiently compute free surface flows.

However, neither Boussinesq models nor non-hydrostatic models can be directly applied to details of breaking waves, since in both models essential processes such as overturning, air-entrainment and wave generated turbulence, are absent. But, if only the macro-scale effects of wave breaking are of interest, such as the effect on the statistics of wave heights, details of the breaking process can be ignored. By observing that both spilling and plunging breakers eventually evolve into a quasi-steady bore, where the entire front-face of the wave is turbulent (Peregrine, 1983), a breaking wave becomes analogous to a hydraulic jump (e.g. Lamb, 1932). Consequently, its integral properties (rate of energy dissipation, jump height) are approximately captured by regarding the breaking wave as a discontinuity in the flow variables (free surface, velocities). Proper treatment of such a discontinuity in a non-hydrostatic model (conservation of mass and momentum) can therefore be used to determine the energy dissipation of waves in the surfzone (e.g. Hibberd and Peregrine, 1978).

However, compared to the vertical resolutions which are (1–3 layers) sufficient to describe the wave physics outside the surfzone (e.g. refraction, shoaling, diffraction, nonlinear interactions), such a representation of dissipation due to wave breaking requires a disproportional high vertical resolution ( $\sim 10$ – $20$ ). At low resolutions ( $< 5$  layers) the initiation of wave breaking is often delayed when compared to observations, and dissipation in the surfzone is underestimated. Such high resolutions are, at present, not feasibly attainable for extensive horizontal domains (say  $10 \times 10$  wave lengths). Hence, in such cases, an alternative, more efficient approach is required.

To this end we adopt a method which is akin to the approach of Tonelli and Petti (2010) in their Boussinesq model. By enforcing a hydrostatic pressure distribution at the front of a wave, we can locally reduce a non-hydrostatic wave model to the shallow water equations. The wave then rapidly transitions into the characteristic saw-tooth shape and, consistent with the high resolution approach, dissipation is captured by ensuring momentum conservation over the resulting discontinuity. Compared to more involved wave breaking models (e.g. eddy viscosity and surface roller models, Schäffer *et al.*, 1993; Kennedy *et al.*, 2000; Cienfuegos *et al.*, 2010, e.g.), such an approach requires fewer additional parameters (controlling the onset and cessation

of wave dissipation) and is easily extendible to two horizontal dimensions.

In the present work we will demonstrate that: (a) with a sufficiently high vertical resolution non-hydrostatic models can properly determine the dissipation of breaking waves *without* additional model assumptions; and (b) that similar results – at significantly reduced computational cost – can be obtained with a more practical low vertical resolution, *if* locally the non-hydrostatic model is reduced to a hydrostatic model. Furthermore, by comparison to experimental data (Dingemans *et al.*, 1986), we will show that, in contrast to a high resolution model, the latter can be feasibly applied to situations with short-crested waves over two-dimensional topography, including the wave generated mean currents.

This paper is organized as follows: §2 introduces the basic equations that govern the non-hydrostatic model SWASH<sup>1</sup> (Zijlema *et al.*, 2011b) and briefly addresses the relevant details of its numerical implementation. In §3 the hydrostatic front approximation is introduced and in §4 the parameter that controls the onset of wave breaking is estimated from experimental data. Section §5 compares significant wave heights and mean periods obtained from computations using high and low vertical resolutions (using the hydrostatic front approximation) with measured data from flume experiments. Subsequently, in §6 the approximate model is compared to the experiment by Dingemans *et al.* (1986). Finally, we discuss our results and summarize our main findings in §7 and §8.

## 3.2. NON-HYDROSTATIC MODELLING

### GOVERNING EQUATIONS

The non-hydrostatic model SWASH (Zijlema *et al.*, 2011b), is an implementation of the basic 3D mass and momentum balance of a free surface, incompressible fluid with constant density. For reasons of exposition, we present these equations for the 2D vertical plane (the extension to full 3D is straightforward). In terms of Cartesian coordinates  $x, z$  (defined in and normal to the still water level, with  $z$  positive upwards, respectively) and time  $t$ , these equations are

$$\frac{\partial u}{\partial t} + \frac{\partial uu}{\partial x} + \frac{\partial wu}{\partial z} = -\frac{1}{\rho} \frac{\partial(p_h + p_{nh})}{\partial x} + \frac{\partial \tau_{xz}}{\partial z} + \frac{\partial \tau_{xx}}{\partial x} \quad (3.1)$$

$$\frac{\partial w}{\partial t} + \frac{\partial uw}{\partial x} + \frac{\partial ww}{\partial z} = -\frac{1}{\rho} \frac{\partial p_{nh}}{\partial z} + \frac{\partial \tau_{zz}}{\partial z} + \frac{\partial \tau_{zx}}{\partial x} \quad (3.2)$$

$$\frac{\partial u}{\partial x} + \frac{\partial w}{\partial z} = 0, \quad (3.3)$$

in which  $u(x, z, t)$  and  $w(x, z, t)$  are the horizontal and vertical velocity, respectively;  $\rho$  is density;  $p_h$  and  $p_{nh}$  are the hydrostatic and non-hydrostatic pressures, respectively, and  $\tau_{xx}, \tau_{xz}, \tau_{zz}, \tau_{zx}$  are the turbulent stresses. The water column is vertically restricted by the moving free-surface  $\zeta(x, t)$  and stationary bottom  $d(x)$  (measured positive downwards), defined relative to the still water level  $z_0$ . Furthermore, the hydrostatic pressure is explicitly expressed in terms of the free-surface level as

<sup>1</sup>Simulation WAves till SHore, freely available at <http://swash.sourceforge.net/>

$p_h = \rho g(\zeta - z)$  so that  $\partial_z p_h = -g\rho$  (where  $\partial_z$  is short for  $\partial/\partial z$ ) and  $\partial_x p_h = \rho g \partial_x \zeta$  (with  $g = 9.81 \text{ m/s}^2$  the gravitational acceleration). Finally the time evolution of the surface elevation is obtained by considering the mass (or volume) balance for the entire water column

$$\frac{\partial \zeta}{\partial t} + \frac{\partial}{\partial x} \int_{-d}^{\zeta} u \, dz = 0 \quad (3.4)$$

For waves propagating over intermediate distances (say  $O(10)$  characteristic wave lengths), in the absence of strongly sheared currents, the influence of (turbulent-) stresses on the wave motion proper is relatively small (e.g. Mei *et al.*, 2005, Section 9) and can – to a good approximation – be neglected. However, to allow the influence of bottom friction to extend over the vertical (important for low frequency motions), some vertical mixing is introduced by means of stress terms based upon a turbulent viscosity approximation (e.g.  $\tau_{xz} = \nu_v \partial_z u$ , with  $\nu_v$  the vertical mixing coefficient). This also introduces additional vertical coupling, thereby increasing numerical stability. Depending on how well the vertical is resolved the eddy viscosity is estimated with either a constant value, or obtained from a more elaborate  $k - \varepsilon$  closure model (see Appendix A). Finally, to allow for lateral mixing in horizontal circulations due to sub-grid eddies, lateral stresses are added (see Appendix A).

Equations (3.1)–(3.4) are solved for kinematic and dynamic boundary conditions at the surface and at the bottom. The kinematic boundary conditions are that no particle shall leave the surface and no particle shall penetrate the (fixed) bottom, giving

$$w = \frac{\partial \zeta}{\partial t} + u \frac{\partial \zeta}{\partial x} \quad \text{at} \quad z = \zeta(x, t) \quad (3.5)$$

$$w = -u \frac{\partial d}{\partial x} \quad \text{at} \quad z = -d(x) \quad (3.6)$$

The dynamic boundary condition at the surface is a constant pressure (zero atmospheric pressure,  $p_h = p_{nh} = 0$ ) and no surface stresses. Since bottom friction is important for low frequency motions and during wave run-up, a stress term at the bottom boundary  $\tau_b$  is added based on a quadratic friction law

$$\tau_b = c_f \frac{U|U|}{h} \quad (3.7)$$

where  $U$  is the depth averaged current,  $h = d + \zeta$  the water depth and  $c_f$  is a (dimensionless) friction coefficient. A correct estimation of  $c_f$  is important in case of steady horizontal circulations, where the bottom friction balances the forcing by the radiation stress. Here we obtain the friction coefficient from the Manning-Strickler formulation as  $c_f = 0.015 (k/h)^{1/3}$ , where  $k$  is an (apparent) roughness value. In the presence of waves this apparent roughness value is not necessarily related to the bottom roughness. In particular in the surfzone, observations have shown that the apparent roughness (or friction coefficient) can be substantially higher (e.g. Feddersen *et al.*, 2003), because the near bed vertical flux of horizontal momentum is influenced by the breaking induced turbulence. For simplicity, nearshore circulation models often do not separately account for this. Instead, they assume a constant  $c_f$ , which

is obtained by comparison to observations (e.g. Özkan-Haller and Kirby, 1999; Chen *et al.*, 1999; Tonelli and Petti, 2012, among many others). In the present study – for flume-type situations –  $k$  is estimated based upon the surface properties. However, in case of a mean horizontal circulation, we likewise obtain the apparent roughness after calibration.

We assume that the domain is bound horizontally by a rectangular boundary that consists of four vertical planes. Waves are generated by prescribing the horizontal particle velocities normal to the boundary over the vertical. These velocities are either obtained from time-series for each point on the boundary, or by imposing a wave spectrum along the boundary (see Appendix B). Additionally, to allow low frequency wave energy to leave the domain a vertically uniform particle velocity due to this low-frequency motion is included (see Appendix B). At closed boundaries (e.g. vertical walls) the normal velocity is zero and parallel to the boundary a free-slip condition is imposed. If a shoreline is present within the model the boundary is formed by the moving shoreline.

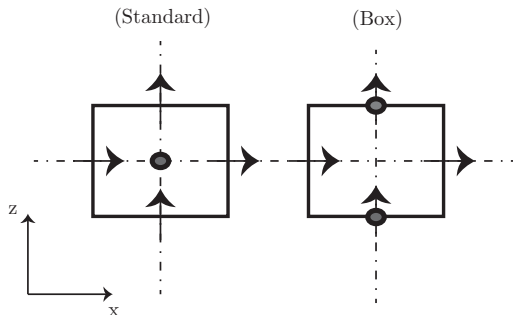


Figure 3.1: The layout of the velocities  $u, w$  (indicated by arrows) and the pressure  $p$  (indicated by dots) for a vertical cell in case of the standard scheme (on the left), and when the Keller Box is used (on the right). The standard scheme uses a conventional staggered layout in both directions ( $x$  and  $z$ ), whereas for the Keller Box scheme  $w$  and  $p$  are both located on the layer interfaces.

## NUMERICAL IMPLEMENTATION

The numerical implementation of SWASH is based on an explicit, second order accurate (in space and time) finite difference method that conserves both mass and momentum at the numerical level. The computational grid consists of columns of constant width  $\Delta x$  and  $\Delta y$  in  $x$ - and  $y$ -direction respectively, vertically discretized with a fixed number of layers of equal thickness between the fixed but spatially varying bottom and the moving, free surface. Horizontally, a staggered grid is employed for the coupling between velocity and pressure. Consequently, the horizontal velocity  $u$  is defined at the central plane of each layer and at the centre of each lateral face of the columns (see Fig. 3.1). The vertical velocities are computed at the interfaces of the layers, at the centre axis of each column. The pressures are also located at the

centre axis of each column, but vertically are located at the central plane (standard layout) or at the layer interface (box scheme).

Depending on the vertical layout of the pressure points, the pressure gradients in the vertical momentum equations are approximated by means of the Keller Box scheme (e.g. Lam and Simpson, 1976) or central differences (e.g. Casulli and Stelling, 1998). At very low vertical resolution (one or two layers), the Box scheme gives good dispersive properties (For two layers roughly 1% error relative to the linear dispersion relation up to  $kd \approx 7$  where  $k$  is a representative wave number Zijlema *et al.*, 2011b), basically because the pressure is defined at both the surface and the bottom (implying a vertical variation, even in a one-layer approach). At high vertical resolutions the standard layout is preferable because it appears to be more robust while its dispersion characteristics are then usually sufficiently accurate. In the present study simulations with 5 layers or less were done with the Keller-Box scheme, while for the other simulations (typically 15–20 layers) the standard layout was employed.

In situations where the wave transforms into a bore, momentum is still conserved on the macro scale of the motion (in nature) whereas energy is not. Preference should then be given to a numerical method that conserves momentum (as in SWASH). Such schemes are conventionally referred to as shock-capturing schemes or approaches (e.g. Hirsch, 2007). To achieve this the advective terms are handled in the manner of Stelling and Duinmeijer (2003). Their approach is momentum conservative, allows for the use of a horizontally staggered grid (thus retaining their efficiency and accuracy, e.g. Stelling, 1983), and is readily extended to three-dimensional, non-hydrostatic flows. In the present study this method was employed in combination with central approximations for the advective fluxes on the cell faces.

When a moving shoreline is present (flooding and drying) it is captured using a simple explicit approach that conserves mass (Stelling and Duinmeijer, 2003). It removes computational (velocity) points from the grid when the water depth  $h$  is below a certain threshold ( $10^{-5}$  m in the present study). Finally, time integration is performed using a time step that, for stability reasons, conforms to the CFL condition  $Cr = \Delta t(c + u)/\Delta x \leq 1$ . Here  $Cr$  is the Courant number and  $c = \sqrt{gh}$  the shallow water wave celerity. For efficiency (and stability) reasons,  $\Delta t$  only remains constant if the maximum of  $Cr$  in the domain remains between two pre-defined values  $Cr_{\min} \leq Cr \leq Cr_{\max}$ , else the time step is either half- or doubled so that the new value again lies within the defined range. For all simulations considered here we set  $Cr_{\min}=0.2$  and  $Cr_{\max}=0.6$  and time steps indicated refer to initial values within that range.

### 3.3. WAVE BREAKING APPROXIMATIONS

The above equations can be directly applied to nonlinear wave motion outside the surfzone. In addition, they can be used to estimate the overall characteristics of a quasi-steady breaking bore in the surfzone, such as its energy dissipation, without needing to resolve complex phenomena such as the overturning of the surface or the wave generated turbulence.

In nature, as the forward pitching of the waves increases, the wave front at a

certain point becomes unstable (spilling breakers), or overturns (plunging breakers) and the entire front face of the wave becomes turbulent. Even though the nonlinear processes that induced the steepening are still present, the downward transport of momentum due to the turbulent stresses stabilize the bore front (Madsen and Svendsen, 1983), and a quasi-steady bore develops. In the model the turbulent motions generated by the breaking process, and thus their stabilizing effects, are not accounted for. Hence, the steepness of the front continues to increase and eventually a jump-discontinuity, with a jump-height equal to the local wave height  $H$ , will develop. By enforcing strict momentum conservation across the discontinuity the energy dissipation rate is then proportional to  $H^3$ , similar to the dissipation rate found in an hydraulic jump (e.g. Lamb, 1932). In the model the flow field in the entire water column below the turbulent front (between trough and crest) is thus considered as a sub-grid phenomenon. Such a treatment of wave breaking has the advantage that it does not require any additional measures, for instance, to initiate or stop breaking, nor a separate approximation to explicitly account for the energy dissipation. However, it does require a high horizontal and vertical resolution.

For relatively small domains the required horizontal resolution is fairly constant, and is typically  $1/50$  or  $1/100$  of the dominant wave length. However, the necessary vertical resolution can change considerably in the domain. For mildly nonlinear waves ( $H/d \leq 0.1-0.4$ ) propagating from intermediate ( $kd \sim 1$ ) into shallow water ( $kd \ll 1$ ), the vertical gradients in the pressure and particle velocities remain small. An accurate description of the flow can then be achieved with a relatively low vertical resolution (1–3 layers). But, due to the decreasing water depth and wave shoaling, the importance of nonlinearity increases ( $H/d$  becomes  $O(1)$ ) and, concurrent with the forward pitching of the waves, strong vertical gradients in the particle velocities develop. In the vicinity of the point where the wave becomes unstable, flow velocities in the upper half of the water column, i.e., near the crest, approach the wave celerity (e.g. Sakai and Iwagaki, 1978; Van Dorn, 1978), whereas in the lower half velocities remain much smaller ( $u/c \sim 0.1-0.4$ , with  $c$  the wave celerity). An accurate description of the flow in the region just prior to the breakpoint thus requires a comparatively high vertical resolution (10–20 layers).

Once a turbulent bore is formed, vertical velocity gradients directly under the front remain large (e.g. Van Dorn, 1978; Stive, 1980; Lin and Liu, 1998), but the relative importance of the non-hydrostatic pressure gradient diminishes, and its influence on the depth integrated momentum balance becomes small (e.g. Madsen and Svendsen, 1983). In fact, measurements (e.g. Stive, 1980) and computations with more advanced models (e.g. Lin and Liu, 1998) indicate that near the bed the maximum deviation from hydrostatic pressure at the bore front is in the order of 10 percent. Moreover, in the regions before and after the turbulent front, the pressure is approximately hydrostatic, and the horizontal particle velocity is almost depth uniform. Since, in the model the front is not resolved, a relatively low-vertical resolution could be applied again.

### HYDROSTATIC FRONT APPROXIMATION

A coarse vertical resolution can thus be applied almost everywhere in the nearshore, except to predict the onset of wave-breaking. Here, a coarse resolution will result in an underestimation of the horizontal velocities near the crest, and thus an underestimation of the nonlinear (advective) contributions. This underestimation implies that at low vertical resolution the influence of the non-hydrostatic pressure gradient is overestimated. Consequently, the stabilizing dispersive effects (i.e. the non-hydrostatic pressures) postpone the transition into the characteristic saw-tooth shape and therefore also the onset of dissipation.

The subsequent dissipation is well described by assuming depth uniform velocities and a hydrostatic pressure distribution. In fact, these assumptions often form the basis to derive dissipation formulations to account for depth induced breaking in energy balance type models (e.g. Battjes and Janssen, 1978, among many others). Hence, prescribing a hydrostatic pressure distribution in the model around the discontinuity should result in the correct bulk dissipation. The model then reduces to the conventional nonlinear shallow water equations (NSWE), which previously have been successfully applied in the surfzone (e.g. Peregrine, 1983), supporting this conjecture.

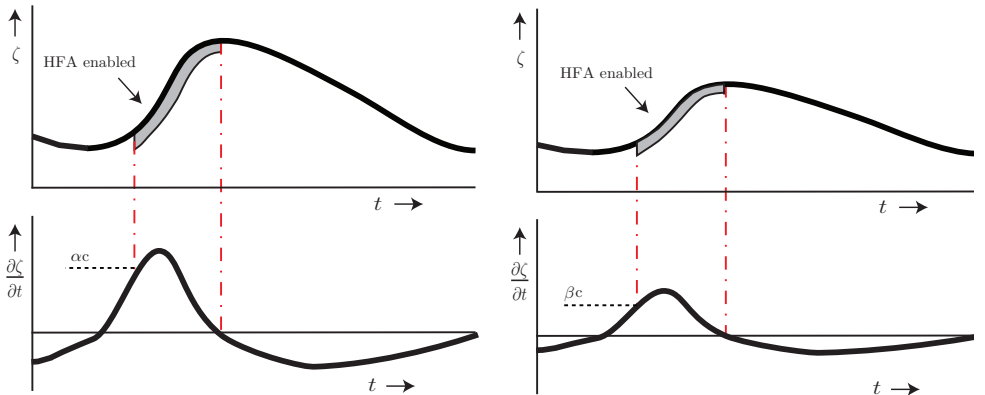


Figure 3.2: Sketch of the free surface  $\zeta$  (top panels) and the rate of surface rise  $\partial_t \zeta$  (bottom panels) as a function of time. Grey patches indicate regions where the HFA is enabled based on  $\partial_t \zeta > \alpha c$  (left panels) or on the reduced criterion  $\partial_t \zeta > \beta c$ , if the HFA is active in a neighbouring point (right panels).

There is no need to assume a hydrostatic pressure distribution if the vertical resolution is sufficient. However, imposing a hydrostatic distribution resolutions at low resolutions will ensure that, due the absence of dispersive effects, the front quickly transitions into a bore like shape. Hence, it can be used to initiate the onset of wave-breaking, thus allowing for the use of low-vertical resolutions throughout the domain. This approach, which we refer to as the Hydrostatic Front Approximation (HFA), is akin to the disabling of the dispersive terms in the Boussinesq equations (Tonelli and Petti, 2010; Tissier *et al.*, 2012) and essentially regards the entire turbulent front as

a sub-grid feature of the flow. In practice this means that once a mesh-point is in the front of a breaking wave, vertical accelerations are no longer resolved, and the non-hydrostatic pressure is set to zero.

The boundary of the horizontal region in which the model should operate in hydrostatic mode, as described above, varies in time and horizontal space. We assume that this mode is valid if the local surface steepness  $\partial_x \zeta$  exceeds a predetermined value  $|\partial_x \zeta| > \alpha$ . However, this criterion was found to be sensitive to numerical noise in the surface elevation. As an alternative we therefore consider the evolution equation for a shallow-water wave of constant form over a flat bottom (e.g.  $\partial_t \zeta + c \partial_x \zeta = 0$ ) and re-express the steepness criterion in terms of the rate of surface rise, i.e.  $\partial_t \zeta > \alpha c$  (Kennedy *et al.*, 2000, see also Appendix C). The wave celerity is estimated as  $c = c' + \Delta c$ , with  $c' = \sqrt{gh}$  the wave celerity in the absence of an ambient current. Here  $\Delta c = \bar{U} \cos \Delta \theta$  is a correction to  $c$  due to the presence of an ambient current with magnitude  $\bar{U}$  at a mutual angle of  $\Delta \theta$  with the wave direction (e.g. for a strictly following or opposing current  $\Delta c = \pm \bar{U}$ ).

This criterion has the advantage that for a weak ambient current ( $\bar{U}/c' \ll 1$ ) it is based on local scalar quantities and independent of wave direction (as  $\Delta c \approx 0$ ) so that it can be used unmodified in either one- or two-dimensional situations. This contrasts with criteria based on the wave profile (e.g. wave height, Tonelli and Petti, 2010), the extension of which to two horizontal dimensions is generally not trivial. However a disadvantage is that when  $\bar{U}/c' \sim O(1)$  such a criterion is Doppler shifted, potentially resulting in premature or delayed activation of the HFA. In this case  $\Delta c$  should be included, requiring estimation of the the ambient current vector  $\bar{U}$  and its mutual angle to the local instantaneous wave direction. For a non-blocking current these can be estimated in the manner as described in Appendix B.

A grid point is therefore labelled for hydrostatic computation if  $\partial_t \zeta > \alpha c$ . Once labelled, a point only becomes non-hydrostatic again if the crest of the wave has passed. This is assumed to occur when  $\partial_t \zeta < 0$ . Furthermore, because grid points only become active again when the crest passes (where  $w \approx 0$ ), vertical velocities (essentially diagnostic variables when the pressure is hydrostatic) are set to  $w = 0$  on the front. To represent persistence of wave breaking, we locally reduce the criterion  $\alpha$  to  $\beta$  if a neighbouring grid point (in  $x$ - or  $y$ -direction) has been labelled for hydrostatic computation. In this case a point is thus also labelled for hydrostatic computation if  $\partial_t \zeta > \beta c$ , with  $\beta < \alpha$ . In all other grid points, the computations are non-hydrostatic. The activation and deactivation of the HFA based upon these considerations is illustrated in Fig. 3.2.

The range of maximum steepness (or  $\alpha$ ) values found in the literature is relatively wide, ranging from  $\alpha = 0.3$  (Schäffer *et al.*, 1993) to  $\alpha = 0.6$  (Lynett, 2006), because its value is sensitive to how well the model can represent the wave shape for highly nonlinear waves. Hence, to estimate  $\alpha$ , we use experimental data (see §4) to obtain its model value near observed breaking locations. This results in  $\alpha = 0.6$ . The value for the persistence parameter  $\beta$  also depends on the model behaviour in the surfzone, and for the cases considered in the present work  $\beta = 0.3$  appears to give reasonable results. Because we represent a breaking wave as a shock, this is substantially higher than reported values of a similar parameter in Boussinesq models, which ranges from

0.15 to 0.18 (Schäffer *et al.*, 1993; Kennedy *et al.*, 2000; Lynett, 2006; Cienfuegos *et al.*, 2010).

Finally, if the HFA is used some additional horizontal viscosity is included to prevent generation of high frequency noise in the wave profile due to the discrete activation of the HFA. These frequencies are introduced because the model has to adapt to the enforced hydrostatic pressure distribution. Assuming that the strength of such components is related to local gradients in the horizontal particle velocity, the additional viscosity  $\nu_h^{\text{HFA}}$ , included once the HFA is activated, is expressed as

$$\nu_h^{\text{HFA}} = L_{\text{mix}}^2 \sqrt{\left(\frac{\partial U_1}{\partial x_1}\right)^2 + \left(\frac{\partial U_2}{\partial x_2}\right)^2} \quad (3.8)$$

where  $L_{\text{mix}}$  is a typical horizontal length scale over which mixing occurs which we assume is a fraction  $\mu$  of the local depth, i.e.  $L_{\text{mix}} = \mu h$ . Once sufficient dissipation is present, the predicted wave height become relatively insensitive to a broad range of values for  $\mu$  (0.75 – 3, see next section). This insensitivity confirms that the primary dissipation mechanism is due to the formation of a shock. The inclusion of the additional viscosity is mainly intended to prevent spurious components, and we primarily regard  $\mu$  as a numerical parameter and therefore simply set  $\mu = 1$  without further calibration.

### 3.4. MONOCHROMATIC WAVE BREAKING OVER A SLOPING BEACH

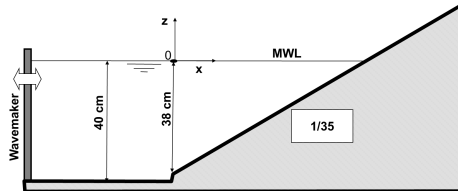


Figure 3.3: The experimental setup from Ting and Kirby (1994)

To demonstrate that the estimation of dissipation by wave breaking is reasonably accurate in SWASH, and to estimate the steepness  $\alpha$  that controls the onset of dissipation, we consider two laboratory experiments by Ting and Kirby (1994). In these experiments, mechanically generated, monochromatic, cnoidal-type waves (wave height  $H=0.125$  m; period  $T=2$  s or 5 s) propagate in a flume (40 m long, 0.6 m wide and 1 m deep) over a 1/35 plane beach (see Fig. 3.3). In the experiment with  $T = 2$  s, the breaking waves are of the spilling type, whereas they are of the plunging type in the experiment with  $T = 5$  s. After steady conditions were reached, measurements of the free surface elevation were taken throughout the tank for a duration of 102 periods. Here SWASH is employed with a horizontal resolution of  $\Delta x=0.025$  m

and an initial time step of  $\Delta t=0.001$  s. Simulations are performed with a high (20 layers) and low (2–5 layers) vertical resolutions. In the high resolution computations the HFA is always disabled. At low resolutions, simulations with and without the HFA are conducted. At the incoming boundary we impose a second-order cnoidal wave solution for the velocities (e.g. Svendsen, 2006, section 9.5), including a mass flux contribution due to the return flow.

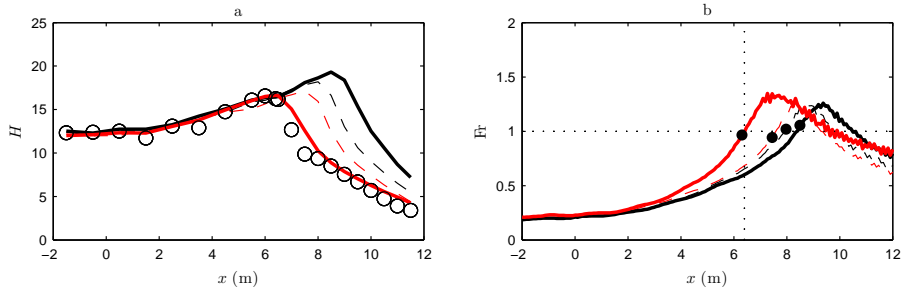


Figure 3.4: Wave heights  $H$  for spilling breakers in the Ting and Kirby (1994) experiment on the left (panel a) and maximum Froude number  $Fr (= u_{\max}/\sqrt{gd})$  in the upper most layer for different vertical model resolutions on the right (panel b). Comparison between measurements (circle markers, only for wave heights) and computations without HFA using two (solid black line), three (dashed black line), five (dashed red line) and twenty (solid red line) layers. In the right panel dots indicate the location of the maximum wave height in the respective simulations and the dotted vertical line indicates the observed breakpoint that is located near the maximum observed wave height.

To illustrate the erroneous model behaviour at low vertical resolutions, we first carry out computations without the HFA for the spilling breaker case using 2, 3, 5 and 20 layers. The resulting wave heights compared with observations are shown in Fig. 3.4a. It is clearly seen that at the lower resolutions (2–5 layers), compared with the observations, the onset of dissipation is postponed. Once the vertical resolution becomes sufficiently high (20 layers), wave heights correspond well with the observations. Inspection of the particle velocities in the upper layer shows, that the onset of breaking in the computations approximately coincides with the occurrence of supercritical flow, i.e.  $u_{\max}/\sqrt{gd} > 1$ . Here  $u_{\max}$  is the maximum velocity that occurs during a wave period (see Fig. 3.4b). Thus, wave breaking is initiated when velocities exceed the wave celerity. When the vertical resolution is coarse, particle velocities near the free-surface are simply underestimated ( $Fr < 1$ , see 3.4b), and the formation of a shock wave – and therefore the onset of dissipation – is delayed.

In the region prior to the observed breaking location, which occurred where the observed wave height attained its maximum ( $x = 6.45$  m, Ting and Kirby, 1994), computed wave heights are insensitive to the vertical resolution. This confirms that outside the surfzone a coarse resolution (2 layers) suffices. To investigate if enabling the HFA can improve results in the surfzone, we must first estimate the breaker parameter  $\alpha$ . Hereto, we obtain the maximum value of  $\partial_t \zeta$  at the observed breaking location ( $x = 6.45$  m) from the previous calculations; this was found to be approximately  $\partial_t \zeta = (0.6 \pm 0.04)c'$ . Hence,  $\alpha=0.6$ , which was also found by (Lynett, 2006)

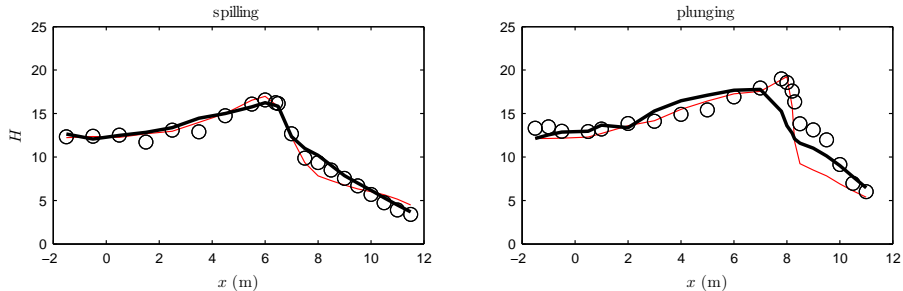


Figure 3.5: Wave heights  $H$  for spilling (left panel) and plunging (right panel) breakers in the Ting and Kirby (1994) experiment. Comparison between measurements (circle markers) and computations using two layers with HFA (black line), and twenty layers (thin line).

suggesting that model behaviour near the breaking point at lower resolutions is similar to his multi-layered Boussinesq model.

The wave height evolution, but now with HFA (using  $\alpha = 0.6$ ) at low resolutions (2 layers), is shown in Fig. 3.5. In the experiment with spilling breakers, both high and low resolution computations now predict the evolution of the wave height well. The location of the outer edge of the surfzone, the maximum wave height there and the decay inside the surfzone are well reproduced. In the experiment with plunging breakers dissipation is initially overestimated. At that location the physics of a plunging breaker are poorly described by a bore analogy, but deep in the surfzone a quasi-stationary bore is formed, and the computational results converge towards the observations (for  $x > 10\text{m}$ ). In the low-resolution computations, the over-estimation of the dissipation starts just outside the surfzone. Again, deep in the surfzone the computational results converge towards the observations (for  $x > 10\text{m}$ ).

Outside the surfzone the wave profile is well reproduced ( $x < 6.4\text{ m}$  and  $x < 7.9\text{ m}$  for respectively the spilling breaker and plunging breakers experiments), although the slope of the wave front is slightly too gentle for the spilling waves (see Fig. 3.6). Inside the surfzone, the absence of the stabilizing effects of turbulence in the high-resolution computations, results in a continued steepening of the front of both spilling and plunging breakers until it is almost vertical in case of the plunging breakers. This contrasts with the effects of the added horizontal viscosity in the low-resolution computations. This viscosity, which was added for numerical reasons in the HFA, counteracts wave steepening such that the wave fronts are slightly less steep than observed.

The maximum wave-induced setup is predicted well (see Fig. 3.7), particularly in the plunging breaker case where the error in the wave height is relatively large (i.e., 20%). This indicates that the radiation stress gradient in SWASH is well predicted even if the wave height is (slightly) under-estimated. It does appear that for spilling breakers neither model is able to reproduce the observed jump in mean water level (MWL) around  $x = 5\text{m}$ . This jump precedes the decrease in wave height, so that its physical origins are not obvious. This jump is also absent in results that were

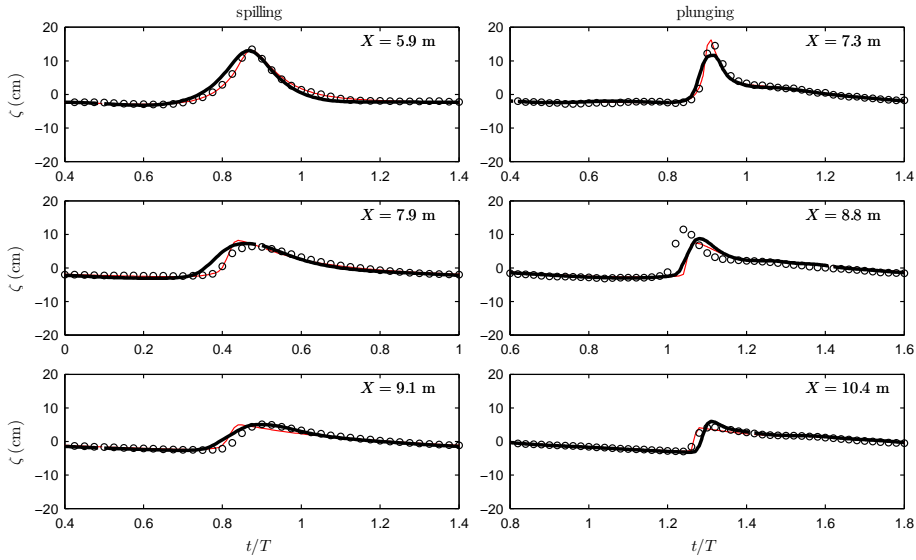


Figure 3.6: Phase-averaged profiles of the free surface elevation  $\zeta$  for spilling (left panel) and plunging (right panel) breaking waves at the indicated locations. Comparison between measurements (circle markers) and computations using two layers with HFA (black line), and twenty layers (thin lines).

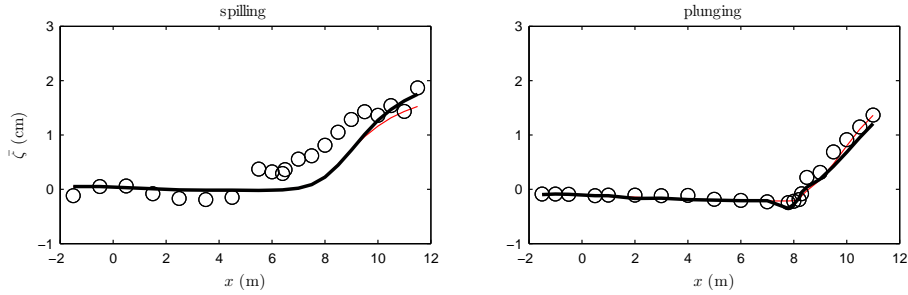


Figure 3.7: Mean water-level setup  $\bar{\zeta}$  for spilling (left panel) and plunging (right panel) breakers in the Ting and Kirby (1994) experiment. Comparison between measurements (circle markers) and computations using two layers with HFA (black line), and twenty layers (thin line).

obtained by others (e.g. Cienfuegos *et al.*, 2010; Tonelli and Petti, 2010), and

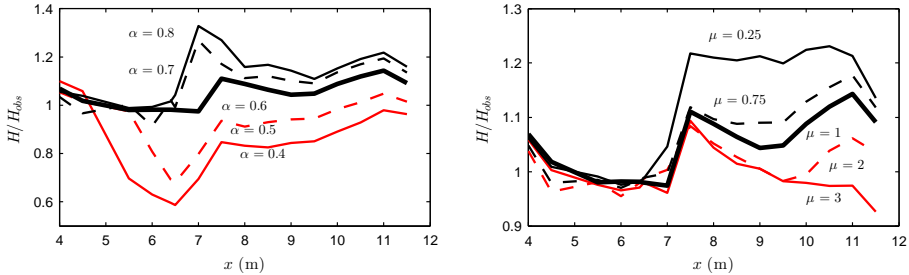


Figure 3.8: Sensitivity of computed wave heights (normalized with observations) in case of spilling breakers to variations in the maximum steepness  $\alpha$  (left panel) and relative mixing length  $\mu$  (right panel).

Finally, the sensitivity of computed wave heights to changes in  $\alpha$  (0.4–0.8) and  $\mu$  (0.25–3) is shown in Fig. 3.8. Results are scaled with the observed wave heights to better illustrate the differences, especially where wave heights are low. As anticipated, variation of  $\alpha$  either causes premature ( $\alpha < 0.6$ ) or delayed ( $\alpha > 0.6$ ) initiation of dissipation, therefore resulting in over- and under-prediction of wave heights in the surfzone. Sensitivity of results to  $\mu$  appears to be relatively small. Increasing  $\mu$  from 0.25 to 3, a twelvefold increase, gives 30 percent difference in wave heights. Best correspondence is obtained with  $\mu=2$ , but differences mainly occur deep in the surfzone where wave heights are small, and within the range  $\mu = 0.75$ –3 results are therefore not significantly different.

In general, the low-resolution computations (the two-layer model) combined with the Hydrostatic Front Approximation, reproduces wave heights and wave profiles quite accurately inside and outside the surfzone, although slightly better for spilling breakers than for plunging breakers. However, it must be emphasized that the low resolution computation with HFA uses the  $\alpha$  value estimated from this same experiment. Conversely, the high-resolution computation does not use any information from the experiment. This demonstrates that the high resolution can inherently describe dissipation due to breaking without additional measures.

### 3.5. RANDOM WAVES BREAKING OVER BARRED TOPOGRAPHY

To verify the two approaches of the high (15 layers) and low (2 layer) resolution with the estimated coefficient from the Ting and Kirby (1994) experiment, we compare model predictions with laboratory measurements that include depth-induced breaking of broad-banded random waves over 1D barred topographies.

We consider laboratory experiments by Battjes and Janssen (1978), Dingemans *et al.* (1986), Boers (1996) and Van Gent and Doorn (2000). In all experiments (except one) a wave maker situated at the end of a 1D flume generated broad banded waves that propagated over a bar-type topography (see Fig. 3.9) where a large portion

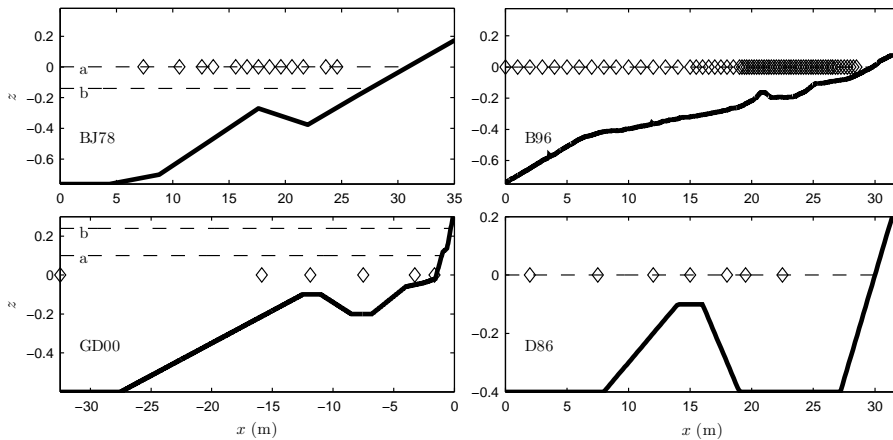


Figure 3.9: Layout of the different flume experiments depicting the bed level locations  $z$  (thick solid line), still water level(s) (dashed lines) and wave gauges (diamonds).

Table 3.1: Wave parameters at the boundary for the different flume experiments. Listed are the names as used here (Experiment) and as referred to in the original study (their case), the significant wave height  $H_{m0}$ , peak period  $T_p$ , relative depth  $k_p d$  (with  $k_p$  the wave number at the peak), relative wave height  $H_{m0}/d$  and still water level  $z_0$ .

Experiment	their case	$H_{m0}$ (m)	$T_p$ (s)	$k_p d$	$H_{m0}/d$	$z_0$ (m)
Battjes and Janssen (1978)a	run 13	0.147	2.01	1	0.19	0
Battjes and Janssen (1978)b	run 15	0.202	1.89	1.07	0.27	-0.14
Boers (1996)a	1A	0.157	2.05	0.96	0.2	0.
Boers (1996)b	1B	0.206	2.03	0.97	0.27	0.
Boers (1996)c	1C	0.103	3.33	0.55	0.13	0.
Dingemans <i>et al.</i> (1986)a	me25	0.1	1.25	1.22	0.25	0.
Van Gent and Doorn (2000)a	test 1.04	0.11	1.42/1.8	1.45	0.17	0.05
Van Gent and Doorn (2000)b	test 2.51	0.15	1.77	1.13	0.21	0.11

of the wave energy is dissipated by wave breaking. The exception is the experiment by Dingemans *et al.* (1986) which was carried out in a 2D basin, but the variation across the basin was sufficiently small that it can be treated as a 1D experiment. With the exception of Van Gent and Doorn (2000), which used a double peaked spectrum obtained from scaled-down version of field measurements during a storm at the north sea coast of the Netherlands (Petten sea defence), wave spectra at the boundary are JONSWAP spectra (Hasselmann *et al.*, 1973). A summary of the wave parameters at the wave maker in each of the experiments is given in Tab. 1.

In each case the numerical model is set-up along a one-dimensional transect of length  $L_f$  (with horizontal resolution  $\Delta x$ ) in the centre of the flume (or basin), and ran for a duration  $D$  (with initial time step  $\Delta t$ ). For case specific model parameters we refer to Table 3.2. At the wave maker boundary a wave spectrum is imposed, whereas at the opposite boundary wave energy is dissipated at a numerical beach. After a spin-up time of  $D_s$  ( $\geq 4L_f/c_g$ , using the group velocity  $c_g(f_p)$  calculated

Table 3.2: Numerical setup used to simulate the flume experiments. Listed are the horizontal mesh-size  $\Delta x$ , initial time step  $\Delta t$ , domain length  $L_f$ , duration  $D$ , output duration  $D_o$  and sampling rate  $f_s$ .

Experiment	$\Delta x$ (m)	$\Delta t$ (s)	$L_f$ (m)	$D$ (s)	$D_o$ (s)	$f_s$ (Hz)
Battjes and Janssen (1978)a	0.04	0.005	38.8	1890	1800	10
Battjes and Janssen (1978)b	0.05	0.005	38.8	1890	1800	10
Boers (1996)a	0.02	0.002	32.	1890	1800	10
Boers (1996)b	0.02	0.002	32.	1890	1800	10
Boers (1996)c	0.02	0.002	32.	2460	2400	5
Dingemans <i>et al.</i> (1986)a	0.02	0.005	2400	1350	20	20
Van Gent and Doorn (2000)a	0.025	0.0025	32.5	1290	1200	10
Van Gent and Doorn (2000)b	0.025	0.0025	32.5	1320	1200	10

at the boundary), output is generated using a sampling frequency of  $f_s \approx 20f_p$  for a duration of  $D_o$  seconds. Variance density spectra are generated using the recorded free surface elevations (with 60 degrees of freedom and  $\Delta f = 30/D_o$ ). In the present work we primarily compare integral parameters derived from the moments  $m_n (= \int f^n E(f) df)$  of the measured variance density spectra  $E(f)$  (with  $f$  frequency). These include the significant wave height  $H_{m_0} (= 4m_0^{0.5})$  and the mean zero-crossing period  $T_{m_{02}} (= (m_0/m_2)^{0.5})$ . Prior to calculating the integral primary wave parameters the spectra were band-pass filtered (pass-band  $0.5f_p \leq f \leq 4f_p$ ). This is done to exclude infra-gravity wave energy and prevent undue influence on estimates of  $T_{m_{02}}$  by errors in the high frequency tail.

The computed significant wave heights are compared with observations in Fig. 3.10. It is obvious that the high- and the low-resolution computations predict the development the significant wave height well. This implies that both types of computations correctly predict the onset of breaking, and the continued dissipation inside the surfzone. In this respect the two types of computations are similar, although the high resolution results are generally slightly better. Furthermore, not only is the onset and rate of breaking well predicted, but also the reduction of breaking when the waves enter deeper water between two bars or between a bar and the beach. This is visible behind the bar in the Dingemans *et al.* (1986) experiment, and to a lesser extent between the two bars ( $20 < x < 25$ ) in the Boers (1996) experiments. Moreover, SWASH reproduces the wave height evolution reasonably well when breaking is mild and therefore the wave decay gentle. For instance in (Boers, 1996)b, and to a lesser extent (Boers, 1996)a, the wave conditions were such that a small fraction of the waves (a: 0–5% percent, b: 10–15% percent) were 'breaking' (white water near the crest) on the gentle foreshore ( $x < 17\text{m}$ ) in front of the bar (Boers, 2005). Since the criterion of breaking is identical for each individual wave, the difference in intensity of breaking is due to the difference in the fraction of breaking waves.

The computed mean wave periods, in all cases (except one) defined as  $T_{m_{02}}$ , are compared in Fig. 3.11 with the observed mean wave periods. The exception is the Dingemans *et al.* (1986) experiment, where the comparison is between the mean zero-crossing periods  $T_0$  obtained from a zero-crossing analysis of the time-series (observations of  $T_{m_{02}}$  were unavailable). Furthermore, only 6 cases are shown, since the required information is not available for the experiment of Battjes and Janssen

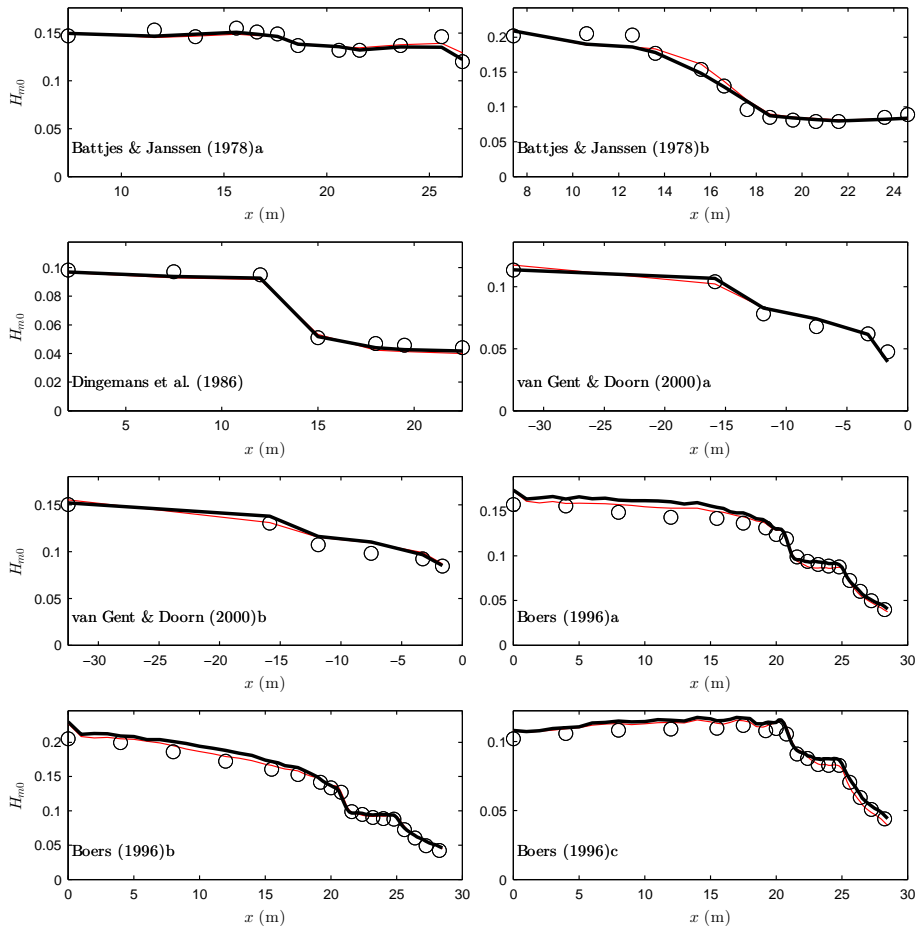


Figure 3.10: Spatial variation of the significant wave height  $H_{m0}$  in the various experiments. Comparison between measured (circle markers) and predicted values (low resolution model: black line, high resolution model: thin line).

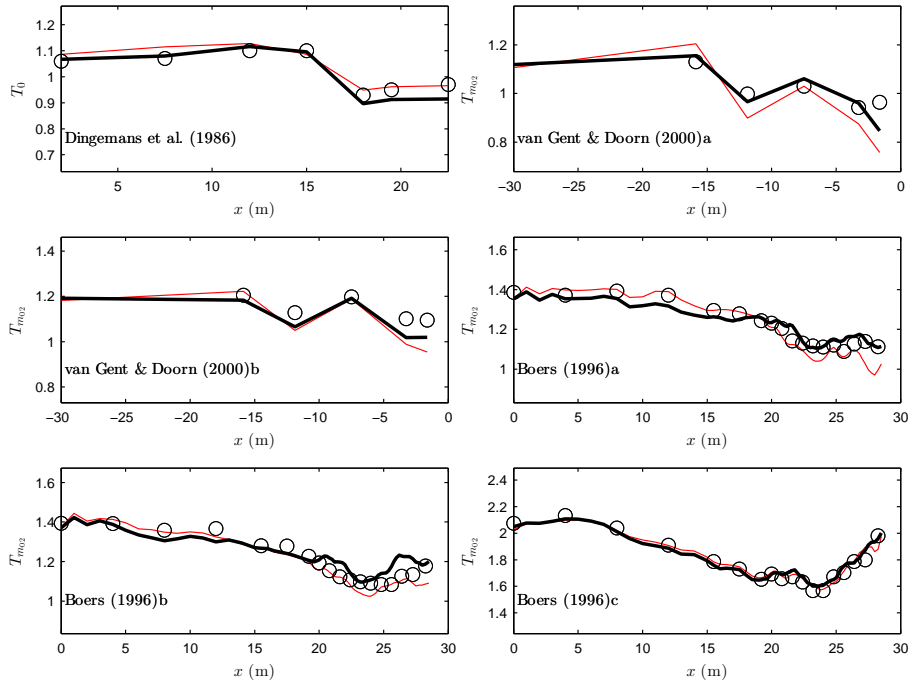


Figure 3.11: Spatial variation of the mean zero-crossing period  $T_0$  (Dingemans *et al.* (1986), top left panel) or  $T_{m02}$  (other panels) in the various experiments. Comparison between measured (circle markers) and predicted values (low resolution model: black line, high resolution model: thin line).

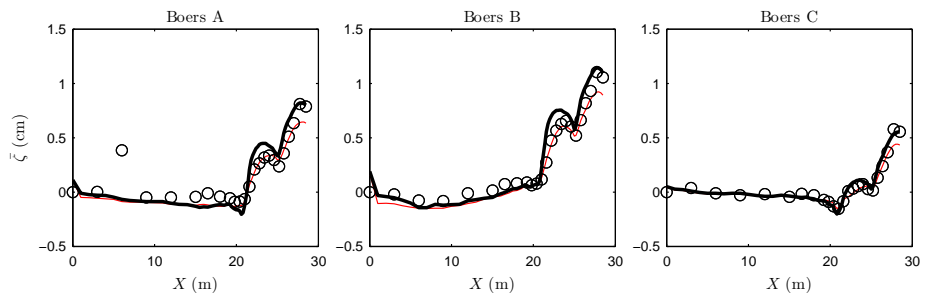


Figure 3.12: Mean water-level setup  $\bar{\zeta}$  in Boers (1996), case a–c. Comparison between measured (circle markers) and predicted values (low resolution model: black line, high resolution model: thin line).

(1978). Both high- and low-resolution models reproduce the observed periods well outside the surfzone. Inside the surfzone discrepancies with the observed periods are somewhat larger, resulting in for instance an underestimation of the mean periods in Van Gent and Doorn (2000)b, but overall predictions for the mean periods are reasonable for both models.

The computed wave induced setup is compared to observations from Boers (1996) in Fig. 3.12. For the other cases the observed mean water levels were not available. The high resolution model slightly underestimates the maximum setup near the shoreline, whereas the low-resolution model somewhat overestimates the setup on the bar in cases A and B. However, in general, both models are able to predict the mean water level setup due to the gradients in the radiation stress well.

### 3.6. SHORT-CRESTED WAVES OVER 2D TOPOGRAPHY

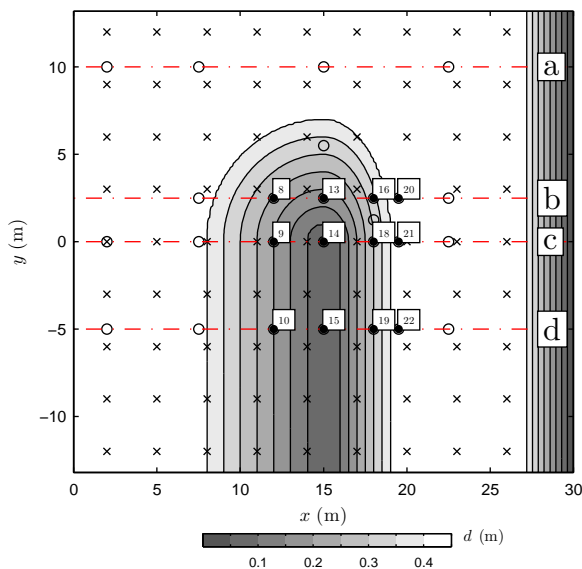


Figure 3.13: Depth contours at 5 cm intervals of the Dingemans *et al.* (1986) experiment (case me35). Wave gauges and current meters are indicated with circle markers and crosses respectively. The solid circles indicate selected gauges for which the wave spectrum is given in Fig. 3.16

The final test in this study is the application of SWASH to a case in the 2D basin of Dingemans *et al.* (1986), but now with a submerged breakwater extending across half the basin (see Fig. 3.13), so that in this case the situation is two-dimensional with the waves inducing a net horizontal circulation. The selected case is of particular interest as it includes short-crested waves, thus enabling us to ascertain how well the HFA performs under field-type conditions. Furthermore, the observations encompass roughly 1500 wave periods, which combined with the extensive horizontal extent of the basin ( $17 \times 13$  wave lengths), implies that using high vertical resolutions is no

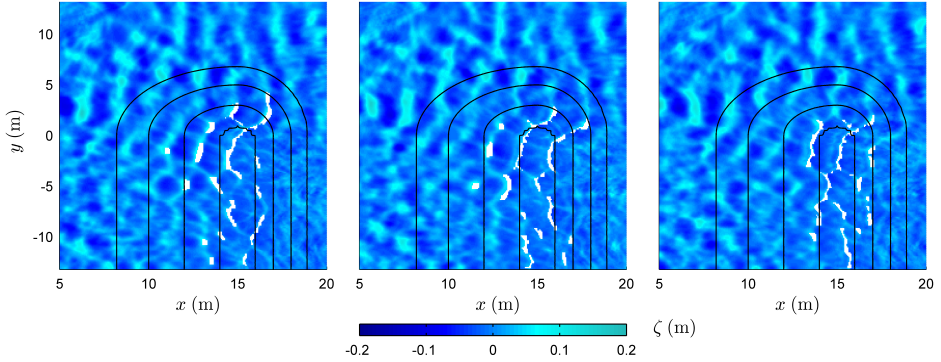


Figure 3.14: Three successive snapshots of the free surface taken 0.8 s apart ( $\sim$  one wave period). The first snapshot, after roughly 31 minutes, has been randomly selected. White patches indicate regions where the HFA is active. Depth contour lines (from 0.4 m to 0.1 m at 0.1 m intervals) depict the location of the breakwater.

longer feasible.

The observations of Dingemans *et al.* (1986) were obtained in a 2D basin of  $34 \times 26.4$  m<sup>2</sup> surface area in which short-crested waves were generated along the shorter side. A submerged bar, parallel with the wave maker, spanned half across an otherwise flat basin (water depth was 0.4 m). Both bar and basin floor were covered with smoothly finished concrete. Over the horizontal top of the submerged bar, which was 2 m long in the wave direction, the still water depth was 0.1 m. The approach slope was 1:20 and the back slope was 1:10. The side walls of the basin were fully reflective and the back wall was a wave-absorbing gravel beach with a 1:7 slope. The incident wave spectrum was a standard JONSWAP spectrum with significant wave height 0.097 m and peak frequency 0.80 Hz (i.e. wave length  $\sim$ 2 m). The observed  $H_{m_0}$  varied slightly along the stations near the wave maker (by less than 10%), and on average was approximately 0.105 m. The short-crestedness was defined with a  $\cos^m \theta$ -directional energy distribution at the wave maker (with  $m=4$ , or a directional width of  $25^\circ$  Kuik *et al.*, 1988) and mean direction normal to the breakwater, i.e.  $\theta_0=0^\circ$ . The surface elevation was measured at 26 locations (see Fig. 3.13) and currents were measured on a equidistant  $9 \times 9$  grid (with 3 m spacing), centred near the tip of the breakwater ( $x=14$  m,  $y=0$  m). It was assumed that stationary conditions were reached after 11 minutes (Dingemans *et al.*, 1986), and measurements were taken for the subsequent 21 minutes.

The horizontal resolution is set to approximately  $1/40^{\text{th}}$  of a wave length in the mean wave and  $1/60^{\text{th}}$  of a wave length in the lateral direction. This resulted in  $700 \times 880 \times 2$  mesh points with  $\Delta x = 0.05$  m and  $\Delta y = 0.03$  m. Default parameters were used for the HFA ( $\alpha = 0.6$  and  $\beta = 0.3$ ). Since the observed circulation attains relatively high flow velocities over the crest of the bar ( $U \approx 0.3$  m/s, so that  $U/ct \approx 0.3$ ), we included the effect of an ambient current in our estimation of the

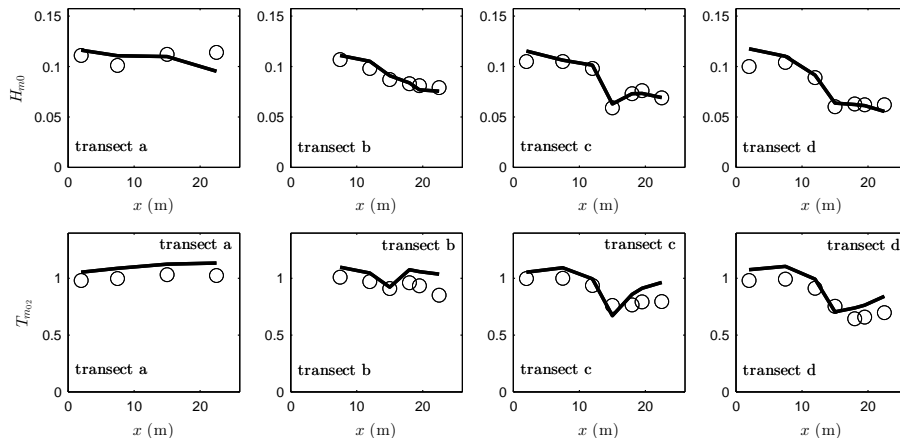


Figure 3.15: Cross-sections (see Fig. 3.13) of the significant wave height  $H_{m0}$  (top panels) and mean zero crossing period  $T_{m02}$  (lower panels) in the Dingemans *et al.* (1986) experiment (case me35). Comparison between measured (circle markers) and computed values (solid lines).

wave celerity (see appendix C). At the wave-maker boundary a JONSWAP spectrum is imposed, including the observed variation in significant wave height along the boundary. After calibration a roughness coefficient of  $k = 0.005$  is found to give a good correspondence between the measured and computed mean flow field. The friction coefficient thus varies between  $c_f = 0.005$  (0.1 m depth) and  $c_f = 0.003$  (0.4 m depth) and is similar to the value of  $c_f = 0.006$  used by Chen *et al.* (1999) for modelling a rip-current system. The initial time step is set to  $\Delta t = 0.005$  s and after 660 s output is generated at a sampling frequency of 20 Hz. Variance density spectra and derived quantities are obtained in a similar manner as in the previous section. As the recorded signals of the surface elevation at the wave gauges are no longer available<sup>2</sup>, observed spectra are obtained from Ris *et al.* (2002).

Three successive snapshots of the free surface, overlaid with white patches to indicate regions where the HFA is active, are depicted in Fig. 3.14. These snapshots, in addition to others (not shown), suggest that the HFA is only active in the shallow region near the crest of the bar. In general the HFA is activated on individual crests approaching the bar in between the 0.2 m and 0.1 m depth contours, which as expected roughly corresponds to the region where  $H_{m0}/d \sim 0.5-1$ . Activation starts on separate sections of the crest, but once initiated the active region usually spreads along the crest. The HFA then generally remains active on the front-face of the wave until it passes the bar and enters deeper water.

For a quantitative assessment of model performance, we compare the computed wave height  $H_{m02}$  and period  $T_{m02}$  with the observed values in Fig. 3.15. The predicted wave heights generally correspond well with the measurements. In accordance with observations the wave decay is gradual in the transect (b) skirting the break-

<sup>2</sup>personal communication with M.W.Dingemans (2012)

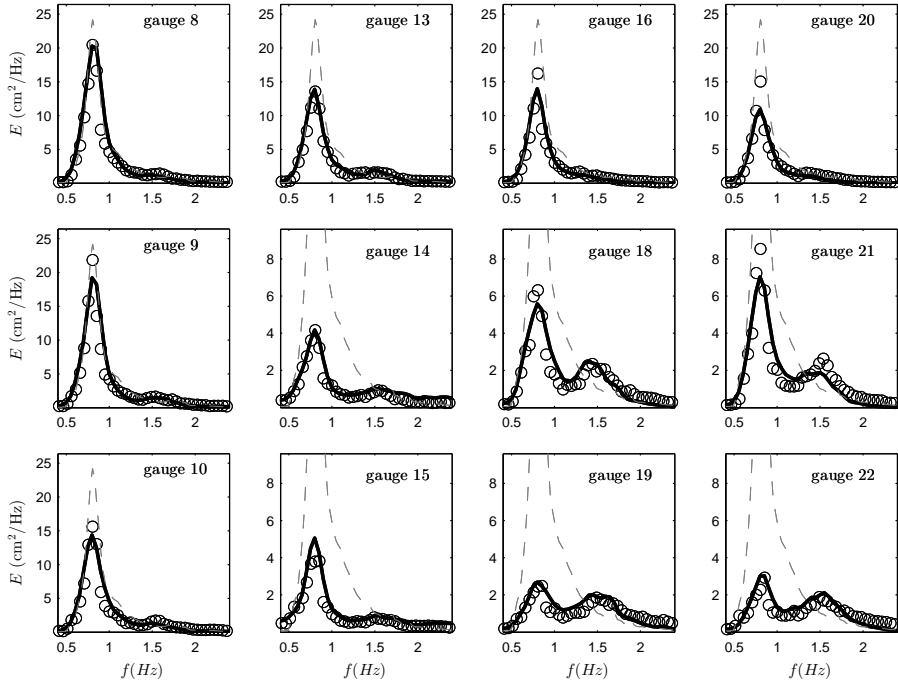


Figure 3.16: Comparison between measured (circle markers) and computed (solid lines) variance density spectra in the Dingemans *et al.* (1986) experiment. The mean incident wave spectrum is indicated with a thin dashed line. Stations are ordered according to their geographic location, see also Fig. 3.13.

water tip, whereas it is more abrupt in the transects that traverse the bar (c and d). Furthermore, the model reproduces the slight increase in significant wave height that occurs after breaking in section c, which is probably due to refraction, diffraction and directional spreading. Mean wave periods are less well resolved and are generally overestimated. This particularly occurs past the crest of the bar, in transects b and c. This implies that, even though the total wave energy (or wave height) is well resolved, discrepancies occur in the spectral shape.

Close inspection of the spectra along transects (b), (c) and (d) (see Fig. 3.16) confirms this. On the forward slope (stations 8–10) and crest (stations 13–15) of the bar computed spectra correspond well with observations whereas on the downward slope (stations 16–18), and behind the bar (stations 20–21), the peak is slightly underestimated. Furthermore, energy densities above twice the peak frequency ( $f > 1.6\text{Hz}$ ) are somewhat lower than observed, in particular at station 21. Notwithstanding these discrepancies, the model reproduces the primary characteristics of the wave spectra well. Away from the breakwater tip (stations 19 and 22), where effects due to the lateral heterogeneity of the topography are negligible, the peak is well resolved. Near the tip the model captures the increase of the peak level of the spectrum that occurs

between stations 14–21 which is likely due to refraction, diffraction and directional spreading. Moreover, in accordance with observations the model reproduces the secondary peak at twice the peak frequency behind the bar. The development of such a peak in shallow water is characteristic for triad wave-wave interactions (e.g. Freilich and Guza, 1984).

Since dissipation – as observed and in the model computations – is concentrated near the bar, locally large gradients in the wave induced momentum flux are present. This forces a wave-induced current field the overall appearance of which, i.e. flow directions and relative magnitudes, is primarily determined by the topography. Comparing model predictions with the observations the model faithfully reproduces the mean flow pattern (see 3.17); the anti-clockwise circulation cell is centred near  $x = 20$  m,  $y = 0$  m and the high flow velocities on top of the breakwater. Quantitatively, inspection of the flow directions and magnitudes in Figures 3.18 and 3.19 demonstrates that the correspondence with model predictions is very good. Especially the flow magnitudes over the breakwater are well captured (transect along  $x = 14$  m). Even though we calibrated the friction coefficient, that this suggests that the wave averaged momentum balance, and in particular the wave momentum flux gradient, is well approximated. This conjecture is supported by: (1) the reasonable approximation of the wave height gradients over the bar; and (2) that the current field is well approximated before and after the bar. These suggests that the net transfer of energy from the wave field to the mean circulation, in addition to the energy dissipation in the rest of the domain, is correctly represented.

### 3.7. DISCUSSION

The above example demonstrates that the non-hydrostatic wave model SWASH combined with the HFA can resolve most of the relevant nearshore wave processes, including wave breaking and wave-driven circulations, in a reasonably accurate way. It shows that for practical applications a coarse vertical resolution suffices in large parts of the domain. Furthermore in regions where breaking dominates, which otherwise would require high vertical resolutions, the HFA forms an effective and efficient approximation. Indeed, when compared to high resolution computations the computed integral wave parameters – as the flume experiments demonstrate – compare equally well with observations while the computational time typically reduces by a factor 5–10 when the vertical resolution was lowered from 15 to 2 layers.

The primary disadvantage of using low vertical resolutions combined with the HFA is that the model no longer intrinsically accounts for the transition into a turbulent bore. Instead, the HFA is initiated once the rate of surface rise exceeds a pre-determined value  $\alpha$  which thus is a model parameter. This in addition to the persistence parameter  $\beta$  and the additional viscosity (controlled by  $\mu$ ). In the present work we primarily focussed on the potential of this approach, without performing a full sensitivity analysis for the empirical tuning coefficients. Instead, we estimated  $\alpha$  and  $\beta$  by comparison to observations and an ad-hoc choice for  $\mu$ . That this leads to reasonable results, even in a complex case, demonstrates the robustness of the present method.

Similar results as obtained here – at least for the flume experiments – can most

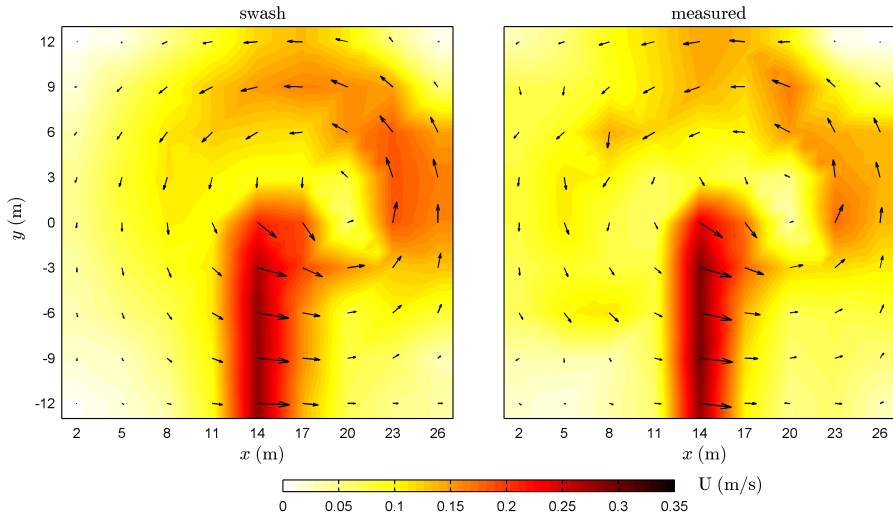


Figure 3.17: Measured (right panel) and computed (left panel) wave induced current field. (Dingemans *et al.*, 1986, case me35).

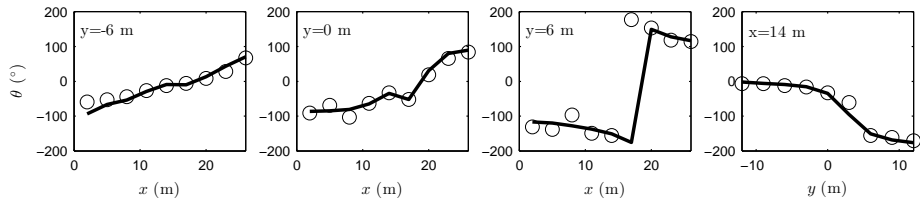


Figure 3.18: Measured (circle markers) and computed (solid lines) current direction  $\theta$  ( $\theta$  in degrees, with  $\theta = 0^\circ$  pointing in the  $x$ -direction) along indicated transects in the  $x$ - (first three panels) and  $y$ -direction (last panel) in the Dingemans *et al.* (1986) (case me35) experiment.

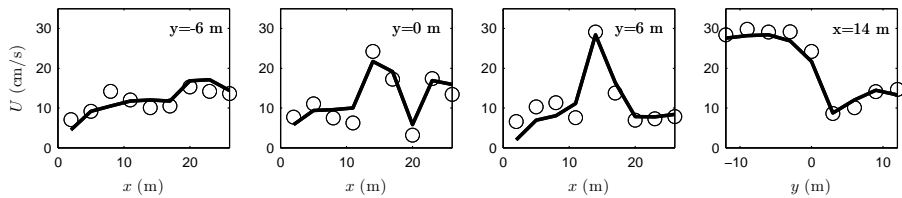


Figure 3.19: Measured (circle markers) and computed (solid lines) current magnitude  $U$  along indicated transects in the  $x$ - (first three panels) and  $y$ -direction (last panel) in the Dingemans *et al.* (1986) (case me35) experiment.

likely also be achieved in SWASH by means of an adaptation of more conventional breaking parametrisations, e.g. the roller or eddy viscosity models. However, the advantage of the present approach is its simplicity. Compared to more elaborate formulations (e.g. Cienfuegos *et al.*, 2010; Schäffer *et al.*, 1993) it requires less additional model parameters. Furthermore, the bulk dissipation due to wave breaking is still accounted for using shock capturing numerics, which thus remains consistent with the high resolution model. Most importantly the application to short-crested waves, as demonstrated in the present study, is straightforward and does not require additional modifications.

Finally, even when the HFA is used, the computational effort to simulate intermediate to large areas (say a harbour basin of  $\sim 10 \times 10$  wave lengths) at time scales of interest (say  $\sim 2000$  waves) remains formidable. The principle computational effort at each step arises from the need to solve a discrete Poisson equation to obtain the non-hydrostatic pressure. This entails that at each step a large, sparse, non-symmetric  $M \times M$  matrix equation needs to be solved where for  $m \times n$  horizontal points and  $k$  layers,  $M = mnk$ . The resulting system is solved iteratively in SWASH, requiring roughly  $O(M^{1.25})$  operations (for details we refer to Zijlema and Stelling, 2005). For example, the simulations for the Dingemans *et al.* (1986) experiment, which were performed on the Lonestar computer at TACC (Texas Advanced Computing Center) in Austin, USA, using 132 processors and where  $M = 1.2 \times 10^6$ , required roughly 10 hours to complete. Although – at present – this prohibits routine application within an engineering context, it does indicate that for selected critical scenarios application on the intermediate scale is feasible. Practical application is then best performed in synergy with regional wave models (spectral shallow water wave models, e.g. the SWAN<sup>3</sup> model, Booij *et al.*, 1999, from the same suite as SWASH), where results obtained by the regional model can be used to determine where and for which conditions more detailed computations are necessary.

### 3.8. CONCLUSIONS

In the present study we have introduced the hydrostatic front approximation as an effective and efficient approximation to wave breaking in the non-hydrostatic phase resolving model SWASH. It assumes a hydrostatic pressure distribution at the front of a breaking wave once the rate of change of the free-surface exceeds a predetermined threshold. The associated energy dissipation is accounted for by ensuring that mass and momentum are conserved once the wave has transferred into bore-like shape. The threshold, which is essentially a proxy for the maximum surface steepness, is estimated from experimental data. Simulations of flume experiments demonstrate that model results correspondent well with observed wave heights and periods. Furthermore, model results, for both waves and currents, are in agreement with observations of short-crested waves in a two-dimensional wave basin. This demonstrates that the non-hydrostatic wave model SWASH including HFA can resolve most of the relevant nearshore wave processes in a short-crested wave-field, including dissipation due to wave breaking, and wave-driven circulations.

---

<sup>3</sup>Simulation WAVes Nearshore, freely available at <http://swanmodel.sourceforge.net/>

## ACKNOWLEDGMENTS

The authors would like to extend their gratitude to Dr. Leo Holthuijsen who has had a substantial influence on this paper. Furthermore, we thank Prof. Clint Dawson and Dr. Casey Dietrich from the Institute for Computational Engineering and Sciences at the university of Texas, Austin (USA), whom graciously allowed us to make use of the computing facilities at the Texas advanced computing center.

# Appendices

## 3.A. TURBULENT STRESS APPROXIMATIONS

In this section we will give the expressions used for the turbulent stresses used in the full 3D formulation of the model. To this end we introduce the horizontal particle velocity vector  $\mathbf{u}$ , with components  $u_1$  and  $u_2$  directed along the horizontal  $x_1$  and  $x_2$  (or  $x, y$ ) axes and write the turbulent stress terms as

$$\tau_{z,x_i} = \nu_v \frac{\partial u_i}{\partial z} \qquad \tau_{x_j,x_i} = \nu_h \left( \frac{\partial u_i}{\partial x_j} + \frac{\partial u_j}{\partial x_i} \right), \qquad (3.9)$$

$$\tau_{x_j,z} = \nu_h \frac{\partial w}{\partial x_j} \qquad \tau_{z,z} = \nu_v \frac{\partial w}{\partial z}. \qquad (3.10)$$

Here  $\nu_v$  and  $\nu_h$  are the turbulent viscosities related to the vertical and horizontal exchange of momentum.

A vertical eddy viscosity is included to allow the effect of bottom stress to influence the entire water column and to increase numerical stability by enhancing the vertical coupling between layers. At high vertical resolutions ( $>10$  layers), the eddy viscosity is obtained using the  $k - \varepsilon$  model (Launder and Spalding, 1974) as a closure approximation, whereas at low resolutions a constant eddy viscosity ( $\nu_v = 10^{-4} m^2/s$ ) has been used.

In addition, to allow for horizontal mixing due to sub-grid eddies in the mean flow, a horizontal viscosity  $\nu_h$  is included. It is estimated using a Smagorinsky-type approximation (Smagorinsky, 1963)

$$\nu_h^{\text{cur}} = (C_s L_s)^2 \sqrt{2 \sum_{i,j=1}^2 S_{ij}^2} \qquad S_{ij} = \frac{1}{2} \left( \frac{\partial U_i}{\partial x_j} + \frac{\partial U_j}{\partial x_i} \right). \qquad (3.11)$$

Here,  $C_s (=0.1)$  is the Smagorinsky constant,  $U_1, U_2$  are the depth-averaged horizontal velocities and the typical length scale of the sub-grid eddies is related to the horizontal mesh size  $(\Delta x, \Delta y)$  as  $L_s = \sqrt{\Delta x \Delta y}$ .

## 3.B. WAVE GENERATING BOUNDARY CONDITIONS

To obtain the normal velocities  $u_n$  to the boundary at  $s$  (measured along the boundary) from a prescribed (spatially varying) variance density spectrum  $E(\theta, f, s)$  the spectrum is sampled  $N$  discrete frequencies from at  $\Delta f$  intervals. In the present work spectra were sampled from  $f_0 = 1/2f_p$  till  $f_N \leq f_{\text{nyq}}$  so that  $f_j = f_0 + j\Delta f$  and  $f_{\text{nyq}} = 1/(2\Delta t)$  is the Nyquist frequency. To avoid repetition of the signal we set  $\Delta f = 1/D$ , with  $D$  the duration of the simulation. Each frequency band

corresponds to a long crested wave with direction  $\theta_j$ , spatially varying amplitude  $A_j(s) (= \sqrt{2\Delta f \int E_j(\theta, s) d\theta})$  and random phase  $\phi_j$ . For unidirectional waves  $\theta_j$  is equal to the mean wave direction  $\theta_0$  (with  $\theta = 0$  in the direction normal to the boundary). For short-crested waves with a given  $\cos^m \theta$  directional distribution (assumed constant along the boundary), the direction of each component is drawn randomly using the directional distribution as a probability density function. This ensures that the wave variance along the boundary as obtained from the resulting signal is quasi-homogeneous (Miles and Funke, 1989), but requires that the spectrum is sampled using a large number of frequency components. The normal velocity at the boundary is then given as

$$u_n(s, z, t) = u_r(u, t) + \sum_{j=1}^N \hat{u}_j \cos(\theta_j) \sin [k_j \cos(\theta_j) s - 2\pi f_j t + \phi_j], \quad (3.12)$$

where  $k_j$  is the wave number;  $\hat{u}_j(z)$  is the vertically varying velocity amplitude that is related to  $A_j$  by means of linear wave theory; and  $u_r(u, t)$  represents a contribution to allow reflected long waves to leave the domain. To estimate  $u_r(u, t)$  the reflected waves are assumed to be small amplitude shallow water waves propagating perpendicular to the boundary. The surface elevation due to the reflected wave can be estimated by subtracting the surface elevation due to the incident waves  $\zeta_w$  from the instantaneous surface elevation. Using a radiation condition (e.g. Vreugdenhil, 1994, Section 5.2) and the continuity equation then gives the reflected wave contribution as  $u_r = \sqrt{g/d}(\zeta(y, t) - \zeta_w(y, t))$ . This approximation is based on the assumption that high frequency energy, for which this approach is not accurate, has dissipated in the domain to the extent that it may be neglected when it leaves the domain.

### 3.C. WAVE BREAKING INITIATION CRITERION

The criterion to initiate the HFA, which is similar to the criterion used in Kennedy *et al.* (2000), applies equally well to one and two-dimensional situations. Only when a strong ambient current is present do we need to take wave direction into account. To substantiate this, and to show how to take the presence of an ambient current into account, we note that for a wave of (nearly) constant form propagating (in the direction  $\theta_w$ ) over a flat bottom in a region with a uniform current  $\bar{U}$  (with direction  $\theta_c$ ) we have

$$\frac{\partial \zeta}{\partial t} + (\mathbf{c}' + \bar{\mathbf{U}}) \cdot \nabla \zeta = 0, \quad (3.13)$$

where  $\mathbf{c}' = c' [\cos \theta_w, \sin \theta_w]$  is the wave celerity in the absence of a current and  $\bar{\mathbf{U}} = \bar{U} [\cos \theta_c, \sin \theta_c]$ . Let us define a coordinate system with  $m$  parallel to the wave crest, and  $n$  perpendicular to the wave crest. Upon assuming that along the wave crest there are no gradients in the surface ( $\partial_m \zeta' = 0$ ), equation (3.13) transforms into

$$\frac{\partial \zeta'}{\partial t} + (c' + \Delta c) \frac{\partial \zeta'}{\partial n} = 0, \quad (3.14)$$

where  $\zeta'(m, n, t)$  is the free surface and  $\Delta c = \bar{U} \cos(\Delta\theta)$  is the correction to the wave celerity due to the presence of a current at a mutual angle  $\Delta\theta = \theta_w - \theta_c$  with the

local wave direction. Assuming that dissipation initiates when the surface slope  $|\partial_n \zeta|$  exceeds  $\alpha$ , we thus consider that waves are breaking when  $\partial_t \zeta'$  is larger than  $\alpha(c + \Delta c)$ . When  $U/c' \ll 1$ , which is often the case in the nearshore, the correction  $\Delta c$  to  $c'$  due to the currents can be neglected. Moreover, as the waves are in shallow water to a good approximation we have  $c' \approx \sqrt{gh}$ , and obtain the relatively simple breaking criterion  $\partial_t \zeta > \alpha\sqrt{gh}$  (since  $\partial_t \zeta = \partial_t \zeta'$  at any location). In such cases the trigger is thus independent of wave direction, simplifying its application in two-dimensional situations.

However, neglecting  $\Delta c$  when  $\bar{U}/c'$  is  $O(1)$  can lead to premature ( $|\Delta\theta| < 90^\circ$ , following current) or delayed ( $|\Delta\theta| > 90^\circ$ , opposing current) initiation of breaking. Furthermore, as it also affects the persistence criterion, it can also prolong (following currents) or shorten (opposing currents) the duration of a breaking event. Hence, in such cases it is desirable to include an estimate for  $\Delta c$ . Hereto we assume that  $c' + \Delta c > 0$  (thus excluding wave blocking) so that  $\partial_n \zeta' = -\text{sgn}(\partial_t \zeta)|\nabla \zeta|$  in which case  $\Delta c$  can be estimated by

$$\Delta c = -\text{sgn}(\partial_t \zeta) \frac{\nabla \zeta}{|\nabla \zeta|} \cdot \bar{\mathbf{U}}, \quad (3.15)$$

which, for robustness, is only calculated when  $|\nabla \zeta| > 10^{-3}$  and set  $\Delta c = 0$  elsewhere. Finally, in order to estimate the mean current  $\bar{\mathbf{U}}$  from the instantaneous depth average current  $\mathbf{U}$ , we use a relaxation model

$$\frac{\partial \bar{\mathbf{U}}}{\partial t} = -\frac{1}{T_r} (\bar{\mathbf{U}} - \mathbf{U}) \quad (3.16)$$

where  $T_r$  is a relaxation time scale which is taken to be in the order of five to ten peak periods.



# 4

## Non-hydrostatic modelling of surfzone wave dynamics

Non-hydrostatic models such as Surface WAVes till SHore (SWASH) resolve many of the relevant physics in coastal wave propagation such as dispersion, shoaling, refraction, dissipation and nonlinearity. However, for efficiency, they assume a single-valued surface and therefore do not resolve some aspects of breaking waves such as wave overturning, turbulence generation, and air entrainment. To study the ability of such models to represent nonlinear wave dynamics and statistics in a dissipative surfzone, we compare simulations with SWASH to flume observations of random, unidirectional waves, incident on a 1:30 planar beach. The experimental data includes a wide variation in the incident wave fields, so that model performance can be studied over a large range of wave conditions. Our results show that, without specific calibration, the model accurately predicts second-order bulk parameters such as wave height and period, the details of the spectral evolution, and higher-order statistics, such as skewness and asymmetry of the waves. Monte Carlo simulations show that the model can capture the principal features of the wave probability density function in the surfzone, and that the spectral distribution of dissipation in SWASH is proportional to the frequency squared, which is consistent with observations reported by earlier studies. These results show that relatively efficient non-hydrostatic models such as SWASH can be successfully used to parametrise surfzone wave processes.

### 4.1. INTRODUCTION

In the nearshore region and surfzone, ocean waves undergo a dramatic transformation mostly due to nonlinear wave-wave interactions and breaker dissipation. These

---

This chapter has been published as: SMIT, P.B., JANSSEN, T.T., HOLTHUIJSEN, L.H. and SMITH, J.M., 2014b Non-hydrostatic modelling of surf zone wave dynamics. *Coast. Eng.*, 83, 36–48.

dynamics play a central role in nearshore circulation and transport processes, e.g. by controlling wave setup (e.g. Longuet-Higgins and Stewart, 1964), driving nearshore currents (e.g. Longuet-Higgins and Stewart, 1964; Longuet-Higgins, 1970; Svendsen, 1984; MacMahan *et al.*, 2006), and causing morphodynamic evolution (e.g. Hoefel and Elgar, 2003). Understanding these processes and the development of predictive models is important for both scientific research and engineering in the coastal zone. Since most coastal and coastline processes take place on much longer scales than that of the individual waves, predictive models are generally used to estimate wave statistics (e.g. significant wave height, mean period) and variations therein. However, modelling waves statistics in the nearshore is complicated both by the strong influence of nonlinear processes and an incomplete understanding of dissipation of wave energy in shoaling and breaking waves.

Stochastic (or phase-averaged) wave models for coastal applications are usually based on some form of energy (or action) balance equation (e.g. The WAMDI Group, 1988; Komen *et al.*, 1994; Wise Group, 2007), which assumes that the wave field is (and remains) quasi-homogeneous and near-Gaussian. However, due to nonlinearity, surfzone wave statistics are generally strongly non-Gaussian, and apart from variance, higher cumulants (e.g. skewness and kurtosis) are required to completely describe the wave statistics. This poses high demands on the model representation of the nonlinear and nonconservative dynamics. In particular, for statistical models, the representation of nonlinearity invariably requires some form of closure approximation and involves evolution equations for higher-order correlations, both of which generally render the model considerably more complicated and computationally intensive (e.g. Herbers and Burton, 1997; Herbers *et al.*, 2003; Janssen, 2006; Smit and Janssen, 2013b).

Deterministic (and phase-resolving) wave models can generally incorporate nonlinearity more easily, and naturally include full coupling to the wave-induced circulations. However, although a model based on the Reynolds Averaged Navier-Stokes (RANS) equations can model surface wave dynamics in great detail, and resolve very small scales of motion (e.g. Torres-Freyermuth *et al.*, 2007), the computational cost can become prohibitive, even for small-scale applications. For wave modelling of most coastal-scale applications, and in particular for coastal engineering, more approximate but efficient models, such as so-called non-hydrostatic models or models based on a Boussinesq approximation are generally more useable. Boussinesq-type wave models have evolved from weakly nonlinear and weakly dispersive models (see Peregrine, 1967), to nearly fully dispersive and highly nonlinear models (e.g. Nwogu, 1993; Wei *et al.*, 1995; Madsen *et al.*, 2002), at the expense however, of much increased complexity of the underlying model equations and numerical implementations. In contrast, non-hydrostatic models are essentially numerical implementations of the basic conservation equations for mass and momentum (e.g. Stelling and Zijlema, 2003; Yamazaki *et al.*, 2009; Ma *et al.*, 2012), which can be directly used for wave propagation problems if sufficient spatial resolution, in particular in the vertical, is provided. As a consequence, such models are relatively simple, and grid resolution can be readily adapted to a particular application and allow propagation of waves from deep to shallow water.

However, such non-hydrostatic models (and Boussinesq models for that matter), do not model all aspects of surfzone waves. In particular, for the sake of efficiency, these models assume a single-valued representation of the free surface in the horizontal plane, which implies that processes such as overturning, air entrainment, and wave-generated turbulence are not resolved. Instead, integral properties of breaking waves (including energy dissipation rate) are estimated by treating the breaking wave as a discontinuity in the flow variables (free surface, velocities) and maintaining momentum (and mass) conservation across the discontinuity (Smit *et al.*, 2013). Although this gives good results for the second-order bulk statistics (such as the significant wave height), it is not clear whether such an integral approach, where some of the details of breaking waves are treated as sub-grid processes, can actually resolve the nonlinear and dissipative processes in the surfzone, and thus predict the details of the spectral evolution and nonlinear statistics there.

In the present work we set out to study these issues by comparing simulations with the non-hydrostatic model Surface WAVes till SHore (SWASH, Zijlema *et al.*, 2011b) to flume observations of random waves over a 1:30 planar beach (see Smith (2004)). The motivation behind this work is to assess whether an efficient non-hydrostatic model such as SWASH can be a viable tool to study surfzone dynamics and accurately capture the statistics of strongly nonlinear and breaking waves.

In §2 we present the model equations, numerical approximations, and breaker modelling in SWASH. The laboratory experiments and specific model settings are described in §3 and we present our results (model-data comparison) in §4. We discuss and sum up our principal findings and their implications in sections 5 and 6.

## 4.2. MODEL DESCRIPTION

The non-hydrostatic model SWASH (Zijlema *et al.*, 2011b), is an implementation of the Reynolds-averaged Navier-Stokes equations for a incompressible, constant-density fluid with a free surface. In the present work we use this model to study one-dimensional wave propagation in a flume. In Cartesian coordinates, with  $x$  and  $z$  the horizontal and vertical coordinate respectively, and with  $z$  measured up from the still-water level  $z_0$ , the governing equations can be written as

$$\frac{\partial u}{\partial t} + \frac{\partial uu}{\partial x} + \frac{\partial wu}{\partial z} = -\frac{1}{\rho} \frac{\partial(p_h + p_{nh})}{\partial x} + \frac{\partial \tau_{xz}}{\partial z} + \frac{\partial \tau_{xx}}{\partial x}, \quad (4.1)$$

$$\frac{\partial w}{\partial t} + \frac{\partial uw}{\partial x} + \frac{\partial ww}{\partial z} = -\frac{1}{\rho} \frac{\partial p_{nh}}{\partial z} + \frac{\partial \tau_{zz}}{\partial z} + \frac{\partial \tau_{zx}}{\partial x}, \quad (4.2)$$

$$\frac{\partial u}{\partial x} + \frac{\partial w}{\partial z} = 0, \quad (4.3)$$

where  $t$  is time,  $u(x, z, t)$  and  $w(x, z, t)$  are the horizontal and vertical velocities, respectively, and  $\rho$  is the (constant) density. Further, the hydrostatic pressure  $p_h = \rho g(\zeta - z)$  (with  $g$  being gravitational acceleration) and  $p_{nh}$  represents the non-hydrostatic pressure contribution. The turbulent stresses  $\tau_{\alpha\beta}$  are obtained from a turbulent viscosity approximation (e.g.  $\tau_{xz} = \nu \partial_z u$ , with  $\nu$  the kinematic eddy-viscosity) using a standard  $k-\epsilon$  model closure approximation (Launder and Spalding,

1974). The water column is vertically restricted by the (time-varying) free-surface  $z = \zeta(x, t)$  and immobile bottom  $z = -d(x)$ . Here  $d$  is the still water depth and the location of the free surface  $\zeta$  is found from continuity, expressed as

$$\frac{\partial \zeta}{\partial t} + \frac{\partial}{\partial x} \int_{-d}^{\zeta} u \, dz = 0. \quad (4.4)$$

Equations (4.1)–(4.4) are solved for constant pressure at the free-surface (i.e.  $p = 0$ ), while accounting for the kinematic free-surface and bottom boundary conditions,

$$w = \frac{\partial \zeta}{\partial t} + u \frac{\partial \zeta}{\partial x} \quad (z = \zeta), \quad \text{and} \quad w = -u \frac{\partial d}{\partial x} \quad (z = -d). \quad (4.5)$$

At the up-wave boundary, waves are generated by prescribing the horizontal velocity  $u(z, t)$  at that location, whereas opposite of the wavemaker the boundary is formed by the moving shoreline.

Since the objective is to study surfzone wave dynamics, we need to include motions in the infragravity band, which are generated in the shoaling process and released during breaking. These low-frequency components are much longer than the primary waves and much more strongly affected by bottom friction. To incorporate this, we include a bottom stress at the bottom boundary assuming a logarithmic velocity profile (Lauder and Spalding, 1974) and a typical roughness height  $d_r$ .

## NUMERICAL APPROXIMATIONS

For non-breaking waves these equations describe nonlinear shoaling, and thus include the energy transfers across different length scales in the wave spectrum due to triad and higher-order nonlinearities. The accuracy with which these processes are represented in numerical models such as SWASH, depends on the numerical methods used to approximate the governing equations, and the spatial (horizontal and vertical) and temporal resolutions used in the simulation. Moreover, when extending such models to the surfzone, careful attention must be paid to the conservation properties (in particular of momentum) of the numerical method (see Zijlema *et al.* (2011b) for a more general discussion of the numerical methods used in SWASH).

To accurately resolve wave motion in a phase-resolving model, the horizontal resolution  $\Delta x$  must be a fraction of the shortest wave length  $L$  that needs to be resolved, i.e.  $L/\Delta x = O(10)$ . Similarly, the timestep  $\Delta t$  is usually a fraction of the shortest wave period  $T$ , i.e.  $T/\Delta t = O(10)$ . To allow for accurate, undamped propagation over long distances, SWASH uses a staggered horizontal grid combined with a second-order (in space and time), explicit, finite-difference method that is neutrally stable (no numerical damping) for small amplitude (linear theory) waves. The vertical resolution, and numerical approximations of the vertical pressure gradient, determines how well the model approximates the linear dispersion relation for surface gravity waves  $\omega(k) = \sqrt{gk \tanh(kd)}$ , which strongly affects propagation and dispersive characteristics of the wave field.

Non-hydrostatic models often make use of a boundary-fitted vertical grid that divides the instantaneous water depth  $h (= \zeta + d)$  in a constant number of layers  $N$ , with variable vertical mesh-size  $\Delta z = h/N$ . The required number of layers  $N$  then

generally depends on the deepest parts of the domain, and increases with the vertical variability of the wave-induced velocity profile, for free-surface waves represented by the relative depth  $kd$ . Hence, in shallow water ( $kd \ll 1$ ), a coarse resolution generally suffices, whereas in deep water ( $kd \gg 1$ ) a vertical resolution similar to the horizontal resolution is required,  $\Delta z/\Delta x = O(1)$  (at least near the surface). Traditionally, this has severely limited the application of these models to wave propagation, as the number of layers required to accurately capture dispersion (say a relative error smaller than 1%) at high  $kd$  ( $O(10)$ ) can become very large ( $N > 20$ ), resulting in excessive computational times. These constraints are significantly relaxed in SWASH due to the use of an edge-based vertical grid combined with a compact numerical scheme for the approximation of the vertical pressure-gradient (i.e., the Keller-box scheme; see Lam and Simpson, 1976). Hence, for  $N = 6$ , the maximum relative error of the numerical dispersion relation  $\omega_n$ , compared with  $\omega$  (or alternatively the wave celerity), remains below 0.1% for  $kd < 40$  (see appendix A). This numerical efficiency is important in the surfzone where very short waves exchange energy through nonlinear interactions, thus potentially imposing high demands on both horizontal and vertical resolutions.

## WAVE BREAKING APPROXIMATIONS

Since SWASH assumes the free surface to be a single-valued function  $\zeta(x, t)$ , it cannot model processes such as overturning, air-entrainment, and the production of wave-induced turbulence after the wave form becomes unstable and breaking is initiated. However, if we are not principally interested in the details of these fine-scale processes associated with breaking waves, this approach can be very useful (and efficient) to capture the larger-scale wave and current dynamics in the surfzone (e.g. Ma *et al.*, 2012; Smit *et al.*, 2013).

In a non-hydrostatic model like SWASH, a breaking wave develops into a discontinuity (or hydraulic jump), which is similar to that predicted by the (non-dispersive) shallow-water equations. If momentum conservation is maintained across the discontinuity by employing shock-capturing numerical methods (in SWASH this is done using the method by Stelling and Duinmeijer, 2003) then, in analogy to hydraulic jump dynamics, energy is dissipated at a rate proportional to the cube of the bore height. In this way the entire turbulent front is essentially reduced to a sub-grid phenomenon.

However, when waves approach breaking, wave steepening introduces strong vertical gradients in the flow variables, which requires a very high vertical resolution locally to accurately capture the bore dynamics using shock-capturing numerics. If the resolution is insufficient, velocities are generally underestimated, and the initiation of breaking is delayed (Smit *et al.*, 2013). We avoid using a fine vertical resolution by using a hydrostatic front approximation (HFA), inspired by similar developments in Boussinesq models (e.g. Tonelli and Petti, 2012; Tissier *et al.*, 2012), and described in detail in Smit *et al.* (2013). The HFA method implemented here considers the (non-dimensional) rate of change of the free surface elevation,  $\zeta'_t = \partial_t \zeta / \sqrt{gh}$  and forces the pressure at the wave front to be hydrostatic, i.e.  $p_{\text{nh}} = 0$ , once this exceeds a certain threshold (i.e.  $\zeta'_t > \alpha$ ). Effectively, near the bore front, the model reduces to

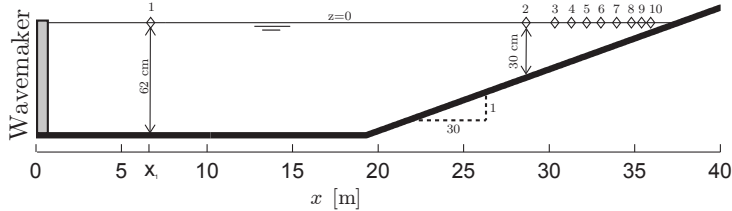


Figure 4.1: Layout of the flume experimental setup by Smith (2004). The diamond markers at still-water level ( $z = 0$ ) indicate measurement locations.

the nonlinear shallow-water equations, causing the front to assume a characteristic sawtooth-like shape, and dissipate wave energy at a rate consistent with that of an hydraulic jump. Once breaking is initiated, the breaking threshold  $\alpha$  is reduced to  $\beta$  (with  $\beta < \alpha$ ) in neighboring points to allow the breaker to more easily persist and produce more realistic breaker dynamics.

The threshold value,  $\alpha$ , at which the HFA is initiated, depends on the wave dynamics leading up to breaking, and thus depends on the number of layers used in the model. For two layers, Smit *et al.* (2013) found  $\alpha = 0.6$  by estimating the maximum value of  $\zeta'_t$  at the observed breaking point in the experiments of Ting and Kirby (1994). Recalibration for 6 layers (as will be used here) using the same analysis method and data set as in Smit *et al.* (2013), resulted in  $\alpha = 1$ . This value produces similar model-data agreement for the Ting data set with the six-layer model (not shown) as found in Smit *et al.* (2013) for a two-layer model. The persistence parameter  $\beta$  was found much less sensitive to the number of layers used, and is therefore set to the value of  $\beta = 0.3$  (suggested by Smit *et al.*, 2013).

Lastly, to prevent generation of high-frequency noise in the wave profile due to the discrete activation of the HFA, some additional horizontal viscosity is introduced, of the form

$$\nu = L_{\text{mix}}^2 \left| \frac{\partial U}{\partial x} \right|. \quad (4.6)$$

Here  $L_{\text{mix}}$  is a typical horizontal mixing length, set as a fraction  $\mu$  of the local depth (i.e.  $L_{\text{mix}} = \mu h$ ), and  $U$  is the depth-averaged horizontal velocity. For  $0.25 \leq \mu < 3$ , this parameter suppresses the generation of such noise, but has a marginal effect on the bulk energy dissipation. To minimize its influence, we set  $\mu = 0.25$  in the present study.

### 4.3. EXPERIMENT AND MODEL SETUP

We compare SWASH simulations to a series of laboratory observations performed by Smith (2004) at the US Army Engineer Research and Development Center, Coastal and Hydraulics Laboratory. The experiments were performed in a 0.45 m wide, 45.7 m long and 0.9 m deep flume (see Fig. 4.1), with glass walls and a smooth concrete bottom. Waves are generated by a horizontally moving piston-type wave generator

Table 4.1: Instrument location  $x$  (m) and still-water depth  $d$  (m) during experiments (see Smith, 2004).

	1	2	3	4	5	6	7	8	9	10
$x$	6.7	28.7	30.3	31.3	32.2	33	33.9	34.8	35.4	35.9
$d$	0.62	0.3	0.24	0.21	0.18	0.15	0.12	0.09	0.07	0.05

located at one end of the flume (at  $x = 0$  m), and propagate over a horizontal section onto a 1:30 beach that starts at  $x = 19.3$  m.

The surface elevation was measured at 10 locations (see Fig. 4.1), and sampled at 5 Hz for a duration of 550 s. Data acquisition was started after 50 s, thus allowing for spin-up time and prevent transient effects in the observations. The wave gauge closest to the wavemaker, located on the horizontal section, is used as a boundary condition for the model. The other gauges are placed on the slope, from a depth of 0.3 m to 0.05 m, at intervals varying from 0.5 to 1.6 m (see Table 4.1).

Irregular waves were generated using either a single- or double-peaked spectrum. The individual spectral peaks are described by a parametric TMA shape (Bouws *et al.*, 1985), and the high-frequency peak of the double-peaked spectra always contained two-thirds of the total energy (see Smith (2004)). In our analysis, to avoid ambiguity, we refer to the low-frequency peak as the primary peak, and to the high-frequency peak (if present) as the secondary peak; additional peaks that arise in the spectrum due to nonlinear interactions are referred to as (higher) harmonic peaks, or simply harmonics.

The experiments consider a range of incident wave conditions (see Table 4.2 for an overview) by varying the TMA peakedness parameter  $\gamma$ , considering single and double-peaked spectra, varying the peak period of the low frequency peak  $T_p^{(1)} = 1/f_p^{(1)}$ , and including two different significant wave heights  $H_{m_0}$ . A total of 31 experiments, including 30 different wave conditions, were performed (case 11b was repeated once). If a secondary peak is included in the incident wave spectrum, it is generated at  $f_p^{(2)} = 1$  Hz. The Iribarren number,  $\xi$  (definition in caption to Table ) was below 0.5 (see Table 4.2), which suggests that the surfzone for the cases consisted mostly of spilling breakers (see e.g. Holthuijsen, 2007). Since the wavemaker was not equipped with either second-order control or reflection compensation, some spurious second-order wave motion was generated, and long waves radiated back from the beach were re-reflected into the flume.

Table 4.2: Wave conditions considered in the experiments by Smith (2004).  $T_p^{(1)}$  refers to the primary peak period, whereas  $T_p^{(2)}$  refers to the period of the secondary peak (if applicable). Wave steepness is defined from the wave number spectrum  $E(k)$ , with  $k$  the wave number, as  $\sqrt{\int k^2 E(k) dk}$ . The Iribarren number  $\xi$  is defined as  $\xi = \tan \alpha / \sqrt{H_{m0}/L_p}$ , with  $H_{m0}$  the significant wave height as listed,  $\tan \alpha = 1/30$  the bottom slope and  $L_p = g \left( T_p^{(2)} \right)^2 / 2\pi$  the deep-water wave length. Listed values for  $k_p^{(1)} d$  are calculated using the primary peak period and  $d = 0.62$  m. All other variables are defined as in the main text. Cases considered individually in figures or discussed in the main text are marked with an asterisk.

Case	$T_p^{(1)}$ (s)	$T_p^{(2)}$ (s)	$H_{m0}$ (m)	$\gamma$			Wave steepness			$k_p^{(1)} d$	$\xi$
				(a)	(b)	(c)	(a)	(b)	(c)		
1	2.5	1.0	9.0	3.3*	20	100*	0.13	0.12	0.11	0.68	0.34
2	2.0	1.0	9.0	-	20*	-	-	0.12	-	0.88	0.27
3	1.75	1.0	9.0	3.3	20*	100	0.13	0.13	0.11	1.00	0.24
4	1.5	1.0	9.0	-	20	-	-	0.13	-	1.3	0.20
5	1.25	1.0	9.0	3.3	20	100	0.14	0.13	0.12	1.7	0.17
6	2.5	-	9.0	3.3*	20	100*	0.07	0.05	0.05	0.68	0.32
7	2.0	-	9.0	-	20*	-	-	0.04	-	0.88	0.26
8	1.75	-	9.0	3.3	20*	100	0.1	0.07	0.05	1.00	0.23
9	1.5	-	9.0	-	20	-	-	0.06	-	1.3	0.20
10	1.25	-	9.0	3.3*	20	100*	0.13	0.11	0.08	1.7	0.17
11	1.0	-	9.0	3.3*	20*	100*	0.15	0.12	0.13	2.5	0.14
12	2.5	1.0	6.0	-	20	-	-	0.08	-	0.68	0.41
13	2.0	1.0	6.0	-	20	-	-	0.08	-	0.88	0.32
14	1.75	1.0	6.0	-	20	-	-	0.08	-	1.00	0.28
15	1.5	1.0	6.0	-	20	-	-	0.09	-	1.3	0.25
16	1.25	1.0	6.0	-	20*	-	-	0.09	-	1.7	0.20

The model domain extends from the first observation point at  $x_1 = 6.7$  m, to 45 m. To ensure that the model accurately describes the wave characteristics over a wide frequency range of at least  $0 \leq f \leq 4f_p$  (with  $f_p$  the peak frequency<sup>1</sup>), which includes the high-frequency tail, the horizontal resolution is set at  $\Delta x = 0.01$  m. Such high resolution is needed to resolve the higher frequencies with wave lengths 0.1 to 0.4 m, and to accurately propagate these components over  $O(10^2)$  wave lengths. Moreover, to correctly describe linear dispersion at high  $kd$  values (maximum value of  $kd$  at  $4f_p$  is approximately 40), the vertical resolution is set to 6 layers, so that within the prescribed frequency range the relative error in wave celerity stays below 0.1%. From a nonlinear perspective, this also ensures that the resonant mismatch is well predicted for interactions below  $4f_p$  (see Appendix A). Time integration was performed for a duration of 600 s with a time step of  $\Delta t = 0.005$  s (so that  $4f_p\Delta t \geq 50$  in all cases). The bottom roughness height  $d_r$  was set to a value of  $4.5 \times 10^{-4}$  m, which is representative for smooth concrete (e.g. Chow, 1959). Each individual simulation (each case) takes approximately 30 minutes to complete on a 6-core Intel Xeon 3.2 GHz CPU desktop computer.

### WAVE FORCING

The model is forced with the measured free-surface records at the first wave gauge, which implies that the model-data comparisons are essentially deterministic. To directly force the model using the data, we relate the time-varying, layer-averaged horizontal velocity  $u_n(t)$  for each vertical layer  $n$  (with  $n = 1 \dots N$ , and  $n = 1$  denoting the bottom layer), required to drive the model at the up-wave boundary, to the measured free-surface elevation at that location. Therefore we consider the Fourier sum of the free-surface elevation and horizontal velocity,

$$\zeta(t) = \sum_{j=-J}^J \widehat{\zeta}_j \exp[i2\pi f_j t], \quad u(z, t) = \sum_{j=-J}^J \widehat{u}_j(z) \exp[i2\pi f_j t], \quad (4.7)$$

where  $f_j = j\Delta f$ ,  $\Delta f = 1/T$  and  $i^2 = -1$ . The horizontal velocity (using linear wave theory) is found from

$$\widehat{u}_j(z) = 2\pi f_j \widehat{\zeta}_j \frac{\sinh[k_j(z+d)]}{\sinh(k_j d)} \quad (4.8)$$

where  $k_j$  is the wavenumber related to  $f_j$  by the linear dispersion relation. The layer-averaged velocity  $u_n(z, t)$  is then obtained by integration over the  $n^{\text{th}}$  layer, and subsequently dividing by the layer thickness,

$$u_n(z, t) = \frac{1}{\Delta z} \sum_{j=-J}^J \int_{z_{n-1}}^{z_n} \widehat{u}_j(z, t) \exp[i2\pi f_j t] dz, \quad (4.9)$$

where  $z_n = n\Delta z - d$  and  $\Delta z = d/N$ .

---

<sup>1</sup>Note that  $f_p^{(1)}$  and  $f_p^{(2)}$  specifically refer to the locations of the incident waves, whereas we will use  $f_p$  to refer to the local peak frequency. We will use the same convention for peak wave periods and wave numbers.

Although presumably, due to the lack of second-order control, some spurious and second-order low-frequency motion is generated at the wavemaker, most of the low-frequency energy present at the offshore gauge consists of low-frequency energy generated in the breaking process through subharmonic triad interactions, reflected off the beach, and subsequently re-reflected off the wavemaker. To model this consistently, the model is forced with the high-pass filtered observed time series (for  $f > f_p^{(1)}/2$ ) at the offshore gauge (gauge 1), and the offshore boundary is set to be fully reflective (to mimic the reflecting wavemaker). In this way, the low-frequency motion is thus not forced into the model at the wavemaker, but allowed to develop in the surfzone and reflect back into the model domain (as happens in the flume).

#### 4.4. RESULTS

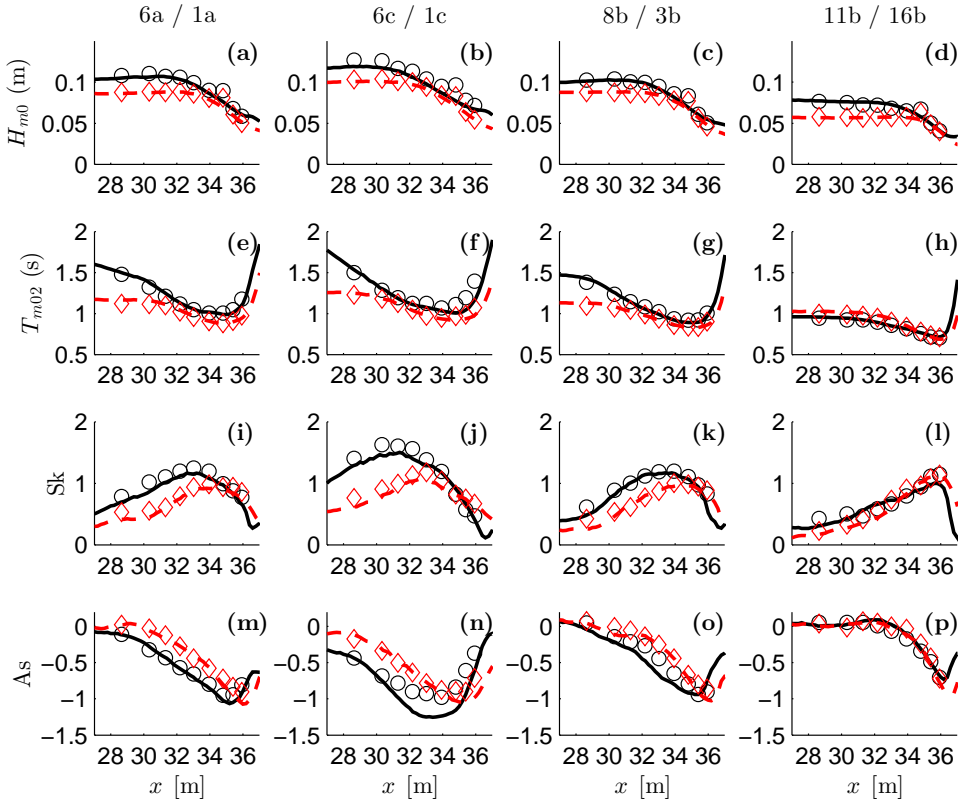


Figure 4.2: Comparison between modeled (lines) and observed (symbols) values of significant wave height (panels a–d), mean period (e–h), skewness (i–l) and asymmetry (m–p). In each column a single-peaked (black solid line/circles) and double-peaked (red dashed line/diamonds) case with the same  $H_{m0}$ ,  $T_p^{(1)}$ , and  $\gamma$  are shown (the only difference between these cases is the single- or double-peakedness of the spectrum). Case numbers (single/double) are indicated above each column.

To assess overall model performance we first consider several bulk parameters. In particular, we consider significant wave height  $H_{m0} = 4\sqrt{m_0}$  and mean period  $T_{m02} = \sqrt{m_2/m_0}$ , where  $m_n = \int f^n E(f) df$ , and higher-order bulk statistics of skewness Sk and asymmetry As, which are defined as

$$\text{Sk} = \frac{\langle \zeta^3 \rangle}{\langle \zeta^2 \rangle^{3/2}}, \quad \text{As} = \frac{\langle \zeta_h^3 \rangle}{\langle \zeta^2 \rangle^{3/2}}. \quad (4.10)$$

Here  $\zeta_h$  is the imaginary part of the Hilbert transform of  $\zeta$  (from which the mean contribution is subtracted) and  $\langle \dots \rangle$  denotes a time average.

The significant wave height and mean period are second-order bulk statistics which are a measure of the total amount of energy, and a measure of period, respectively. The mean period  $T_{m02}$  also provides some insight in the distribution of wave energy across frequencies. Skewness and asymmetry are third-order bulk statistics, measuring the wave asymmetry, around a horizontal and vertical plane, respectively. Positive skewness is associated with steeper, higher peaks and flatter troughs (e.g. second-order Stokes waves), and negative asymmetry is associated with the forward pitching, saw-tooth like appearance of waves in the surfzone (Elgar and Guza, 1985). Since for a Gaussian wave field both skewness and asymmetry are zero (as are all cumulants higher than the second), the comparison between observed and modeled skewness and asymmetry values measures the accuracy of the nonlinear dynamics in the model, and - in the surfzone - the interplay between nonlinear and dissipative processes (Chen *et al.*, 1997).

All spectral estimates (for calculations and observations) are obtained from detrended and windowed Fourier transforms of 18.3 s length segments with 50% overlap, which are subsequently ensemble averaged to yield estimates for  $E(f)$  with a resolution of  $\Delta f = 0.055$  Hz and approximately 110 degrees of freedom.

The spatial evolution of the significant wave height and the mean period in the surfzone is generally well captured by the model as illustrated by the eight cases shown in Fig. 4.2. These results are representative and similar results were found for the other cases (not shown). It can be seen that the location where intense breaking starts (abrupt decrease in wave height), and the spatial variations in mean period through the surfzone, are accurately resolved by the model. Only at gauge 8 ( $x = 34.8$  m third observation point from the right), the model systematically underpredicts the observed wave heights. Variations in  $T_{m02}$  are, apart from dissipation, also strongly affected by nonlinearity. In the shoaling region, i.e. outside the surfzone proper,  $T_{m02}$  is reduced by the development of higher harmonics in the wave spectrum (to be treated below, see Fig. 4.4), whereas inside the surfzone short waves are rapidly dissipated and nonlinearity drives the generation of low-frequency infragravity waves, thus resulting in the observed (and modeled) increase in  $T_{m02}$ .

On the horizontal section, the waves are weakly nonlinear, with low asymmetry and skewness values, generally consistent with Stokes second-order waves. On the slope, skewness increases as the waves become more 'peaked', and asymmetry takes on larger negative values, indicative of the pitch-forward shapes developing as the wave approach breaking (or are breaking). Near the shore, the magnitude of skewness and asymmetry generally reduces resulting in statistics that are closer to Gaussian.

The variability of these third-order statistics is quite accurately reproduced by the model (see Fig. 4.2). For the narrow-band case, 6c, there is somewhat less good correspondence between observed and modeled surfzone wave asymmetry than for the other cases (see Fig. 4.2n, black line/markers). This is likely due to the hydrostatic bore approximation which generates near-vertical fronts in breaking waves, whereas in reality wave-induced turbulence would stabilize the front toward a more moderate slope of the face of the breaking wave (e.g. Madsen and Svendsen, 1983). This exaggeration of wave asymmetry by the hydrostatic bore approximation, mostly affects narrow-band waves; in wider-band wave fields (e.g. case 6a shown in panel m of Fig. 4.2), which we are more likely to encounter on natural beaches, the intermediate steep bores ride on a background of irregular smooth waves, which apparently smoothes the statistics, and produces model results in very close agreement with observations (see Fig. 4.2).

Considering all 31 cases, the comparison between observed and modeled bulk statistics shows excellent agreement (see Fig. 4.3), with  $R^2$  values larger than 0.9. The agreement is best for the significant wave height and period. For the wave heights, there is however a clustering of points that lie below the main diagonal. This cluster is associated with observations made by gauge 8, which (as seen before in Fig. 4.3a) recorded consistently slightly higher values than model predictions for all cases and wave conditions, and which stands out relative to other (surrounding) observations (see Fig. 4.3a). Moreover, the fact that there are no such differences in the results for  $T_{m02}$ , the skewness or asymmetry, led us to believe that these differences are due to a slight gauge calibration inconsistency (experimental error), rather than a systematic model error.

The higher-order statistics of skewness and asymmetry are in excellent agreement, but have slightly more scatter. Skewness is generally slightly under-predicted, whereas the modeled asymmetry is slightly more negative than observed. However, these higher-order statistics strongly depend on both nonlinearity and a correct representation of wave dissipation, and the good agreement suggest that the model captures these processes very well.

## EVOLUTION OF WAVE SPECTRA

Apart from dissipation and linear shoaling effects, the enhancement of skewness, asymmetry, and the evolution of  $T_{m02}$  in the surfzone (see Fig. 4.2), indicate that redistribution of energy due to nonlinear triad interactions plays an important role in the wave evolution. To investigate this in more detail we consider the evolution of observed and modeled spectra.

Harmonic amplification due to triad interactions becomes more pronounced in shallow water since the interactions approach resonance. The development of such higher harmonic contributions is most pronounced for narrow-band waves where the primary and harmonic peaks are well defined, with limited phase mixing. For instance, for case 6c ( $k_p^{(1)}d=0.68$ ,  $\gamma = 100$ ) some harmonic amplification already occurs on the flat (see Fig. 4.4a), and at gauge 2 we can clearly distinguish – in both the model and the observations – the first three harmonics of the peak (0.4 Hz), located at 0.8, 1.2 and 1.6 Hz respectively (see Fig. 4.4a). In the surfzone (Fig. 4.4b–c),

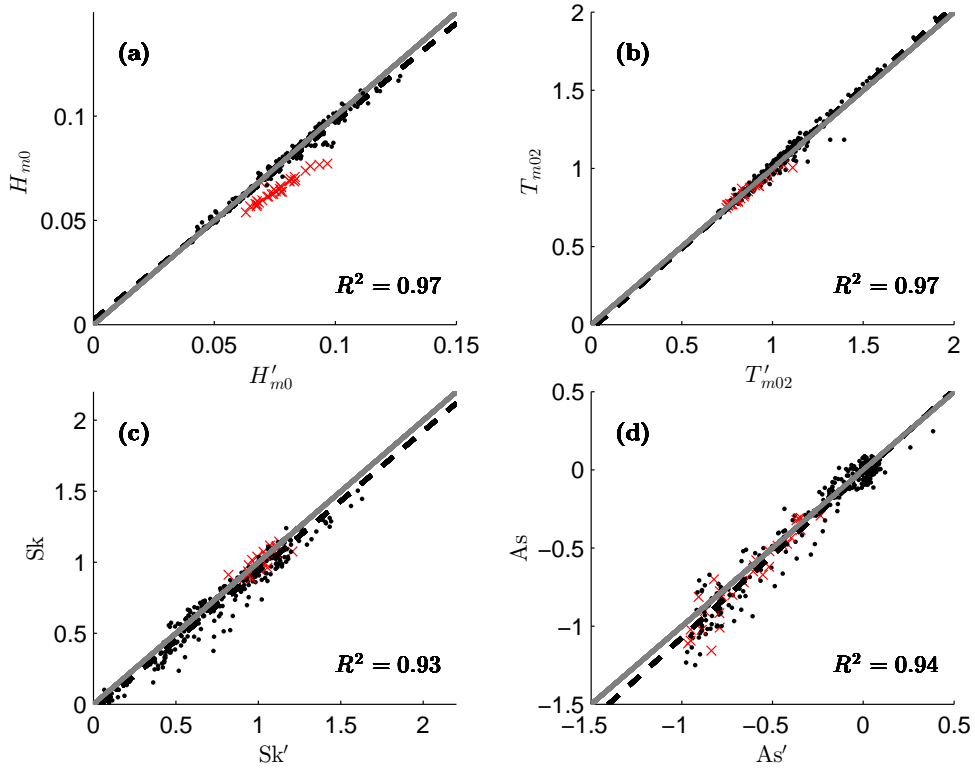


Figure 4.3: Scatter plots of observed (primed variables) versus computed values for: (a) significant wave height, (b) mean period, (c) skewness and (d) asymmetry. The solid grey line indicates one-to-one correspondence, whereas the dashed line is the best fit regression line ( $R^2$  values indicated in each panel). Red crosses correspond to values obtained from observations at gauge 8.

the combined effects of three-wave interactions and dissipation due to wave breaking strongly attenuates the spectral peaks, so that in the inner surfzone only the primary peak and sub-harmonics remain. Qualitatively, the picture is similar for other cases although for higher-frequency incident waves (e.g. case 11c, Fig. 4.4d–f) and more broad-banded wave fields (e.g. case 1a, Fig. 4.4j–l) the harmonic development is less pronounced.

There are several sources of long wave motion in the flume. In the shoaling process, three-wave interactions amplify bound long-wave components (here roughly defined as components with frequencies  $f < 0.5f_p$ ), which are subsequently released in the breaking process (e.g. Janssen *et al.*, 2003; Battjes *et al.*, 2004). Most of the energy contained in these frequencies subsequently reflects at the beach and radiates back out through the surfzone as free long waves. In the field such components would continue to propagate offshore (unless refractively trapped), but in the flume they are almost completely re-reflected by the wavemaker. Although some low-frequency energy is associated with second-order bound waves, and some spurious wave mo-

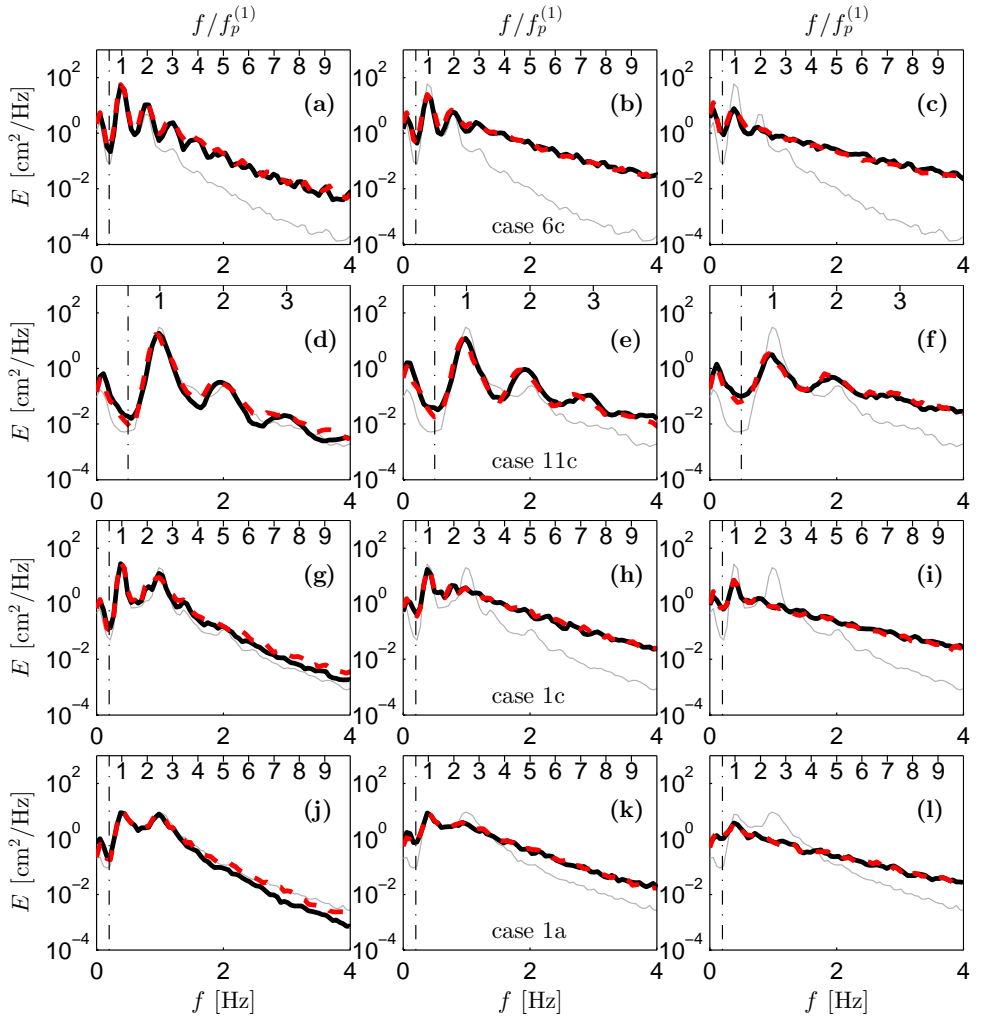


Figure 4.4: Comparison between the observed (dashed red lines) and computed (solid black lines) energy density spectra for four different cases (ordered from top to bottom) at gauge 2 (left panels), gauge 6 (center panels), and and gauge 10 (right panels). The lower horizontal axis indicates the absolute frequency, whereas the upper axis in each panel indicates the relative frequency  $f/f_p^{(1)}$ . Incident wave spectrum at the up-wave boundary is indicated by the thin grey line and the dash-dot line indicates the upper frequency  $(f_p^{(1)}/2)$  of the infra-gravity (ig) range.

tion due to the first-order wavemaker control, by far the largest contribution to the low-frequency energy is associated with these reflected and re-reflected free-wave components generated in the shoaling and breaking process by nonlinear three-wave interactions (see e.g. Battjes *et al.*, 2004). The level of agreement between model and observations suggests that the nonlinear surfzone wave-dynamics are captured accurately. The remaining differences between model and observations could be due to errors in the estimate for bottom friction, which is one of the primary mechanisms (in addition to breaking of long waves, e.g. Van Dongeren *et al.*, 2007) by which the longer waves loose energy.

One aspect that makes the present experimental dataset (Smith, 2004) particularly interesting, is the fact that it includes several cases with double-peaked spectra. These cases show a dramatic spectral evolution across the flume. Similar to previous laboratory observations by Smith and Vincent (1992), the secondary peak, which initially contains the bulk of the energy, diminishes rapidly on the slope, whereas the low frequency peak appears to grow at its expense. This behavior, which is also largely due to triad interactions, is clearly seen in the observed spectra for the double peaked cases, both for narrow or wide-band initial spectra, as exemplified here in cases 1c and 1a, respectively (see Fig. 4.4, panels g–l). The model also reproduces this reduction of the secondary peak (at 1 Hz), which is initially still visible at gauge 2 (panels g/j), but has virtually disappeared at gauges 6 (panels h/k) and 10 (panels i/l).

## ENERGY FLUXES

The effects of nonlinearity and dissipation on the various spectral regions can be further illustrated by considering the spatial evolution of the linear energy flux,  $F(f, x) = c_g E(f, x)$  at distinct frequencies. Since for linear and conservative wave propagation the wave energy flux is constant, changes in this flux indicate where nonlinear effects and dissipation are present. To reduce the sensitivity of the results to the details of the spectral analysis (e.g. such as the frequency resolution), we consider the normalized flux integrated over a finite frequency band  $\Delta f_n$ ,

$$\Delta F_n(x) = \frac{\int_{\Delta f_n} F(f, x) df}{F_{\text{tot}}(x_1)}, \quad (4.11)$$

where we normalized with the total energy flux  $F_{\text{tot}}(x) = \int F(f, x) df$  at the up-wave boundary (located at  $x_1$ ). The frequency band  $\Delta f_n$  is defined as a narrow frequency band around the  $n^{\text{th}}$  harmonic frequency, i.e.  $\Delta f_n$  is defined as the interval  $0.95(n+1)f_p^{(1)} < f < 1.05(n+1)f_p^{(1)}$ . In the following we consider the integrated energy flux for the primary peaks ( $\Delta F_0$ ), and their respective first ( $\Delta F_1$ ) and second harmonics ( $\Delta F_2$ ).

On the flat and at the start of the slope, the model shows near constant energy fluxes (see Fig. 4.5), indicating that there is very little dissipation or nonlinear transfers before the waves reach the slope. On the slope, the energy flux for the primary peak reduces, in part due to dissipation, and in part due to transfers to higher and lower frequencies, consistent with the increase in energy flux at the harmonic peaks at roughly the same location.

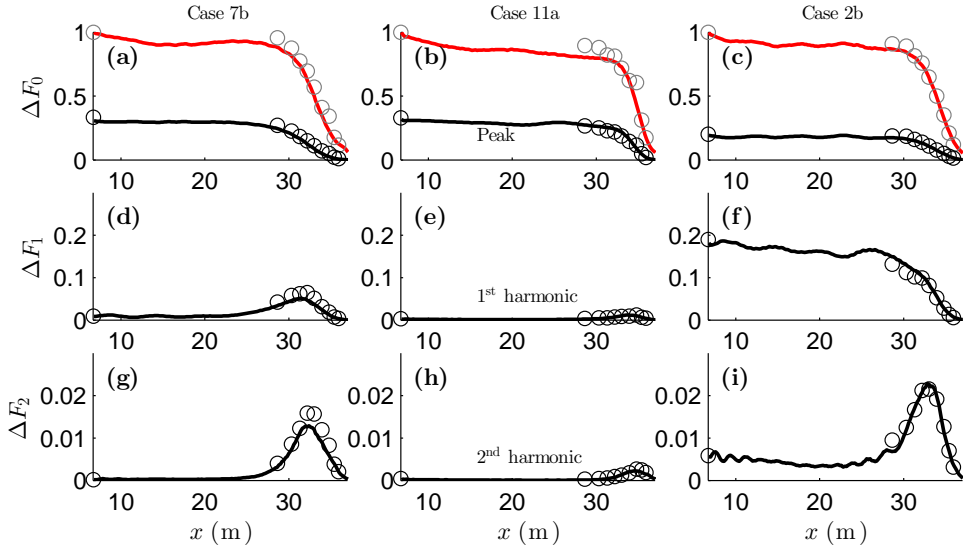


Figure 4.5: Comparison between the observed (symbols) and computed (lines) energy flux  $\Delta F_n$  (defined in (4.11)) contained in a frequency band around the peak (panels a–c), the first harmonic (panels d–f) and the second harmonic (panels g–i). Each column represents a different case (indicated on top). In the upper panels (a–c) the normalized total flux ( $= F_{\text{tot}}(x)/F_{\text{tot}}(x_1)$ ) is included (red lines/symbols) for reference.

At the start of the slope ( $x = 19$  m, see Fig. 4.1), dissipation is still weak as the total energy flux remains constant, so that for relatively long, narrow-band waves (e.g. case 7b, with  $k_p^{(1)}d = 0.88$ ,  $\gamma = 20$ ) the amplification of the higher harmonics can be clearly distinguished (panels a, d, and g in Fig. 4.5). In case of relatively high-frequency, broad-banded waves (e.g. case 11a, with  $k_p^{(1)}d = 2.5$ ,  $\gamma = 3.3$ ) such amplification is less pronounced, as the waves are in relatively deeper water and three-wave interactions therefore further from resonance. Moreover, for broad-banded waves, each frequency participates in more triads, thus broadening the resulting secondary peaks and resulting in less distinct spectral features than for narrow-band waves. Further up the slope, for higher-frequency, broader-band cases, amplification generally occurs only in the very shallow part of the flume (e.g. panels b, e, and h in Fig. 4.5). For both broad and narrow-banded cases, once dissipation becomes dominant, the energy flux around the peak and its harmonics is rapidly reduced. Overall, observed and modeled evolution of the primary and harmonic energy bands are in very good agreement.

The difference between the evolution of a single and double peaked spectrum is illustrated by comparing case 7b with case 2b, which differ only in their spectral shape. The evolution of the total energy flux, and that of the primary peak is relatively similar (viz. panel a and c in Fig. 4.5). However, for  $20 < x < 30$  no amplification occurs at the secondary peak (see Fig. 4.5f), despite the fact that in this case it coincides with the 1<sup>st</sup> harmonic of the primary peak (i.e.  $f_p^{(2)} = 2f_p^{(1)}$ ).

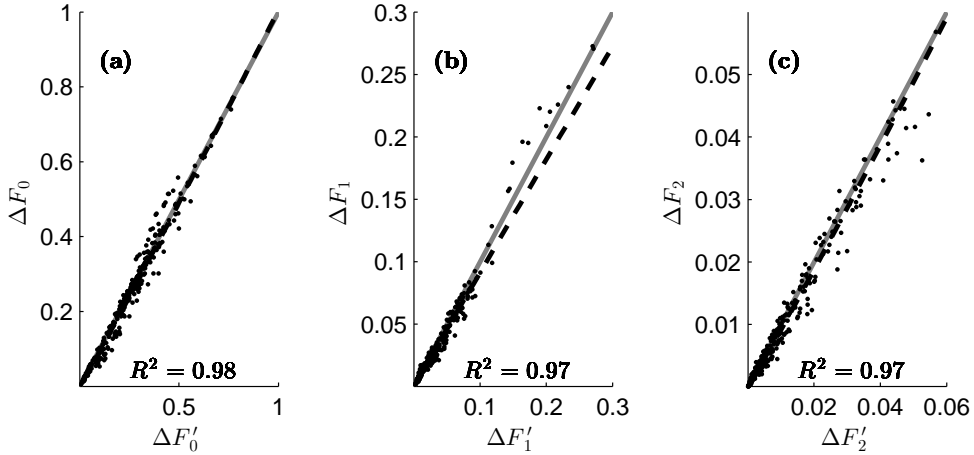


Figure 4.6: Comparison between the observed ( $\Delta F'_n$ ) and computed ( $\Delta F_n$ ) normalized energy fluxes at the primary peak (left panel), and its first (middle panel) and second (right panel) harmonic. The grey line indicates one-to-one correspondence, whereas the dashed line is the best fit linear regression line ( $R^2$  values given in panels).

In contrast, even before the onset of strong dissipation (which occurs for  $x > 30$ , see Fig. 4.5c), the energy flux around the secondary peak is attenuated, presumably due to nonlinear transfer to other frequencies. The regions where amplification and attenuation of the energy flux around the 2<sup>nd</sup> harmonic ( $3f_p^{(1)}$ ) occur, and the relative magnitudes of the respective fluxes, are again very similar (viz. Fig. 4.5g and 4.5i).

The overall performance of the model with regard to  $\Delta F_n$ , including contributions up to the second harmonic, is summarized in the scatter plots in Fig. 4.6a–c. The absence of outliers, and the high  $R^2$  values, confirms that the model captures the development up to and including the second harmonic very well. It should be noted that  $R^2$  values in this case are inflated due to the large range within the data, where the highest and lowest  $\Delta F_n$  can differ a factor factor 10<sup>2</sup>; even for large relative errors, small values in the data contribute little to the total variance of the error, but significantly to the observed variance, thus somewhat inflating values of  $R^2$ .

#### SHAPE OF THE HIGH-FREQUENCY TAIL IN THE SURFZONE

The wave spectra presented in Fig. 4.4 demonstrate that the strong amplification of the spectral energies in the high-frequency tail ( $f > 2.5f_p$ ), by at least an order of magnitude when compared to the incident spectra, is reproduced by the model. Furthermore, in all cases the model relaxes the high frequency tail into a fairly featureless shape in the surfzone. The development of such an asymptotic form in shallow water has been previously observed in both field and laboratory observations, which led Smith and Vincent (2003) to propose a universal parametric tail in the surfzone. Expressed in terms of the wave number spectrum  $E(k)$  (obtained from a linear transformation), their parametric tail consists of two ranges: the Toba range ( $kd > 1$ ), and the Zakharov range ( $2k_p d \leq kd \leq 1$ , with  $k_p$  the peak wave number).

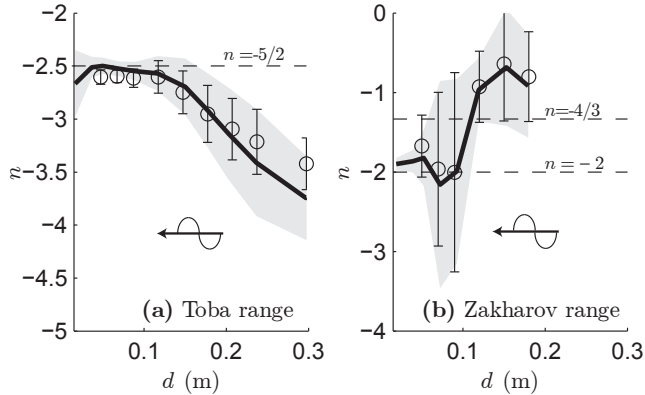


Figure 4.7: The slope  $n$  of best fit line to the log of the wavenumber spectrum  $E(k)$  within the Toba ( $kd > 1$ ) and Zakharov ( $k_p < kd < 1$ ) range. In both panels the mean  $n$  as calculated from observations (symbols) and from model results (line) is plotted as a function of depth. The region that lies within one standard deviation from the mean is indicated by bars for the observations, and as a shaded area for the model simulations. The arrow indicates that the wave direction in the figure is towards shallow water.

For the Toba range, Smith and Vincent (2003) found that the spectrum scales as  $E(k) \sim k^{-5/2}$ . For the Zakharov range they found that the spectrum scales as  $E(k) \sim k^{-4/3}$ , similar to the tail in shallow water proposed by Zakharov (1999). As noted by Kaihatu *et al.* (2007), referring to these ranges as the Toba and Zakharov range is somewhat questionable for strongly nonlinear, breaking surfzone waves. Toba proposed his asymptotic form based on observations of wind-driven, deep-water waves (which obviously does not apply here), and the strongly nonlinear conditions found in the surfzone are outside the range where the theory by Zakharov (1999) can be applied. Regardless of whether the eponymous naming of these spectral ranges is entirely justified, the observations considered by Kaihatu *et al.* (2007) generally supported the results of Smith (2004) at the edge of the surfzone, although they also found that the spectrum has a clear  $E(k) \sim k^{-2}$  asymptote in very shallow water.

Because in the present data set the Zakharov range only exists at the most shoreward location (elsewhere  $2k_p d > 1$ ), we extended – following Kaihatu *et al.* (2007) – this range to  $k_p d \leq kd \leq 1$ . For each case we transformed the spectra to wavenumber space using linear theory, and determined the exponent,  $n$ , of the shape function  $\alpha k^n$  that best fitted the data from the slope of the linear regression line between  $\log[E(k)]$  and  $\log(k)$ . This analysis was performed for the Zakharov and Toba ranges separately, yielding a value for  $n$  in either range at each separate gauge for all of the 31 experiments. Subsequently, at each gauge the mean value and the standard deviation were determined, yielding a mean value  $n_{\text{Zak}}$  and  $n_{\text{Toba}}$ , and standard deviation  $\sigma_{\text{Zak}}$  and  $\sigma_{\text{Toba}}$ , for the Zakharov and Toba range respectively, the results of which are shown in Fig. 4.7.

In very shallow water ( $d < 0.15$  m), the mean value of  $n_{\text{Toba}}$  compares well with the earlier reported values (see Fig. 4.7a); it tends to  $-5/2$  with relatively small

scatter around the mean in both the observed or computed data ( $\sigma_{\text{Toba}} < 0.1$  for  $0.05 < d < 0.12$  m). For increasing depth, values for  $n_{\text{toba}}$  obtained from computed spectra are at some variance with the observations ( $d > 0.2$  m), with increased scatter around the mean ( $\sigma_{\text{Toba}} > 0.3$ ), but generally larger scatter in the computed than in the observed results. This larger scatter in the spectral shape for the Toba range in the deeper parts of the flume, and also the lesser agreement with observations, are likely due to being in the vicinity to the wavemaker, so that the spectrum is still adjusting from the artificial wavemaker input, and has not yet developed into an equilibrium shape. A better correspondence with the observed tail most likely requires that the numerical wavemaker exactly reproduces the high-frequency tail, including possible nonlinear contributions.

For the Zakharov range, the agreement with observations, both in the mean trend and in the scatter, is excellent (Fig. 4.7b), with good correlation ( $R^2 = 0.97$ ) between results obtained from observations and computations (not shown). However, although the averages in the surfzone are close to theoretical value of  $n_{\text{zak}} = -4/3$  (they are -1.3 and -1.41 for observations and model, respectively), neither the model nor observations appear to converge to this value when nearing the shoreline. In general, the scatter is quite large, but near the shore-line (between a depth of 0.05 to 0.1 m)  $\sigma_{\text{Zak}}$  this scatter is significantly reduced, both in the observations (from 1.3 to 0.3) and computations (from 1.3 to 0.1). As  $d \rightarrow 0$  the model seems to converge to  $n_{\text{zak}} = -1.9$  with  $\sigma_{\text{Zak}} = 0.08$ , in accordance with  $E(k) \sim k^{-2}$  asymptote in very shallow water as found by Kaihatu *et al.* (2007).

#### NONLINEAR ENERGY TRANSFER

In shallow water, the dominant nonlinear energy transfer is associated with near-resonant triad interactions, the strength of which generally depend the coupling coefficient, energy content of the components involved in the interaction, and how close the interaction is to resonance. To compare transfer rates inferred from observations and model results therefore requires the evaluation of a nonlinear source term  $S_{\text{nl}}$  that depends on the bispectrum  $\mathcal{B}(f_1, f_2, x)$ , and which has the general form (e.g. Herbers and Burton, 1997; Becq-Girard *et al.*, 1999; Janssen, 2006)

$$S_{\text{nl}}(f) = 4 \int_0^f C(f', f - f') \mathcal{B}_{\text{im}}(f', f - f') df' - 8 \int_0^\infty C(f + f', -f') \mathcal{B}_{\text{im}}(f, f') df', \quad (4.12)$$

where  $C$  is a (real) coupling coefficient and  $\mathcal{B}_{\text{im}}$  denotes the imaginary part of the bispectrum. The bispectrum captures the phase relationship between a triad of waves  $f_1, f_2$  and  $f_3 = f_1 + f_2$ , and describes the third-order statistics of the wave field. For instance, skewness and asymmetry can be obtained from the real or imaginary part of the integral over the bispectrum, respectively, i.e.  $\text{Sk} + i\text{As} = \iint \mathcal{B}(f_1, f_2) df_1 df_2 / m_0^{3/2}$ . The source term  $S_{\text{nl}}(f)$  includes all sum and difference contributions to frequency  $f$ . For second-order Stokes waves on a horizontal bottom  $\mathcal{B}_{\text{im}}(f_1, f_2) = 0$ , and no energy transfer occurs.

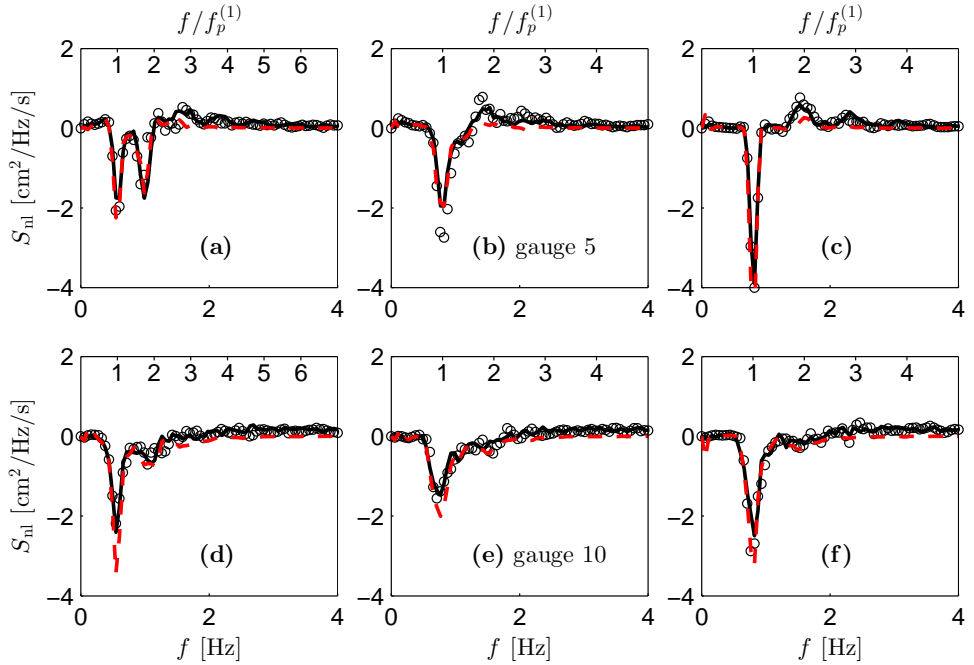


Figure 4.8: The nonlinear source term  $S_{nl}$  computed at two different gauges (ordered from top to bottom) for case 3b (left panels), case 10a (middle panels), and case 10c (right panels). The source term is computed from the bispectrum obtained from the observations (markers) and computations (solid black line). In addition the linear flux gradient  $F_x$  (dashed red line) estimated from model results is included. The lower horizontal axis indicates the absolute frequency, whereas the upper axis in each panel indicates the relative frequency  $f/f_p^{(1)}$ .

Since the observation points are in shallow water ( $k_p d < 1$ ) we use Boussinesq theory (Herbers and Burton, 1997; Herbers *et al.*, 2000) to evaluate  $S_{nl}$ , so that  $C(f_1, f_2) = 2\pi(f_1 + f_2)/d$ . The use of Boussinesq theory only affects the interaction kernel, which will be the same for both model results and observations (the bispectrum is estimated from observations and model results directly), so that the inter-comparison is consistent. We approximate the integrals over the bispectrum using the trapezoidal rule with an upper-frequency of 6 Hz in the second term on the RHS of Eq. (4.12). Bispectra are obtained using the same spectral analysis of observed and computed time series as before.

Results for three representative cases, including a wide (10a), narrowband (10c), and double-peaked (3b) incident spectrum, are shown in Fig. 4.8. The transfer rates computed from the model simulation results are in good agreement with the values computed from the observations, with overall better correspondence in the energetic part of the spectrum ( $f < 2f_p$ ), and slightly worse correspondence in the tail. The nonlinear interactions transfer energy from the primary peak(s) of the spectrum to the higher (and lower) frequencies. For instance, in case 10c at gauge 5 (Fig. 4.8c), energy is transferred from the spectrum peak ( $f = 0.8$ Hz), to its first ( $f = 1.6$ Hz),

second ( $f = 2.4$  Hz) and (presumably) higher harmonics. In the case of more broad-banded irregular waves, the great number of interactions that take place result in a more uniform shape of  $S_{\text{nl}}$  at the frequencies above the peak (e.g. Fig. 4.8a/c). In the inner surfzone (gauge 10), energy is mostly transferred from  $0.5f_p \leq f \leq 2f_p$ , toward higher frequencies ( $f > 2f_p$ ), regardless of the width of the incident spectrum (viz. case 10a with case 10c in Fig. 4.8e/f, respectively).

In the absence of dissipation  $S_{\text{nl}}$  approximately balances with  $F_x$ , and large differences between  $S_{\text{nl}}$  and  $F_x$  are therefore indicative of dissipation. The gauge spacing (varying from 0.5 to 1.6 m) is too large to obtain estimates for  $F_x$  from the observations directly in the highly dynamic surfzone. However, such estimates can be readily obtained from the more finely spaced model results using second-order finite differences,

$$F_x(f, x) \approx \frac{F(f, x + \Delta x) - F(f, x - \Delta x)}{2\Delta x} \quad (4.13)$$

where  $\Delta x$  is the computational mesh-size. Near the peak of the spectrum (see Fig. 4.8 panels a-c) changes in  $F_x$  are approximately balanced by  $S_{\text{nl}}$ , suggesting that for  $f < 2f_p$  the evolution of the spectrum is primarily determined by nonlinearity whereas the dissipation rates – even in the inner surfzone – remains relatively small in this spectral range (e.g. panels d–f). For  $f > 2f_p$  the evolution of  $F_x$  is minimal, suggesting that dissipation and nonlinear transfers are nearly in balance. This (model) behavior shows that energy is not dissipated in the energetic range of the spectrum, but instead is transferred from the peak to the higher frequencies, where it is subsequently dissipated, consistent with observations by other researchers (e.g. Herbers *et al.*, 2000).

## 4.5. DISCUSSION

The results presented thus far are quasi-deterministic, in the sense that all results were derived from a single, relatively short realization using deterministic boundary conditions. The differences between model and observations can therefore be ascribed to modelling inaccuracies (we ignore measurement noise or errors, except for the possible gauge calibration issue at gauge 8) and are not due to uncertainty in statistical estimates, which would be inevitable for a finite-length time series. Since the deterministic comparison showed excellent agreement between model and data for all relevant surfzone wave processes studied here, we expand on this here to study the surfzone statistics and dissipation characteristics from Monte Carlo simulations with the model. The Monte Carlo simulations consist of 10 realizations for each case considered. Each realization is forced with randomized initial conditions (from the observed spectrum with added random phases). This extends the total number of data points  $N^{\text{tot}}$  from  $1.2 \times 10^4$  to  $1.2 \times 10^5$ .

For these 2DV simulations (1D wave propagation), the complete Monte Carlo simulation (10 realizations) takes about 300 minutes per case on a 6-core Intel Xeon 3.2 GHz CPU. When considering 2D wave propagation, computational times are considerably higher but feasible on larger multi-processor systems, in particular since even a more coarse vertical grid (i.e. 2 vertical layers) can still yield reliable estimates

for the bulk parameters and wave spectrum up to three times the peak frequency (see e.g. Smit *et al.*, 2013).

### FREE-SURFACE STATISTICS

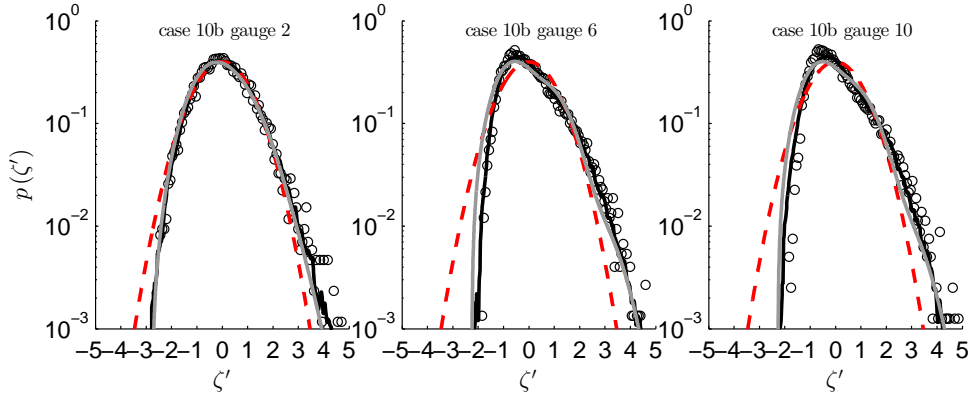


Figure 4.9: Probability density functions (pdf) for the normalized free surface  $\zeta' = \zeta/\sqrt{m_0}$  estimated from the observations (circles) and from the Monte Carlo simulations (solid black line), compared with a Gaussian distribution (dashed red line) and a two-term Gram-Charlier (Eq. (4.14)) series (grey line) using the skewness values obtained from the Monte Carlo simulations.

The probability density function for Case 10b, characterized by relatively short incident waves ( $k_p^{(1)}d = 1.7$ ) with a fairly narrow-band spectrum ( $\gamma = 20$ ), is shown in Fig. 4.9. The theoretical distribution in that figure is a two-term Gram-Charlier expansion (Longuet-Higgins, 1963), which can be expressed as

$$p(\zeta') = \frac{P(\zeta', \text{Sk})}{\sqrt{2\pi}} \exp\left[-\frac{1}{2}(\zeta')^2\right]. \quad (4.14)$$

For  $P = 1$  this is the normalized Gaussian distribution, whereas for the nonlinear pdf the polynomial  $P(\zeta', \text{Sk})$  depends only on variance and skewness (for details of  $P$ , see Longuet-Higgins, 1963).

At the edge of the surfzone (left panel of Fig. 4.9) the pdf is strongly skewed, which increases at the locations further inside the surfzone (centre and right panel of Fig. 4.9). The deviation from the Gaussian distribution shows that the waves are nonlinear, with relatively sharp and tall peaks, and shallow and elongated troughs, which shows that a nonlinear wave model is required to reliably estimate surfzone statistics. Although a direct comparison with the observed pdf for  $|\zeta'| > 3$  is difficult due to the relatively short time series (and thus relatively low data density to populate the tails of the distribution), the agreement between the observations, Monte Carlo simulations, and the theoretical distribution is very good. Comparisons for other cases showed similar agreement (not shown). This shows that nonlinear effects are important for surfzone statistics, but that knowledge of the lowest two moments, variance and skewness, suffices to capture the principal characteristic of the pdf. As shown in the model results, SWASH can accurately model and predict these moments.

## SPECTRAL DISTRIBUTION OF DISSIPATION

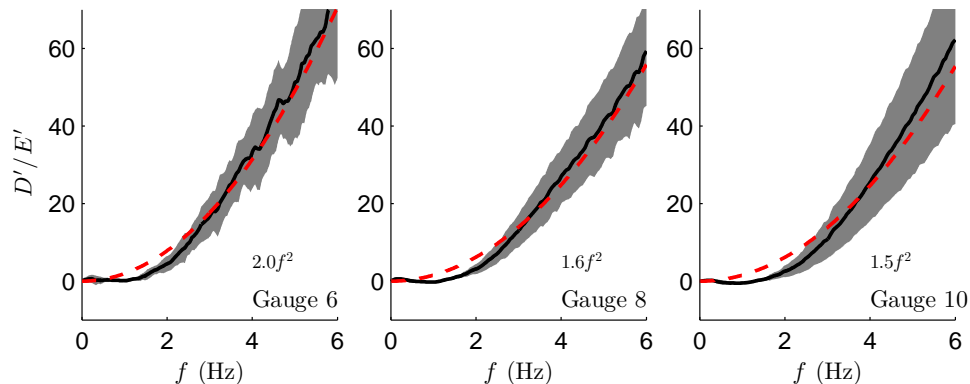


Figure 4.10: Mean (over all 31 cases) of the distribution function scaled with the normalized energy,  $D'(f)/E'$  (solid black line), compared with a least squares fit  $\alpha f^2$  shape (dashed line). The patched area indicates the region within one standard deviation of the mean.

Energy dissipation due to wave breaking is arguably the most important, and yet the least understood process in the surfzone (e.g. Peregrine, 1983). In general, bulk dissipation rates are reasonably well estimated by semi-empirical formulations based on a bore analogy (e.g. see Salmon *et al.*, 2014b, for an extensive overview), however, spectral models require a spectral distribution of the dissipation, which is not available from theory or observations. As a consequence, spectral breaker dissipation functions  $D(f)$  are invariably expressed as  $D(f) = D_0 D'(f)$ , where  $D'(f)$  is an unknown distribution function, for which  $\int D'(f) df = 1$  and  $D_0$  is the bulk dissipation. Eldeberky (1996) assumed that the distribution function  $D'(f)$  is proportional to the normalized spectrum,  $D'(f) = E'(f)$ , where  $E'(f) = E(f)/m_0$ , so that dissipation is stronger in the more energetic ranges of the spectrum. Other studies found that better results for third-order bulk statistics are obtained by weighting the dissipation function toward higher frequencies using  $D'(f) = f^2 E'(f)$  (e.g. Kirby and Kaihatu, 1996; Chen *et al.*, 1997), or a linear combination of the two shapes (Mase and Kirby, 1992). Weighting the dissipation toward higher frequencies is consistent with the observation that dissipation takes place mostly at the higher frequencies but is not very strong in the energy-carrying ranges (see e.g. Section 4.4 of the present work or e.g. Herbers *et al.*, 2000).

In SWASH, we do not impose any distribution as wave breaking is handled in the time domain, but the resulting spectral signature can be estimated from the model results. Assuming that dissipation is the term responsible for closing the balance between  $F_x$  and  $S_{nl}$ , i.e.  $D(f, x) = F_x(f, x) - S_{nl}(f, x)$ ,  $D'(f)$  can be directly estimated from the Monte Carlo simulation. In Fig. 4.10, we show the mean and standard deviation from the 31 Monte Carlo simulations for the ratio  $D'(f)/E'(f)$ , which measures the dissipation rate at each frequency relative to the amount of energy. In the presence of strong dissipation in the inner surfzone, the mean of  $D'/E'$  strongly emphasizes higher frequencies (see Fig. 4.10). At deeper, more offshore,

locations (i.e. gauge 2–5) dissipation is weak, so that  $D'(f)/E'(f)$  is more variable and noisy, and no clear pattern can be discerned (not shown). For  $f < 2\text{ Hz}$  the computed ratio can become slightly negative, which would seem to imply 'positive dissipation', but is likely caused by small relative errors in the estimation of  $S_{nl}$  and  $F_x$ , which dominate the balance in this region (although dissipation is small here, it results as the difference of two large, but opposing, terms). Overall, the model-predicted dissipation rate  $D'(f)$  agrees fairly well with the earlier suggested  $f^2$  weighting (see Fig. 4.10). Since in SWASH  $D'(f)$  is not prescribed but rather follows from the Monte Carlo data directly, this result appears to corroborate the use of an  $f^2$  weighting for breaking dissipation. More generally, this also illustrates how a fairly detailed non-hydrostatic model can be a valuable tool in developing or testing parameterisations used in operational (e.g. Tolman, 1991; Booij *et al.*, 1999) or research spectral wave models.

## 4.6. CONCLUSIONS

In the present work we considered modelling of wave dynamics in the surfzone using the non-hydrostatic model SWASH. Detailed comparison to flume observations shows that a relatively efficient model such as SWASH, in which the details of the breaking process such as overturning and turbulence are not resolved, can reliably predict surfzone (non-Gaussian) wave statistics. Our results show that even without calibration or fine-tuning, the model accurately predicts both second-order bulk parameters such as wave height and period, higher-order statistics, including skewness and asymmetry of the waves, and the details of the spectral evolution (up to 10 times the peak frequency). The generally excellent agreement between the model results and the observations, demonstrates that the model accurately captures the macro-effects of the dominant nonlinear and dissipative processes in the surfzone, in particular the triad wave-wave interactions and the dissipation due to breaking. These results show that for the predominantly spilling breaker conditions considered, a non-hydrostatic model with a single-valued representation of the free surface, can provide an accurate presentation of the wave statistics in the surfzone. Hence, the representation of the free-surface as a single-valued function appears not to prevent an accurate representation of the wave statistics in the surfzone, at least in case of spilling breakers. The pdf of the free-surface, estimated by Monte Carlo simulations, compares well with a theoretical nonlinear pdf that depends on the first two moments, variance and skewness, both of which can be reliably estimated from SWASH simulations. From the energy balance we derived that the wave dissipation in SWASH is proportional to a frequency-squared distribution function, which is consistent with observations in other studies. Although the present study considers one-dimensional wave propagation in a flume, we note that triad nonlinear and dissipation processes are not fundamentally different for 2D surfzones with short-crested waves, so that our conclusions are probably also valid under such conditions. Overall, the findings of this study suggest that SWASH is a viable tool for modelling wave and wave-driven dynamics in a nonlinear, dissipative surfzone.

## ACKNOWLEDGMENTS

This research is supported by the U.S. Office of Naval Research (Littoral Geosciences and Optics Program and Physical Oceanography Program) and by the National Oceanographic Partnership Program.



# Appendix

## 4.A. FREQUENCY DISPERSION IN SWASH

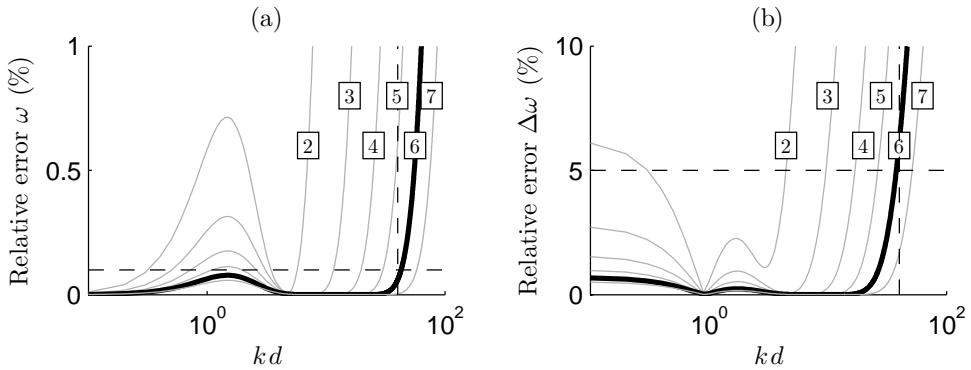


Figure 4.11: Absolute relative error (in percent) in (a) the angular frequency  $\omega(k)$ , and (b) resonant mismatch for self-self interactions  $\Delta\omega(k, k) = 2\omega(k) - \omega(2k)$ , when using the dispersion relation obtained from an  $N$  layer system,  $\omega_N$  compared to using the linear dispersion relation,  $\omega$ , as a function of the relative depth  $kd$ . Depicted are the error curves for  $N$  between 2 to 7, which shows that for  $N = 6$  (thick solid line) the error remains below 0.1 and 5 percent (horizontal dashed lines), respectively, for  $kd < 40$  (vertical dashed line).

To a large extent, the magnitude of the nonlinear transfers is determined by the resonant mismatch,  $\Delta\omega(k_1, k_2) = \omega(k_1) + \omega(k_2) - \omega(k_1 + k_2)$  among a triad of waves with wavenumber  $k_1, k_2, k_3$  so that  $k_3 = k_1 + k_2$ . A correct representation of nonlinear interactions therefore not only requires a good approximation to linear dispersion of the three interacting components, but also of their resonant mismatch. In general, for non-hydrostatic models, the horizontal scales are well resolved, whereas the vertical resolution is relatively coarse. Hence the accuracy of the linear dispersive behavior of the numerical model is largely determined by the vertical resolution, and can therefore be estimated from the semi-discrete system obtained by discretization of the vertical. In the case of SWASH, the linear, semi-discrete system corresponding to Eq. (4.1) to (4.4), for  $N$  vertical layers, is given by application of an edge-based grid in the vertical combined with the Keller-box approximation for the vertical pressure

gradients,

$$\frac{\partial u_{n-\frac{1}{2}}}{\partial t} + g \frac{\partial \zeta}{\partial x} + \frac{1}{2} \frac{\partial p_n^{\text{nh}}}{\partial x} + \frac{1}{2} \frac{\partial p_{n-1}^{\text{nh}}}{\partial x} = 0, \quad n = 1..N, \quad (4.15)$$

$$\frac{\partial w_n}{\partial t} + \frac{\partial w_{n-1}}{\partial t} + 2 \frac{p_n^{\text{nh}} - p_{n-1}^{\text{nh}}}{\Delta z} = 0, \quad n = 1..N, \quad (4.16)$$

$$\frac{\partial u_{n-\frac{1}{2}}}{\partial x} + \frac{w_n - w_{n-1}}{\Delta z} = 0, \quad n = 1..N, \quad (4.17)$$

$$\frac{\partial \zeta}{\partial t} + \Delta z \sum_{n=1}^N \frac{\partial u_{n-\frac{1}{2}}}{\partial x} = 0. \quad (4.18)$$

Here, the  $n^{\text{th}}$  pressure and vertical velocity components,  $p_n$  and  $w_n$  (with  $n \in \{0 \dots N\}$ ) are located on the layer interface, whereas the layer averaged velocity  $u_{n-\frac{1}{2}}$  (with  $n \in \{1 \dots N\}$ ) are located in the central plane, where  $\{\dots\}_n = \{\dots\}(x, z_n, t)$  with  $z_n = n\Delta z - d$ , with  $\Delta z = d/N$ . From the dynamic boundary condition at the free surface we have  $p_N^{\text{nh}} = 0$ . Moreover, if we assume a horizontal bottom, we obtain from the kinematic boundary condition at the bed that  $w_0 = 0$ . If we then consider the initial value problem on an infinite domain, we can associate  $\partial_t \zeta \rightarrow -i\omega \hat{\zeta}(k, \omega)$ , and  $\partial_x \rightarrow ik \hat{\zeta}(k, \omega)$ , and similarly for  $u_{n-\frac{1}{2}}, w_n$ , to obtain for each mode  $\omega, k$  a  $(3N + 1) \times (3N + 1)$  linear system  $A(k, \omega)$  in terms of the Fourier amplitudes

$$\hat{y} = \left[ \hat{u}_{\frac{1}{2}}, \dots, \hat{u}_{N-\frac{1}{2}}, \hat{w}_1, \dots, \hat{w}_N, \hat{p}_0, \dots, \hat{p}_{N-1}, \hat{\zeta} \right], \quad (4.19)$$

so that  $A\hat{y} = 0$ . For this system to have solutions other than the trivial solution,  $A$  must be singular, or  $\text{Det}(A) = 0$ , resulting in a polynomial relating  $\omega$  and  $k$ , from which the linear dispersion relation  $\omega_N(k)$  that corresponds to the  $N$  layer system can be determined. As the calculations quickly become involved for  $N > 1$ , this is done using a symbolic algebra system<sup>2</sup>.

From  $\omega_N$  thus obtained, it can be seen that, assuming the horizontal scales are well resolved, the number of layers required to accurately model dispersion mainly depends on the maximum relative depth within the frequency range of interest (see Fig. 4.11a). In the present work this corresponds to waves with  $f < 4$  Hz, or  $kd < 40$ . By using 6 layers, the maximum relative error for  $kd < 40$  remains below 0.1%. A similar analysis can be made for the frequency mismatch  $\Delta\omega(k_1, k_2)$ , when considering the mismatch for the self-self interactions,  $\Delta(k, k)$ , for different values of  $kd$  (see Fig. 4.11b). This shows that for 6 layers, the relative error is less than 6% for  $kd < 40$ .

<sup>2</sup>implemented using the Matlab Symbolic Toolbox.

# 5

## The evolution of inhomogeneous wave statistics through a variable medium

The interaction of ocean waves with variable currents and topography in coastal areas can result in inhomogeneous statistics due to coherent interferences, which affect wave-driven circulation and transport processes. Stochastic wave models, invariably based on some form of the radiative transfer equation (or action balance), do not account for these effects. In the present work we develop and discuss a generalization of the radiative transfer equation that includes the effects of coherent interferences on wave statistics. Using multiple scales, we approximate the transport equation for the (complete) second-order wave correlation matrix. The resulting model transports the coupled-mode spectrum (a form of the Wigner distribution) and accounts for the generation and propagation of coherent interferences in a variable medium. We validate the model through comparison to analytic solutions and laboratory observations, discuss the differences with the radiative transfer equation and the limitations of our approximation, and illustrate its ability to resolve coherent interference structures in wave fields such as those typically found in refractive focal zones and around obstacles.

---

This chapter has been published as: SMIT, P.B. and JANSSEN, T.T., 2013b The Evolution of Inhomogeneous Wave Statistics through a Variable Medium. *J. Phys. Oceanogr.*, 43, 1741–1758.

## 5.1. INTRODUCTION

The dynamics and statistics of ocean waves are important e.g. for upper ocean dynamics (e.g. Craik and Leibovich, 1976; Smith, 2006; Aiki and Greatbatch, 2011), air-sea interaction (e.g. Janssen, 2009), ocean circulation (e.g. McWilliams and Restrepo, 1999), and wave-driven circulation and transport processes (e.g. Hoefel and Elgar, 2003; Svendsen, 2006). Modern stochastic wave models are routinely applied to a wide range of oceanic scales, both in open-ocean applications and the nearshore, and either as stand-alone wave prediction models, or as part of coupled ocean-atmosphere models for global circulation and climate studies (e.g. The WAMDI Group, 1988; Tolman, 1991; Komen *et al.*, 1994; Booij *et al.*, 1999; Wise Group, 2007). These so-called third-generation wave models are invariably based on some form of the radiative transfer equation (or action balance)

$$\partial_t E + \mathbf{c}_x \cdot \nabla_{\mathbf{x}} E + \mathbf{c}_k \cdot \nabla_{\mathbf{k}} E = S, \quad (5.1)$$

which describes the evolution of the variance (or action) density spectrum  $E(\mathbf{k}, \mathbf{x}, t)$  through time  $t$ , geographical space  $\mathbf{x}$ , and wavenumber space  $\mathbf{k}$ , with the transport velocities  $\mathbf{c}_x$  and  $\mathbf{c}_k$ , respectively, and augmented with (parametrised) source terms  $S(\mathbf{k}, \mathbf{x}, t)$  to account for non-conservative and nonlinear processes.

Continuing development of these models is generally through improvements of the source term parameterisations on the right side of equation (5.1), but the left side, the radiative transfer equation (RTE), has not changed since the early development of these models (e.g. The WAMDI Group, 1988; Komen *et al.*, 1994; Wise Group, 2007). The RTE transports wave variance density through a slowly varying medium such that wave energy (or action) is conserved, while assuming that the wave field is (and remains) quasi-homogeneous and near-Gaussian. In the open ocean, where medium variations are generally very weak, and wave statistics evolve principally through the action of wind, dissipation (whitecapping) and third-order nonlinear effects, the assumptions of homogeneity and Gaussianity are often easily met. However, on continental shelves and in coastal regions, where wave fields travel through shallower water, and medium variations are stronger (both currents and topography), the wave field can develop and maintain inhomogeneities that strongly affect the wave statistics (e.g. Janssen *et al.*, 2008; Janssen and Herbers, 2009). For instance, the refraction over coastal topography or currents (e.g. Berkhoff *et al.*, 1982; Vincent and Briggs, 1989; Magne *et al.*, 2007; Janssen *et al.*, 2008), or diffraction around obstacles such as breakwaters, reefs, or headlands (e.g. Penney and Price, 1952), can result in relatively fast variations in wave statistics due to coherent wave interference patterns. The effect of such coherent structures on the wave statistics are not accounted for by the RTE (Vincent and Briggs, 1989; O'Reilly and Guza, 1991).

To account for the effects of coherent interferences on the wave statistics, more general transport models for second-order wave statistics were developed in other fields, such as optics and quantum mechanics (e.g. Wigner, 1932; Bremmer, 1972; Bastiaans, 1979; Cohen, 2010). For ocean waves such models were developed for special cases, including narrow-band waves (e.g. Alber, 1978) and forward-scattered waves through a weakly two-dimensional medium (e.g. Janssen *et al.*, 2008). In the present work we apply the ideas developed in optics (e.g. Bremmer, 1972; Bastiaans,

1979; Cohen, 2010), to derive a more general transport model for ocean wave statistics in the presence of caustics and coherent interferences, which includes the RTE as a special case.

There to we derive a general transport equation for the second-order correlation matrix for linear waves in a slowly varying medium, and – using multiple scales – derive a consistent, quasi-coherent approximation that includes coherent interferences (§5.2). In §5.3, to illustrate the accuracy of our approximations and the differences with the RTE, we compare a numerical implementation of the model to an analytic solution for the evolution of coherent Gaussian wave packets, and compare model simulations to observations of random wave propagation over a two-dimensional shoal (Vincent and Briggs, 1989). We discuss (§5.4) the spectral distribution function (the coupled-mode spectrum), the limits of the approximation, wave diffraction in the quasi-coherent approximation, and show that the quasi-coherent approximation includes earlier results as special cases (e.g. Alber, 1978).

## 5.2. EVOLUTION OF CORRELATORS

To study the generation and propagation of coherent structures in random ocean wave fields propagating through a variable medium, we consider the statistics of the free-surface elevation  $\eta(\mathbf{x}, t)$ , represented as a zero-mean random wave variable and a function of the horizontal coordinates  $\mathbf{x} = (x, y)$  and time  $t$ . We define a complex variable  $\zeta$ , such that  $\eta = \text{Re}\{\zeta\}$ , its real and imaginary parts form a Hilbert transform pair (see e.g. Mandel and Wolf, 1995), and its Fourier transform  $\widehat{\zeta}$  is defined by the transform pair<sup>1</sup>

$$\zeta(\mathbf{x}, t) = \int \widehat{\zeta}(\mathbf{k}, t) \exp(i\mathbf{k} \cdot \mathbf{x}) d\mathbf{k}, \quad (5.2a)$$

$$\widehat{\zeta}(\mathbf{k}, t) = \frac{1}{(2\pi)^2} \int \zeta(\mathbf{x}, t) \exp(-i\mathbf{k} \cdot \mathbf{x}) d\mathbf{x}. \quad (5.2b)$$

We assume that medium variations are relatively slow, varying  $O(1)$  over distances  $l_0/\epsilon$ , with  $l_0$  being a characteristic wave length and  $\epsilon \ll 1$ , so that plane wave solutions are admitted and a dispersion relation of the form  $\omega = \sigma(\mathbf{k}, \mathbf{x})$  exists locally. The free-surface elevation  $\eta$  is considered a superposition of slowly varying wave packets  $\zeta_j$ , each characterized by its position  $\mathbf{x}_j(t)$ , wave number  $\mathbf{k}_j(t)$ , and angular frequency  $\omega_j(t)$ . In the present work we consider medium variations due to variations in depth,  $h(\mathbf{x})$ , so that in absence of currents (and to  $O(\epsilon)$ ) the dispersion relation is  $\sigma(\mathbf{k}, \mathbf{x}) = \sqrt{gk \tanh(kh)}$ , where  $k = |\mathbf{k}|$  (e.g. Dingemans, 1997; Mei *et al.*, 2005).

Our starting point is the equation of motion for the transformed free-surface variable  $\widehat{\zeta}(\mathbf{k}, t)$ , which we write as (e.g. Salmon, 1998; Bremmer, 1972)

$$\partial_t \widehat{\zeta}(\mathbf{k}, t) = -i\Omega(\mathbf{k}, i\nabla_{\mathbf{k}}) \widehat{\zeta}(\mathbf{k}, t). \quad (5.3)$$

<sup>1</sup>Unless made explicit otherwise, integration limits on (Fourier) integrals are from  $-\infty$  to  $+\infty$ , and the transforms are assumed to exist in the context of generalized functions (Strichartz, 1993).

Here we use operator correspondence between conjugate variables:  $-\mathrm{i}\omega_j \rightarrow \partial_t$ ,  $\mathbf{x}_j \rightarrow \mathrm{i}\nabla_{\mathbf{k}}$  and  $\mathbf{k}_j \rightarrow \mathbf{k}$ , to relate the local dispersion relation to an operator  $\sigma(\mathbf{k}_j, \mathbf{x}_j) \rightarrow \Omega(\mathbf{k}, \mathrm{i}\nabla_{\mathbf{k}})$ , which is defined using the Weyl correspondence rule (see Appendix A, and e.g. Agarwal and Wolf, 1970). It can be readily shown that the wave equation (5.3) describes progressive waves (Appendix A), is exact in a homogeneous medium (Appendix A), and is consistent with WKB theory for slowly varying waves (Appendix B). From the wave equation (5.3), an evolution equation for the second-order moments  $\langle \widehat{\zeta}_1 \widehat{\zeta}_2^* \rangle$  is obtained in the usual way<sup>2</sup>, and upon transforming the coordinates to  $\mathbf{k} = (\mathbf{k}_1 + \mathbf{k}_2)/2$  and  $\mathbf{u} = \mathbf{k}_1 - \mathbf{k}_2$ , and Fourier transforming the result with respect to the difference wavenumber  $\mathbf{u}$ , the transport equation for the second-order statistics can be written as (see e.g. Bremmer, 1972; Bastiaans, 1997; Cohen, 2010)

$$\partial_t \mathcal{E} = -\mathrm{i} \left[ \Omega \left( \mathbf{k} - \frac{\mathrm{i}}{2} \nabla_{\mathbf{x}}, \mathbf{x} + \frac{\mathrm{i}}{2} \nabla_{\mathbf{k}} \right) - \Omega \left( \mathbf{k} + \frac{\mathrm{i}}{2} \nabla_{\mathbf{x}}, \mathbf{x} - \frac{\mathrm{i}}{2} \nabla_{\mathbf{k}} \right) \right] \mathcal{E}, \quad (5.4)$$

with

$$\mathcal{E}(\mathbf{k}, \mathbf{x}, t) = \frac{1}{2} \int \langle \widehat{\zeta} \left( \mathbf{k} + \frac{\mathbf{u}}{2}, t \right) \widehat{\zeta}^* \left( \mathbf{k} - \frac{\mathbf{u}}{2}, t \right) \rangle \exp[\mathrm{i}\mathbf{u} \cdot \mathbf{x}] \, d\mathbf{u}. \quad (5.5)$$

Here the  $\langle \rangle$  denote ensemble averaging. The distribution function  $\mathcal{E}$  represents the complete second-order statistics and carries the same information as the two-point correlator  $\langle \widehat{\zeta}_1 \widehat{\zeta}_2^* \rangle$ , but with the wave number separation exchanged for a space coordinate. In appearance it is similar to the widely used variance density spectrum, and likewise, the local wave variance  $\mathcal{V}(\mathbf{x}, t)$  is found from the marginal distribution

$$\mathcal{V}(\mathbf{x}, t) = \int \mathcal{E}(\mathbf{k}, \mathbf{x}, t) \, d\mathbf{k}. \quad (5.6)$$

However, the distribution function  $\mathcal{E}$  is generally not point-wise positive, and can thus not be interpreted as a variance density function (see e.g. Janssen and Claasen, 1985). Only in the limit where the wave field is quasi-homogeneous, is the spectrum  $\mathcal{E}$  positive everywhere and reduces to a variance density function (which is thus a special case). To distinguish  $\mathcal{E}$ , as defined here, from the widely used variance density spectrum, we refer to it as a Coupled-Mode (CM) spectrum.

The evolution equation (5.4) describes the evolution of the CM spectrum through a variable medium, and is exact in the WKB sense in that it does not make any assumption regarding the statistical homogeneity or the scales of variation of the wave statistics. In other words, although the wave components themselves are slowly varying (in accordance with WKB), the statistics can undergo rapid variations (on the scale of individual wave lengths) through the development and propagation of cross-correlations in the wave field, either through the interaction with medium variations, or radiated in from the boundaries.

<sup>2</sup>Multiply (5.3) for  $\widehat{\zeta}_1 = \widehat{\zeta}(\mathbf{k}_1, t)$  by  $\widehat{\zeta}_2^* = \widehat{\zeta}(\mathbf{k}_2, t)$ , and the equation for  $\widehat{\zeta}_2^*$  by  $\widehat{\zeta}_1$ , sum both relations and ensemble average the result.

## AN APPROXIMATE MODEL FOR INHOMOGENEOUS WAVE FIELDS

The transport equation (5.4) governs the evolution of the CM spectrum within a slowly varying medium, but apart from certain special cases, the dynamical implications of the operators in (5.4) are not easily understood, and they cannot be readily numerically evaluated. To derive a consistent approximation to these operators, we introduce the following coordinate scaling. We define two (independent) spatial scales: a slow scale ( $\mathbf{X}_m$ ) associated with the medium variations, and a scale ( $\mathbf{X}$ ) that captures the spatial variations of the spectrum due to the wavenumber mismatches in the cross-correlations, written as

$$\mathbf{X}_m = \epsilon x, \quad \mathbf{X} = \mu x, \quad (5.7)$$

respectively. Here  $\mu = \Delta u/k_0$  (where  $k_0 = 2\pi/l_0$ ), with  $\Delta u$  a representative difference wave number for the cross-correlations and  $k_0$  a characteristic wavenumber of the wave field. Since we consider cross-correlations developed through the interaction with a slowly varying medium, we have  $\mu \ll 1$  (and  $\mu$  is generally of the same order as  $\epsilon$ ), so that  $\mathbf{X}$  is effectively a slow scale (with  $O(1)$  variations on length scales of  $l_0/\mu$ ). To make the width of the spectrum explicit, we consider the wave number scale

$$\mathbf{K} = \delta^{-1} \mathbf{k}, \quad (5.8)$$

where  $\delta = \Delta k/k_0$ , with  $\Delta k$  representing a characteristic width of the spectrum. The  $\delta$  can be thought of as an inverse correlation length scale so that for a highly coherent (narrow-band) wave field  $\delta \ll 1$  (and  $\mathbf{K}$  is a fast scale), whereas for moderate or wide-band wave fields  $\delta \sim O(1)$ . Lastly, we introduce the time scales

$$T_j = \mu^j t, \quad j = 1, 2, \dots, N. \quad (5.9)$$

Using these scales, the dependent variable  $\mathcal{E}$  and the dispersion relation  $\sigma$  become

$$\mathcal{E} = \mathcal{E}(\mathbf{K}, \mathbf{X}, T_1, T_2, \dots, T_N), \quad \sigma = \sigma(\mathbf{k}, \mathbf{X}_m), \quad (5.10)$$

so that, to  $O(\mu^N)$ , the governing equation (5.4) can be expressed as

$$\begin{aligned} \mu^j \partial_{T_j} \mathcal{E} = & -i \left[ \Omega \left( \mathbf{k} - \mu \frac{i}{2} \nabla_{\mathbf{X}}, \mathbf{X}_m + \delta \frac{i}{2} \nabla_{\mathbf{K}} \right) \right. \\ & \left. - \Omega \left( \mathbf{k} + \mu \frac{i}{2} \nabla_{\mathbf{X}}, \mathbf{X}_m - \delta \frac{i}{2} \nabla_{\mathbf{K}} \right) \right] \mathcal{E}. \end{aligned} \quad (5.11)$$

Here the summation over repeated indices is understood (i.e.  $\mu^j \partial_{T_j} = \sum_{j=1}^N \mu^j \partial_{T_j}$ ). To make the magnitude of the various terms in the operators on the right side of equation (5.11) explicit, we write the operators  $\Omega$  as (see Appendix A)

$$\begin{aligned} \Omega \left( \mathbf{k} \mp \mu \frac{i}{2} \nabla_{\mathbf{X}}, \mathbf{X}_m \pm \delta \frac{i}{2} \nabla_{\mathbf{K}} \right) = \\ \exp \left[ \pm \beta \frac{i}{2} \nabla_{\tilde{\mathbf{X}}_m} \cdot \nabla_{\mathbf{K}} \mp \mu \frac{i}{2} \nabla_{\tilde{\mathbf{k}}} \cdot \nabla_{\mathbf{X}} \right] \sigma(\tilde{\mathbf{k}}, \tilde{\mathbf{X}}_m) \Big|_{\tilde{\mathbf{k}}=\mathbf{k}, \tilde{\mathbf{X}}_m=\mathbf{X}}, \end{aligned} \quad (5.12)$$

where  $\beta = \epsilon/\delta$ . Physically,  $\beta$  thus measures the de-correlation length scale of the waves ( $\delta^{-1}$ ) relative to length scale of the medium variations ( $\epsilon^{-1}$ ). If  $\beta \ll 1$  the wave field de-correlates over distances short relative to the bottom variations, so that regions separated by  $O(1)$  medium variations are statistically independent. In fact, if  $O(\mu) = O(\beta) = O(\epsilon) \ll 1$ , equation (5.11) reduces (to lowest order) to the well-known RTE (Bremmer, 1972)

$$\frac{\partial \mathcal{E}}{\partial t} + \nabla_{\mathbf{k}} \sigma \cdot \nabla_{\mathbf{x}} \mathcal{E} - \nabla_{\mathbf{x}} \sigma \cdot \nabla_{\mathbf{k}} \mathcal{E} = 0, \quad (5.13)$$

where we dropped the scaling on the coordinates. From our analysis we see that the RTE (5.13) is valid in a slowly varying medium only if the wave field de-correlates on shorter scales than the scale of the medium variations. In other words, in this limit, cross-correlations induced by medium variations are lost faster than they are generated so that the wave system retains no memory of them and the wave field remains effectively homogeneous (i.e.  $\mu$  remains  $O(\epsilon)$ ). The RTE is thus valid if the spectrum of the medium variations is mostly confined to wavenumbers that are smaller than a characteristic (wavenumber) width of the wave spectrum. Since for most oceanic conditions this condition is easily satisfied, equation (5.13) is widely used and - in one form or another - stands at the heart of most modern, large-scale, stochastic models for ocean wind waves.

However, in coastal areas exposed to ocean swells, the interaction of waves with the seafloor topography on the inner shelf (or coastal currents), or the interaction of narrow-band wave field with coastal structures and headlands, can result in coherent interferences in the wave field that are visible even to a casual observer (e.g. interference in a focal zone induced by currents or topography). In such regions, the length scales of medium variations and decorrelation length scale of the waves can be of similar magnitude, so that  $\beta = O(1)$ , and the approximations implied in the RTE are not valid. In this case, a truncated expansion in  $\beta$  is not a useful approximation, but the general transport equation (5.11) can be alternatively approximated through a Fourier integral representation of the operators as in (see Appendix A)

$$\begin{aligned} \mu^j \partial_{T_j} \mathcal{E}(\mathbf{K}, \mathbf{X}, T_1, \dots, T_N) &= -i \int d\mathbf{Q} \exp[i\mathbf{Q} \cdot \mathbf{X}_m] \times \\ &\left[ \exp \left[ -\frac{i}{2} \mu \nabla_{\mathbf{X}} \cdot \nabla_{\tilde{\mathbf{k}}} \right] \hat{\sigma}(\tilde{\mathbf{k}}, \mathbf{Q}) \right]_{\tilde{\mathbf{k}}=\mathbf{k}} \mu^j \mathcal{E}(\mathbf{K} - \beta \mathbf{Q}/2, \mathbf{X}, T_1, \dots, T_N) \\ &+ \text{C.C.}, \end{aligned} \quad (5.14)$$

where  $\mathbf{Q} = \mathbf{q}/\epsilon$  and C.C. denotes the complex conjugate. On account of the slowly varying medium, major contributions to  $\hat{\sigma}(\mathbf{k}, \mathbf{Q})$ , and thus the integral, are limited to the domain  $|\mathbf{Q}|/k_0 \leq O(1)$  so that the integral in (5.14) can be efficiently numerically approximated and, to  $O(\mu^N)$ , the transport equation (5.14) becomes (in physical coordinates)

$$\begin{aligned} \partial_t \mathcal{E}(\mathbf{k}, \mathbf{x}, t) &= \\ &-i \int_{\mathcal{D}} \hat{\Omega}^{(N)} \left( \mathbf{k} - \frac{i}{2} \nabla_{\mathbf{x}}, \mathbf{q} \right) \mathcal{E} \left( \mathbf{k} - \frac{1}{2} \mathbf{q}, \mathbf{x} \right) \exp[i\mathbf{q} \cdot \mathbf{x}] d\mathbf{q} + \text{C.C.} \end{aligned} \quad (5.15)$$

Here  $\mathcal{D}$  denotes the domain of integration such that  $|\mathbf{q}|/k_0 \leq O(\epsilon)$ , and the kernel  $\widehat{\Omega}^{(N)}$  operating on  $\mathcal{E}$  is defined as

$$\widehat{\Omega}^{(N)} \left( \mathbf{k} - \frac{i}{2} \nabla_{\mathbf{x}}, \mathbf{q} \right) = \sum_{|n|=0}^N \frac{1}{n!} \left( -\frac{i}{2} \right)^{|n|} \frac{\partial^n \widehat{\sigma}}{\partial \mathbf{k}^n} \frac{\partial^n}{\partial \mathbf{x}^n}. \quad (5.16)$$

The expressions (5.15) and (5.16) describe the evolution of the second-order wave statistics while accounting for the generation and transport of coherent structures in the wave field. In this case, cross-correlations can be generated (by medium variations) faster than that they are destroyed, so that they can develop and persist, and affect the wave statistics. Equation (5.16) is a central result of this paper, which we will refer to as the  $N^{\text{th}}$ -order Quasi-Coherent (QC) approximation, or Quasi-Coherent approximation if the order of the approximation is understood. The RTE (5.13) is thus a special case of equation (5.15) where  $O(\beta) = O(\mu) = O(\epsilon) \ll 1$ .

### 5.3. EVOLUTION OF COHERENT WAVE STRUCTURES

To illustrate the implications of the Quasi-Coherent approximation (equation (5.15) with (5.16)), and the differences with the RTE (equation (5.13)), we consider two distinct cases where cross-correlations affect wave statistics. The first example considers the evolution of a group of wave packets through a homogeneous medium, where the inhomogeneity is fully determined by the initial condition and then transported through the domain. The second example considers the evolution of ocean waves over a two-dimensional topographic feature (shoal); in this case, the incident wave field is homogeneous and cross-correlations are generated through the interaction with the variable medium and transported down-wave of the shoal.

#### GAUSSIAN PACKETS THROUGH A HOMOGENOUS MEDIUM

We consider a wave field consisting of three coherent Gaussian wave packets propagating in deep water, for which the surface elevation at some arbitrary initial time ( $t = 0$ ) can be written as

$$\zeta(\mathbf{x}, 0) = \exp\left(-\alpha |\mathbf{x}|^2\right) \sum_{j=1}^3 A_j \exp(i\mathbf{k}_j \cdot \mathbf{x}). \quad (5.17)$$

Here the  $A_j$  are the (complex) packet amplitudes and  $\mathbf{k}_j$  is the carrier wavenumber. The initial spectrum (at  $t = 0$ ),  $\widehat{\mathcal{E}}(\mathbf{k}, \mathbf{u}, 0)$ , is then given by

$$\widehat{\mathcal{E}}(\mathbf{k}, \mathbf{u}, 0) = \sum_{m,n=1}^3 \frac{\langle A_m A_n^* \rangle}{32\pi^2 \alpha^2} \times \exp \left[ -\frac{1}{2\alpha} \left| \mathbf{k} - \frac{\mathbf{k}_n}{2} - \frac{\mathbf{k}_m}{2} \right|^2 - \frac{1}{8\alpha} \left| \mathbf{u} - \mathbf{u}_m + \mathbf{u}_n \right|^2 \right]. \quad (5.18)$$

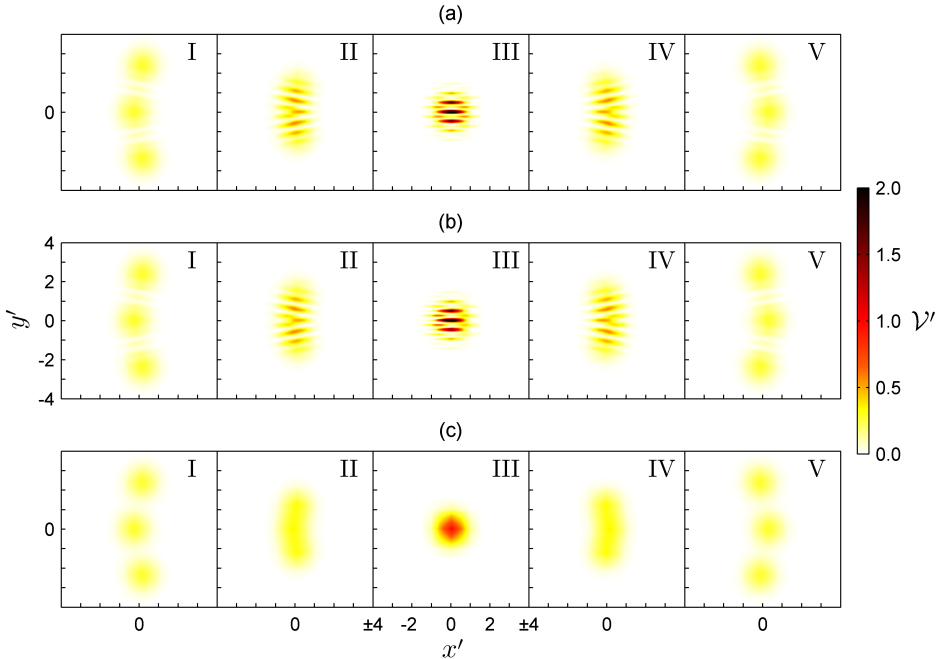


Figure 5.1: Snapshots of normalized wave variance (normalization by  $\frac{3}{2}a^2$ ) of three-packet interference example. Normalized variance is shown at discrete times  $t_{I-V}$ , starting at  $t_I = 110L_p/v_x$  (left panels) increasing in time (from left to right) in intervals of  $\Delta t = 20\lambda/v_x$ . Top panel (a) shows evolution for exact model; middle panel (b) shows the QC-approximation; bottom panel (c) shows the evolution according to the RTE. The  $x'$  and  $y'$  denote the horizontal coordinates normalized by  $6L_p$ .

For a homogeneous medium, and in a reference frame that moves with the mean group velocity, the dispersion relation  $\sigma(\mathbf{k}) = \sqrt{g|\mathbf{k}|} + \mathbf{k} \cdot \mathbf{v}$ , where  $\mathbf{v} = \frac{1}{2}\bar{\mathbf{k}}k_p^{-1}\sqrt{g/k_p}$  and  $\bar{\mathbf{k}}$  is the mean carrier wavenumber, so that equation (5.4) has the exact solution

$$\mathcal{E}(\mathbf{k}, \mathbf{x}, t) = \int \widehat{\mathcal{E}}(\mathbf{k}, \mathbf{u}, 0) \exp[i\mathbf{u} \cdot \mathbf{x} - i\omega_\Delta(\mathbf{k}, \mathbf{u})t] d\mathbf{u}, \quad (5.19)$$

with

$$\omega_\Delta(\mathbf{k}, \mathbf{u}) = \sigma(\mathbf{k} + \mathbf{u}/2) - \sigma(\mathbf{k} - \mathbf{u}/2). \quad (5.20)$$

The relations (5.19) and (5.20) are exact. The  $N^{\text{th}}$ -order QC approximation is obtained by substituting  $\widehat{\sigma}(\mathbf{k}, \mathbf{q}) = \delta(\mathbf{q})\sigma(\mathbf{k})$  in (5.15), where  $\delta(\mathbf{q})$  denotes the Dirac delta function, Fourier transforming with respect to  $\mathbf{x}$ , and solving the resulting ordinary differential equation. On applying the inverse transform with respect to  $\mathbf{u}$ , the result is again (5.19), but with  $\omega_\Delta$  replaced by its  $N^{\text{th}}$ -order Taylor series in  $\mathbf{u}$  around  $\mathbf{u} = 0$ ,

$$\omega_\Delta^{(N)}(\mathbf{k}, \mathbf{u}) = \sum_{|n|=1,3,\dots}^{|n|\leq N} \frac{\mathbf{u}^n}{n! 2^{|n|-1}} \frac{\partial^n \sigma}{\partial \mathbf{k}^n}. \quad (5.21)$$

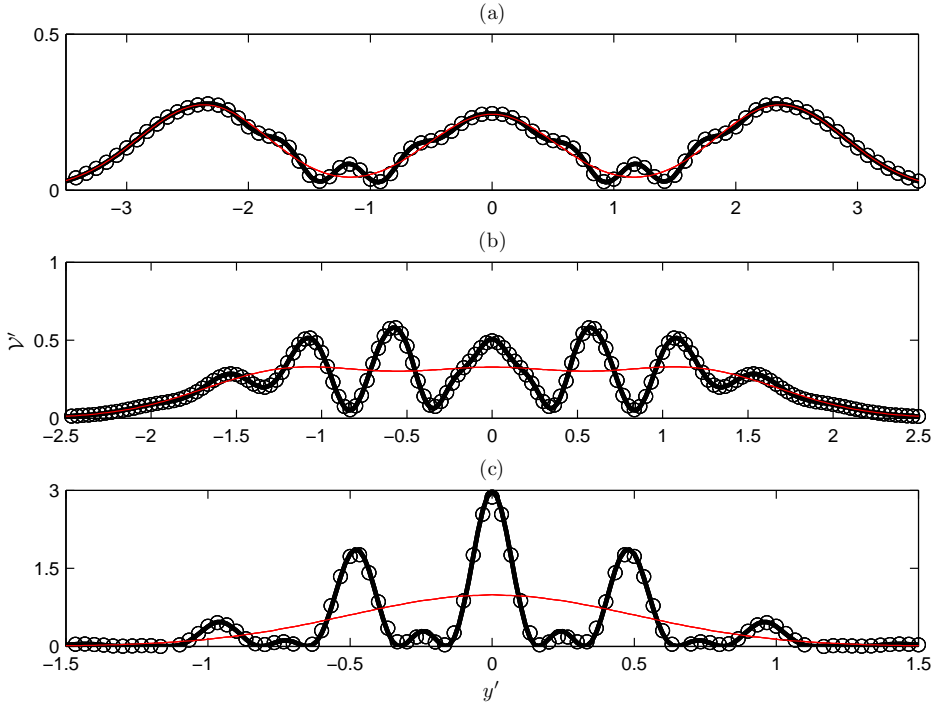


Figure 5.2: Cross-sections (at  $x' = 0$ ) of normalized wave variance of three-packet interference example. The wave variance is shown at discrete times  $t_{I-III}$ , starting at  $t_I$  (a) and increasing in time (from left to right). Comparison between exact model (solid line), the QC-approximation (circle markers) and the evolution according to the RTE (thin line). Normalization of vertical and horizontal scales and discrete times as in Figure 5.1. Note that the horizontal and vertical range can vary between panels.

In what follows, we consider three coherent packets of the same energy and carrier wave length ( $|A_j| = a$ ,  $|\mathbf{k}_j| = k$ ), that propagate at angles of  $-20, 0, 20$  degrees relative to the positive  $x$ -axis. We set  $\alpha = \frac{1}{36}L_p^{-2}$ , so that a characteristic length scale of the packets is roughly six wave lengths ( $\mu \approx 1/6$ ), and we consider the evolution from  $t = -150T_p$  to  $t = 20T_p$  (with  $T_p = L_p/v_x$  a characteristic period). The QC approximation is initialized at  $t = -150T_p$  using the exact solution.

Since the simulation time is roughly  $T_p/\mu^3$ , we use a third-order QC approximation (by truncating (5.21) after the second term). Each packet is calculated individually on a discrete equidistant  $\mathbf{k}$ -mesh centered at  $\mathbf{k}_{mn}$  using thirty points in each direction with a mesh-size of  $\Delta k = \sqrt{\alpha}/5$ . The Fourier integrals are approximated using a Fast Fourier Transform with  $u_1$  and  $u_2$  discretized as  $[-31 \dots 31] \Delta u$ , with  $\Delta u = \sqrt{\alpha}/5$ , and the result interpolated to a discrete  $241 \times 241$   $\mathbf{x}$ -mesh centered at the origin with mesh-size  $\Delta x = \Delta y = L_p/5$ .

The initial evolution of the wave system is characterized by convergence and interference of the wave packets (Figure 5.1a), followed by de-focusing and divergence,

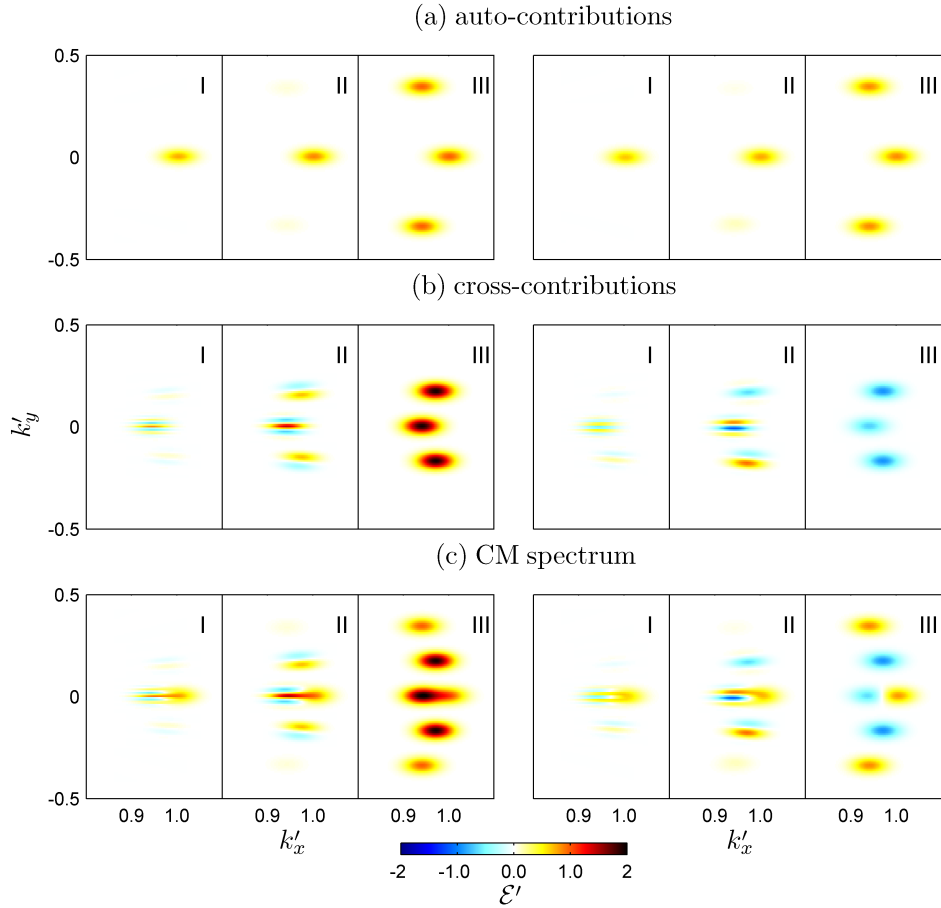


Figure 5.3: Spectral evolution of the three-packet interference example (5.18) evaluated at  $(x', y') = 0$  (left panels) and  $(x', y') = (0, \frac{1}{6})$  (right panels) for  $t_{I-III}$  (times as defined in caption Figure 5.1). Top panels (a) show the auto-variance contributions; (b) shows the cross-variance contributions; (c) shows the resulting CM spectrum (sum of auto- and cross-variance contributions). The spectral coordinates  $k'_x$  and  $k'_y$  are normalized with  $k_p$  and spectra are normalized with the peak contribution of an individual packet  $(4\pi\alpha)^{-1}$ .

after which the packets emerge unchanged and the initial state is recovered. The QC approximation captures the principal dynamics of the wave evolution, including the coherent interference (Figures 5.1b and 5.2), which confirms that the QC approximation accurately represents cross-correlations in the evolution of random waves associated with the coherent interference of wave packets traveling at moderate angles. In contrast, the wave packet evolution as represented by the RTE (Figures 5.1c and 5.2) is dramatically different from the exact result; in particular, the interference pattern at  $t = t_{III}$  is not resolved since the RTE does not account for the transport of cross-variance contributions ( $m \neq n$ ).

The differences in evolution are apparent also from the spectra (left panels in Figure 5.3). The variance density spectrum at  $\mathbf{x}' = 0$  (where  $\mathbf{x}' = \mathbf{x}/L_p$ ) contains a single positive peak for  $t_I$  and  $t_{II}$  related to the central packet, and three peaks at  $t_{III}$  when the three packets have converged (Figure 5.3a). Since the CM spectrum accounts for inter-mode coupling, it contains additional interference peaks, which travel along rays midway between the rays of the auto-variance contributions involved in the interference. For the case considered here, at  $\mathbf{x}' = 0$ , the cross-variance at  $t_I$  consists of a single interference peak (Figure 5.3b), which represents the coherence between the outer packets, and travels along the ray  $y' = 0$ . Coherence between the centre and outer packets travels along different rays and only manifests itself at  $t_{II}$  and  $t_{III}$  where these rays cross through  $y' = 0$ . The CM spectrum is the sum of the interference contributions and (auto-)variance density spectrum (Figure 5.3c). The spectral interference terms capture the rapid spatial oscillations of the wave statistics due to wave interference in the focal zone (Figure 5.1c). This fast-scale variability is also seen in the spectral domain, when the spectra are evaluated at a slightly offset location (compare left and right panels in Figure 5.3). Note that the wave packets in this example do not 'interact' with each other in the usual sense, and the coherent interference is completely determined a-priori by the inclusion of interference peaks in the initial condition. No cross-correlations are generated (or destroyed) in the course of the evolution.

### COHERENT INTERFERENCE PATTERNS INDUCED BY TOPOGRAPHY

To consider the generation and persistence of coherent interference patterns through the interaction with a slowly varying medium, we compare model simulations to laboratory observations of waves traveling over a submerged shoal (Vincent and Briggs, 1989). In these experiments, an elliptic shoal with its crest 15.24 cm below still-water level was placed in a wave basin with a uniform depth of  $h=45.72$ cm (See Figure 5.4). We consider a case with monochromatic waves (M2) and random waves with a TMA spectrum (N4); for the latter, the peak enhancement factor  $\gamma=20$ , directional spreading is approximately  $10^\circ$  (as defined by Kuik *et al.*, 1988), and the (significant) wave height and (peak) period are 2.54 cm and 1.3 s, respectively. For additional details we refer to Vincent and Briggs (1989).

We compare model simulations with a first-order QC model and the RTE to the laboratory observations. Since the observational data is sparse, we also include comparison to simulations with a deterministic hydrodynamical model (SWASH), which has been independently validated (see Zijlema *et al.*, 2011b).

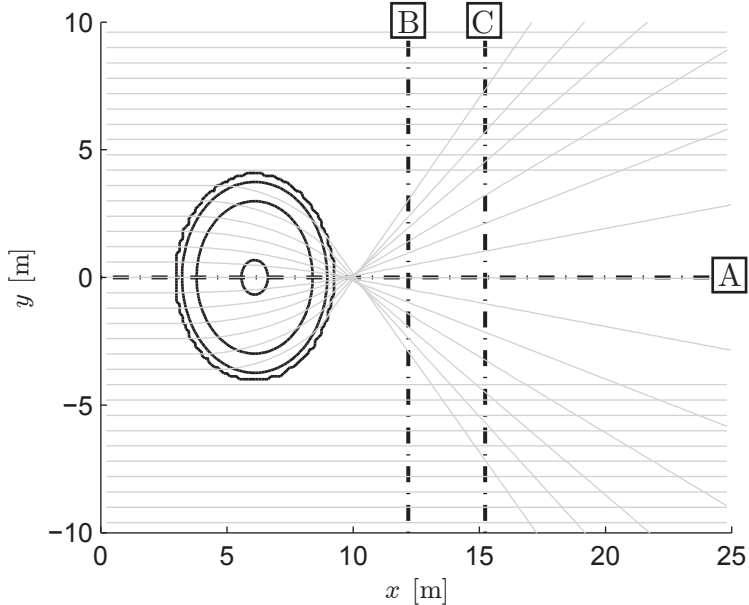


Figure 5.4: Plan view of the experimental setup by Vincent and Briggs (1989) including a ray-traced solution (thin grey lines) for unidirectional monochromatic waves (period 1.3 s, incident direction  $\theta_0 = 0^\circ$ ). Depth contours (drawn at 0.15–0.45 m, at 0.1 m intervals) are indicated by black solid lines; instrumented transects (at  $y = 0$  m,  $x = 12.19$  m and  $x = 15.24$  m) are indicated with dashdot lines.

The spectral models are numerically evaluated on a rectangular spatial ( $30 \times 25$  m<sup>2</sup>) and spectral domain ( $4k_p \times 3k_p$ , starting at  $\mathbf{k} = [-0.5k_p, -1.5k_p]$ ), uniformly discretized with mesh sizes  $\Delta x = \Delta y = 12.5$  cm and  $\Delta \mathbf{k}/k_p = [18, 20]$ . We use slope limited second-order finite difference approximations for the spatial (and spectral) gradients, in combination with an explicit first-order time stepping. The integral in equation (5.15) is approximated by a second-order numerical quadrature on the domain  $\mathcal{D}$  delimited by  $|\mathbf{q}| < 2k_p$ . At the wave maker, the incident spectrum is imposed, and periodicity is assumed in the lateral direction. Combined with a radiation type boundary condition opposite to the wave-maker, the solution is then marched in time until a steady state is reached.

Over the shoal, the incident monochromatic waves (case M2) are refracted in different directions, resulting in fast lateral variations in wave variance behind the shoal, due to the coherent interference of the crossing wave components. The QC model captures the variations in wave energy induced by these interferences and agrees well with observations and the deterministic model (5.5). In contrast, the RTE predicts much stronger focusing and lower wave heights in the shadow zone (see Figure 5.6), and does not resolve the fine-scale structure in wave energy associated with wave coherency.

For the random incident wave field (case N4), due to the increased dispersion

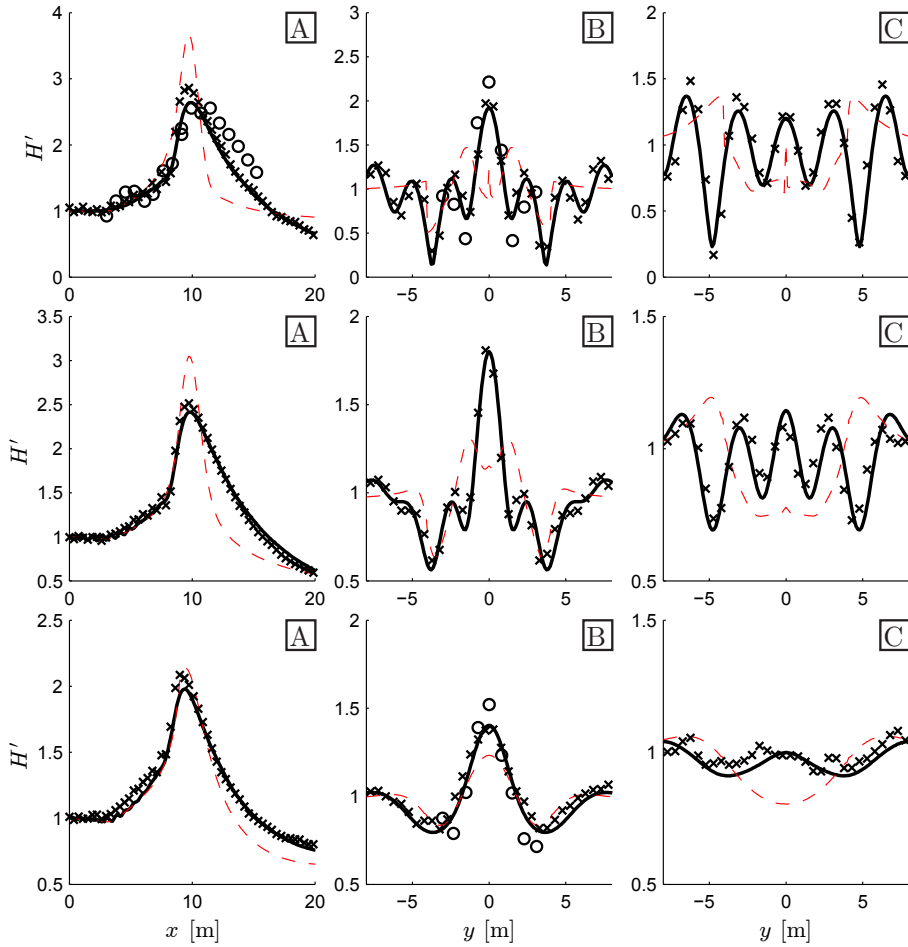


Figure 5.5: Shown are normalized wave heights along transects across (panels marked with A) and behind the shoal (marked with B and C, see Figure 5.4 for locations) as considered by Vincent and Briggs (1989) for case M2 (top panels), case N4 (lower panels) and the additional case N4' considered in the present work (middle panels). Comparison is between the  $QC_1$  approximation (solid black line), observations (circle markers, when available), the deterministic model SWASH (crosses), and the RTE (dashed red line).

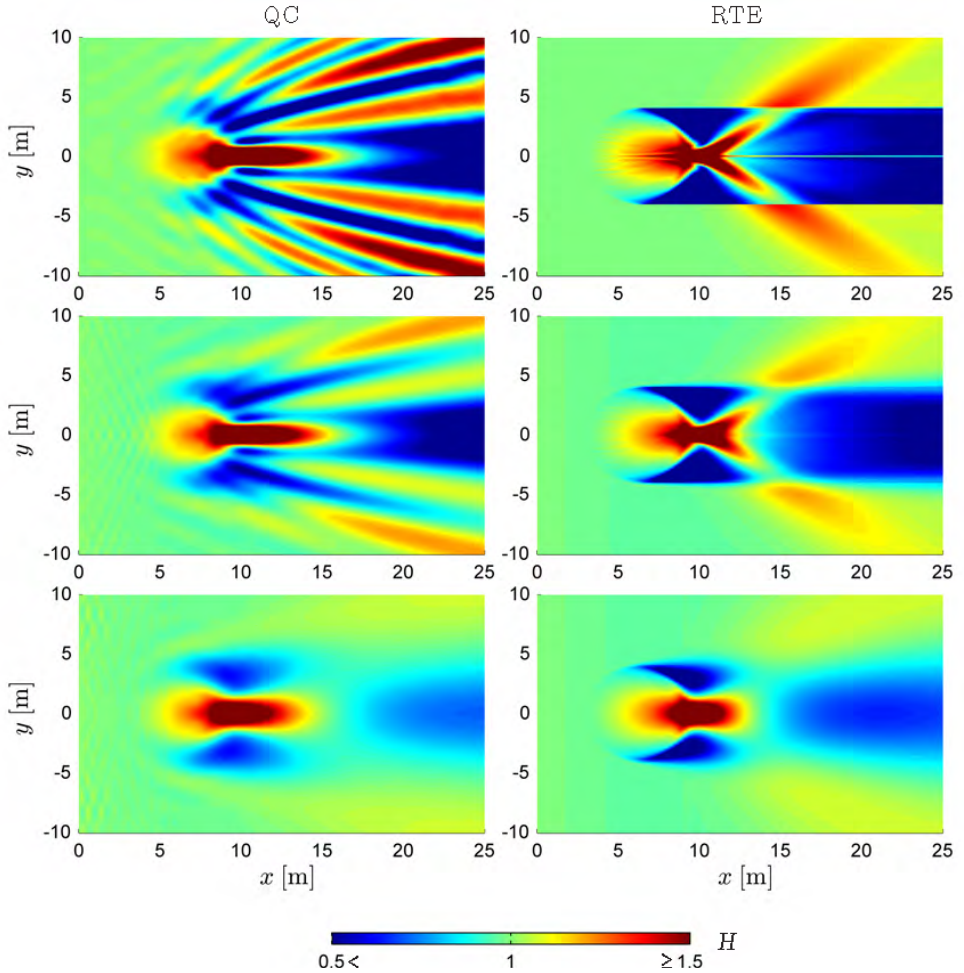


Figure 5.6: Plan view of modeled (normalized) wave heights for the experimental set-up as considered by Vincent and Briggs (1989) for case M2 (top panels), case N4 (lower panels) and the additional case N4' considered in the present work (middle panels). Comparison between the QC<sub>1</sub> approximation (left panels) and the RTE (right panels) shows that the QC<sub>1</sub> approximation, in contrast to the RTE, resolves the fine-scale interference pattern in the focal zone of a topographical lens.

(mostly directional), the wave field decorrelates faster, resulting in a smoothing of the wave statistics behind the shoal (see Figure 5.6). In this case, the QC results are qualitatively more similar to the RTE result, although several differences remain. In the region directly behind the shoal, wave heights predicted by QC theory are consistent with observations and those obtained with the deterministic model, whereas the wave heights predicted by the RTE are approximately 20% lower. If the directionality (and thus dispersion) is reduced, say to  $3^\circ$  (N4') a well-defined interference pattern emerges again and the QC model provides a much more realistic presentation of the wave statistics than the RTE<sup>3</sup>. These cases, which can represent the propagation of narrow-band swell waves over coastal topography, show that including coherent effects can be significant for situations that are of practical interest. The emergence and persistence of coherent interferences in narrow-band random waves over coastal topography can be important for regional wave statistics and thus affect wave-driven circulation and transport processes in such areas.

## 5.4. DISCUSSION

Coherent wave interference patterns are common in the coastal ocean, for instance due to the interaction with submerged topography, currents, islands, headlands, or coastal structures. Statistical models based on the RTE do not account for such interference patterns, and this can result in systematic differences between observed variations in wave statistics and model predictions. In this work we introduce a new transport model for what we refer to as a Coupled-Mode (CM) spectrum, which includes the effects of coherent interference on the wave statistics. The concept of a CM spectrum to describe the statistical evolution of inhomogeneous random processes is not new, but has been developed independently across various fields, such as the Wigner distribution in Quantum mechanics and Optics (e.g. Bastiaans, 1997; Bremmer, 1972; Wigner, 1932), the concept of generalized radiance in radiometry (Walther, 1968), and the Wigner-Ville distribution in signal processing (Ville, 1948; Cohen, 1989). Here we apply these ideas to ocean waves traveling through a variable medium and in the presence of caustics, such as are commonly found in e.g. coastal areas and other regions characterized by relatively strong two-dimensional medium variations.

### INTERFERENCE TERMS

Apart from energy (or variance) contributions, the coupled-mode spectrum carries cross-correlation and cross-phase information on coherent interferences between non-collinear wave components in the wave field. For example, if we revisit the correlated wave packet example in §5.3, and - for convenience - reduce it to two packets propagating at some equal but opposite angle with respect to the positive  $x$ -axis, so that  $\mathbf{k}_1 = (z, \lambda)$ ,  $\mathbf{k}_2 = (z, -\lambda)$ , and  $A_j = a_j \exp i\phi_j$ , with  $a_j = |A_j|$  and  $\phi_j = \arg A_j$ , the

---

<sup>3</sup>This case was not considered by Vincent and Briggs.

CM spectrum can be written as

$$\mathcal{E}(\mathbf{k}, \mathbf{x}) = \frac{1}{2} \int \widehat{\mathcal{E}}(\mathbf{k}, \mathbf{u}) \exp[i\mathbf{k} \cdot \mathbf{u}] d\mathbf{u} = \frac{e^{-2\alpha|\mathbf{x}|^2}}{4\pi\alpha} \left[ \langle a_1^2 \rangle G_{11} + \langle a_2^2 \rangle G_{22} + 2\langle a_1 a_2 \rangle G_{12} \cos(2\lambda y + \langle \phi_1 - \phi_2 \rangle) \right], \quad (5.22)$$

where the  $\widehat{\mathcal{E}}(\mathbf{k}, \mathbf{u})$  is the same as in equation (5.18) and

$$G_{ij} = \exp \left[ \frac{1}{2\alpha} \left| \mathbf{k} - \frac{\mathbf{k}_i}{2} - \frac{\mathbf{k}_j}{2} \right|^2 \right]. \quad (5.23)$$

The last term in (5.22) is a coupled-mode contribution that represents the contribution from the coherent interference between the two packets. This contribution is located midway between the associated auto-variance contributions (Hlawatsch and Flandrin, 1997), can become negative and, since it does not directly correspond to a field component, does not carry energy itself.

Instead, this contribution determines how the energy of the wave field is distributed between kinetic and potential energy. After all, in a statistically homogeneous (and linear) wave field, the energy is equipartitioned between potential and kinetic energy so that knowledge of either potential or kinetic energy suffices. On the other hand, in a wave field that undergoes coherent interference, information on the distribution of potential and kinetic energy is required to fully characterize the wave field statistics. This information is provided by the cross-contributions in the coupled-mode spectrum. In our example (equation (5.22)), the interference results in a coherent standing wave motion along the  $y$ -coordinate where the wave packets alternately interfere constructively and destructively; the coupled mode thus contributes negatively in the nodes (where more energy is kinetic) and positively in the anti-nodes (where more energy is potential).

### APERTURE LIMITATION ON WAVE INTERFERENCES

The CM spectrum is a general representation of the complete second-order statistics, including interferences between wave component with arbitrary mutual orientation, and without inherent aperture limitation. However, the QC transport equation, which is based on a series expansion of  $\widehat{\sigma}(\mathbf{k} \pm \frac{\mathbf{u}}{2}, \mathbf{q})$  in  $\mathbf{u}$  (equation (5.33)), is fundamentally more restricted, and cannot accurately transport cross-correlations between waves that enclose an angle greater than  $\pi/2$ . This limitation can be understood from the fact that the kernel  $\widehat{\Omega}^{(N)}$  (equation (5.16)) is obtained by Fourier transforming (with respect to  $\mathbf{u}$ ) the series expansion of  $\widehat{\sigma}(\mathbf{k} \pm \frac{\mathbf{u}}{2}, \mathbf{q})$  (equation (5.33)). Before truncation (for  $N \rightarrow \infty$ ), this is exact if the series approximation to  $\widehat{\sigma}(\mathbf{k} \pm \frac{\mathbf{u}}{2}, \mathbf{q})$  converges  $\forall \mathbf{u}$ . However, the dispersion relation for ocean waves depends on  $|\mathbf{k}|$ , so that  $\nabla_{\mathbf{k}}\sigma$  is singular at  $\mathbf{k} = 0$ , and the radius of convergence of the series expansion for  $\sigma(|\mathbf{k}|)$  around  $\mathbf{k}_0$  is  $|\mathbf{k}_0|$ . As a consequence, the operators are generally approximations and, since in the QC approximation the expansions are in  $\frac{1}{2}\mathbf{u}$ , the maximum enclosed angle is  $\pi/2$  ( $\mathbf{k}^+ \cdot \mathbf{k}^- = 0$ ,  $\mathbf{k}^\pm = \mathbf{k} \pm \frac{\mathbf{u}}{2}$ ), when both wave components are on the circle  $|\mathbf{u}| = 2k$  (see Figure 5.7). Therefore, if  $\mathbf{k}_0$  is a typical wave

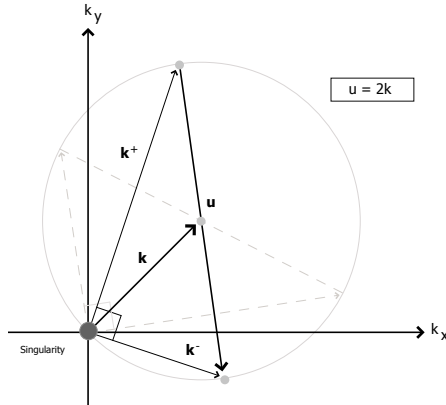


Figure 5.7: Sketch of wave interference geometry on the radius of convergence. For a dispersion relation  $\Omega(|\mathbf{k}|)$  (where  $|\mathbf{k}|$  is singular at the origin, as indicated in the Figure), the radius of convergence of the QC approximation (for a particular  $\mathbf{k}$ ) is given by  $|\bar{\mathbf{u}}| = 2k$ . Consequently, components  $(\mathbf{k}^+, \mathbf{k}^-)$  with average wavenumber  $\mathbf{k} = (\mathbf{k}^+ + \mathbf{k}^-)/2$ , which are located on the limit circle ( $|\mathbf{k}^+ - \mathbf{k}^-| = 2|\mathbf{k}|$ ), propagate perpendicular to each other, as shown in the Figure (solid black and striped gray lines).

number, the smallest spatial scale that can be resolved by the QC approximation is limited to  $\pi/k_0$ . Such aperture restrictions only apply to the coherent interference terms; the spectrum of the auto-mode distributions (variance-carrying contributions) is arbitrary.

## WIDE-ANGLE DIFFRACTION

The propagation of ocean waves around thin barriers and obstructions results in coherent interferences, associated with diffraction. From a statistical viewpoint, such diffraction patterns are a coherent interference pattern originating from the interaction with the barrier. Although these effects are ignored by the RTE, they can be readily accounted for in the QC approximation.

To illustrate this, we apply the QC approximation to the propagation of waves through a gap (extending over  $-G_1 < y < G_2$ ), in an otherwise rigid, but fully absorbing barrier (situated at  $x = 0$ ). Apart from the obstacle, the medium is uniform and the dispersion relation of the form  $\sigma = \sigma(|\mathbf{k}|)$ . The incident wave field is homogeneous, unidirectional, and normally incident on the barrier with a known variance density spectrum  $\mathcal{S}_0(\omega)$ . Using the Kirchhoff, or physical optics, approximation (see Appendix C), and a third-order QC approximation, we obtain the  $\mathcal{E}$  spectrum just behind the barrier ( $x = 0^+$ ),  $\mathcal{E}_0(\mathbf{k}, y)$ .

Behind the barrier, the coupled-mode spectrum is given by (5.19), and for a stationary solution we have  $\omega_\Delta(\mathbf{k}, \mathbf{u}) = \sigma(|\mathbf{k} + \mathbf{u}/2|) - \sigma(|\mathbf{k} - \mathbf{u}/2|) = 0$  (see (5.20)), so that  $|\mathbf{k} + \mathbf{u}/2| = |\mathbf{k} - \mathbf{u}/2|$  and  $\mathbf{k} \cdot \mathbf{u} = 0$ . Therefore we have  $\hat{\mathcal{E}}(\mathbf{k}, \mathbf{u}) = \hat{\mathcal{E}}(\mathbf{k}, u_y)\delta(u_x +$

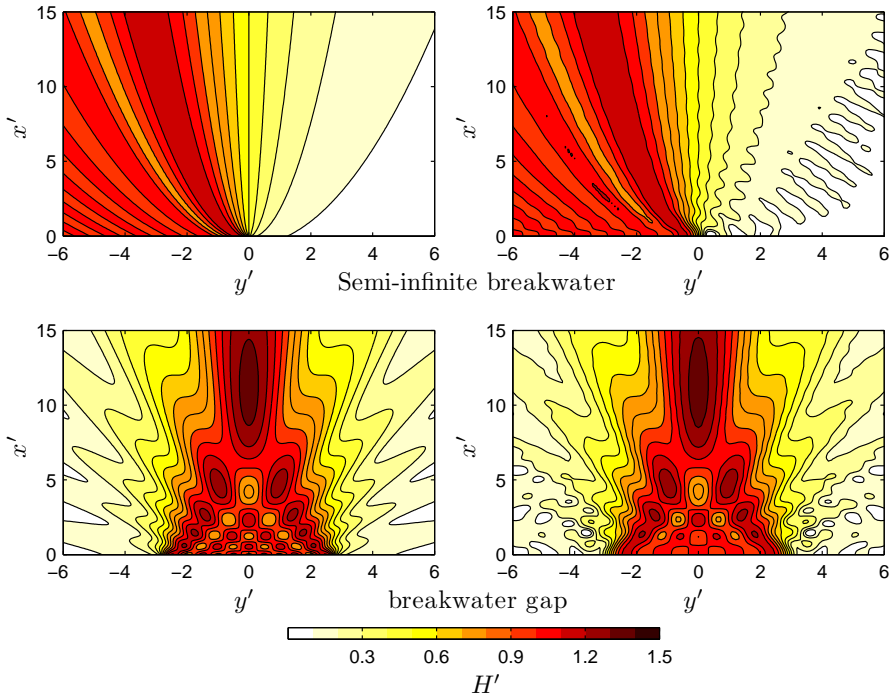


Figure 5.8: Contours of normalized wave height  $H' = \sqrt{\mathcal{V}/\mathcal{V}_0}$  (where  $\mathcal{V}_0$  is the variance of the incident waves) behind a semi-infinite breakwater (top panels) and a breakwater gap (bottom panels). Left panels show the analytic solution (Penney and Price, 1952); right panels show the QC approximation. The incident wave field consists of unidirectional waves, normally incident onto the breakwater, with a peak angular frequency of  $\omega_p = \pi$  rad/s,  $k_p h = 1.2$  and a narrow-band Gaussian-shaped frequency distribution with characteristic width of  $\Delta\omega = \frac{1}{100}\omega_p$ . The horizontal coordinates  $(x', y')$  are normalized with the peak wave length.

$u_y k_y k_x^{-1}$ ) for  $k_x > 0$  (and zero elsewhere), and (from (5.19)) find that

$$\mathcal{E}(\mathbf{k}, \mathbf{x}) = \int \widehat{\mathcal{E}}(\mathbf{k}, u_y) \exp(iu_y y - iu_y k_y k_x^{-1} x) du_y. \quad (5.24)$$

The wave statistics for  $x > 0$ , including coherent interferences associated with diffraction, are thus entirely determined from the boundary condition  $\widehat{\mathcal{E}}(\mathbf{k}, u_y)$  at  $x = 0$  (the gap). No new information is added as the waves travel behind the barrier, and the diffraction effects commonly seen in harbors or from areal photography of waves around islands, are - from a statistical point of view - simply the manifestation of cross-correlations determined by the up-wave boundary conditions, transported by (5.24).

In Figures 5.8 and 5.9 we compare simulation results to analytic solutions (Penney and Price, 1952) for a monochromatic incident wave field impinging on a semi-infinite breakwater ( $G_1 = \frac{L_y}{2}$  and  $G_2 = 0$ , with  $L_y$  the lateral extent of the domain), and

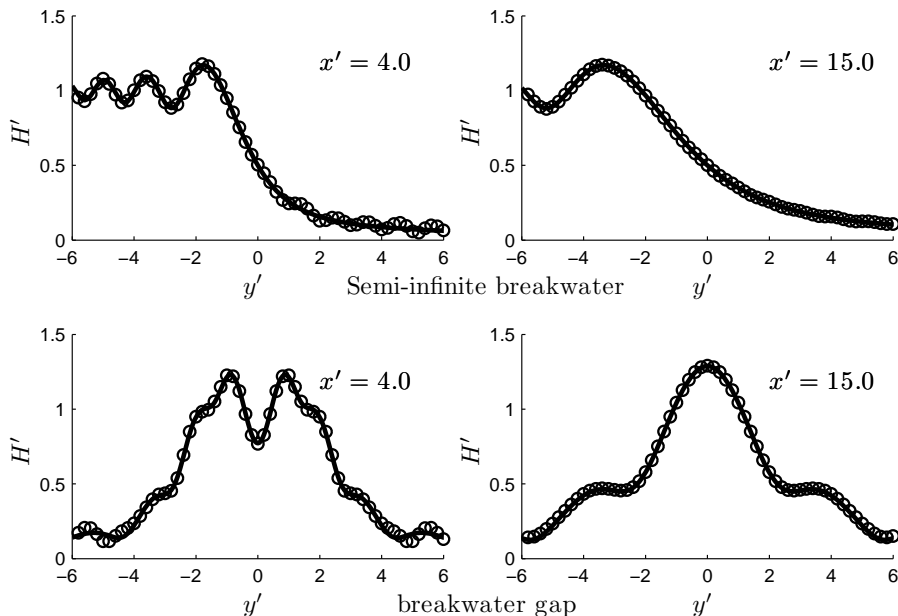


Figure 5.9: Cross-sections of normalized wave height  $H' = \sqrt{\mathcal{V}/\mathcal{V}_0}$  (where  $\mathcal{V}_0$  is the variance of the incident waves) along  $x' = 4$  (left) and  $x' = 15$  (right) behind a semi-infinite breakwater (top) and a breakwater gap (bottom). Shown are the analytic solution (solid line Penney and Price, 1952) and the QC approximation (circle markers). Incident wave field and coordinates as in Figure 5.8.

a barrier gap ( $G_1 = G_2 = 2.65L_p \ll L_y$ ). The QC approximation is in excellent agreement with the analytic solution for distances greater than about 4 wave lengths behind the barrier ( $x/L_p > 4$ ), which confirms the accuracy of this approach in the intermediate to far-field. Differences in the near-field are principally due to the omission of evanescent modes (especially in the region  $x/L_p < 1$ ), and the use of an approximate (Kirchhoff) boundary condition (see e.g. Stannes, 1986). These examples illustrate that the QC approximation, despite its fundamental  $\pi/2$  aperture restriction on interference terms, can accurately represent wide-angle coherencies due to diffraction, as implied by the good agreement with the analytic solutions.

#### RELATION TO OTHER TRANSPORT EQUATIONS

In the derivation of the stochastic model (5.4) we started, following Bremmer (1972), from the wave equation (5.3). This approach is quite general, and makes no explicit assumptions regarding the bandwidth of the wave field. Alternatively, if we restrict our derivation to narrow-band waves from the outset, we could, following Wigner (1932) and Alber (1978), start with specific evolution equations for a narrow-band wave train. To show that our approach and resulting transport equations are indeed consistent with earlier results for narrow-band waves, we consider the free-surface

elevation  $\zeta$  of a zero-mean, narrow-band wave field in deep water, given by  $\zeta(\mathbf{x}, t) = A(\mathbf{x}, t) \exp(i\mathbf{k}_0 \cdot \mathbf{x} - i\omega_0 t)$ , where  $\mathbf{k}_0 = [k_0, 0]^T$  is the principal wavenumber,  $\omega_0 = \sigma(k_0)$  the angular frequency, and  $A(\mathbf{x}, t)$  denotes the slowly changing wave envelope. Assuming that the bandwidth  $\Delta k/k_0$  is  $O(\delta)$  and the steepness is small ( $A_0 k_0 \ll \delta$ , with  $A_0$  a typical wave amplitude), the linear evolution of the envelope, up to  $O(\delta^3)$ , is governed by the linear part of the Dysthe equation (Dysthe, 1979)

$$\left[ \frac{\partial}{\partial t} + \sigma_{k_0}^{(1)} \frac{\partial}{\partial x} - \frac{i}{2} \sigma_{k_0}^{(2)} \frac{\partial^2}{\partial x^2} - \frac{i}{2k_0} \sigma_{k_0}^{(1)} \frac{\partial^2}{\partial y^2} - \frac{1}{2k_0^2} \left( k_0 \sigma_{k_0}^{(2)} - \sigma_{k_0}^{(1)} \right) \frac{\partial^3}{\partial x \partial y^2} - \frac{1}{6} \sigma_{k_0}^{(3)} \frac{\partial^3}{\partial x^3} \right] A = 0. \quad (5.25)$$

The procedure for obtaining the evolution equations for the CM spectrum from the governing equation (5.25) is essentially the same as that followed in Section (5.2), and equivalent to the procedure followed by Alber (1978) and Cohen (2010). We evaluate equation (5.25) at two different locations for  $A_1 = A(\mathbf{x}_1, t)$  and  $A_2^* = A^*(\mathbf{x}_2, t)$ ; we multiply the first equation with  $A_2^*$ , the second with  $A_1$ , sum the two resulting equations and ensemble average the result. After introducing the spatial average and difference coordinates  $\mathbf{x} = (\mathbf{x}_1 + \mathbf{x}_2)/2$  and  $\boldsymbol{\xi} = \mathbf{x}_1 - \mathbf{x}_2$ , we obtain an evolution equation for the product  $\rho = \frac{1}{2} \langle A_1 A_2^* \rangle$ . Upon applying the Fourier transform with respect to  $\boldsymbol{\xi}$ , we can express (5.25) in terms of the CM spectrum

$$\left[ \frac{\partial}{\partial t} + \left( \sigma_{k_0}^{(1)} + (k_x - k_0) \sigma_{k_0}^{(2)} \right) \frac{\partial}{\partial x} + \frac{k_y}{k_0} \sigma_{k_0}^{(1)} \frac{\partial}{\partial y} - \frac{1}{24} \sigma_{k_0}^{(3)} \frac{\partial^3}{\partial x^3} + \frac{1}{2} (k_x - k_0)^2 \sigma_{k_0}^{(3)} \frac{\partial}{\partial x} - \frac{1}{k_0^2} \left( k_0 \sigma_{k_0}^{(2)} - \sigma_{k_0}^{(1)} \right) \left( \frac{1}{8} \frac{\partial^3}{\partial x \partial y^2} - \frac{k_y^2}{2} \frac{\partial}{\partial x} - (k_x - k_0) k_y \frac{\partial}{\partial y} \right) \right] \mathcal{E} = 0, \quad (5.26)$$

where we used that  $\mathcal{E}(\mathbf{k}, \mathbf{x}) = \widehat{\rho}(\mathbf{k} - \mathbf{k}_0, \mathbf{x})$ , with  $\widehat{\rho}$  denoting the transform of  $\rho$  with respect to  $\boldsymbol{\xi}$ . The first three terms inside the brackets on the left side of (5.26) correspond to the linear spectral evolution equation of Alber (1978). Moreover, equation (5.26) is a narrow-band approximation (around  $\mathbf{k}_0$ ) of the third-order QC approximation in a uniform medium. This can be seen if we consider the Taylor approximations for  $\widehat{\Omega}^{(3)}(\mathbf{k} \mp \frac{i}{2} \nabla_{\mathbf{x}}, \mathbf{q})$  in  $\mathbf{k}$  around  $\mathbf{k}_0$  which, when retaining terms up to  $O(\delta^3)$ , reads

$$\widehat{\Omega}^{(3)} \left( \mathbf{k} \mp \frac{i}{2} \nabla_{\mathbf{x}}, \mathbf{q} \right) = \mp \frac{i}{2} \delta(\mathbf{q}) \left[ \left( \sigma_{k_0}^{(1)} + (k_x - k_0) \sigma_{k_0}^{(2)} + \frac{1}{2} (k_x - k_0)^2 \sigma_{k_0}^{(3)} + \frac{k_y^2}{2k_0^2} \left( k_0 \sigma_{k_0}^{(2)} - \sigma_{k_0}^{(1)} \right) \right) \frac{\partial}{\partial x} + \left( \frac{k_y}{k_0} \sigma_{k_0}^{(1)} + \frac{(k_x - k_0) k_y}{k_0^2} \left( k_0 \sigma_{k_0}^{(2)} - \sigma_{k_0}^{(1)} \right) \right) \frac{\partial}{\partial y} - \frac{\sigma_{k_0}^{(3)}}{24} \frac{\partial^3}{\partial x^3} - \frac{1}{8k_0^2} \left( k_0 \sigma_{k_0}^{(2)} - \sigma_{k_0}^{(1)} \right) \frac{\partial^3}{\partial x \partial y^2} \right]. \quad (5.27)$$

If the expression (5.27) is substituted in the transport equation (5.15), equation (5.26) follows, which shows that our results are consistent with earlier results for narrow-band wave fields, and contain the linear part of the Alber equation as a special case.

## 5.5. CONCLUSIONS

We have presented a new transport model for the statistics of inhomogeneous wave fields of arbitrary bandwidth propagating through a variable medium. The model accounts for the generation and transport of coherent interferences between wave components that enclose angles smaller than  $\pi/2$  radians. The theoretical framework presented here is a natural extension of the radiative transfer equation, and valid for arbitrary spectral width. We show that in the limit of narrow-band waves, the transport equation reduces to the linear Alber equation, which is thus a special case. Moreover, for homogeneous waves with an arbitrary spectrum, our result is consistent with the radiative transfer equation for the transport of the variance (or action) density spectrum. Comparison with analytic solutions for wave packet interference, and with observations of random surface wave propagation over a two-dimensional bottom feature, confirm that the Quasi-Coherent (QC) approximation accurately represents both the generation and transport of cross-correlations in the wave field, and resolves the fine-scale interference patterns associated with crossing waves. The effects of diffraction on statistics of waves around and behind obstacles and barriers, can be accurately modeled by including appropriate boundary conditions on the QC approximation. These results show that the application of QC theory to ocean waves can resolve some of the restrictions of quasi-homogeneous theory (the radiative transfer equation) in areas characterized by two-dimensional medium variations and caustics. This is likely to be of particular importance for wave-driven circulation and transport processes in coastal areas and inlets.

## ACKNOWLEDGMENT

This research is supported by the U.S. Office of Naval Research (Coastal Geosciences Program and Physical Oceanography Program) and by the National Oceanographic Partnership Program. The authors thank Leo Holthuijsen whose continuing support made it possible for PBS to pursue this research.



# Appendices

## 5.A. OPERATOR DEFINITION

We assume that the wavefield consists of a large number of progressive wave-packets, and each packet  $j$  has a location  $\mathbf{x}_j(t)$ , slowly varying wavenumber  $\mathbf{k}_j(t)$ , and angular frequency  $\omega_j(t)$ , which are related by a dispersion relation,  $\omega_j = \sigma(\mathbf{k}_j, \mathbf{x}_j)$ . To obtain an evolution equation for the transformed free-surface variable  $\widehat{\zeta}(\mathbf{k}, t)$ , we associate the (dependent) wave variables  $\mathbf{x}_j, \mathbf{k}_j, \omega_j$  with operators on  $\widehat{\zeta}(\mathbf{k})$ , i.e.  $\mathbf{k}_j(t) \rightarrow \mathbf{k}$ ,  $\mathbf{x}_j(t) \rightarrow i\nabla_{\mathbf{k}}$  and  $\omega(t) \rightarrow i\partial_t$ . So that the dispersion relation defines a linear operator  $\Omega$  on  $\widehat{\zeta}$ , written as

$$\partial_t \widehat{\zeta}(\mathbf{k}, t) = -i\Omega(\mathbf{k}, i\nabla_{\mathbf{k}})\widehat{\zeta}(\mathbf{k}, t). \quad (5.28)$$

Although equation (5.28) can be justified by the analogy between the ray equations of geometric optics and the canonical equations of Hamilton (e.g. Salmon, 1998), the definition of the operator  $\Omega$  requires particular consideration due to non-commutability of the operators (e.g. Torre, 2005). Here we follow the Weyl correspondence rule (e.g. Agarwal and Wolf, 1970) to uniquely define the operator  $\Omega$  so that the resulting linear operator is Hermitian with real eigenvalues (i.e. the angular frequencies), and orthogonal eigenfunctions. Thereto we expand  $\sigma$  in terms of its Fourier integral,

$$\sigma(\mathbf{k}, \mathbf{x}) = \iint \widehat{\sigma}(\mathbf{p}, \mathbf{q}) \exp[i\mathbf{p} \cdot \mathbf{k} + i\mathbf{q} \cdot \mathbf{x}] d\mathbf{q}d\mathbf{p}, \quad (5.29)$$

where  $\widehat{\sigma}(\mathbf{p}, \mathbf{q})$  denotes the Fourier transform of  $\sigma(\mathbf{k}, \mathbf{x})$  with respect to  $(\mathbf{p}, \mathbf{q})$ . After Taylor expanding the exponential function, applying the operator correspondence and associate any products with the sum of all its possible permutations (e.g.  $\mathbf{k}_j \mathbf{x}_j \rightarrow \frac{i}{2} \mathbf{k} \nabla_{\mathbf{k}}(\dots) + \frac{i}{2} \nabla_{\mathbf{k}}(\mathbf{k} \dots)$ ), we have

$$\Omega(\mathbf{k}, i\nabla_{\mathbf{k}}) = \iint \widehat{\sigma}(\mathbf{p}, \mathbf{q}) \exp[i\mathbf{p} \cdot \mathbf{k} - \mathbf{q} \cdot \nabla_{\mathbf{k}}] d\mathbf{q}d\mathbf{p}. \quad (5.30)$$

Here the exponential operator is defined in terms of its Taylor series expansion

$$\exp[i\mathbf{p} \cdot \mathbf{k} - \mathbf{q} \cdot \nabla_{\mathbf{k}}] = \sum_{|n|=0}^{\infty} \frac{1}{n!} (i\mathbf{p} \cdot \mathbf{k} - \mathbf{q} \cdot \nabla_{\mathbf{k}})^n, \quad (5.31)$$

and  $n$  is a multi-index. With these definitions in place, equation (5.28) describes periodic and undamped wave motion over topography and is consistent with WKB theory (See appendix B). Moreover, for an ocean of constant depth (5.28) is exact since we have  $\widehat{\sigma}(\mathbf{p}, \mathbf{q}) = \sigma(\mathbf{k})\delta(\mathbf{p})$ , so that  $\Omega(\mathbf{k}, i\nabla_{\mathbf{k}})$  reduces to a Fourier multiplier  $\sigma(\mathbf{k})$ .

To demonstrate that equation (5.12) and subsequently (5.14) follow from the definition (5.30), we introduce the sum and difference coordinates  $\mathbf{k}$  and  $\mathbf{u}$  in (5.30) to obtain

$$\begin{aligned} \Omega \left( \mathbf{k} \pm \frac{1}{2} \mathbf{u}, i \nabla_{\mathbf{u}} \pm \frac{i}{2} \nabla_{\mathbf{k}} \right) \widehat{\mathcal{E}}(\mathbf{k}, \mathbf{u}) &= \\ \iint \exp[-\mathbf{q} \cdot \nabla_{\mathbf{u}}] \widehat{\sigma}(\mathbf{p}, \mathbf{q}) \exp \left[ i \mathbf{p} \cdot \left( \mathbf{k} \pm \frac{\mathbf{u}}{2} \right) \right] \exp \left[ \mp \mathbf{q} \cdot \frac{1}{2} \nabla_{\mathbf{k}} \right] d\mathbf{q} d\mathbf{p} \widehat{\mathcal{E}}(\mathbf{k}, \mathbf{u}) &= \\ \int \exp[-\mathbf{q} \cdot \nabla_{\mathbf{u}}] \widehat{\sigma} \left( \mathbf{k} \pm \frac{\mathbf{u}}{2}, \mathbf{q} \right) \exp \left[ \mp \mathbf{q} \cdot \frac{1}{2} \nabla_{\mathbf{k}} \right] d\mathbf{q} \widehat{\mathcal{E}}(\mathbf{k}, \mathbf{u}). \end{aligned} \quad (5.32)$$

We replace  $\widehat{\sigma} \left( \mathbf{k} \pm \frac{\mathbf{u}}{2}, \mathbf{q} \right)$  by its Taylor series expansion in  $\mathbf{u}$  around  $\mathbf{k}$ ,

$$\widehat{\Omega}^{(\infty)} \left( \mathbf{k} \pm \frac{\mathbf{u}}{2}, \mathbf{q} \right) = \sum_{|n|=0}^{\infty} \frac{1}{n!} \frac{\partial^n \widehat{\sigma}(\pm \mathbf{u})^n}{\partial \mathbf{k}^n \frac{2^{|n|}}{2^{|n|}}}, \quad (5.33)$$

so that, upon Fourier transforming with respect to  $\mathbf{u}$ , (5.32) can be written as

$$\begin{aligned} \Omega^{\pm} \mathcal{E}(\mathbf{k}, \mathbf{x}) &= \\ \int \exp[i\mathbf{q} \cdot \mathbf{x}] \widehat{\Omega}^{(\infty)} \left( \mathbf{k} \mp \frac{i}{2} \nabla_{\mathbf{x}}, \mathbf{q} \right) \exp \left[ \mp \mathbf{q} \cdot \frac{1}{2} \nabla_{\mathbf{k}} \right] d\mathbf{q} \mathcal{E}(\mathbf{k}, \mathbf{x}), \end{aligned} \quad (5.34)$$

where we used  $\Omega^{\pm} = \Omega \left( \mathbf{k} \mp \frac{i}{2} \nabla_{\mathbf{x}}, \mathbf{x} \pm \frac{i}{2} \nabla_{\mathbf{k}} \right)$ . If  $\widehat{\sigma} \left( \mathbf{k} \pm \frac{\mathbf{u}}{2}, \mathbf{q} \right)$  is analytic, the Taylor series approximation (5.33) converges and equation (5.34) is exact. If the series only converges on some sub-domain of  $\mathbf{u}$ , equation (5.34) formally only applies to contributions to  $\mathcal{E}$  that originate from contributions in  $\widehat{\mathcal{E}}$  on that domain; the implications of this in the context of ocean waves are considered in §4b.

After integration with respect to  $\mathbf{q}$ , equation (5.34) can be written in the form of equation (5.12), written here as

$$\begin{aligned} \Omega^{\pm} \mathcal{E}(\mathbf{k}, \mathbf{x}) &= \exp \left[ \pm \frac{i}{2} \nabla_{\tilde{\mathbf{x}}} \cdot \nabla_{\mathbf{k}} \right] \Omega^{(\infty)} \left( \tilde{\mathbf{k}} \mp \frac{i}{2} \nabla_{\mathbf{x}}, \tilde{\mathbf{x}} \right) \Big|_{\tilde{\mathbf{k}}=\mathbf{k}, \tilde{\mathbf{x}}=\mathbf{x}} \mathcal{E}(\mathbf{k}, \mathbf{x}) \\ &= \left( \exp \left[ \pm \frac{i}{2} \nabla_{\tilde{\mathbf{x}}} \cdot \nabla_{\mathbf{k}} \mp \frac{i}{2} \nabla_{\tilde{\mathbf{k}}} \cdot \nabla_{\mathbf{x}} \right] \sigma(\tilde{\mathbf{k}}, \tilde{\mathbf{x}}) \right) \Big|_{\tilde{\mathbf{k}}=\mathbf{k}, \tilde{\mathbf{x}}=\mathbf{x}} \mathcal{E}(\mathbf{k}, \mathbf{x}). \end{aligned} \quad (5.35)$$

Alternatively, if we observe that  $\exp \left[ -\frac{1}{2} \mathbf{q} \cdot \nabla_{\mathbf{k}} \right]$  operating on  $\mathcal{E}$  is equivalent to a Taylor series of  $\mathcal{E} \left( \mathbf{k} - \frac{1}{2} \mathbf{q}, \mathbf{x} \right)$ , we can write equation (5.34) as

$$\begin{aligned} \Omega^{\pm} \mathcal{E}(\mathbf{k}, \mathbf{x}) &= \\ \int d\mathbf{q} \left( \exp[i\mathbf{q} \cdot \mathbf{x}] \exp \left[ \mp \frac{i}{2} \nabla_{\tilde{\mathbf{k}}} \cdot \nabla_{\mathbf{x}} \right] \widehat{\sigma}(\tilde{\mathbf{k}}, \mathbf{q}) \right) \Big|_{\tilde{\mathbf{k}}=\mathbf{k}} \mathcal{E} \left( \mathbf{k} - \frac{1}{2} \mathbf{q}, \mathbf{x} \right), \end{aligned} \quad (5.36)$$

which is the operator in equation (5.14).

## 5.B. RELATION TO GEOMETRIC OPTICS

To show that the wave equation (5.3) (or (5.28)), combined with the definition (5.30), is consistent with WKB theory (to  $O(\epsilon)$ ), and describes progressive ocean waves in a slowly varying medium, we rewrite equation (5.28) in the spatial domain, as

$$\partial_t \zeta(\mathbf{x}, t) = -i\Omega(-i\nabla_{\mathbf{x}}, \mathbf{x})\zeta(\mathbf{x}, t). \quad (5.37)$$

We assume that the wave field is characterized by a carrier wavenumber  $\mathbf{k}_0$ , and frequency  $\sigma_0(\mathbf{k}_0, \mathbf{x}_0)$ , and write the operator  $\Omega$  as

$$\begin{aligned} \Omega(-i\nabla_{\mathbf{x}}, \mathbf{x}) &= \iint \hat{\sigma}(\mathbf{p}, \mathbf{q}) \exp[-\mathbf{p} \cdot \nabla_{\mathbf{x}} + i\mathbf{q} \cdot \mathbf{x}] d\mathbf{q}d\mathbf{p} \\ &= \iint \hat{\sigma}(\mathbf{p}, \mathbf{q}) \exp\left[-\frac{i}{2}\mathbf{p} \cdot \mathbf{q}\right] \exp[i\mathbf{q} \cdot \mathbf{x}] \exp[-i\mathbf{p} \cdot \nabla_{\mathbf{x}}] d\mathbf{q}d\mathbf{p} \\ &= \exp\left[-\frac{i}{2}\nabla_{\tilde{\mathbf{k}}} \cdot \nabla_{\tilde{\mathbf{x}}}\right] \exp[-i\nabla_{\tilde{\mathbf{k}}} \cdot (\nabla_{\mathbf{x}} - \mathbf{k}_0)] \sigma(\tilde{\mathbf{k}}, \tilde{\mathbf{x}}) \Big|_{\tilde{\mathbf{k}}=\mathbf{k}_0, \tilde{\mathbf{x}}=\mathbf{x}}, \end{aligned} \quad (5.38)$$

where the extra factor  $\exp[-\frac{i}{2}\mathbf{p} \cdot \mathbf{q}]$  in the second line appears because the products in the arguments of the exponentials do not commute, i.e.  $\nabla_{\mathbf{x}}(\mathbf{x} \dots) \neq \mathbf{x} \cdot \nabla_{\mathbf{x}}(\dots)$  (see e.g. Messiah, 1961, p. 442). We introduce the slow coordinates  $T = \epsilon t$ ,  $\mathbf{X} = \epsilon \mathbf{x}$ , substitute the ansatz  $\zeta(\mathbf{X}, T) = A(\mathbf{X}, t) \exp[iS(\mathbf{X}, T)]$  in (5.37), and assume that the amplitude and phase are real and can be expanded as  $A = A_0 + \epsilon A_1 + \dots$  and  $S = \epsilon^{-1}S_0 + S_1 + \dots$ , respectively. On expanding the exponential operators in a Taylor series and retaining terms up to  $O(\epsilon^1)$ , while dropping the scaling of the coordinates, we obtain the eikonal equation for the phase function

$$\begin{aligned} \partial_t S_0 &= - \sum_{|n|=0}^{\infty} \frac{1}{n!} [(\nabla_{\mathbf{x}} S_0 - \mathbf{k}_0) \cdot \nabla_{\mathbf{k}}]^n \sigma(\mathbf{k}, \mathbf{x}) \Big|_{\mathbf{k}_0, \mathbf{x}} \\ &= -\sigma(\nabla_{\mathbf{x}} S_0, \mathbf{x}). \end{aligned} \quad (5.39)$$

Similarly, the amplitude evolution equation becomes

$$\begin{aligned} \partial_t A_0 &= - \sum_{|n|=0}^{\infty} \frac{1}{n!} [(\nabla_{\mathbf{x}} S_0 - \mathbf{k}_0) \cdot \nabla_{\mathbf{k}}]^n \times \\ &\quad \left[ \nabla_{\mathbf{x}} A_0 + \frac{1}{2} A_0 \nabla_{\mathbf{x}}^2 S_0 \nabla_{\mathbf{k}}^2 + \frac{1}{2} A_0 \nabla_{\mathbf{x}} \cdot \nabla_{\mathbf{k}} \right] \sigma(\mathbf{k}, \mathbf{x}) \Big|_{\mathbf{k}_0, \mathbf{x}} \\ &= - \left[ \nabla_{\mathbf{k}} \sigma \cdot \nabla_{\mathbf{x}} + \frac{1}{2} \nabla_{\mathbf{k}} \cdot \nabla_{\mathbf{x}} \sigma \right] A_0, \end{aligned} \quad (5.40)$$

where the derivatives of  $\sigma$  are evaluated at  $(\nabla_{\mathbf{x}} S_0, \mathbf{x})$ . If we multiply equation (5.40) by  $\rho g A_0$ , with  $\rho$  the density, and define the wave energy as  $E = \frac{1}{2} \rho g A_0^2$ , we find

$$\partial_t E + \nabla_{\mathbf{x}} \cdot (\nabla_{\mathbf{k}} \sigma E) = 0. \quad (5.41)$$

Equations (5.39) and (5.41) are the usual geometric optics approximations for waves in a slowly varying medium (e.g. Dingemans, 1997; Mei *et al.*, 2005), which shows that the wave equation (5.3) is consistent with WKB theory (to the order considered).

## 5.C. BOUNDARY CONDITION FOR WIDE-ANGLE DIFFRACTION

To derive a boundary condition for the diffraction example, we use the expression derived by Janssen *et al.* (2008), based on a forward-scattering assumption and a Kirchhoff approximation (e.g. Born and Wolf, 1999, p. 422). To transform the mutual spectrum used by Janssen *et al.* (2008) to  $\widehat{\mathcal{E}}(\mathbf{k}, u_y)$  used in (5.24), we express the frequency as a function of both  $\mathbf{k}$  and  $\mathbf{u}$ , i.e.  $\omega = \omega(\mathbf{k}, \mathbf{u})$ . In a homogeneous medium (this case), this can be done by noting that each contribution to the CM spectrum  $\mathcal{E}$  involves two coherent waves  $\zeta_{\pm} = \widehat{\zeta}(\mathbf{k}^{\pm}) \exp[-i\omega^{\pm}t]$ , with wavenumbers  $\mathbf{k}^{\pm} = \mathbf{k} \pm \mathbf{u}/2$  and frequencies  $\omega^{\pm} = \sigma(\mathbf{k}^{\pm})$ . Associated with these components we then have a beat frequency  $\omega^+ - \omega^-$ , related to the slow scale changes in time of the variance, and a mean frequency  $\omega^+ / 2 + \omega^- / 2$ , associated with the fast scale oscillations; the former corresponds to  $\omega_{\Delta}(\mathbf{k}, \mathbf{u})$  whereas the latter serves as our definition of  $\omega(\mathbf{k}, \mathbf{u})$ . To obtain a consistent QC approximation, we replace (as before)  $\omega(\mathbf{k}, \mathbf{u})$  with its Taylor approximation, so that

$$\omega^{(N)}(\mathbf{k}, \mathbf{u}) = \sum_{|n|=0,2,\dots}^{|n|\leq N} \frac{\mathbf{u}^n}{n! 2^{|n|+1}} \frac{\partial^n \sigma}{\partial \mathbf{k}^n}. \quad (5.42)$$

Using a third-order approximation, the CM spectrum becomes  $\widehat{\mathcal{E}}(\mathbf{k}, u_y) = \mathcal{S} \left| \frac{d\omega^{(3)}}{dk_x} \right|$ , for  $k_x > 0$  (and zero elsewhere), where

$$\mathcal{S}(\omega^{(3)}, k_x, u_y) = \frac{1}{\pi^2} S_0(\omega^{(3)}) \exp(-iu_y G_{\Delta}) \frac{|\mathbf{k}|^2 + u_y^2 (1 + k_y^2 k_x^{-2})}{k_x^2 - \frac{1}{4} k_x^{-2} k_y^2 u_y^2} \frac{\sin((-k_y - u_y/2)G_m)}{(k_y + u_y/2)} \frac{\sin((-k_y + u_y/2)G_m)}{(k_y - u_y/2)}, \quad (5.43)$$

with  $S_0(\omega)$  the incident, unidirectional frequency spectrum and  $G_{\Delta} = (G_2 - G_1)/2$ ,  $G_m = (G_1 + G_2)/2$ .

To approximate (5.24) numerically, we consider the solution on an equidistant Cartesian grid with horizontal resolution  $\Delta x = \Delta y = \frac{1}{10} L_p$  (where  $L_p$  is the peak wave length), and define the  $\mathbf{k}$ -mesh as  $\mathbf{k}_{i,j} = (i, j) \Delta k$ , with  $i = 1 \dots 100$ ,  $j = -200 \dots 200$  and  $\Delta k = 0.011 k_p$  (where  $k_p = 2\pi/L_p$ ). For each wave number  $\mathbf{k}_{i,j}$  the Fourier integral in (5.24) is approximated using a Fast Fourier Transform on an equidistant discrete array  $[-N \dots N] \Delta u$  for  $u_y$  with mesh-size  $\Delta u = 2\pi L_y^{-1}$  and  $L_y = (2N + 1) \Delta x$ . Since the accuracy of the approximate transformation deteriorates for  $u/k > 1.5$  the contributions for these high wavenumbers are set to zero.

# 6

## The evolution of narrow-band wave statistics over complex nearshore topography

The statistical evolution of narrow-band waves in a variable medium can result in fast-scale variations in the (mean) wave statistics, which cannot be resolved using conventional third-generation stochastic wave models based on the radiative transport equation. In the present work we therefore consider the application of a recently developed quasi-coherent wave theory that can account for inhomogeneous statistics on the wave length scale. Hereto, we derive a consistent model formulation and present a numerical implementation suitable for large-scale application over complex topography. We show that the generalized stochastic model can be written in the form of an inhomogeneous radiative transport equation, including a scattering term that accounts for the generation of coherent contributions to the wave statistics. Comparison with a laboratory and field observations of swell waves propagating over topography demonstrates that the quasi-coherent model allows for a more complete description of the evolution of the second-order statistics over complex topography compared to the traditional radiative transport equation.

### 6.1. INTRODUCTION

The evolution of wind-driven surface waves on the open ocean is largely determined by the action of wind (Phillips, 1957; Miles, 1957), dissipation (white capping, Hasselmann, 1974) and third-order nonlinear effects (or quadruplet wave-wave interactions,

---

The work in this Chapter has been presented in Honolulu, USA, as: SMIT, P.B., JANSSEN, T.T. and HERBERS, T.H.C., 2014a Refractive focusing of coherent waves. In *Paper presented at the Ocean Sciences Meeting, Honolulu, USA, 23–28 February*. It forms the core of a journal manuscript to be submitted later in 2014 to Ocean Modelling.

Hasselmann, 1962). In the shallower waters over the continental shelves, ocean waves are affected by refraction, shoaling, bottom friction, and eventually - near the coast - second-order nonlinearity (or triad wave-wave interactions, Eldeberky, 1996; Janssen *et al.*, 2006), and depth-induced breaking (Hasselmann *et al.*, 1973; Komen *et al.*, 1984; Battjes and Janssen, 1978; Salmon *et al.*, 2014b). Although the instantaneous action of some of these processes is highly nonlinear and difficult to quantify (e.g. wave breaking, white-capping), on average their effect on the mean energy is weakly nonlinear and well described in a stochastic framework formulated in terms of the directional variance density spectrum (Komen *et al.*, 1994; Holthuijsen, 2007).

As a result, for quasi-homogeneous wave fields, in which the mean wave statistics (e.g. variance) varies on spatial scales much longer than a characteristic wave length, the evolution of the variance density spectrum  $E(\mathbf{k}, \mathbf{x}, t)$  through time  $t$ , geographical space  $\mathbf{x}$ , and wavenumber space  $\mathbf{k}$  is described by the radiative transport equation (RTE),

$$\partial_t E + \mathbf{c}_x \cdot \nabla_{\mathbf{x}} E + \mathbf{c}_k \cdot \nabla_{\mathbf{k}} E = S. \quad (6.1)$$

The left side of (6.1) represents the conservation of wave energy in a slowly varying medium, with  $\mathbf{c}_x$  and  $\mathbf{c}_k$  denoting transport velocities through geographic and spectral space, respectively (Willebrand, 1975). The forcing term,  $S(\mathbf{k}, \mathbf{x}, t)$ , on the right of eq. (6.1) represents source term contributions to account for non-conservative and nonlinear processes. Apart from the quadruplet interactions (Hasselmann, 1962), the source terms are mostly empirical and accompanied by large uncertainties. For this reason, continuing development of the stochastic description has generally focussed on improvements of the source term parameterisations on the right side of the RTE. With proper tuning of the various source terms, and on larger scales, the RTE (eq. (6.1)) often provides a very good approximation to the evolution of the mean wave characteristics (Wise Group, 2007).

Apart from the usual WKB assumptions regarding the slow variations of the medium, the statistical description of wave evolution using the RTE to propagate the variance density spectrum  $E$ , implies the assumption that wave components are statistically independent (Komen *et al.*, 1994). In deep water, where medium variations are generally very weak, and the evolution is mostly dominated by the source term balance, the premise of quasi-homogeneous (and Gaussian) statistics often holds very well. However, in progressively shallower water, interaction with the slowly varying topography (or currents) becomes increasingly more important, and scattering of narrow-band wave fields can cause coherent interferences in coastal wave fields, which can result in fast scale oscillations of the variance as the wave components move in and out of phase with one another (Janssen *et al.*, 2008). For broad-banded waves such coherency effects - although still present - are suppressed in the mean statistics, which are thus well described by the RTE. (Vincent and Briggs, 1989; O'Reilly and Guza, 1991). In contrast, for narrow-band waves, coherent interferences can have an  $O(1)$  effect on the mean statistics, in particular when the topography varies on scales shorter than the coherent length scale the wave field (Smit and Janssen, 2013b, SJ13 hereafter). In the latter case, since the wave field de-correlates slower than the medium varies, it retains a memory of the coherency introduced by the medium scattering. The RTE keeps no track of wave field coherence, and to account

for these effects SJ13 derived a new evolution equation, which they referred to as the Quasi-Coherent Approximation (QCA) and represents a generalization of the RTE (left side of (6.1)) to account for the generation and propagation of inhomogeneous effects in the wave field.

In the present work we revisit the theoretical result from SJ13, develop a consistent numerical implementation for this model, validate the model against laboratory and field observations, and explore the use of the additional information available in the coupled-mode spectrum (as opposed to the variance density spectrum). Thereto we briefly summarize the principal results from SJ13 (see §2), derive and discuss a consistent approximation for medium variations based on the wave field de-correlation length scale (§2.2), and present simulations with the new model of laboratory flume experiments (§3) and field observations of ocean waves across a nearshore submarine canyon (NCEX, see Magne *et al.*, 2007).

## 6.2. EVOLUTION OF INHOMOGENEOUS WAVE FIELDS

To describe the evolution of inhomogeneous surface wave statistics in a variable medium, we consider the transport of what we refer to as the Coupled-Mode (CM) spectrum (see SJ13), defined as

$$\mathcal{E}(\mathbf{k}, \mathbf{x}, t) = \mathcal{F}_{\boldsymbol{\xi}, \mathbf{k}}\{\Gamma(\boldsymbol{\xi}, \mathbf{x}, t)\}, \quad (6.2)$$

where  $\mathcal{F}_{\boldsymbol{\xi}, \mathbf{k}}\{\dots\}$  denotes the Fourier transform from spatial lag  $\boldsymbol{\xi}$  to wavenumber  $\mathbf{k}$  (see Appendix A), and the correlation function  $\Gamma$  is defined as

$$\Gamma(\boldsymbol{\xi}, \mathbf{x}, t) = \frac{1}{2} \langle \zeta(\mathbf{x} + \boldsymbol{\xi}/2, t) \zeta^*(\mathbf{x} - \boldsymbol{\xi}/2, t) \rangle. \quad (6.3)$$

Here  $\zeta(\mathbf{x}, t)$  is a complex, zero-mean, Gaussian variable, of which the real part is the surface elevation  $\eta(\mathbf{x}, t) = \text{Re}\{\zeta(\mathbf{x}, t)\}$  and the imaginary part its Hilbert transform (see e.g. Mandel and Wolf, 1995), and  $\langle \dots \rangle$  denotes the ensemble average. Since  $\Gamma$  is symmetrical with respect to the separation distance  $\boldsymbol{\xi}$ , it follows that  $\Gamma(\boldsymbol{\xi}, \mathbf{x}, t) = \Gamma^*(-\boldsymbol{\xi}, \mathbf{x}, t)$ , and thus  $\mathcal{E}$  is real. Although the Coupled-Mode (CM) spectrum  $\mathcal{E}$  is generally not pointwise positive, and can thus generally not be interpreted as a variance density function (see SJ13), the marginal distribution  $\mathcal{V}(\mathbf{x}, t) = \int \mathcal{E}(\mathbf{k}, \mathbf{x}, t) d\mathbf{k}$  does represent the bulk wave variance. The CM spectrum represents the complete second-order wave statistics, including cross-variance contributions, which can produce negative contributions to the spectrum. Such contributions are omitted in the variance density spectrum, which only accounts for variance (and not cross-variance) contributions.

Under the assumption that the wave field consists of progressive plane surface gravity waves propagating through a slowly varying medium, such that the wavenumber and frequency are related by a linear dispersion relation, an evolution equation for the coupled-mode spectrum, can be derived (see SJ13)

$$\partial_t \mathcal{E}(\mathbf{k}, \mathbf{x}, t) = -i \int d\mathbf{q} \left[ \exp[i\mathbf{q} \cdot \mathbf{x}] \widehat{\Omega}(\mathbf{k}, \mathbf{q}) \mathcal{E}\left(\mathbf{k} - \frac{1}{2}\mathbf{q}, \mathbf{x}\right) \right] + *, \quad (6.4)$$

where  $*$  denotes the complex conjugate, and the kernel  $\widehat{\Omega}$  operates only on  $\mathcal{E}$ , and is defined as

$$\widehat{\Omega}(\mathbf{k}, \mathbf{q}) = \widehat{\sigma} - \frac{i}{2} \widehat{\sigma}_k \tilde{\mathbf{k}} \cdot \nabla_{\mathbf{x}}. \quad (6.5)$$

Here  $\widehat{\sigma}(\mathbf{k}, \mathbf{q})$  denotes the spatial Fourier transform ( $\mathbf{x}' \rightarrow \mathbf{q}$ ) of the dispersion relation, such that  $\widehat{\sigma}(\mathbf{k}, \mathbf{q}) = \mathcal{F}_{\mathbf{x}', \mathbf{q}}\{\sigma(\mathbf{k}, \mathbf{x}')\}$ . Furthermore, in equation (6.5),  $\widehat{\sigma}_k$  is short for  $\partial_k \widehat{\sigma}$ , the wavenumber  $\mathbf{q} = [q_1, q_2]$  is associated with spatial variations of the medium, and  $\tilde{\mathbf{k}} = \mathbf{k}/k$  (with  $k = |\mathbf{k}|$ ). For brevity, here and in the remainder of this paper, we use the shorthand  $\int d\mathbf{q} = \iint dq_1 dq_2$ . In the following, we assume that the dispersion relation  $\sigma$  and  $\sigma_k$  are given by the relations obtained from linear theory as

$$\sigma = \sqrt{gk \tanh(kh)} \quad \sigma_k = \frac{\sigma}{k} \left[ \frac{1}{2} + \frac{kh}{\sinh(2kh)} \right] \quad (6.6)$$

with  $g(=9.81\text{m}^2/\text{s})$  the gravitational acceleration, and  $h(\mathbf{x})$  the mean depth.

Combined, the equations (6.4) and (6.5) summarize the principal theoretical result from SJ13 and represent the starting point of this work. Notably, (6.4) includes the RTE as a special case, which we will show in what follows.

### MEDIUM VARIATIONS IN A COHERENT WAVE FIELD

To develop (6.4) into a form that is more easily related to the RTE, and to derive a consistent numerical implementation, we consider some properties of this equation that require attention.

From the Fourier transform on the right side of eq. (6.4) it is clear that in this form the evolution of the Coupled-Mode spectrum depends on medium variations throughout the entire spatial domain. Not only is this impractical from a numerical viewpoint, it is also unexpected from physical considerations. After all, the wave field has a finite decorrelation length scale so that medium variations outside this coherent radius should not affect the local statistics.

In the following we consider that the slow medium variations are characterized by the small parameter  $\epsilon \ll 1$ , so that the medium varies  $O(1)$  over distances  $L_0/\epsilon$ , with  $L_0$  being a characteristic wave length. Inhomogeneities in the wave field, induced through medium variations, cause  $O(1)$  variations in the wave field statistics on the scale  $L_0/\mu$ , with  $\mu \ll 1$ , being a measure of the wavenumber mismatch between coherent components. The width of the spectrum is measured by the parameter  $\delta = \Delta k/k_0$ , where  $\Delta k$  is a characteristic width and  $k_0 = 2\pi/L_0$ . The latter is used to define a coherent length scale as  $\xi_c = L_0/\delta$  so that  $\Gamma(\boldsymbol{\xi}, \mathbf{x}) \rightarrow 0$  as  $|\boldsymbol{\xi}| \rightarrow \xi_c$ . For narrow-band waves  $\delta \ll 1$ , implying that the wave field remains correlated over many wavelengths. To relate the coherent radius to the variations in the medium, we consider the ratio  $\beta = \epsilon/\delta$ , such that for  $\beta \ll 1$  changes in topography occur over distances much larger than the decorrelation scale, whereas for  $\beta = O(1)$  significant changes occur within the coherent radius of the waves. The latter parameter,  $\beta$ , is of great importance in making suitable approximations to the stochastic model.

To illustrate how the coherent radius constrains the effect of medium variations, and thus derive a consistent and local approximation, we write (6.4) as

$$\partial_t \mathcal{E}(\mathbf{k}, \mathbf{x}, t) = G(\mathbf{k}, \mathbf{x}, t) + *, \quad (6.7)$$

where

$$G = \frac{-i}{(2\pi)^4} \iint \Omega(\mathbf{k}, \mathbf{x}') \Gamma(\boldsymbol{\xi}, \mathbf{x}) \delta(\mathbf{x} + \frac{1}{2}\boldsymbol{\xi} - \mathbf{x}') \exp[-i\mathbf{k} \cdot \boldsymbol{\xi}] d\boldsymbol{\xi} d\mathbf{x}'. \quad (6.8)$$

Here we substituted  $\mathcal{F}_{\mathbf{x}', \mathbf{q}}\{\Omega(\mathbf{k}, \mathbf{x}')\}$  for  $\widehat{\Omega}(\mathbf{k}, \mathbf{q})$  and  $\mathcal{F}_{\boldsymbol{\xi}, \mathbf{k}}^{-1}\{\Gamma(\boldsymbol{\xi}, \mathbf{x}, t)\}$  for  $\mathcal{E}(\mathbf{k}, \mathbf{x}, t)$ . For waves with a finite coherent radius  $\xi_c$ , we have that  $\Gamma(\boldsymbol{\xi}, \mathbf{x}) = 0$  for  $\xi_j > \xi_c$  so that the integration over  $\boldsymbol{\xi}$  can be limited to  $|\xi_j| \leq \xi_c$ , which in turn implies that  $|x'_j - x_j| \leq \xi_c/2$ , and (6.8) can be written as

$$G = \frac{-i}{(2\pi)^4} \iiint_{\substack{|x'_j| \leq \xi_c/2 \\ |\xi_j| \leq \xi_c}} \Omega(\mathbf{k}, \mathbf{x} + \mathbf{x}') \Gamma(\boldsymbol{\xi}, \mathbf{x}) \exp\left[\mathbf{i}\mathbf{q} \cdot \left(\frac{1}{2}\boldsymbol{\xi} - \mathbf{x}'\right) - i\mathbf{k}\boldsymbol{\xi}\right] d\boldsymbol{\xi} d\mathbf{x}' d\mathbf{q}. \quad (6.9)$$

In (6.9) the evolution of the statistics is thus only affected by medium variability within the region of statistical dependence, as would be expected on physical grounds. Although here we make such approximations explicitly, the same approximation is implicit in the RTE. After all, if we assume that the wave field is relatively broadband with a small coherent radius (relative to the medium variations), we have that  $\beta \ll 1$ . In this case, the wavefield decorrelates before significant changes in the topography occur and it is reasonable to express the medium variability as a local Taylor expansion around  $\mathbf{x}' = 0$ , so that  $\Omega \rightarrow \Omega_{\text{RTE}}$ , with

$$\Omega(\mathbf{k}, \mathbf{x} + \mathbf{x}') \approx \Omega_{\text{RTE}}(\mathbf{k}, \mathbf{x}, \mathbf{x}') = \sigma + \mathbf{x}' \cdot \nabla_{\mathbf{x}'} \sigma + \frac{i}{2} (\sigma_{\mathbf{k}} + \mathbf{x} \cdot \nabla_{\mathbf{x}} \sigma_{\mathbf{k}}) \tilde{\mathbf{k}} \cdot \nabla_{\mathbf{x}}. \quad (6.10)$$

Substituting the local approximation (6.10) into eq. (6.9), we can show that (6.7) reduces to the RTE as in

$$\partial_t \mathcal{E} = G_{\text{RTE}} + * = -c_k^{\text{rte}} \cdot \nabla_{\mathbf{k}} \mathcal{E} - c_x^{\text{rte}} \cdot \nabla_{\mathbf{x}} \mathcal{E} \quad (6.11)$$

where  $c_k^{\text{rte}} = -\nabla_{\mathbf{x}} \sigma$  and  $c_x^{\text{rte}} = \nabla_{\mathbf{k}} \sigma$ . Note that  $c_k^{\text{rte}}$  is determined by the slope and  $c_x^{\text{rte}}$  by the intercept of the (local) plane approximations to  $\sigma$  and  $\partial_{\mathbf{k}} \sigma$ , respectively (see equation (6.10)). The RTE is thus a special case of the transport equation (6.7), which is obtained when assuming that the wave field decorrelates on a much faster scale than the medium varies ( $\beta \ll 1$ ), in which case only the local bathymetry (depth and bottom slope) are relevant to the evolution of the wave field statistics. In reality, wave fields described by the RTE have a finite spectral width and coherent radius and whether the assumptions implied by the RTE are reasonable depends entirely on the nature of the medium variations and the width of the spectrum.

To write the general transport equation (6.7) in a form similar to the RTE, but with an additional source term that accounts for the development of inhomogeneities by medium variations (e.g. coherent interferences), we write

$$\Omega(\mathbf{x} + \mathbf{x}') = \Omega_{\text{plane}}(\mathbf{x}, \mathbf{x}') + \Delta\Omega(\mathbf{x}, \mathbf{x}'), \quad (6.12)$$

so that  $\partial_t \mathcal{E} = G_{\text{plane}} + G_{QC} + *$ , and thus

$$\partial_t \mathcal{E} + c_k \cdot \nabla_{\mathbf{k}} \mathcal{E} + c_x \cdot \nabla_{\mathbf{x}} \mathcal{E} = G_{QC} + * \quad (6.13)$$

Analogous to  $\Omega_{\text{RTE}}$ ,  $\Omega_{\text{plane}}$  represents a plane approximation but with the slope and intercept defined somewhat more general to ensure that  $c_k$  and  $c_x$  represent the topographical variations within the coherent radius (instead of a strictly local approximation). Such variations, due to small local disturbances – even when  $\beta \ll 1$  – might differ significantly from a strictly local first-order Taylor expansion (see Fig. 6.1). Instead, to achieve better correspondence for the plane approximation throughout the coherent footprint, we determine the plane coefficients for  $\Omega_{\text{plane}}$  by means of a least-squares fit to  $\sigma$  and  $\partial_k \sigma$  of which the slope and intercept then define  $c_k$  and  $c_x$ , respectively (see Fig. 6.1). Note that the definition of  $\Omega_{\text{plane}}$  only influences the relative significance of  $\Omega_{\text{plane}}$  compared to  $\Delta\Omega$ , it has no influence on the resultant operator  $\Omega$ .

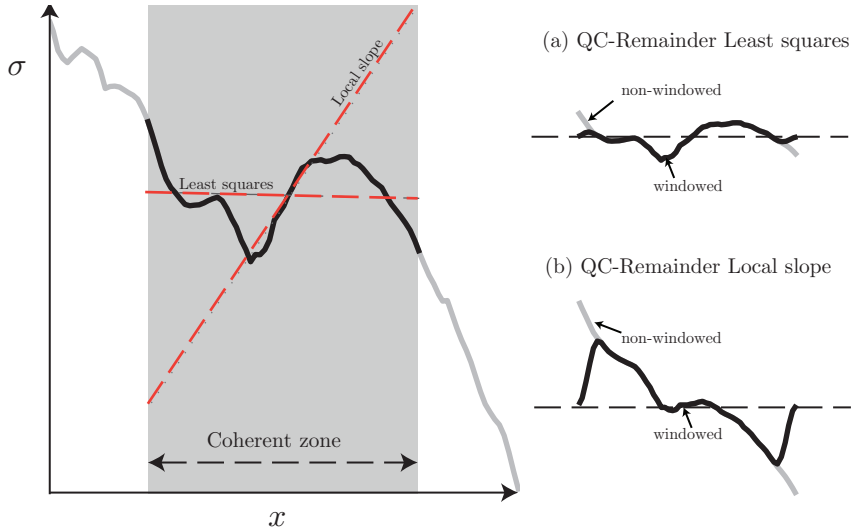


Figure 6.1: Sketch of a local slope and a least squares fit to  $\sigma$  (or  $\sigma_k$ ) within the predefined coherent zone. Panel (a) and (b) illustrate the remainder which is absorbed into the QC approximation when using a windowed (black) or non-windowed (gray) least-squares (a) or a local slope (b) plane approximation. The least squares approximation likely leads to smaller differences and a less abrupt relaxation to the plane approximation.

The source term  $G_{QC}$  is approximated through discretizing the integral over  $\mathbf{q}$  such that  $\mathbf{q} = [m_1^q \Delta q, m_2^q \Delta q]$ , with  $\Delta q = 2\pi/\xi_c$ , so that the complete coherent footprint is included, and  $G_{QC}$  can be written as

$$G_{QC} = \frac{-i(\Delta q)^2}{(2\pi)^4} \sum_{\mathbf{q}} \iint \Delta \hat{\Omega}^{\mathbf{q}}(\mathbf{k}, \mathbf{x}) \Gamma(\xi, \mathbf{x}) \exp \left[ i\xi \left( \frac{1}{2} \mathbf{q} - \mathbf{k} \right) \right] d\xi. \quad (6.14)$$

Since the truncation of the integration domain implies that  $\Delta\Omega$  is periodic, we apply a Tukey window so that  $\Delta \hat{\Omega}^{\mathbf{q}} = \mathcal{F}_{\mathbf{x}, \mathbf{q}} \{W \Delta\Omega\}$  to prevent any errors due to possible

jump discontinuities. At the extremities of the domain (where the wave field is nearly decorrelated),  $\Omega$  is thus relaxed to the  $\Omega_{\text{plane}}$ . Note that now the definition of  $\Omega_{\text{plane}}$  is significant, as it determines how the far-field representation of  $\Omega$  is included. Upon substituting (6.14) into (6.7), and upon applying the Fourier integral with respect to  $\xi$  in (6.14), we thus have

$$\partial_t \mathcal{E} + c_k \cdot \nabla_{\mathbf{k}} \mathcal{E} + c_x \cdot \nabla_{\mathbf{x}} \mathcal{E} = -i \sum_{\mathbf{q}} \Delta \widehat{\Omega}^{\mathbf{q}}(\mathbf{k}, \mathbf{x}) \mathcal{E}(\mathbf{k} - \mathbf{q}/2, \mathbf{x}) + *. \quad (6.15)$$

The equation (6.15) is a consistent approximation of the Quasi-Coherent theory developed by SJ13 for variable bathymetry, and can be readily numerically evaluated. In what follows we will refer to (6.15) as the Quasi-Coherent approximation. Although the equation (6.15) closely resembles the RTE with a source term to incorporate inhomogeneous effects, there are some subtle, but important, differences. After all, the transported variable  $\mathcal{E}$  is generally a coupled-mode spectrum, and not a variance density, and the transport velocities  $c_k$  and  $c_x$  are not strictly local but defined as the slope and intercept of a least-squares fit to  $\sigma$  and  $\partial_k \sigma$ , respectively.

In the simulations presented in this work, we consider steady state solutions to equation (6.15) (such that  $\partial_t \mathcal{E} = 0$ ) computed on a discrete grid by means of a finite difference approximation using an algorithm similar to that found in (Booij *et al.*, 1999). For details on the implementation we refer to appendix B.

### 6.3. WAVE DEFORMATION BY AN ELLIPTICAL SHOAL

A monochromatic, unidirectional wave field can be considered as the archetype of coherent wave fields – albeit mostly of academic interest. It also represents a rather severe test for the stochastic model, since formally the QC approximation is based on the premise that the wavefield has a finite coherent radius (or finite  $\Delta q$ ). For a strictly monochromatic and unidirectional wave field we would formally have  $\xi_c \rightarrow \infty$  so that  $\Delta q \rightarrow 0$ , whereas in the stochastic model we will by necessity assume a narrow, but finite-width spectrum (and thus a finite coherent radius). Despite this, a monochromatic unidirectional example will most clearly show the differences between the RTE and a QC approximation.

Therefore we consider the wave basin experiment by Berkhoff *et al.* (1982), where monochromatic (period 1 s), unidirectional waves (wave height  $H = 0.0464$  m) were generated at the wavemaker (at  $x = -10$ , depth 0.45 m) and propagated towards a shoal (crest located at  $\mathbf{x} = 0$  m, depth of 0.135 m) situated on a 1:50 slope (see Fig. 6.1). Wave heights were measured along 8 transects at regular intervals, of which we consider 6 in the present work (see Fig. 6.2).

The spectral models are numerically evaluated on a rectangular spatial ( $20 \times 20$  m<sup>2</sup>) and spectral domain ( $10 \times 10$  rad<sup>2</sup>/m<sup>2</sup>, starting at  $\mathbf{k} = [-0.05, -5]$  rad/m), uniformly discretized with mesh sizes  $\Delta x = \Delta y = 5$  cm and  $\Delta k_x = \Delta k_y = 0.1$  rad/m. Moreover  $\Delta q = 0.2$  so that  $\xi_c = 31.4$  m, and we include components  $\mathbf{q}$  up to  $k_p/2$ , where  $k_p$  is the peak wave length. At the boundary, the wave spectrum  $\mathcal{E}$  is assumed Gaussian, with the spectral peak at  $k_p = 4.21$  rad/m and a width of 0.2 rad/m; this effectively corresponds to a narrow-band longcrested wavefield with a width of 0.1 Hz. and 1.5° in frequency and directional space, respectively.

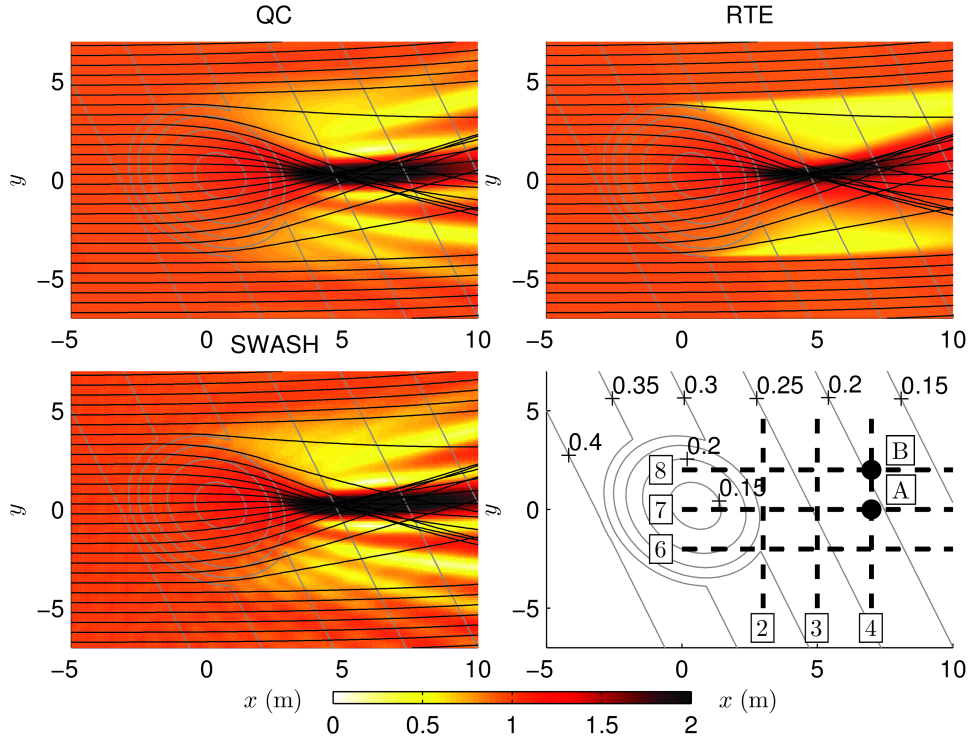


Figure 6.2: Plan view of normalized wave heights obtained using the QC approximation, the RTE and the ‘linear’ SWASH model for the experimental setup by Berkhoff *et al.* (1982). Grey lines indicate bottom contours (drawn between 0.4 m till 0.1 m at 0.05 m intervals), while the solid lines correspond to a ray-traced solutions. The bottom right panel indicates the instrumented transects.

Although no wave breaking was observed in the experiment, the wave height to depth ratio along the observed transects is large ( $H/d \approx 0.5$ ), in particular in the focal region behind the shoal, so that nonlinear dynamics significantly influence the pattern behind the shoal (see also results by Janssen, 2006). Because our focus is on linear interference effects, we include model simulations with the deterministic model Surface Waves till SHore (SWASH Zijlema *et al.*, 2011b), which effectively solves the 3D Euler (or RANS) equations for a free-surface fluid of constant density. This model reproduces the observations very accurately (see, e.g. Stelling and Zijlema, 2003; Smit, 2008), and from it – by reducing the incident wave height to  $H = 0.01$  m – near-linear results are obtained. For brevity, we shall therefore refer to the deterministic model forced with observed wave heights as the “nonlinear” SWASH model, and the results obtained with the reduced wave height as the “linear” SWASH model.

The SWASH model used the same model domain and horizontal resolution, whereas the vertical was subdivided into two layers. A duration of 1 min was simu-

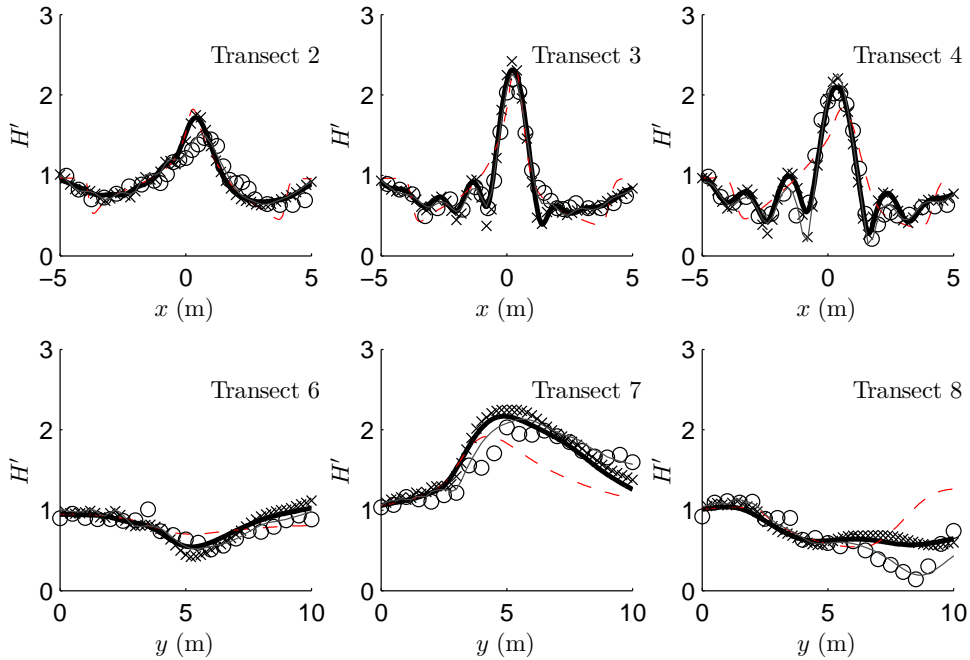


Figure 6.3: Normalized wave height  $H'$  (normalized with incident wave height) along the indicated transects. Comparison between observations (symbols), and relative wave heights obtained with the QC-approximation (solid line), the RTE (dashed line), 'linear' and 'nonlinear' Swash (Crosses and grey solid lines, respectively)

lated (using a time step of 0.01 s) of which the first 40 s were discarded to remove transient effects pertaining to the model initialization. For the final 20 s the situation was assumed stationary (with regard to mean parameters), and  $\zeta$  was recorded at 20 Hz from which mean wave heights were obtained from a zero-crossing analysis (see e.g., Holthuijsen, 2007).

The refractive focussing of the waves introduces a lateral interference pattern in the wake of the shoal (Fig. 6.2). The fine-scale pattern is reproduced by the QC model, and normalized wave heights correspond well with observations (Fig. 6.3). In contrast, the quasi-homogeneous model (RTE) underestimates wave heights along the central transect 7, and does not reproduce the lateral interference patterns evident in transects 3 and 4 resulting in the dramatic difference in the pattern behind the shoal (Fig. 6.2). Marked discrepancies between observations and the QC model do occur in transect 8, which we attribute to the omission of nonlinear effects. This is confirmed by comparison with the deterministic results, where the nonlinear model reproduces the node near  $y = 8$  m in transect 8, and produces overall better correspondence with measurements, whereas the results from the linear model are consistent with those of the QC model.

## WAVE SPECTRA AND COHERENCE FUNCTIONS

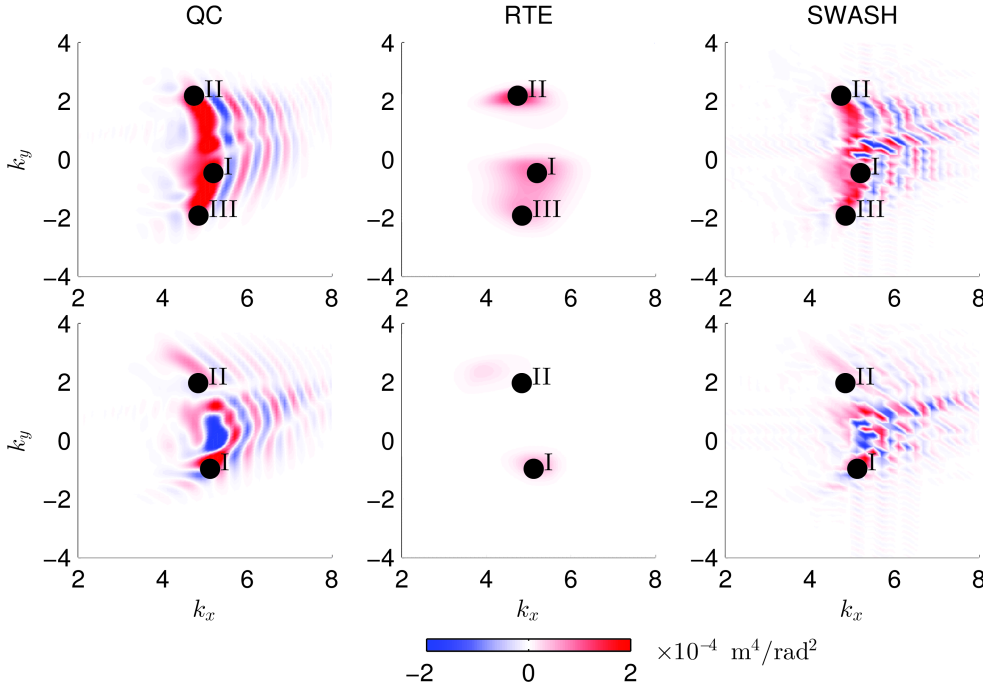


Figure 6.4: Coupled mode (QC and SWASH, left and right panels) or variance density (RTE, centre panel) spectra at points A (top panels) and B (bottom panels) located down wave of the shoal (see Fig. 6.2).

To compare the results in more detail, we further consider the wavenumber spectra as calculated by the different models. Although we cannot verify this directly by comparison to observations (as observed time series are not available), these can be compared to spectra obtained from the linear SWASH results. To obtain the wave spectrum from the SWASH results, we first approximate  $\Gamma(\mathbf{x}, \boldsymbol{\xi})$  with the ensemble mean, and then approximate the continuous CM spectrum with

$$\mathcal{E}(\mathbf{k}, \mathbf{x}) \approx \frac{\overline{\mathcal{F}_{\boldsymbol{\xi}, \mathbf{k}}\{\Gamma(\boldsymbol{\xi}, (\mathbf{x}))\}}}{\Delta k_x \Delta k_y}, \quad (6.16)$$

where  $\Delta k_x$  and  $\Delta k_y$  are the wavenumber intervals in the discrete Fourier transform. The spectrum is evaluated at two points A and B (located at  $\mathbf{x}_A = [7, 0]$  and  $\mathbf{x}_B = [7, 2]$ , respectively, see Fig. 6.2).

At point A, the ray-traced solution indicates that geometric optics predicts three separate contributions within the spectrum (marked I, II and III), which are indeed faithfully reproduced in the RTE model (see Fig. 6.4). Correspondence is not exact, since the spectral representation of monochromatic waves – and numerical diffusion – introduce widening of the peaks, but significant variance is located around those

wavenumbers also found in the ray-traced solution. Yet these results stand in stark contrast with those from SWASH and the QC model, which predict a much richer structure due to the occurrence of coherent interference. For instance, there is a large positive band between I and II, related to the constructive interference behind the shoal. At point B, this band becomes negative, indicative of the destructive interference and the rapid reduction in wave height that occurs at point B (see also Fig 6.3, transect 4 at  $y=2$  m). More obscure are the alternating positive and negative contributions that emerge at both points right of the main lobe, at wavenumber magnitudes well beyond those that occur in the geometric optics solution. Presumably, these are related to changes in the mean statistics along the wave direction. Their net contribution to the local variance is however small, as the alternating contributions tend to cancel one-another. Qualitatively, the QC solution agrees well with those from SWASH, as the main features are all present, although the QC solution is generally smoother.

Since the CM spectrum contains cross-variances, it is not a strictly local variable, which can make it more difficult to interpret. However, the CM spectrum carries additional information and this can be explored by considering  $\Gamma$ , which is related to the directly observable covariance between two points. Although at large mutual separations, such dependence cannot be accounted for within the QC model (or the RTE), the real part of the co-variance function  $\Gamma$  should approximate the covariance between  $\eta(\mathbf{x} + \boldsymbol{\xi}/2, t)$  and  $\eta(\mathbf{x} - \boldsymbol{\xi}/2, t)$  at small mutual separations. Moreover, the modulus of the covariance function ( $|\Gamma|$ ) removes the fast scale oscillations and thus effectively captures the slow scale changes (or envelope) of the covariance function – that is, it represents the changes in the mean statistics.

For a strictly monochromatic wave field, the wave statistics do not decouple anywhere in the basin, which is reflected in the envelope of the normalized covariances function  $|\Gamma'_{A/B}(\xi)|$ , where

$$\Gamma'_{A/B}(\xi) = \frac{\Gamma(\boldsymbol{\xi}, \mathbf{x}_{A/B})}{\Gamma_{\text{SWASH}}(\mathbf{0}, \mathbf{x}_{A/B})}, \quad (6.17)$$

which has covariance contributions at arbitrary spatial lags away from the centre<sup>1</sup>.

If we consider cross-sections along the coordinate axis (Fig. 6.6), we can clearly discern that  $|\Gamma'_{A/B}(\xi)| \rightarrow 0$  in the far field ( $\xi/L \ll 1$ ) for both the RTE and the QC, whereas the deterministic model can even predict far field covariance contributions exceeding those at  $\xi = 0$  (e.g. Transact 2, Point B). Despite this damped behaviour, which reflect the finite coherence length inherent within stochastic models, it is evident that the QC approximation can resolve the second-order correlation matrix up to  $\xi/L \approx 5$ , including the fast oscillations due to the wave motion.

## 6.4. SWELL OVER SUBMARINE CANYONS

Offshore of the coastline just north of San Diego, stretching from Black's Beach up until La Jolla point, in the Southern California Bight (see Fig. 6.7), the seafloor

<sup>1</sup>Whereas in a homogeneous field  $\Gamma$  thus normalized would be strictly contained between -1 and 1, this is not the case in a spatially inhomogeneous field

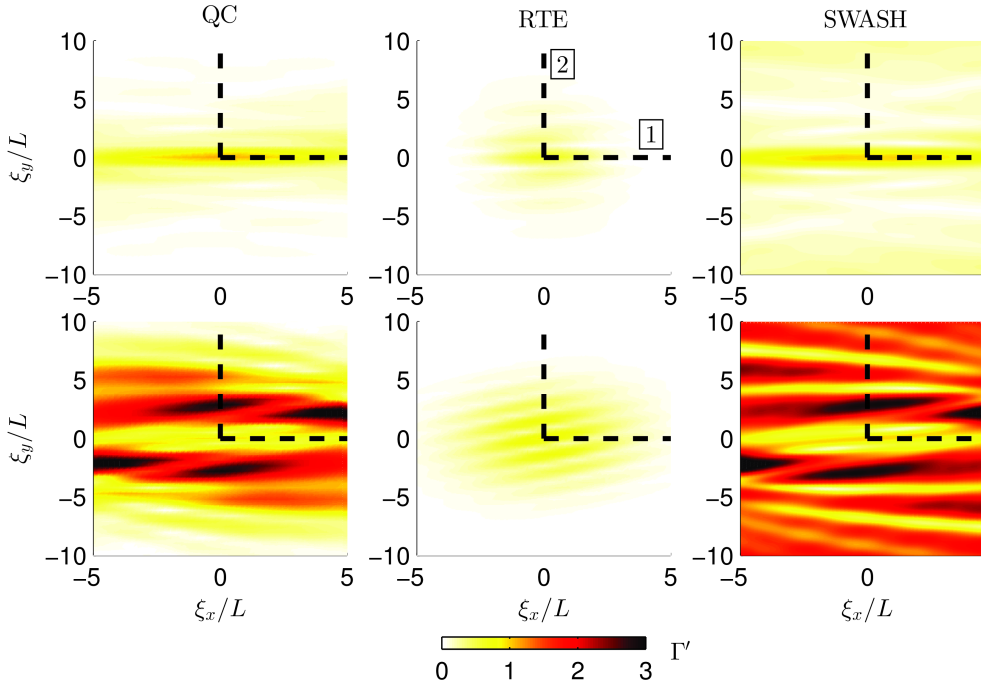


Figure 6.5: Normalized modulus of  $\Gamma'(\xi, \mathbf{x})$  (normalized with local variance) at points A (top panels) and B (bottom panels, see Fig. 6.2 for locations) as predicted by the QC approximation, a RTE based model and SWASH (left to right). The spatial-lag coordinates  $\xi_x$  and  $\xi_y$  are scaled with the local wave length  $L$ .

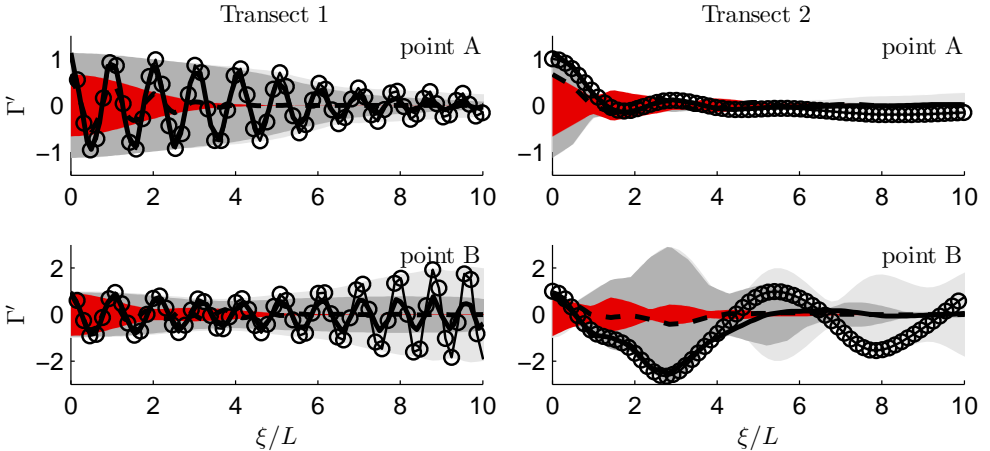


Figure 6.6: Normalized covariance functions  $|\Gamma'|$  (shaded regions, QC: Dark, RTE: red, SWASH: light) and  $Re\{\Gamma'\}$  (lines, QC: solid line, RTE: dashed line, SWASH: markers), both normalized with local variance. The functions are evaluated at points A (top panels) and B (bottom panels) along the indicated transects. The spatial-lag coordinate  $\xi$  is scaled with the local wave length  $L$ .

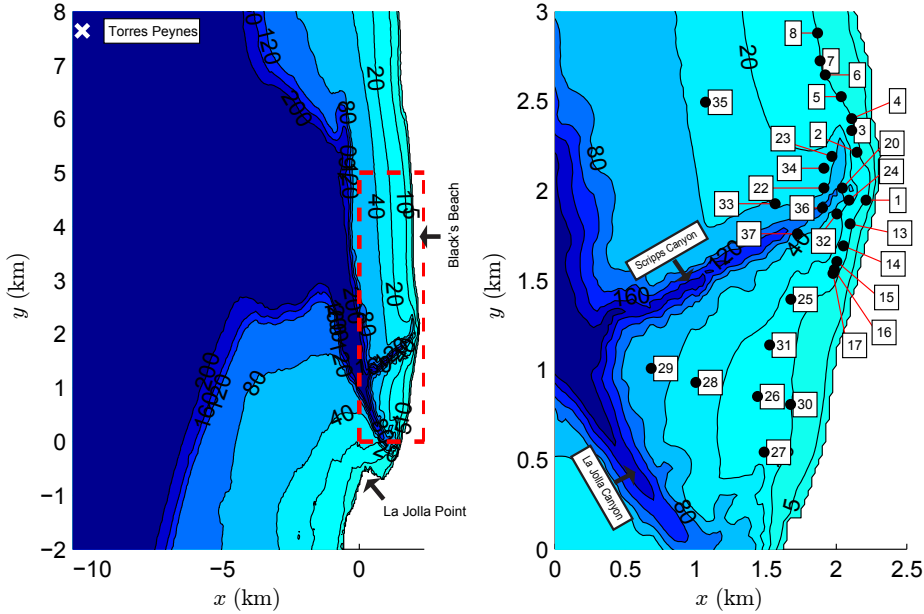


Figure 6.7: Bathymetry near Scripps and La Jolla canyon (left and right panel), and locations of observation points (right panel). Contourlines drawn at depths of 5, 10, 20, 40, 80, 120, 160 and 200 m. The origin is located at a latitude and longitude of  $32^{\circ} 49.7' N$  and  $117^{\circ} 21.9' W$ . with the positive coordinate axis orientated along the North ( $y$ -axis) and East ( $x$ -axis) direction.

bathymetry is characterized by two steep submarine canyons, Scripps canyon ( $\sim 150$  m deep and  $\sim 250$  m wide) and La Jolla canyon ( $\sim 120$  m deep and  $\sim 350$  m wide). Along these canyons (see Fig. 6.7), which extend to 200 m from the shore, strong wave refraction occurs due to steep slopes along the canyon walls (locally exceeding  $45^{\circ}$ ). Specifically for swell waves, refraction can introduce large spatial gradients in wave height in these circumstances, so that locally coherent effects such as diffraction may become important.

In the fall of 2003 the Nearshore Canyon Experiment (NCEX) was conducted to study wave transformation over the canyons, with a particular focus on Scripps Canyon. Pressure sensors, Waverider directional buoys and NORTEK vector current meters (PUV<sup>2</sup>) were deployed around the canyons, of which a subset of 18 pressure sensors, 5 buoys and 12 PUV's are used in the present study (see Fig. 6.7b for locations). The offshore wave conditions were recorded by the permanently deployed Outer Torres Peynes directional Waverider buoy, that is located approximately 12.5 km offshore at 549 m depth (see Fig. 6.7a).

For the pressure sensors and PUV's, variance density spectra are obtained from the de-trended 3 h time-record which is subdivided in windowed segments with 50%

<sup>2</sup>So called because they measure Pressure, the two horizontal particle velocities ' $U$ ' ' $V$ ' and in addition the vertical component  $W$ .

Table 6.1: Model parameters used for the different nested grids I to III. The spectral resolution was set to  $\Delta k = 0.01$  rad/m in all cases.

Grid	$x$ (km)	$y$ (km)	$\Delta x$ (m)	$N_x$ (-)	$N_y$ (-)	$k_x$ rad/m	$k_y$ rad/m	$M_x$ (-)	$M_y$ (-)
I	-11	-25	50	180	660	-0.0205	-0.0605	121	121
II	-8	-2	25	120	360	-0.0205	-0.1005	121	201
III	0	0	25	100	200	-0.0205	-0.1505	171	301

overlap. These are Fourier transformed and ensemble averaged to yield estimates of the pressure spectrum (with 50 degrees of freedom and frequency resolution  $\Delta f = 0.0025$  Hz). Subsequently, the band-passed ( $0.03 \text{ Hz} < f < 2 \text{ Hz}$ ) free surface spectrum is obtained using a transfer function from linear theory. For the wave buoys, the spectrum is estimated by averaging six spectra, each obtained from 26 min-long records, with  $\Delta f = 0.0025$  Hz, yielding approximately 50 degrees of freedom. The directional spectrum, needed to force the models at the offshore boundary, is estimated from the measured first four directional Fourier moments using a Maximum Entropy Method (Lygre and Krogstad, 1986). The spectral models are numerically evaluated on a set of nested rectangular spatial grids (see Tab. 6.1). The coarsest grid (I) is forced by the buoy data, and extends well beyond the southern border of Fig. 6.7a to ensure that southern incident swell is well reproduced. The finest grid (III) is focused near the NCEX site, and coincides with the area depicted in 6.7b. Moreover, going from I to III, the spectral domain is successively enlarged to ensure that the wave spectrum falls within the computational domain. The RTE was employed on grid I, because those parts that affect the subsequent nested grids are mostly located in sufficiently deep water, so that differences between the RTE and QC are expected to be small. For the remaining domains, results were obtained using both the RTE and the QC model.

From the 3-month period during which the NCEX experiment was conducted, we selected two cases to compare the QC and RTE with observed wave conditions. Because coherent effects are expected to be most dominant for directionally narrow fields (Smit and Janssen, 2013b), we consider two cases in which narrow swell waves are incident from either the west or the south.

### SOUTHERN SWELL

On November 16, 2003, the wave field at the NCEX site, was composed of a distinct swell peak from the south, and a mixed sea-swell system incident from the west (see Fig. 6.8). The south swell had a mean (nautical) direction of  $197^\circ$ , a peak period of 18.2s, significant wave height of  $H_{m_0} = 0.45$  m and a narrow directional spreading of  $7^\circ$  (defined according to Kuik *et al.*, 1988)). The sea-swell system was more energetic ( $H_{m_0} = 1.26$  m) and comprised of shorter more directionally spread waves, with the swell and sea peaks located at 11.8s and 5.8s, respectively. In the present analysis we only consider the southern swell peak at the up-wave boundary. This peak is distinctly located in the directional spectrum  $E(f, \theta)$  between  $145^\circ$  to  $235^\circ$  degrees for  $f < 0.07$  Hz, the other contributions to the wave spectrum are discarded.

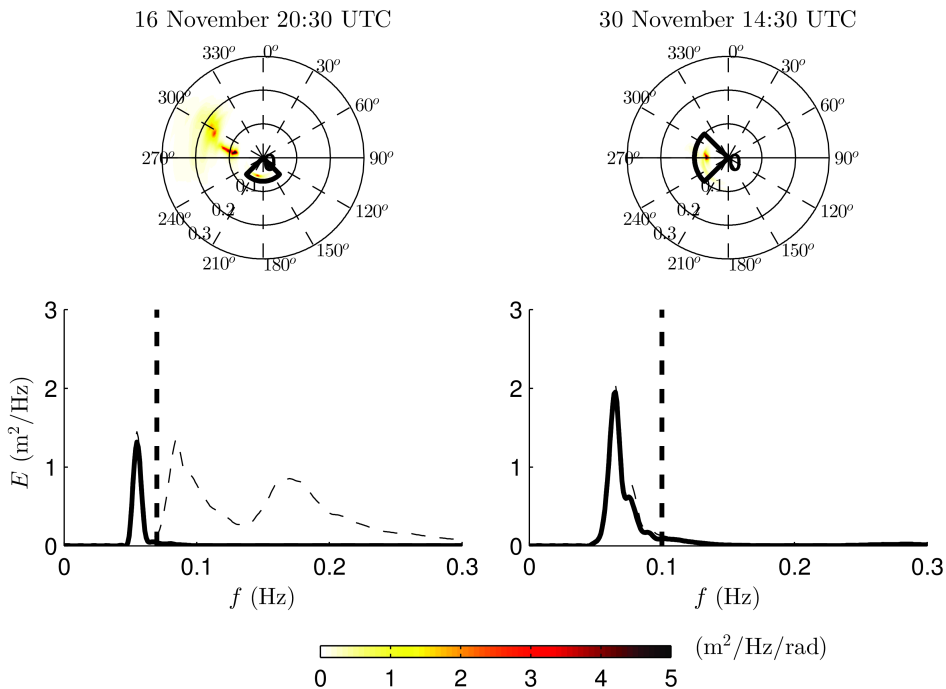


Figure 6.8: Directional wave spectra (top panels) and integrated frequency spectra (bottom panels) as observed at the Torres Peynes outer buoy on the 16<sup>th</sup> and 30<sup>th</sup> of November, 2003. The arc in the directional spectra indicates the swell fields considered in the present work. Frequency spectra are integrated over the indicated directional range (solid line) or over all directions (dashed lines).

Observed spectra are also band-pass filtered for  $0.025 < f < 0.07$  to remove the contributions of the mixed sea-swell system, and to remove low-frequency ig-wave energy generated by nonlinear interactions.

For southern swell, the QC model predicts that a significant part of the energy is refracted towards the coast before it arrives at the NCEX site due to the relatively shallow region south of the canyons (see Fig. 6.7). Hence, wave energy is already much reduced as it arrives at the NCEX site (see Fig. 6.9). Because these are long period waves, they subsequently reflect strongly over the steep canyon walls, which is clearly visible in the bands of enhanced mean wave height along the south part of La Jolla, and the Northern part of Scripps canyon. In between the canyons, the convex shape of the topography focusses wave energy so that a mild focal zone emerges. In between this focal zone and either of the two canyons virtually no wave energy is able to penetrate.

Qualitatively, differences between the QC and RTE predictions appear to be minor. The only significant difference in pattern is found north of the tip of Scripps Canyon. To compare the models in more detail with each-other, and with observa-

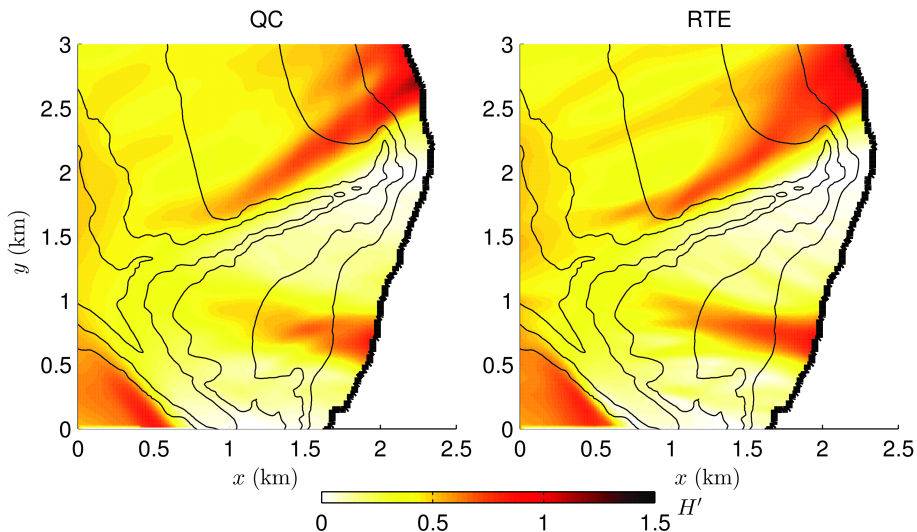


Figure 6.9: Normalized wave heights (normalized with incident wave height) near the NCEX site on 16 November, as predicted by the QC model (Left panel) and by the RTE (right panel).

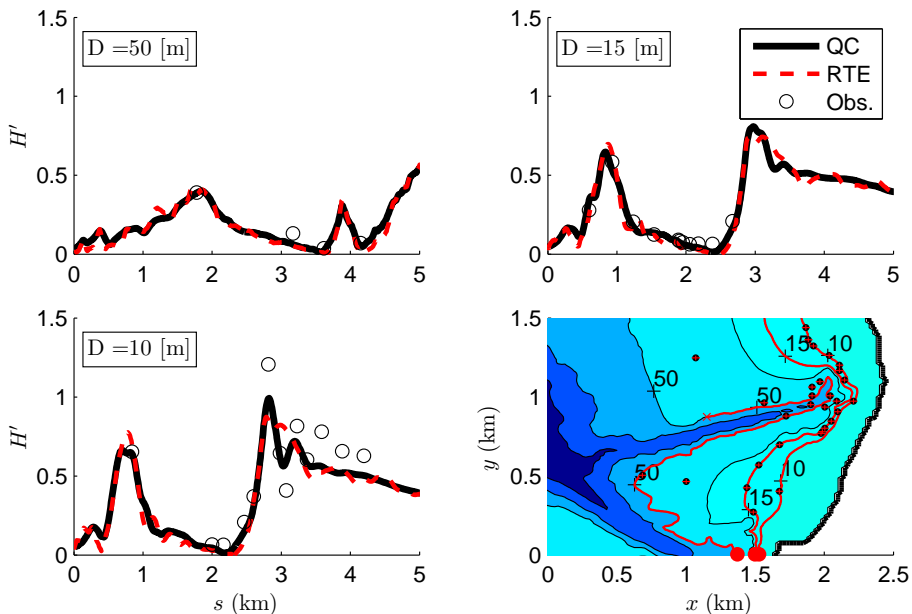


Figure 6.10: Normalized wave height  $H'$  along the indicated depth contours on 16 November. The coordinate  $s$  represents the along-contour distance measured from the starting point ( $S = 0$ , red dot) of the contour lines as indicated in the lower right panel.

tions, we consider transects of the wave height along different depth contours (Fig. 6.10). Overall correspondence between the observations and both models is very reasonable, specifically for the 50 m and 15 m contour lines. In these, there is very little to distinguish between the RTE or the QC approximation. Only along the 10 m contour line, starting at the eastern end of Scripps Canyon (around  $s = 2.5$  km) do significant differences between the observations and the models, and interestingly in-between the models themselves, show-up.

In this region waves that are refracted out of the canyon in a Northern direction cross waves that travel in a roughly south-western direction. Because for narrow-band swell the wave field remains coherent over significant distances, they interfere with one-another, which results in the fairly rapid oscillations found in the observed wave heights. This pattern is qualitatively reproduced (at least near  $s = 3$  km) in the QC model, though the size of the oscillations is underestimated. In contrast, the RTE model merely shows an enhanced sea state, but fails to reproduce oscillatory behaviour.

## WESTERN SWELL

On November 30, 2003, a westerly swell (mean direction  $272^\circ$ ) with a peak period of 15.4s, significant wave height  $H_{m0} = 0.77$  m, and a directional spreading of  $9^\circ$  (defined according to Kuik *et al.*, 1988), was measured at the Torres Peynes outer buoy. For this case, we band-pass filter the boundary signal and the observations between  $0.025 < f < 0.1$ .

This system, owing to the steep drop-off west of the NCEX site, arrives at the eastern boundary with wave heights similar to those off-shore. The subsequent pattern is again dominated by the local geometry of the Canyons. Similar as before, waves are refracted out of the canyons so that along the canyon walls we again see a band of enhanced wave energy, and also a focal region in between the two canyons (Fig. 6.11). However, due to the incidence angle of the waves, and the larger directional distribution off-shore, more wave energy is able to penetrate the regions between the focal zone and the respective canyons.

Qualitatively, differences are again small, but more pronounced than before. The QC solution, in particular in the focal region, is fairly smooth, whereas the RTE produces a more banded pattern of energy. This difference is likely because the RTE reacts more volatily to local disturbances in the topography; a local steep slope can introduce strong refraction. In the QC model, which accounts for the topography within the entire coherent footprint, such a local topographical feature becomes less significant for the evolution of the wave statistics (see also Fig. 6.1).

This difference in behaviours is also visible when considering cross-sections of the wave height along different contour lines. Again, both models are very similar around the 50 m contour. However, in this case the RTE shows rapid oscillations in the region between the canyons ( $s < 2.5$ ) along the 15 m contour line, associated with the banded patterns mentioned above. The QC appears to be in better agreement with observations as neither the QC nor the observations reproduce these oscillations. Though, the magnitude of the oscillations is small, and the RTE results are still in relatively good agreement with the observations.

Again, on the 10 m contour the most significant difference occurs North of Scripps canyon, where the observations indicate the occurrence of a single peak followed by fairly homogeneous conditions north of the canyon ( $s > 3$  km). This behaviour is faithfully reproduced by the QC, though wave heights are somewhat overestimated for ( $s > 3$  km). However, in this case the RTE produces two distinct peaks, where the erroneous secondary peak (at  $s = 3$  km) locally overestimates the wave heights by 20%. Further north, where the topography has almost parallel depth contours, the QC and RT are yet again virtually indistinguishable.

## 6.5. DISCUSSION AND CONCLUSIONS

In the present we considered the application of the quasi-homogeneous wave theory for random wave propagation in a varying medium as presented by Smit and Janssen (2013b). To derive a consistent model suitable for large scale application over complex topography, we first demonstrated that for wave fields with a finite coherence length, only the topographical variation within the coherent footprint influences the evolution of the wave statistics. Subsequently, on the premise of a finite coherence length we derived an augmented form of the radiative transport equations (RTE), which includes a scattering term accounting for the generation of coherent contributions within random wave fields, and which we refer to as the Quasi-Coherent (QC) approximation. Comparison with a monochromatic wave experiment of wave scattering over a submerged shoal, demonstrated that, even when the wave field remains correlated over large distances, the resulting model is able to capture not only the bulk parameters, but also provides a good approximation to the wave spectrum and to its Fourier transform, the covariance function. Moreover, hind-casts of swell wave conditions that occurred during the ONR NCEX experiment show that wave heights predicted by the QC agree with observations, and are a slight improvement on those predicted by the RTE.

The modelling paradigm introduced in the present study extends conventional stochastic models to include the effects of coherent interference. This not only gives a more complete description of the bulk second-order statistics in case of complex topography, but also describes the covariance structure of the waves – which cannot be predicted using quasi-homogeneous theory alone. In particular for narrow-band swell conditions, focussing of the waves might introduce coherent interference patterns in the wave field that require an extended description of the covariance structure to fully capture the fast spatial variations in the wave field. Moreover, an extended description of the second-order statistics is not only important for predicting the bulk wave parameters, but due to the resulting fast scale gradients in the momentum flux (or radiation stress), also influences the mean circulation and through it nearshore transport processes. For these reasons, extension of existing third-generation wave models to include the QC scattering term, can help improve the prediction of the wave statistics, and possible wave-driven circulations, in complex topographical environments.

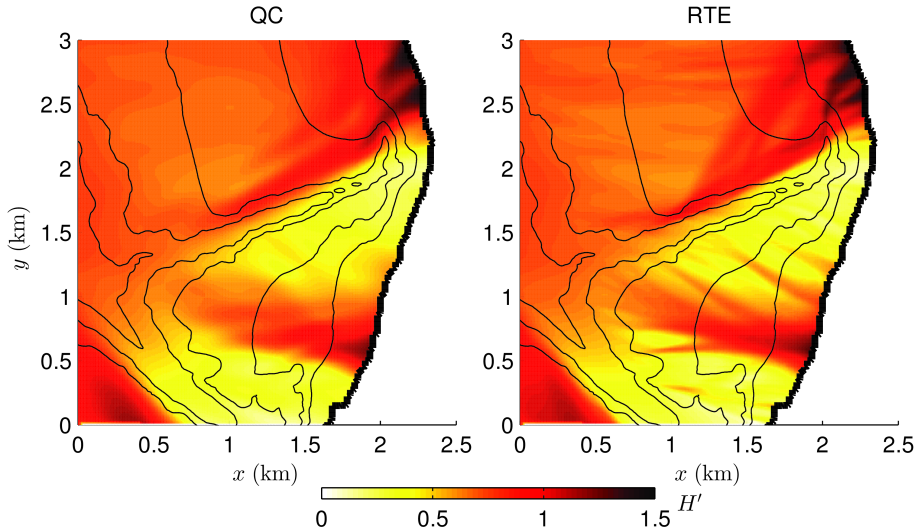


Figure 6.11: Normalized wave heights (normalized with incident wave height) near the NCEX site on 30 November, as predicted by the QC model (Left panel) and by the RTE (right panel).

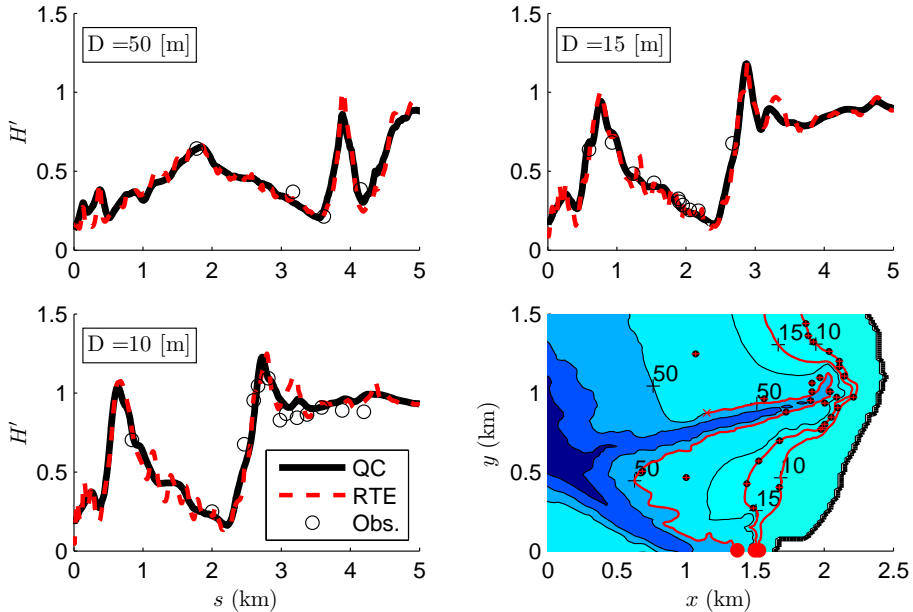


Figure 6.12: Normalized wave height  $H'$  along the indicated depth contours on 30 November. The coordinate  $s$  represents the along-contour distance measured from the starting point ( $S = 0$ , red dot) of the contour lines as indicated in the lower right panel.

## ACKNOWLEDGMENTS

This research is supported by the U.S. Office of Naval Research (Littoral Geosciences and Optics Program and Physical Oceanography Program) and by the National Oceanographic Partnership Program. We would like to thank dr. M. Zijlema, who supplied the initial version of the BiCGSTAB solver used in the present work, and dr. L. Holthuijsen, who, through his continuous support of PBS, made the present work possible.

# Appendices

## 6.A. FOURIER TRANSFORM OPERATORS

As we make frequent use of continuous and discrete Fourier transforms, it is convenient to introduce the following operators. Let  $\zeta$  be a dummy continuous function, for which we denote the conjugate pair as  $\zeta(\mathbf{x}), \hat{\zeta}(\mathbf{k})$ , such that  $\hat{\zeta}(\mathbf{k}) = \mathcal{F}_{\mathbf{x},\mathbf{k}}\{\zeta(\mathbf{x})\}$  and  $\zeta(\mathbf{x}) = \mathcal{F}_{\mathbf{k},\mathbf{x}}^{-1}\{\hat{\zeta}(\mathbf{k})\}$ , with

$$\mathcal{F}_{\mathbf{x},\mathbf{k}}\{\zeta(\mathbf{x})\} = \frac{1}{(2\pi)^2} \int \zeta(\mathbf{x}) \exp[-i\mathbf{k} \cdot \mathbf{x}] d\mathbf{x} \quad (6.18)$$

$$\mathcal{F}_{\mathbf{k},\mathbf{x}}^{-1}\{\hat{\zeta}(\mathbf{k})\} = \int \hat{\zeta}(\mathbf{k}) \exp[i\mathbf{k} \cdot \mathbf{x}] d\mathbf{k} \quad (6.19)$$

In a similar fashion, we define the discrete conjugate Fourier transform pair for a periodic function  $\zeta(\mathbf{x})$  with period  $L$ , as  $\zeta(\mathbf{x}), \hat{\zeta}_{\mathbf{k}}$  where

$$\hat{\zeta}_{\mathbf{k}} = \bar{\mathcal{F}}_{\mathbf{x},\mathbf{k}}\{\zeta(\mathbf{x})\} = \frac{1}{L^2} \int_{-L/2}^{L/2} \zeta(\mathbf{x}) \exp[-i\mathbf{k} \cdot \mathbf{x}] d\mathbf{x} \quad (6.20)$$

$$\zeta(\mathbf{x}) = \bar{\mathcal{F}}_{\mathbf{k},\mathbf{x}}^{-1}\{\hat{\zeta}_{\mathbf{k}}\} = \sum_{\mathbf{k}} \hat{\zeta}_{\mathbf{k}} \exp[i\mathbf{k} \cdot \mathbf{x}]. \quad (6.21)$$

From these definitions we see that, for a function that is strictly zero outside a certain rectangular domain centred at the origin, and with sides smaller than  $L$ , the sampled values of  $\zeta(\mathbf{k})$  at  $\mathbf{k} = [m_1, m_2]\Delta k$  (with  $\Delta k = 2\pi/L$ ) are equal to  $\hat{\zeta}(\mathbf{k}) = \hat{\zeta}_{\mathbf{k}}/(\Delta k^2)$ .

## 6.B. DISCRETE MODEL

To consider the numerical solution of the QC approximation, we consider the solution on a discrete regular rectangular mesh in both geographical and wavenumber space. For the spatial and wavenumber mesh we set

$$\mathbf{x}_{m_1^x, m_2^x} = \mathbf{x}_0 + [m_1^x \Delta x_1, m_2^x \Delta x_2], \quad \mathbf{k}_{m_1^k, m_2^k} = \mathbf{k}_0 + [m_1^k \Delta k_1, m_2^k \Delta k_2], \quad (6.22)$$

with  $m_j^x \in \{0 \dots M_j^x\}$ ,  $m_j^k \in \{0 \dots M_j^k\}$  and where  $\mathbf{x}_0, \mathbf{k}_0$  denote the coordinates of the lower left corner of the geographical and wavenumber grid, respectively. For brevity, we denote the discrete coupled mode spectrum evaluated at  $\mathbf{x}_{m_1^x, m_2^x}, \mathbf{k}_{m_1^k, m_2^k}$  as  $\mathcal{E}^{\mathbf{k},\mathbf{x}}(t)$ , where the dependency on the subscripts  $m_j^x, m_j^k$  is implied. With these definitions in place the spatially-discrete, stationary, version of the Quasi-Coherent approximation can be expressed as

$$c_k \cdot \mathcal{D}_{\mathbf{k}} \mathcal{E}^{\mathbf{k},\mathbf{x}} + c_x \cdot \mathcal{D}_{\mathbf{x}} \mathcal{E}^{\mathbf{k},\mathbf{x}} = -i \sum_{|\mathbf{q}| \leq q_{\max}} \left[ \Delta \hat{\sigma}^{\mathbf{q}} - \frac{i\tilde{\mathbf{k}}}{2} \Delta \hat{\sigma}_k^{\mathbf{q}} \cdot \mathcal{D}_{\mathbf{x}} \right] \mathcal{E}^{\mathbf{k}-\mathbf{q}/2, \mathbf{x}} + * \quad (6.23)$$

Here  $\mathcal{D}_{\mathbf{x}}$  and  $\mathcal{D}_{\mathbf{k}}$  denote linear finite difference operators which approximate  $\nabla_{\mathbf{x}}$  or  $\nabla_{\mathbf{k}}$ , respectively, by means of second-order upwind approximations. The operator  $\mathcal{D}_{\mathbf{x}}\mathcal{E}^{\mathbf{k},\mathbf{x}}$  is defined as

$$\mathcal{D}_{x_j}\mathcal{E}^{\mathbf{k},\mathbf{x}} = s_j \frac{3\mathcal{E}^{\mathbf{k},\mathbf{x}} - 4\mathcal{E}^{\mathbf{k},\mathbf{x}-\Delta\tilde{\mathbf{x}}^j} + \mathcal{E}^{\mathbf{k},\mathbf{x}-2\Delta\tilde{\mathbf{x}}^j}}{2\Delta x_j} \quad (6.24)$$

with  $\mathbf{s} = \text{sgn}(\mathbf{k})$  and  $\Delta\tilde{\mathbf{x}}^j = s_j[\delta_{1j}\Delta x_1, \delta_{2j}\Delta x_2]$  where  $\delta_{ij}$  denotes the Kronecker delta. The operator  $\mathcal{D}^{\mathbf{k}}\mathcal{E}_{\mathbf{k},\mathbf{x}}$  is defined analogously, but then along the spectral dimensions

$$\mathcal{D}_{k_j}\mathcal{E}^{\mathbf{k},\mathbf{x}} = \tilde{s}_j \frac{3\mathcal{E}^{\mathbf{k},\mathbf{x}} - 4\mathcal{E}^{\mathbf{k}-\Delta\tilde{\mathbf{k}}^j,\mathbf{x}} + \mathcal{E}^{\mathbf{k}-2\Delta\tilde{\mathbf{k}}^j,\mathbf{x}}}{2\Delta k_j} \quad (6.25)$$

where  $\tilde{\mathbf{s}} = \text{sgn}(\mathbf{c}_x)$  and  $\Delta\tilde{\mathbf{k}}^j = \tilde{s}_j[\delta_{1j}\Delta k_1, \delta_{2j}\Delta k_2]$ .

To exclude interactions between waves and topographical variations on the infra-wave scale, which are excluded at the order  $O(\epsilon)$  considered, the sum over  $\mathbf{q}$  is restricted to  $|\mathbf{q}| \leq q_{\max}$ . Here,  $q_{\max}$  is the minimum of  $|\mathbf{k}|/2$  or a pre-described maximum bottom wavenumber component. When solving for the RTE, we disregard this sum altogether.

At the geographic boundary (along the lines  $m_1^x = 0, m_1^x = M_1^x$  and  $m_2^x = 0, m_2^x = M_2^x$ ) the wave spectrum is prescribed for wavenumbers directed into the computational domain. For the spectral boundary (along the lines  $m_1^k = 0, m_1^k = M_1^k$  and  $m_2^k = 0, m_2^k = M_2^k$ ) we assume that it is located at wavenumbers which are effectively deep water waves, so that the interaction with components outside the computational domain (assumed to be zero) can be neglected. Moreover, at points adjacent to the geographic or spectral boundary (e.g., along the line  $m_1^x = 1$ ) first-order approximations are used if eqs. (6.24) or (6.25) reference points outside the computational domain. Here the discrete operators  $\mathcal{D}_{x_j}$  and  $\mathcal{D}_{k_j}$  are locally reduced to

$$\mathcal{D}_{x_j}\mathcal{E}^{\mathbf{k},\mathbf{x}} = s_j \frac{\mathcal{E}^{\mathbf{k},\mathbf{x}} - \mathcal{E}^{\mathbf{k},\mathbf{x}-\Delta\tilde{\mathbf{x}}^j}}{\Delta x_j}, \quad \mathcal{D}_{k_j}\mathcal{E}^{\mathbf{k},\mathbf{x}} = \tilde{s}_j \frac{\mathcal{E}^{\mathbf{k},\mathbf{x}} - \mathcal{E}^{\mathbf{k}-\Delta\tilde{\mathbf{k}}^j,\mathbf{x}}}{\Delta k_j}, \quad (6.26)$$

respectively.

Due to the second-order approximations, the resulting numerical model does not preserve monotonicity in the solution, which might give erroneous results near sharp spatial (or spectral) gradients in the spectral densities. For the QC model, which generally produces smooth results, this is not an issue problem. However, in case of the RTE, which does introduce strong spatial gradients in focal regions (e.g., as in Fig. 6.2), this can introduce numerical artefacts in the solution, such as negative spectral densities. In principle, this can be addressed by for instance introducing total variation diminishing approximations for the discrete operators (e.g., Hirsch, 2007). However, these approximations are nonlinear, and therefore would introduce additional complexity in the iterative solution algorithm introduced below. In the problems considered here, because this is only an issue in a few points of the domain, this is considered overly complex. Instead, we avoid negative values in the RTE by simply reducing the discrete operator to first order approximations whenever negative densities occur in the iteration process described below.

## COEFFICIENTS

When considering the RTE, the geographic and spectral propagation velocities are defined as  $\mathbf{c}_x = \mathbf{k}\sigma_k$  and  $\mathbf{c}_k = -\nabla_{\mathbf{x}}\sigma$  and  $\Delta\hat{\sigma}^{\mathbf{q}} = \Delta\hat{\sigma}_k^{\mathbf{q}} = 0$ . However, for the QC-approximation,  $\mathbf{c}_k, \mathbf{c}_x$  in eq. (6.23) are obtained from a local least-squares approximation to  $\sigma, \sigma_k$ , whereas the remainder is used to calculate  $\Delta\hat{\sigma}, \Delta\hat{\sigma}_k$ . To calculate these, we define a local geographic grid  $\mathbf{x}'$  over the coherent footprint centred at  $\mathbf{x}$ , and its conjugate set of wavenumers  $\mathbf{q}$  as

$$\mathbf{x}'_{m_1^{x'}, m_2^{x'}} = [m_1^{x'} \Delta x_1, m_2^{x'} \Delta x_2], \quad \mathbf{q}_{m_1^q, m_2^q} = [m_1^q \Delta q_1, m_2^q \Delta q_2], \quad (6.27)$$

with  $m_j^{x'}, m_j^q \in \{-M_j^q/2 \dots M_j^q/2\}$ ,  $M_j^q = 2q_{\max}/\Delta q_j$ , and  $\Delta x_j = 2\pi(M_j^q \Delta q_j)^{-1}$ . To avoid interpolation it is convenient to ensure the sum in eq. (6.23) over  $\mathbf{q}$  coincides with the  $\mathbf{k}$  grid, so we set  $\Delta q_j = 2\Delta k_j$ , assuming that  $\Delta k_j \leq 2\pi/\xi_c$ .

With these definitions in place, we define a plane approximation on  $\mathbf{x}'$  to  $\mathbf{c}_k, \mathbf{c}_x$  as

$$\sigma_{(k)}^{\text{plane}}(\mathbf{k}, \mathbf{x}', \mathbf{x}) = \alpha_{(k)} + \beta_{(k)} \cdot \mathbf{x}', \quad (6.28)$$

where the optional subscript  $(k)$ , is omitted to obtain the expression for  $\sigma^{\text{plane}}$ , or replaced with  $k$  to denote  $\sigma_k^{\text{plane}}$ . Furthermore, the slope and intercept coefficients  $\alpha_{(k)}, \beta_{(k)}$  are obtained from least squares approximations to  $\sigma(\mathbf{k}, \mathbf{x} + \mathbf{x}')$  and  $\sigma_k(\mathbf{k}, \mathbf{x} + \mathbf{x}')$ . From these, the propagation speeds are defined from the slope and intersect as  $\mathbf{c}_k = -\beta$  and  $\mathbf{c}_x = \alpha_k \tilde{\mathbf{k}}$ , so that the QC remainder, defined as the difference between the plane approximation and the exact expressions, becomes

$$\Delta\sigma_{(k)}(\mathbf{k}, \mathbf{x}', \mathbf{x}) = \sigma_{(k)}(\mathbf{k}, \mathbf{x} + \mathbf{x}') - \sigma_{(k)}^{\text{plane}}(\mathbf{k}, \mathbf{x}', \mathbf{x}) \quad (6.29)$$

Arguable,  $\Delta\hat{\sigma}, \Delta\hat{\sigma}_k$  can now be obtained by a discrete Fourier transform. However, to avoid errors due to jump discontinuities between the non-smoothly matching domain borders in a periodic extension of  $\Delta\sigma_{(k)}$ , we define the transform as

$$\Delta\hat{\sigma}_{(k)} = \bar{\mathcal{F}}_{\mathbf{x}', \mathbf{q}} \{W_1(x'_1)W_2(x'_2)\Delta\sigma_{(k)}\} \quad (6.30)$$

where  $W_j(x'_j)$  are window functions that smoothly transitions to 0 near the edges of the domain, and for which in the present work we use a tapered cosine (Tukey) window which is given by

$$W_j(x'_j) = \begin{cases} \frac{1}{2} + \frac{1}{2} \cos\left(\pi \left[\frac{x'_j - l_j + \gamma l_j}{\gamma l_j}\right]\right) & \text{if } x'_j > (1 - \gamma)l_j \\ \frac{1}{2} + \frac{1}{2} \cos\left(\pi \left[\frac{x'_j}{\gamma l_j} - 1\right]\right) & \text{if } x'_j < \gamma l_j \\ 1 & \text{elsewhere} \end{cases} \quad (6.31)$$

Here,  $l_j = 2\pi/\Delta q_j$  is the length of the  $j^{\text{th}}$  side of the  $\mathbf{x}'$  domain, and  $\gamma$  is a dimensionless width parameter controlling the length of the transitional area where  $W \rightarrow 0$  and which is set to  $\gamma = 0.1$ .

## ITERATIVE SOLUTION TECHNIQUE

The resulting set of equations involve  $M = M_1^x M_2^x M_1^k M_2^k$  variables so that solving for the steady state involves inverting a large sparse  $M \times M$  matrix. Solving this

system directly is difficult, as even for a moderate number of grid point in each of the for dimensions the total number of points quickly becomes large. However, because propagation principally occurs in geographic space, and is dominated by the LHS of (6.24), the system can be solved iteratively in a marching fashion, similar to the method employed in Booi *et al.* (1999), explained in detail in (Zijlema and van der Westhuysen, 2005).

Hereto,  $\mathbf{k}$  space is subdivided into four quadrants, each bounded by the cartesian axes, which we will number 1 till 4 in a counter-clockwise fashion, where quadrant 1 is the set  $Q_1 = \{\mathbf{k}, \mathbf{x} | k_1 > 0 \wedge k_2 \geq 0\}$ . During a single Gauss-Seidel iteration, each of the four quadrants of the spectral domain is visited consecutively using four sweeps per iteration. During each sweep, only points that belong to the quadrant are updated. For example, during iteration step  $n$ , in the  $m^{\text{th}}$  sweep ( $n_m$ ) the quadrant  $m$  is considered, and for all points  $\mathbf{P} = [k_1, k_2, x_1, x_2]$  where  $\mathbf{P} \in Q_m$ , we substitute the unknown  $\mathcal{E}_{\mathbf{P}}^{n_m}$  in eq. (6.23)  $\forall \mathbf{P}$ . Conversely, for all points  $\mathbf{R} = [k_1, k_2, x_1, x_2]$  where  $\mathbf{R} \notin Q_m$  are approximated by the values from the most recent update at  $n_{m-1}$  (with  $n_0 = (n-1)_m$ ), and for these we therefore substitute the known values  $\mathcal{E}_{\mathbf{R}}^{n_{m-1}}$ .

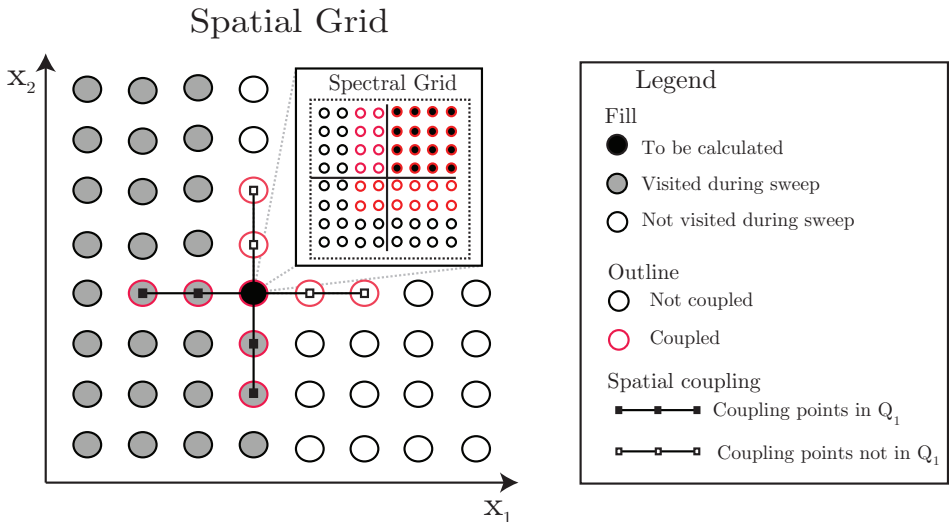


Figure 6.13: Illustration of the four directional sweep method used in the present study. Because the spatial coupling between computational points in  $Q_1$  is only in the up-wave direction, points in  $Q_1$  can be calculated successively by marching in the wave direction. Contributions due to points in the other directional sectors are included by using the latest available estimate.

Not only does this reduce the number of unknowns per sweep, the structure of the resulting matrix is such that spatial dependencies involving  $\mathcal{E}_{\mathbf{P}}^{n_m}$  only occur in the downwave direction. Hence, for the first sweep, when starting at the spatial point with indices  $m_1^x = 1$  and  $m_2^x = 1$  (denoted  $P_{1,1}$ ,  $\forall \mathbf{k}$  such that  $P_{1,1} \in Q_1$ ), all downwave information is known (from the boundary), and to solve for  $\mathcal{E}^{n_m} \forall \mathbf{k}$  in that

point we therefore only need to invert a  $M_1^k M_2^k$  by  $M_1^k M_2^k$  matrix involving those wavenumbers  $\mathbf{k}$  in the Quadrant, whereas the dependencies on the other quadrants are included explicitly from the last sweep over that quadrant. Similarly, with  $P_{1,1}$  known, when marching forward, all downwave information for points  $P_{1,2}$  or  $P_{2,1}$  is available, and the solution is again found by inverting a small local matrix. Hence, when marching forward in this way, starting at the appropriate corner for each sweep, down-wave points of the quadrant have been visited previously during the sweep (or are known from the boundary), and can be included in a Gauss-Seidel manner, and we only need to solve a linear system containing the spectral mesh-points in the quadrant under consideration as unknowns (see Fig. 6.13). Nevertheless, if the topography is captured with  $M_7^2$  Fourier modes, this can give a dense linear system containing  $M_1^q M_2^q$  diagonals. However, given that for slowly varying topography the off-diagonal contributions are small, the resulting system can still be solved relatively fast using the BicGStab method with an ILU-preconditioner (Van der Vorst, 1992).

In the cases considered, the resulting algorithm always converged to a solution within relatively few iterations ( $n < 10$ ), where the solution was considered to be converged at after a complete iteration  $n_4$ , when the following criterion was met

$$\frac{\sum_{\mathbf{k}} (\mathcal{E}_{\mathbf{k},\mathbf{x}}^{n_4} - \mathcal{E}_{\mathbf{k},\mathbf{x}}^{(n-1)_4})^2}{\sum_{\mathbf{k}} (\mathcal{E}_{\mathbf{k},\mathbf{x}}^{n_4})^2} < \alpha^2, \quad \forall \mathbf{x}. \quad (6.32)$$

Here  $\alpha$  is the convergence criterion, set to  $\alpha = 10^{-4}$  in the present study.



# 7

## Conclusions and outlook

In the present work we considered advances in the prediction of two complementary type of models for simulating wave conditions on the continental shelf up until the coastline. We investigated this in the context of advancing predictive capability and understanding of wave dynamics, and in particular the evolution of wave statistics, in shallow water. Hereto, two separate (though related) paths were pursued. First, we considered an evolutionary approach within deterministic nearshore wave modelling (Chapters 3 and 4), where we considered an efficient and accurate way of approximating dissipation due to wave breaking in non-hydrostatic models (in the SWASH model in particular). We explored how well this reproduces not only bulk statistics, but also higher-order wave-statistics in a dissipative surfzone. Next, on the premise of dispersive wave motion over slowly varying topography, we derived a generalisation of the radiative transport equation that governs the evolution of the complete second-order statistics (Chapters 5 and 6), including coherent interference. In what follows, we will summarize the main results, and provide an outlook on possible future developments and applications.

### 7.1. CONCLUSIONS

#### NON-HYDROSTATIC MODELLING

Conceptually, non-hydrostatic models resolve the Reynolds-averaged Navier-Stokes equations using a single-valued approximation for the free surface, and as such implicitly account for the relevant wave dynamics (e.g. shoaling, refraction, diffraction, wave-current interaction, etc.) for intermediate to shallow-water wave propagation over relatively small distances ( $O(10)$  wave lengths). Their accuracy is in principal only restricted by model resolution in space and time. Arguably, their most attractive feature is that, when combined with shock-capturing numerics, the dissipation due to wave breaking is implicitly accounted for. Unfortunately, as demonstrated in this thesis, correctly resolving the location of incipient breaking requires fine vertical resolutions (see, for instance, Fig. 3.4), much finer than required to resolve the

nonlinear wave dynamics found in the shoaling region. At coarse vertical resolutions flow velocities near the crest are underestimated so that the kinematic instability associated with wave breaking (particle velocity exceeds wave celerity) is postponed, and wave shoaling continues past observed experimental breaking locations.

Consequently, the requirement of fine vertical resolutions in a small, but dynamically important, region introduces prohibitive computational costs for spatial and temporal scales in the order of  $O(10)$  wave lengths and  $O(100)$  periods, even on large scale multi-processor machines. Hence, problems including 2D wave propagation over extended nearshore topography, or the generation of a large ensemble to estimate nonlinear wave statistics, cannot be resolved in this manner. In this context, inspired by prior research demonstrating that the evolution of the bore is well described by the NSWE (Hibberd and Peregrine, 1978), we introduced the hydrostatic front approximation to wave breaking to make model application to such problems feasible.

The method, referred to as the Hydrostatic Front Approximation (HFA), enforces a hydrostatic pressure distribution under the front of a wave. This initiates the transition into a near-vertical sawtooth like wave, so that the associated energy dissipation can be accounted for by ensuring that mass and momentum are conserved over the resulting shock – in-line with the analogy between a breaking wave and a hydraulic jump. The hydrostatic pressure is activated point-wise once non-dimensional rate of change of the free-surface ( $\partial_t \zeta / \sqrt{gd}$ ) exceeds a predetermined threshold  $\alpha$ , and the full non-hydrostatic computations are restored once the wave crest has passed, or when  $\partial_t \zeta < 0$ . The threshold, which is essentially a proxy for the maximum surface steepness, is obtained from computed values of  $\alpha (=0.6)$  at observed breaking locations of monochromatic wave breaking on a planar beach (Ting and Kirby, 1994). Moreover, to represent persistence of wave breaking, the criterion  $\alpha$  is reduced to  $\beta (=0.3)$  in locations where in neighbouring points the HFA is active; this ensures that wave breaking continues until the steepness of the front becomes small, and the wave reforms.

Comparison with several laboratory observations of random waves breaking over barred topography (Battjes and Janssen, 1978; Boers, 1996; Dingemans *et al.*, 1986; Van Gent and Doorn, 2000) demonstrates that the HFA – without further calibration – is able to predict not only bulk parameters, such as significant wave height and mean zero-crossing period, but also the wave-induced mean set-up, using a relatively coarse resolution in the vertical (2 layers). Furthermore, the obtained results are virtually indistinguishable from those obtained from more involved computations using a high resolution model. Comparison to observed wave propagation in a 2D wave basin (Dingemans *et al.*, 1986) confirms that the method is equally applicable to short-crested waves; computed wave heights and wave spectra compare favourably with observations, and the measured wave-induced circulation is faithfully reproduced in both a qualitative and quantitative manner.

Nonlinear phase-resolving models are of interest because they can account for strongly nonlinear wave dynamics in the surfzone; this includes not only predicting the bulk parameters, but also higher order statistics, and the details of the spectral evolution. To ascertain whether a relatively efficient model such as SWASH, in

which the details of the breaking process such as overturning and turbulence are not resolved, can reliably predict surfzone (non-Gaussian) wave statistics, we performed a comparison to a large number of flume observations of random waves (Smith, 2004). Because interest included the high-frequency tail, this required a higher vertical resolution (6 layers) compared with previous simulations in this thesis to resolve dispersion for such relatively deep water waves; nevertheless, inclusion of the HFA prevented the need for an even finer mesh size in the surfzone.

In accordance with previous results the model accurately predicts second-order bulk parameters such as wave height and period; this without requiring calibration. In addition, bulk higher-order statistics, i.e. skewness and asymmetry, also agree well with observations, although in the case of narrow-band spectra asymmetry values are somewhat exaggerated in the surfzone. This is likely due to the exclusion of breaking-induced turbulence, which in reality stabilizes the bore front to a finite steepness; for wider-band fields, the statistics are smoothed, providing better agreement with observations.

Yet, the most profound result is that development of spectral levels is well reproduced throughout the surfzone: from the attenuation of the spectral peak(s) and the amplification of higher harmonics, to the increase of energy in the high frequency tail by as much as two orders of magnitude. This demonstrates that a non-hydrostatic model with a single-valued representation of the free surface can provide an accurate presentation of the concomitant action of the dominant nonlinear and dissipative processes that govern the evolution of the spectrum in the surfzone. The former is further corroborated by agreement between nonlinear transfer rates estimated from observed and computed bispectra. More so, agreement extends well beyond the energetic part of the spectrum, to up to ten times the peak frequency, and the resulting shape of the spectral tail conforms with speculations in the literature that in shallow water the tail approaches an asymptotic form (Smith and Vincent, 2003; Kaihatu *et al.*, 2007). Whether or not an asymptote of the tail in the surfzone exists is yet to be conclusively demonstrated, but results and observations are in line with suggestions presented by Smith and Vincent (2003) and Kaihatu *et al.* (2007).

The second-order statistics, as encapsulated by the variance density spectrum, are thus well resolved in SWASH, whereas agreement with observations for the third-order moments suggests that the non-Gaussian statistics that occur in the surfzone can be predicted by SWASH as well. This is further corroborated by comparison of the probability density function (pdf) of the free surface, estimated by Monte Carlo simulations, with the observed pdf, and a theoretical nonlinear pdf (Longuet-Higgins, 1963). Though the observations are relatively short, so that the tails of the estimated pdf from observations are not reliable, the predicted pdf agrees well with observations, and with the theoretical pdf that only depends on the first two moments, variance and skewness.

These findings suggested that the influence of fourth and higher order moments on the statistics is relatively minor. Presumably the nonlinear wave dynamics are therefore well approximated using second-order theory, i.e. the primary energy balance in the surfzone is between the flux gradient, triad nonlinear interactions and dissipation. Because the flux gradient and the nonlinear term can be estimated from

second-order theory combined with calculated (bi)spectra from SWASH, we could estimate the dissipation as the term that closes the balance. From this energy balance we derived that the wave dissipation in SWASH is proportional to a frequency-squared distribution function, which is consistent with observations in other studies. Though not conclusive, it illustrates that SWASH can be used to investigate properties which are not easily accessible by observations, for instance to verify or obtain better approximations for use in more economic models.

The SWASH model combined with the HFA as considered in the present study has proven to be a remarkably robust, accurate and relatively efficient tool to predict surfzone dynamics. Although the detailed analysis in the present study primarily considers one-dimensional wave propagation in a flume, we note that triad nonlinear and dissipation processes are not fundamentally different for 2D surfzones with short-crested waves, so that our latter conclusions are probably also valid under such conditions. This is somewhat corroborated by the 2D basin experiment we considered, though computational restrictions prevent more detailed analysis in that case. Overall, the findings of this study suggest that SWASH is a viable tool for modeling wave and wave-driven dynamics in a nonlinear, dissipative surfzone.

#### STOCHASTIC MODELING

The interaction of ocean waves with ambient currents and topography in coastal areas can result in a wave focal zone where, due to coherent interferences, the mean wave statistics (e.g. mean wave heights) become strongly non-homogeneous. This can affect wave-driven circulation and transport processes, yet stochastic wave models, invariably based on some form of the radiative transfer equation (or action balance), do not account for these effects. In the present thesis, to extend the stochastic framework to include effects of coherent interference, we therefore derived a new transport model that accounts for the statistics of inhomogeneous wave fields of arbitrary bandwidth propagating through a variable medium.

Our starting point was a linear description of the underlying dynamics, in which the medium (i.e. the topography) is assumed to slowly change its properties compared to the wave motion proper. On the premise that the frequency and wavenumber of local plane wave solutions are then coupled by the linear dispersion relation, we used an operator correspondence argument based on the Weyl association rule to define a deterministic integro-differential equation that governs the linear wave motion. For mild slopes this equation (to the order considered) reproduces geometric optics, yet makes no a-priori assumptions on spectral bandwidth.

Based on the deterministic equation, we derive an evolution equation for the second-order statistics which, by exchanging a wavenumber coordinate for a spatial coordinate through an inverse Fourier transformation, is cast in terms of an evolution equation for the Wigner – or Coupled Mode (CM) – spectrum. This spectrum accounts for the complete second-order correlation matrix, and occupies an intermediate position between a full spectral and spatial description of the correlation function, much like the well-known variance density spectrum. In fact, when Quasi-Homogeneous (QH) theory applies, the CM spectrum reduces to the variance density spectrum, whereas it is a natural generalisation thereof in case of strongly heterogeneous statistics (e.g. in a wave focal zone). For narrow-band waves travelling in

a homogeneous medium the transport equation reduces to the linear Alber equation (Alber, 1978), which is thus a special case. Moreover, when quasi-homogeneous theory applies, the transport equation reduces to the Radiative Transport Equation (RTE) for the transport of the variance density spectrum.

Subsequently we demonstrate by means of a multiple scale analysis that the RTE is only valid for small values of the ratio  $\beta$  between the coherence length scale, and a scale on which the medium (topography) changes ( $\beta \ll 1$ ). If  $\beta$  is  $O(1)$ , as is typical for strong wave focal zones, a truncated series expansion of the operator cannot account for the ensuing fast spatial variations in the wave statistics, and because the effect is non-perturbative, the series approximation must be replaced by an integral representation which we refer to as the Quasi-Coherent (QC) approximation. To derive a consistent model suitable for large scale application over complex topography, we demonstrated that for wave fields with a finite coherence length, only the topographical variation within the coherent footprint influences the evolution of the wave statistics. Subsequently, on the premise of a finite coherence length we derived an augmented form of the radiative transport equations, which includes a scattering term accounting for the generation of coherent contributions within random wave fields. The resulting model accounts for the generation and transport of coherent interferences between wave components that enclose angles smaller than  $\pi/2$  radians, and the theoretical framework presented here forms a natural extension of the radiative transfer equation.

To illustrate the difference between the traditional QH approach and the QC-approach we considered the convergence of multiple coherent wave packets, for which an analytical solution can be derived. The lateral standing wave pattern that occurs in the convergence point is faithfully represented by the QC-approach, whereas the QH approximation assumes mutual independence of the wave packets, and is therefore unable to resolve the fine scale oscillations in the variance (or mean wave height). Strong differences occur not only in the wave variance, but also in the wave spectra where, due to the inclusion of coherent interference, negative values occur. This prohibits the interpretation of the CM spectrum as an energy density function. We argue that the appearance of these negative terms can be interpreted as a departure from the equal partitioning between the mean kinetic and potential energy found under progressive wave. For instance, in the node of a standing wave pattern there is no potential energy associated with the wave motion due to interference; in the coupled mode spectrum this results in negative contributions of equal magnitude but opposite sign to the variance (or energy) associated with the interfering waves such that the surface variance disappears.

We further verified the QC theory, including its ability to generate coherency due to the interaction with the topography, by comparison with observations of the experiments by Vincent and Briggs (1989) and Berkhoff *et al.* (1982). These experiments considered the wave statistics, in particular wave heights, in the focal zone of a submerged shoal. Especially for nearly unidirectional waves the QC approximation is a marked improvement over the traditional RTE, and is not only able to capture the bulk parameters, but also provides a good approximation to the wave spectrum and to its Fourier transform, the covariance function. Differences become less pro-

nounced as directionality increases. Effectively, with increased directional spreading,  $\beta$  decreases, implying that the RTE becomes an increasingly viable alternative. Nevertheless, for moderately spread waves (say  $10^\circ$ ), representing a realistic swell field, the QC results are in better agreement with observations. Finally, we considered field observations of swell propagation over submerged canyons as observed during the ONR NCEX experiment. Model predictions of swell compare well with observations, and form a slight improvement on those predicted by the RTE. This confirms that the QC approximation can be used to predict the wave statistics for complex nearshore topography

Comparison with analytic solutions, and with observations of random surface wave propagation in the laboratory and in the field confirm that the Quasi-Coherent (QC) approximation accurately represents both the generation and transport of cross-correlations in the wave field, and resolves the fine-scale interference patterns associated with crossing waves. The effects of diffraction on statistics of waves around and behind obstacles and barriers can be accurately modelled by including appropriate boundary conditions on the QC approximation. These results show that the application of QC theory to ocean waves can resolve some of the restrictions of quasi-homogeneous theory (the radiative transfer equation) in areas characterized by two-dimensional medium variations and caustics. This is likely to be of particular importance for wave-driven circulation and transport processes in coastal areas and inlets.

## 7.2. OUTLOOK

The breathtaking speed at which computational capabilities evolve<sup>1</sup>, and our increasing understanding of nearshore wave dynamics, likely implies that as time progresses the more simple wave models will be increasingly abandoned in favour of physically more complete approximations such as those considered here. However, within the foreseeable future, it is unlikely that either of the models presented in the present thesis will supplant spectral stochastic models for use in operational forecasting, or in daily engineering practice as there are important fundamental and practical hurdles that will prohibit replacement of such models for now. Nevertheless, both methods show great promise, and can complement such models for select situations where more accurate results are deemed necessary.

If non-hydrostatic models are to be applied on larger scales, generation by wind and dissipation by deep water wave breaking (white capping) need to be accounted for; both of which are not straightforward and require further research to include within the non-hydrostatic modelling framework. It is even debatable whether this, apart for research purposes (e.g. to derive better spectral representations), is worthwhile pursuing; for the open ocean present day spectral models are an order of magnitude more efficient, and are, given the often large uncertainties in the forcing, often sufficiently accurate. Instead, it is in particular near and in the surfzone where the potential lies for further development of the model – and for potential applications

---

<sup>1</sup>The recent introduction of GPU's might well introduce another paradigm shift in scientific computing.

thereof.

Arguably, non-hydrostatic models have reached a maturity that they can now be used to fill gaps not yet covered, or are difficult to acquire, by observations in the surfzone. Naturally, there are still areas that need further validation and improvement; for instance inclusion of wave-breaking induced turbulence can improve wave shapes and may help account for enhanced bed friction coefficients found in the surfzone. The latter is particularly important for infra-gravity (ig) motions, which have not featured prominently in the present work, but are well represented in SWASH (including ig-wave breaking and shoreline reflection, see Rijnsdorp *et al.*, 2014c) – if bed friction is calibrated for. How well ig-waves are resolved in the field, in particular when including short-crested primary waves, is still an open question, though preliminary results are encouraging<sup>2</sup>. Nevertheless, a model like SWASH has the potential to not only investigate the physics, but also to help derive parametrisations of certain processes (e.g. the spectral distribution of dissipation) for use in more approximate models, like SWAN.

However, significant challenges – and research opportunities – not only lie in the wave hydrodynamics proper, but also in the coupling to other processes of interest; for example the transport of (passive) scalar tracers<sup>3</sup>, coupling to morphological models, or the inclusion of layered density flows (e.g. extending Balkema, 2009). This would allow application of the model to investigate the dispersion of chemicals in the surfzone, the morphological development under strongly nonlinear forcing, or the evolution of internal waves.

Whereas non-hydrostatic (and Boussinesq) models are pushed towards deeper water, encompassing increasingly longer temporal and larger spatial scales, the stochastic quasi-coherent model development presented in this thesis in a way represents an analogous push into progressively shallower water, including increasingly fine scale effects due to coherent interference. The great advantage of the QC being that it retains compatibility with the existing stochastic models (e.g. SWAN), so that principally expressions for wave physics (accounting for generation by wind, dissipation, and nonlinear interactions) applicable to those models can be used with minor modifications within the QC framework.

The principle problem remains that because the QC approach evaluates a convolution like integral over the spectrum, it is two orders of magnitude more computationally expensive compared with the RTE. Although still much more efficient than time-domain models like SWASH, this represents a considerable increase in effort that prohibits routine usage. Fortunately, the equations permit easy nesting within operational large scale models. Furthermore, models can locally switch between the RTE or QC approach when appropriate. Combined with a more flexible spatial discretisation based on an unstructured grid, this would allow the model to include fast-scale variations in the statistics when need be, but to switch to the more efficient – and more approximative – RTE when possible.

Besides issues pertaining to the numerical implementation, there are two important theoretical extensions to the QC model that need to be further explored.

---

<sup>2</sup>Personal communication with D.P. Rijnsdorp (2014), manuscript in preparation.

<sup>3</sup>Under development in SWASH, personal communication with M. Zijlema (2014).

Foremost of these is inclusion of ambient currents and its effects on the wave dynamics (shoaling, refraction, etc.). Though this is seemingly straightforward to account for in the derivation – one merely includes the effect of an ambient current in the dispersion relation – the principle issue is to include the energy exchange between the mean current and the waves (and vice versa). Presumably, much like the CM spectrum generalizes the variance density spectrum, this can be achieved through the transport of a generalized action variable which reduces to the wave action if QH assumptions apply.

Secondly, extension towards shallower water into possibly the surfzone will require the inclusion of wave breaking and the energy exchange due to three wave interactions (or triads). Expressions for breaking-induced dissipation are well established, and can easily be incorporated, but triad interactions are at present only approximated in a very rudimentary way. Fundamentally, this requires an evolution equation for three-wave correlators in the form of the bispectrum combined with a suitable closure assumption. Even though what constitutes an appropriate closure assumption for higher-order correlators will likely remain controversial (e.g. see Janssen, 2006, Chapter 4, for a discussion), the same methodology followed in the present work can also be used to derive evolution equations for the bispectrum over topography. This is of theoretical interest as earlier attempts restricted the propagation direction, whereas this would constitute the first isotropic evolution equation. This could help facilitate understanding of the evolution of the third-order statistics over 2D topography. Whether this is also a practical approach is debatable as this entails the evolution of a six dimensional function through time, raising obvious concerns regarding possible storage restrictions and the computational effort involved.

In a way this is indicative of the limitations of the spectral description; after all, these models presume that the motion is weakly nonlinear, with a clear separation of scales between the fast scale wave motion and the mean wave parameters. Even though this approximately holds on the open ocean, within the surfzone the motion becomes strongly nonlinear and the distinction in scales is blurred. Under such conditions, Monte-Carlo simulations using time-domain models likely provide a more convenient, and potentially more accurate, description of the average wave dynamics. Ultimately, this dichotomy between the most suitable application range for stochastic wave models, deep to intermediate water, and for deterministic non-hydrostatic models, from intermediate to shallow water, illustrates that these approaches are not mutually exclusive, but complementary. Hence, barring revolutionary developments in scientific computing, the stochastic and deterministic frameworks are likely to continue to operate in synergy, with operational models based on the RTE – including the QC corrections when deemed necessary – providing the boundary conditions for deterministic models. Hence, within a general engineering or scientific context there is no “better” approach to predict the wave statistics, though – given a particular problem – there might be one which is “best suited”.

# References

- AGARWAL, G.S. and WOLF, E., 1970 Calculus for Functions of Noncommuting Operators and General Phase-Space Methods in Quantum Mechanics. I. Mapping Theorems and Ordering of Functions of Noncommuting Operators. *Phys. Rev. D*, 2, 2161–2186.
- AGNON, Y. and SHEREMET, A., 1997 Stochastic nonlinear shoaling of directional spectra. *J. Fluid Mech.*, 345, 79–99.
- AIKI, H. and GREATBATCH, R.J., 2011 Thickness-Weighted Mean Theory for the Effect of Surface Gravity Waves on Mean Flows in the Upper Ocean. *J. Phys. Oceanogr.*, 42 (5), 725–747.
- ALBER, I.E., 1978 The Effects of Randomness on the Stability of Two-Dimensional Surface Wavetrains. *Philos. T. Roy. Soc. A*, 363 (1715), 525–546.
- BALKEMA, S.H., 2009 *Non-Hydrostatic Modelling of Waves in Layered Fluids*. Master's thesis, Delft, University of Technology.
- BASTIAANS, M.J., 1979 Transport Equations for the Wigner Distribution Function. *Int. J. Optics*, 26 (10), 1265–1272.
- BASTIAANS, M.J., 1997 Application of the Wigner distribution function in optics. In W. Mecklenbrauker and F. Hlawatsch, eds., *The Wigner Distribution - Theory and Applications in Signal Processing*, pp. 375–426. Elsevier Science.
- BATTJES, J., BAKKENES, H., JANSSEN, T. and VAN DONGEREN, A., 2004 Shoaling of subharmonic gravity waves. *J. Geoph. Res-Oceans*, 109 (C2), C02,009.
- BATTJES, J.A. and JANSSEN, J.P.F., 1978 Energy Loss and Set-Up Due to Breaking of Random Waves. In *Proc. 28th Int. Conf. Coastal Eng.*, pp. 569–587. ASCE.
- BECQ-GIRARD, F., FORGET, P. and BENOIT, M., 1999 Non-linear propagation of unidirectional wave fields over varying topography. *Coast. Eng.*, 38 (2), 91 – 113.
- BENOIT, M., MARCOS, F. and BECQ-GIRARD, F., 1996 Development of a Third Generation Shallow-Water Wave Model with Unstructured Spatial Meshing. *Coastal Eng. Proc.*, 1 (25).
- BERKHOFF, J.C.W., BOOIJ, N. and RADDER, A.C., 1982 Verification of numerical wave propagation models for simple harmonic linear water waves. *Coast. Eng.*, 6, 255–279.
- BOERS, M., 1996 *Simulation of a surf zone with a barred beach; part 1: wave heights and wave breaking..* Tech. rep., Delft University of Technology.
- BOERS, M., 2005 *Surf zone turbulence..* Ph.D. thesis, Delft University of Technology.

- BOOIJ, N., HOLTHUIJSEN, L.H. and BENIT, M.P., 2009 A distributed collinear triad approximation in SWAN. In M. Mizuguchi and S. Sato, eds., *Coastal Dynamic 09*, pp. 1–10. ASCE.
- BOOIJ, N., RIS, R.C. and HOLTHUIJSEN, L.H., 1999 A third-generation wave model for coastal regions 1. Model description and validation. *J. Geoph. Res-Oceans*, 104, 7649–7666.
- BORN, M. and WOLF, E., 1999 *Principles of Optics*. Cambridge university press, Cambridge, 7 edn.
- BOUWS, E., GUNTHER, H., ROSENTHAL, W. and VINCENT, C.L., 1985 Similarity of the Wind Wave Spectrum in Finite Depth Water 1. Spectral Form. *J. Geoph. Res-Oceans*, 90 (C1), 975–986.
- BREDMOSE, H., AGNON, Y., MADSEN, P.A. and SCHÄFFER, H.A., 2005 Wave transformation models with exact second-order transfer. *Eur. J. Mech B-fluid.*, 24 (6), 659–682.
- BREMMER, H., 1972 General remarks concerning theories dealing with scattering and diffraction in random media. *Radio Sci.*, 8 (6), 511–534.
- BROCCHINI, M., 2013 A reasoned overview on Boussinesq-type models: the interplay between physics, mathematics and numerics. *Philos. T. Roy. Soc. A*, 469 (2160).
- CASULLI, V. and STELLING, G.S., 1998 Numerical Simulation of 3D Quasi-Hydrostatic, Free-Surface Flows. *J. Hydr. Eng.*, 124 (7), 678–686.
- CAVALERI, L. and RIZZOLI, P.M., 1981 Wind wave prediction in shallow water: Theory and applications. *J. Geoph. Res-Oceans*, 86 (C11), 10,961–10,973.
- CHEN, Q., DALRYMPLE, R.A., KIRBY, J.T., KENNEDY, A.B. and HALLER, M.C., 1999 Boussinesq modeling of a rip current system. *J. Geoph. Res-Oceans*, 104.
- CHEN, Y., GUZA, R.T. and ELGAR, S., 1997 Modeling spectra of breaking surface waves in shallow water. *J. Geoph. Res-Oceans*, 102 (C11), 25,035–25,046.
- CHOW, V.T., 1959 *Open-Channel Hydraulics*. McGraw-Hill.
- CIENFUEGOS, R., BARTHELEMY, E. and P., B., 2010 Wave-Breaking Model for Boussinesq-Type Equations Including Roller Effects in the Mass Conservation Equation. *J. Wat. Port Coast. Ocean Eng.*, 136 (1), 10–26.
- COHEN, L., 1989 Time-frequency distributions – a review. *Proc. IEEE*, 77 (7), 941–981.
- COHEN, L., 2010 Phase-Space Differential Equations for Modes. In B. Schulze and M.W. Wong, eds., *Pseudo-Differential Operators: Complex Analysis and Partial Differential Equations*, pp. 235–250. Birkhäuser Basel.
- CRAIK, A.D.D., 2004 The origins of water wave theory. *Annu. Rev. Fluid Mech.*, 36 (1), 1–28.
- CRAIK, A.D.D. and LEIBOVICH, S., 1976 A rational model for Langmuir circulations. *J. Fluid. Mech.*, 73, 401–426.

- CUI, 2013 *A New Numerical Model for Simulating the Propagation of and Inundation by Tsunami Waves*. Ph.D. thesis, Delft, University of technology.
- CUI, H., PIETRZAK, J.D. and STELLING, G.S., 2012 Improved efficiency of a non-hydrostatic, unstructured grid, finite volume model. *Ocean Modelling*, 54–55 (0), 55 – 67.
- DALRYMPLE, R.A. and KIRBY, J.T., 1988 Models for very wide-angle water waves and wave diffraction. *J. Fluid Mech.*, 192, 33–50.
- DALRYMPLE, R.A. and ROGERS, B.D., 2006 Numerical modeling of water waves with the SPH method. *Coast. Eng.*, 53 (2–3), 141 – 147.
- DE BAKKER, A., TISSIER, M., RUESSINK, B.G., SMIT, P.B. and HERBERS, T.H.C., 2014 Bispectral evolution over a laboratory beach. In *Paper presented at the NCK Days, Delft, The Netherlands, 27–28 March*.
- DINGEMANS, M.W., 1997 *Water Wave Propagation over Uneven Bottoms*, vol. 23 of *advanced series on ocean engineering*. World Scientific.
- DINGEMANS, M.W., STIVE, M.J.F., BOSMA, J., DE VRIEND, H. and VOGEL, J., 1986 Directional nearshore wave propagation and induced currents. In *Proc. 20th Int. Conf. Coastal Eng.*, pp. 1092–1106. ASCE.
- DYSTHE, K.B., 1979 Note on a Modification to the Nonlinear Schrödinger Equation for Application to Deep Water Waves. *Philos. T. Roy. Soc. A*, 369 (1736), 105–114.
- ELDEBERKY, Y., 1996 *Nonlinear Transformation of Wave Spectra in the Nearshore Zone*. Ph.D. thesis, Delft, University of Technology.
- ELDEBERKY, Y. and MADSEN, P.A., 1999 Deterministic and stochastic evolution equations for fully dispersive and weakly nonlinear waves. *Coast. Eng.*, 38, 1–24.
- ELGAR, S. and GUZA, R.T., 1985 Observations of bispectra of shoaling waves. *J. Fluid. Mech.*, 161, 425–448.
- FEDDERSEN, F., GALLAGHER, E., GUZA, R.T. and ELGAR, S., 2003 The drag coefficient, bottom roughness, and wave-breaking in the nearshore. *Coast. Eng.*, 48 (3), 189 – 195.
- FREILICH, M.H. and GUZA, R.T., 1984 Nonlinear Effects on Shoaling Surface Gravity Waves. *Philos. T. Roy. Soc. A*, 311 (1515), 1–41.
- FUHRMAN, D.R. and MADSEN, P.A., 2008 Simulation of nonlinear wave run-up with a high-order Boussinesq model. *Coast. Eng.*, 55 (2), 139 – 154.
- GOMEZ-GESTEIRA, M. and DALRYMPLE, R.A., 2004 Using a Three-Dimensional Smoothed Particle Hydrodynamics Method for Wave Impact on a Tall Structure. *J. Wat. Port Coast. Ocean Eng.*, 130 (2), 63–69.
- GREEN, A.E. and NAGHDI, P.M., 1976 A derivation of equations for wave propagation in water of variable depth. *J. Fluid Mech.*, 78, 237–246.
- HASSELMANN, K., 1962 On the non-linear energy transfer in a gravity-wave spectrum, I. *J. Fluid. Mech.*, 12, 481–500.

- HASSELMANN, K., 1974 On the spectral dissipation of ocean waves due to white capping. *Bound.-Lay. Meteorol.*, 6 (1-2), 107–127.
- HASSELMANN, K., BARNETT, T., BOUWS, E., CARLSON, H., CARTWRIGHT, D., ENKE, K., EWING, J., GIENAPP, H., HASSELMANN, D., KRUSEMAN, P., MEERBURG, A., MULLER, P., OLBERS, D., RICHTER, K., SELL, W. and WALDEN, H., 1973 Measurements of wind-wave growth and swell decay during the Joint North Sea Wave Project (JONSWAP). *Deutsch. Hydrogr., Suppl.*, A8 (12), 95.
- HASSELMANN, S. and HASSELMANN, K., 1985 Computations and parametrizations of the nonlinear energy transfer in a gravity-wave spectrum. I: A new method for efficient computations of the exact nonlinear transfer integral. *J. Phys. oceanogr.*, 15 (11), 1369–1377.
- HERBERS, T.H.C. and BURTON, M.C., 1997 Nonlinear shoaling of directionally spread waves on a beach. *J. Geoph. Res-Oceans*, 102, 21,101–21,114.
- HERBERS, T.H.C., ORZECH, M., ELGAR, S. and GUZA, R.T., 2003 Shoaling transformation of wave frequency-directional spectra. *J. Geoph. Res-Oceans*, 108 (C1), 3013.
- HERBERS, T.H.C., RUSSNOGLE, N.R. and ELGAR, S., 2000 Spectral Energy Balance of Breaking Waves within the Surf Zone. *J. Phys. Oceanogr.*, 30 (11), 2723–2737.
- HIBBERD, S. and PEREGRINE, D.H., 1978 Surf and run-up on a beach: a uniform bore. *J. Fluid Mech.*, 2, 323–345.
- HIRSCH, C., 2007 *Numerical computation of internal & external flows*. John Wiley & Sons, New York, 2nd edn.
- HIRT, C.W. and NICHOLS, B.D., 1981 Volume of fluid (VOF) method for the dynamics of free boundaries. *J. Comput. Phys.*, 39 (1), 201 – 225.
- HLAWATSCH, F. and FLANDRIN, P., 1997 The interference structure of the Wigner distribution and related time-frequency signal representations. In W. Mecklenbrauker and F. Hlawatsch, eds., *The Wigner Distribution - Theory and Applications in Signal Processing*, pp. 59–133. Elsevier.
- HOEFEL, F. and ELGAR, S., 2003 Wave-induced sediment transport and sandbar migration. *Science*, 299, 1885–1887.
- HOLTHUIJSEN, L.H., 2007 *Waves in oceanic and coastal waters*. Cambridge Univ. Press.
- JACOBS, R.P.M., 2010 *Non-hydrostatic Computations of Nearshore Hydrodynamics*. Master's thesis, Delft, University of Technology.
- JANSSEN, A. and CLAASEN, T., 1985 On positivity of time-frequency distributions. *Acoustics, Speech and Sig. Proc., IEEE Trans.*, 33 (4), 1029–1032.
- JANSSEN, P.A.E.M., 1983 Long-time behaviour of a random inhomogeneous field of weakly nonlinear surface gravity waves. *J. Fluid Mech.*, 133, 113–132.

- JANSSEN, P.A.E.M., 2009 *The interaction of Ocean Waves and Wind*. Cambridge Univ. Press.
- JANSSEN, T.T., 2006 *Nonlinear Surface Waves over Topography*. Ph.d. dissertation, Delft, University of technology.
- JANSSEN, T.T., BATTJES, J.A. and VAN DONGEREN, A.R., 2003 Long waves induced by short-wave groups over a sloping bottom. *J. Geoph. Res-Oceans*, 108 (C8).
- JANSSEN, T.T. and HERBERS, T.H.C., 2009 Nonlinear Wave Statistics in a Focal Zone. *J. Phys. Oceanogr.*, 39 (8), 1948–1964.
- JANSSEN, T.T., HERBERS, T.H.C. and BATTJES, J.A., 2006 Generalized evolution equations for nonlinear surface gravity waves over two-dimensional topography. *J. Fluid Mech.*, 552, 393–418.
- JANSSEN, T.T., HERBERS, T.H.C. and BATTJES, J.A., 2008 Evolution of ocean wave statistics in shallow water: Refraction and diffraction over seafloor topography. *J. Geoph. Res-Oceans*, 113 (C3), C03,024.
- KAIHATU, J.M. and KIRBY, J.T., 1995 Nonlinear transformation of waves in finite water depth. *Phys. Fluids*, 7, 1903.
- KAIHATU, J.M., VEERAMONY, J., EDWARDS, K.L. and KIRBY, J.T., 2007 Asymptotic behavior of frequency and wave number spectra of nearshore shoaling and breaking waves. *J. Geoph. Res-Oceans*, 112 (C6).
- KENNEDY, A.B., CHEN, Q., KIRBY, J.T. and DALRYMPLE, R.A., 2000 Boussinesq Modeling of Wave Transformation, Breaking, and Runup. I: 1D. *J. Wat. Port Coast. Ocean Eng.*, 126 (1), 39–47.
- KIRBY, J.T., 1996 *Nonlinear, dispersive long waves in water of variable depth..* Tech. rep., DTIC Document.
- KIRBY, J.T. and KAIHATU, J.M., 1996 Structure of frequency domain models for random wave breaking. In *Proc. 25th Int. Conf. Coastal Eng.*, pp. 1144–1155. ASCE.
- KLOPMAN, G., VAN GROESEN, B. and DINGEMANS, M.W., 2010 A variational approach to Boussinesq modelling of fully nonlinear water waves. *J. Fluid Mech.*, 657, 36–63.
- KOMEN, G., CAVALERI, L., DONELAN, M., HASSELMANN, K., HASSELMANN, S. and JANSSEN, P.A.E.M., 1994 *Dynamics and Modelling of Ocean Waves*. Cambridge Univ. Press.
- KOMEN, G.J., HASSELMANN, K. and HASSELMANN, S., 1984 On the existence of a fully developed wind-sea spectrum. *J. Phys. Oceanogr.*, 14 (8), 1271–1285.
- KUIK, A.J., VAN VLEDDER, G.P. and HOLTHUIJSEN, L.H., 1988 A method for the routine analysis of pitch-and-roll buoy wave data. *J. Phys. Oceanogr.*, 18 (7), 1020–1034.

- LAM, D.C.L. and SIMPSON, R.B., 1976 Centered differencing and the box scheme for diffusion convection problems. *J. Comput. Phys*, 22 (4), 486 – 500.
- LAMB, H., 1932 *Hydrodynamics*. Dover, New York.
- LAUNDER, B.E. and SPALDING, D.B., 1974 The numerical computation of turbulent flows. *Computer Methods in Applied Mech. and Eng.*, 3 (2), 269–289.
- LIN, P. and LIU, P.L.F., 1998 A numerical study of breaking waves in the surf zone. *J. Fluid Mech.*, 359, 239–264.
- LONGUET-HIGGINS, M.S., 1963 The effect of non-linearities on statistical distributions in the theory of sea waves. *J. Fluid Mech.*, 17, 459–480.
- LONGUET-HIGGINS, M.S., 1970 Longshore Currents Generated by Obliquely Incident Sea Waves, 1. *J. Geoph. Res-Oceans*, 75 (33), 6778–6789.
- LONGUET-HIGGINS, M.S. and STEWART, R.W., 1964 Radiation stresses in water waves; a physical discussion, with applications. *Deep Sea Res.*, 11 (4), 529 – 562.
- LØVHOLT, F. and PEDERSEN, G., 2009 Instabilities of Boussinesq models in non-uniform depth. *Int. J. Numer. Meth. Fl.*, 61 (6), 606–637.
- LYGRE, A. and KROGSTAD, H.E., 1986 Maximum entropy estimation of the directional distribution in ocean wave spectra. *J. Phys. Oceanogr.*, 16 (12), 2052–2060.
- LYNETT, P.J., 2006 Nearshore Wave Modeling with High-Order Boussinesq-Type Equations. *J. Wat. Port Coast. Ocean Eng.*, 132 (5), 348–357.
- MA, G., SHI, F. and KIRBY, J.T., 2012 Shock-capturing non-hydrostatic model for fully dispersive surface wave processes. *Ocean Mod.*, 43–44 (0), 22–35.
- MACMAHAN, J.H., THORNTON, E.B. and RENIERS, A.J.H.M., 2006 Rip current review. *Coast. Eng.*, 53 (2–3), 191 – 208.
- MADSEN, A. and SCHÄFFER, H., 1999 A review of Boussinesq-type equations for surface gravity waves. *Advances in coastal and ocean engineering*, 5, 1–94.
- MADSEN, P., BINGHAM, H. and LIU, H., 2002 A new Boussinesq method for fully nonlinear waves from shallow to deep water. *J. Fluid Mech.*, 462, 1–30.
- MADSEN, P., MURRAY, R. and SØRENSEN, O.R., 1991 A new form of the Boussinesq equations with improved linear dispersion characteristics. *Coast. Eng.*, 15 (4), 371–388.
- MADSEN, P.A., FUHRMAN, D.R. and WANG, B., 2006 A Boussinesq-type method for fully nonlinear waves interacting with a rapidly varying bathymetry. *Coast. Eng.*, 53, 487 – 504.
- MADSEN, P.A. and SVENDSEN, I.A., 1983 Turbulent bores and hydraulic jumps. *J. Fluid Mech.*, 129, 1–25.
- MAGNE, R., BELIBASSAKIS, K.A., HERBERS, T.H.C., ARDHUIN, F., O'REILLY, W.C. and REY, V., 2007 Evolution of surface gravity waves over a submarine canyon. *J. Geoph. Res-Oceans*, 112 (C1).

- MANDEL, L. and WOLF, E., 1995 *Optical coherence and Quantum Optics*. Cambridge Univ. Press.
- MASE, H. and KIRBY, J.T., 1992 Hybrid Frequency-domain KDV equation for random wave transformation. In *Proc. 28th Int. Conf. Coastal Eng., Venice*, pp. 474–487. ASCE.
- MCWILLIAMS, J.C. and RESTREPO, J.M., 1999 The wave-driven ocean circulation. *J. Phys. Oceanogr.*, 29, 2523–2540.
- MEI, C., STIASSNIE, M. and YUE, D., 2005 *Theory and applications of ocean surface waves*, vol. 21 of *Advanced Series on Ocean Engineering*. World Scientific.
- MESIAH, A., 1961 *Quantum Mechanics*, vol. I. North-Holland publishing Company, Amsterdam.
- MILES, J.W., 1957 On the generation of surface waves by shear flows. *Journal of Fluid Mechanics*, 3 (02), 185–204.
- MILES, M.D. and FUNKE, E.R., 1989 A Comparison of Methods for Synthesis of Directional Seas. *J. Offshore Mech. Arct.*, 111 (1), 43–48.
- NWOGU, O., 1993 Alternative Form of Boussinesq Equations for Nearshore Wave Propagation. *J. Wat. Port Coast. Ocean Eng.*, 119 (6), 618–638.
- O'REILLY, W.C. and GUZA, R.T., 1991 Comparison of Spectral Refraction and Refraction-Diffraction Wave Models. *J. Wat. Port Coast. Ocean Eng.*, 117 (3), 199–215.
- ÖZKAN-HALLER, H.T. and KIRBY, J.T., 1999 Nonlinear evolution of shear instabilities of the longshore current: A comparison of observations and computations. *J. Geoph. Res-Oceans*, 104 (C11), 25,953–25,984.
- PARKER, B., 2010 *The Power of the Sea: Tsunams, Storm Surges, Rogue Waves and our Quest to predict disasters*. Palgrave MacMillan.
- PENNEY, W.G. and PRICE, A.T., 1952 Part I. The Diffraction Theory of Sea Waves and the Shelter Afforded by Breakwaters. *Philos. T. Roy. Soc. A*, 244 (882), 236–253.
- PEREGRINE, D.H., 1967 Long waves on a beach. *J. Fluid Mech.*, 27 (4), 815–827.
- PEREGRINE, D.H., 1983 Breaking waves on beaches. *Annu. Rev. Fluid Mech.*, 15, 149–178.
- PHILIPS, O., 1960 On the dynamics of unsteady gravity waves of finite amplitude. Part I. *J. Fluid Mech*, 9, 193.
- PHILLIPS, O.M., 1957 On the generation of waves by turbulent wind. *J. Fluid Mech.*, 2 (05), 417–445.
- RIJNSDORP, D.P., SMIT, P.B., RUESSINK, B.G. and ZIJLEMA, M., 2014a Modelling of infragravity waves near Egmond aan Zee with a non-hydrostatic wave model. In *34th Int. Conf. Coastal Eng., Seoul, South Korea, 15-20 June (to be presented)*.

- RIJNSDORP, D.P., SMIT, P.B., RUESSINK, B.G. and ZIJLEMA, M., 2014b Recent experiences with non-hydrostatic modelling of infragravity waves. In *Paper presented at the NCK Days, Delft, The Netherlands, 27–28 March*.
- RIJNSDORP, D.P., SMIT, P.B. and ZIJLEMA, M., 2012 Non-hydrostatic modelling of infragravity waves using SWASH. In *Conference Proceedings, 33rd Int. Conf. Coastal Eng., Santander, Spain*.
- RIJNSDORP, D.P., SMIT, P.B. and ZIJLEMA, M., 2014c Non-hydrostatic modelling of infragravity waves under laboratory conditions. *Coast. Eng.*, 85, 30–42.
- RIS, R.C., HOLTHUIJSEN, L.H., SMITH, J.M., BOOIJ, N. and VAN DONGEREN, A.R., 2002 The ONR virtual testbed for coastal and oceanic wave models. In *Proc. 28th Int. Conf. Coastal Eng.*, pp. 380–391. ASCE.
- SAKAI, T. and IWAGAKI, Y., 1978 Estimation of Water Particle Velocity of Breaking Wave. In *Proc. 16th Int. Conf. Coastal Eng.*, pp. 551–568. ASCE.
- SALMON, J., HOLTHUIJSEN, L.H., SMIT, P.B., VAN VLEDDER, G. and ZIJLEMA, M., 2014a Alternative source terms for SWAN in the coastal region. In *To be presented at: 34th Int. Conf. Coastal Eng, Seoul, South Korea, 15–20 June (to be presented)*.
- SALMON, J.E., HOLTHUIJSEN, L.H., ZIJLEMA, M. and VAN VLEDDER, G., 2014b Scaling Depth-Induced Wave-Breaking in Third-Generation Spectral Wave Models. *submitted to Ocean Modelling*.
- SALMON, R., 1998 *Lectures on geophysical fluid dynamics*. Oxford Univ. Press.
- SCHÄFFER, H.A., MADSEN, P.A. and DEIGAARD, R., 1993 A Boussinesq model for waves breaking in shallow water. *Coast. Eng.*, 20 (3–4), 185–202.
- SERRE, F., 1953 Contribution À L'Étude des Écoulements Permanents et Variables Dans les Canaux. *La Houille Blanche*, 3 (6), 374–388.
- SMAGORINSKY, J., 1963 General circulation experiments with the primitive equations. *Mon. Weather Rev.*, 91 (3), 99–164.
- SMIT, P.B., 2008 *Non-hydrostatic modelling of large scale tsunamis*. Master's thesis, Delft, University of Technology.
- SMIT, P.B. and JANSSEN, T.T., 2011 Coherent Interference and Diffraction in Random Waves. In *Conference Proceedings, 12th Int. Workshop on Wave Hindcasting and Forecasting, Hawai'i, USA*.
- SMIT, P.B. and JANSSEN, T.T., 2013a Evolution of coherent interference in random waves. In *paper presented at Waves in Shallow Environments, Washington, USA, 21–25 April*.
- SMIT, P.B. and JANSSEN, T.T., 2013b The Evolution of Inhomogeneous Wave Statistics through a Variable Medium. *J. Phys. Oceanogr.*, 43, 1741–1758.
- SMIT, P.B., JANSSEN, T.T. and HERBERS, T.H.C., 2012a Coherent interference in random waves. In *Paper presented at the Ocean Sciences Meeting, Salt Lake City*,

USA, 20–24 February.

- SMIT, P.B., JANSSEN, T.T. and HERBERS, T.H.C., 2012b Topography-induced focusing of random waves. In *Conference Proceedings, 33rd Int. Conf. Coastal Eng, Santander, Spain*.
- SMIT, P.B., JANSSEN, T.T. and HERBERS, T.H.C., 2014a Refractive focusing of coherent waves. In *Paper presented at the Ocean Sciences Meeting, Honolulu, USA, 23–28 February*.
- SMIT, P.B., JANSSEN, T.T., HOLTHUIJSEN, L.H. and SMITH, J.M., 2014b Non-hydrostatic modelling of surf zone wave dynamics. *Coast. Eng.*, 83, 36–48.
- SMIT, P.B. and STELLING, G.S., 2009 Accurate prediction of tsunami propagation in complex bathymetries. In *paper presented at Tsunamis and Geophysical Warnings: Workshop at the Lighthill Institute of Mathematical Science, London, UK, 17 December*.
- SMIT, P.B., STELLING, G.S., ROELVINK, D., VAN THIEL DE VRIES, J., MCCALL, R., VAN DONGEREN A., ZWINKELS, C. and JACOBS, R., 2009 *XBeach: Non-hydrostatic model*. Tech. rep., Delft University of Technology and Deltares.
- SMIT, P.B., ZIJLEMA, M. and STELLING, G.S., 2012c Depth-induced Wave Breaking in SWASH. In *paper presented at the 1st International SWASH workshop, Delft, The Netherlands, 24–25 September*.
- SMIT, P.B., ZIJLEMA, M. and STELLING, G.S., 2013 Depth-induced breaking in a non-hydrostatic nearshore wave model. *Coast. Eng.*, 76, 1–16.
- SMITH, J.A., 2006 Observed Variability of Ocean Wave Stokes Drift, and the Eulerian Response to Passing Groups. *J. Phys. Oceanogr.*, 36 (7), 1381–1402.
- SMITH, J.M., 2004 Shallow-water spectral shapes. In *Proc. 29th Int. Conf. Coastal Eng.*, pp. 206–217. World Scientific.
- SMITH, J.M. and VINCENT, C., 1992 Shoaling and Decay of Two Wave Trains on Beach. *J. Wat. Port Coast. Ocean Eng.*, 118 (5), 517–533.
- SMITH, J.M. and VINCENT, L., 2003 Equilibrium ranges in surf zone wave spectra. *J. Geoph. Res-Oceans*, 108 (C11).
- SNYDER, R.L. and ELLIOTT, J., 1981 Array measurements of atmospheric pressure fluctuations above surface gravity waves. *J. Fluid Mech.*, 102 (1), 1–59.
- STAMNES, J.J., 1986 *Waves in focal regions: propagation, diffraction, and focusing of light, sound, and water waves*. A. Hilger, Boston.
- STELLING, G.S., 1983 *On the construction of computational methods for shallow water flow problems..* Ph.D. thesis, Delft University of Technology.
- STELLING, G.S. and DUINMEIJER, S.P.A., 2003 A staggered conservative scheme for every Froude number in rapidly varied shallow water flows. *Int. J. Numer. Meth. Fl.*, 43 (12), 1329–1354.
- STELLING, G.S. and ZIJLEMA, M., 2003 An accurate and efficient finite-difference

- algorithm for non-hydrostatic free-surface flow with application to wave propagation. *Int. J. Numer. Meth. Fl.*, 43 (1), 1–23.
- STIASSNIE, M., REGEV, A. and AGNON, Y., 2008 Recurrent solutions of Alber's equation for random water-wave fields. *J. Fluid Mech.*, 598, 245–266.
- STIVE, M.J.F., 1980 Velocity and pressure field of spilling breakers. In *Proc. 17th Int. Conf. Coastal Eng.*, pp. 547–566. ASCE.
- STRICHARTZ, R., 1993 *A guide to Distribution Theory and Fourier Transforms*. CRC Press.
- SVENDSEN, I.A., 1984 Mass flux and undertow in a surf zone. *Coast. Eng.*, 8 (4), 347 – 365.
- SVENDSEN, I.A., 2006 *Introduction to Nearshore Hydrodynamics*. Advanced Series on Ocean Engineering. World Scientific, Singapore.
- SYMONDS, G., HUNTLEY, D.A. and BOWEN, A.J., 1982 Two-Dimensional Surf Beat: Long Wave Generation by a Time-Varying Breakpoint. *J. Geoph. Res-Oceans*, 87 (C1), 492–498.
- SYNOLAKIS, C.E., 1986 *The run-up of long waves*. Ph.D. thesis, California institute of Technology.
- TEHRANIRAD, B., KIRBY, J.T., MA, G. and SHI, F., 2012 *Tsunami benchmark results for non-hydrostatic wave model NHWAVE Version 1.1*. Tech. rep., Research Report, CACR-12-03, University of Delaware, Newark, Delaware.
- THE WAMDI GROUP, 1988 The WAM Model - A Third Generation Ocean Wave Prediction Model. *J. Phys. Oceanogr.*, 18 (12), 1775–1810.
- THORNTON, E.B. and GUZA, R.T., 1983 Transformation of wave height distribution. *J. Geoph. Res-Oceans*, 88 (C10), 5925–5938.
- TING, F.C.K. and KIRBY, J.T., 1994 Observation of undertow and turbulence in a laboratory surf zone. *Coast. Eng.*, 24 (1–2), 51–80.
- TISSIER, M., BONNETON, P., MARCHE, F., CHAZEL, F. and LANNES, D., 2012 A new approach to handle wave breaking in fully non-linear Boussinesq models. *Coast. Eng.*, 67 (0), 54 – 66.
- TOLEDO, Y. and AGNON, Y., 2012 Stochastic evolution equations with localized nonlinear shoaling coefficients. *Eur. J. Mech B-fluid.*, 34 (0), 13 – 18.
- TOLMAN, H.L., 1991 A Third-Generation Model for Wind Waves on Slowly Varying, Unsteady, and Inhomogeneous Depths and Currents. *J. Phys. Oceanogr.*, 21 (6), 782–797.
- TONELLI, M. and PETTI, M., 2010 Finite volume scheme for the solution of 2D extended Boussinesq equations in the surf zone. *Ocean Eng.*, 37 (7), 567–582.
- TONELLI, M. and PETTI, M., 2012 Shock-capturing Boussinesq model for irregular wave propagation. *Coast. Eng.*, 61 (0), 8 – 19.

- TORRE, A., 2005 *Linear ray and wave optics in phase space: Bridging ray and wave optics via the Wigner phase-space*. Elsevier.
- TORRES-FREYERMUTH, A., LOSADA, I.J. and LARA, J.L., 2007 Modeling of surf zone processes on a natural beach using Reynolds-Averaged Navier-Stokes equations. *J. Geoph. Res-Oceans*, 112 (C9).
- VAN DER VORST, H.A., 1992 Bi-CGSTAB: A fast and smoothly converging variant of Bi-CG for the solution of nonsymmetric linear systems. *SIAM J. Sci. Stat. Comp.*, 13 (2), 631–644.
- VAN DONGEREN, A.R., BATTJES, J.A., JANSSEN, T.T., VAN NOORLOOS, J., STEENHAUER, K., STEENBERGEN, G. and RENIERS, A., 2007 Shoaling and shoreline dissipation of low-frequency waves. *J. Geoph. Res-Oceans*, 112 (C2).
- VAN DORN, W.G., 1978 Breaking Invariants in Shoaling Waves. *J. Geoph. Res-Oceans*, 83 (C6), 2981–2988.
- VAN GENT, M.R.A. and DOORN, N., 2000 *Numerical model investigations on coastal structures with shallow foreshores. Validation of Numerical Models based on Physical Model Tests on the Petten Sea-defence*. Tech. rep., Deltares.
- VAN GROESEN, E. and ANDONOWATI, 2011 Fully dispersive dynamic models for surface water waves above varying bottom, Part 1: Model equations. *Wave motion*, 48 (7), 658–667.
- VILLE, J., 1948 Théorie et applications de la notion de signal analytique. *Cables et transmission*, 2A, 61–74.
- VINCENT, C.L. and BRIGGS, M.J., 1989 Refraction—Diffraction of Irregular Waves over a Mound. *J. Wat. Port Coast. Ocean Eng.*, 115 (2), 269–284.
- VREUGDENHIL, C.B., 1994 *Numerical methods for shallow-water flow*. Water Science and Technology Library. Kluwer Academic Publishers, Dordrecht, The Netherlands.
- WALTHER, A., 1968 Radiometry and Coherence. *J. Opt. Soc. Am.*, 58 (9), 1256–1259.
- WEI, G., KIRBY, J.T., GRILLI, S.T. and SUBRAMANYA, R., 1995 A fully non-linear Boussinesq model for surface waves. Part 1. Highly non-linear unsteady waves. *J. Fluid Mech.*, 294, 71–92.
- WEI, Z. and JIA, Y., 2014 Simulation of nearshore wave processes by a depth-integrated non-hydrostatic finite element model. *Coast. Eng.*, 83, 93 – 107.
- WIGNER, E., 1932 On the Quantum Correction For Thermodynamic Equilibrium. *Phys. Rev.*, 40 (5), 749.
- WILLEBRAND, J., 1975 Energy transport in a nonlinear and inhomogeneous random gravity wave field. *J. Fluid Mech.*, 70 (01), 113–126.
- WISE GROUP, 2007 Wave modelling - The state of the art. *Prog Oceanogr.*, 75 (4), 603–674.
- WITTING, J.M., 1984 A unified model for the evolution nonlinear water waves. *J.*

- Comput. Phys.*, 56 (2), 203–236.
- YAMAZAKI, Y., CHEUNG, K.F. and KOWALIK, Z., 2011 Depth-integrated, non-hydrostatic model with grid nesting for tsunami generation, propagation, and run-up. *Int. J. Numer. Meth. Fl.*, 67 (12), 2081–2107.
- YAMAZAKI, Y., KOWALIK, Z. and CHEUNG, K.F., 2009 Depth-integrated, non-hydrostatic model for wave breaking and run-up. *Int. J. Numer. Meth. Fl.*, 61 (5), 473–497.
- ZAKHAROV, V.E., 1999 Statistical theory of gravity and capillary waves on the surface of a finite-depth fluid. *Eur. J. Mech B-fluid.*, 18 (3), 327–344.
- ZIJLEMA, M. and STELLING, G.S., 2005 Further experiences with computing non-hydrostatic free-surface flows involving water waves. *Int. J. Numer. Meth. Fl.*, 48 (2), 169–197.
- ZIJLEMA, M. and STELLING, G.S., 2008 Efficient computation of surf zone waves using the nonlinear shallow water equations with non-hydrostatic pressure. *Coast. Eng.*, 55 (10), 780–790. 0378-3839.
- ZIJLEMA, M., STELLING, G.S. and SMIT, P.B., 2011a Simulating nearshore wave transformation with non-hydrostatic wave-flow modelling. In *Conference Proceedings, 12th Int. Workshop on Wave Hindcasting and Forecasting, Hawai'i, USA*.
- ZIJLEMA, M., STELLING, G.S. and SMIT, P.B., 2011b SWASH: An operational public domain code for simulating wave fields and rapidly varied flows in coastal waters. *Coast. Eng.*, 58 (10), 992–1012.
- ZIJLEMA, M. and VAN DER WESTHUYSEN, A.J., 2005 On convergence behaviour and numerical accuracy in stationary SWAN simulations of nearshore wind wave spectra. *Coast. Eng.*, 52 (3), 237–256.
- ZIJLEMA, M., VAN VLEDDER, G.P., HOLTHUIJSEN, L.H., SALMON, J.E. and SMIT, P.B., 2013 Swan and its recent developments. In *Conference Proceedings, 13th Int. Workshop on Wave Hindcasting and Forecasting, Banff, Canada*.

# List of figures

2.1	Sketch of a ray pattern induced by the refraction of a monochromatic, unidirectional wave. . . . .	14
3.1	The layout of the velocities $u, w$ (indicated by arrows) and the pressure $p$ (indicated by dots) for a vertical cell. . . . .	21
3.2	Sketch of the free surface $\zeta$ (top panels) and the rate of surface rise $\partial_t \zeta$ (bottom panels) as a function of time. . . . .	24
3.3	The experimental setup from Ting and Kirby (1994) . . . . .	26
3.4	Wave heights and maximum Froude number for spilling breakers in the Ting and Kirby (1994) experiment. . . . .	27
3.5	Wave heights $H$ for spilling (left panel) and plunging (right panel) breakers in the Ting and Kirby (1994) experiment. . . . .	28
3.6	Phase-averaged profiles of the free surface elevation $\zeta$ for spilling and plunging breaking waves. . . . .	29
3.7	Mean water-level setup $\bar{\zeta}$ for spilling and plunging breakers in the Ting and Kirby (1994) experiment. . . . .	29
3.8	Sensitivity of computed wave heights in case of spilling breakers to variations in the maximum steepness and relative mixing length. . . . .	30
3.9	Layout of the different flume experiments. . . . .	31
3.10	Spatial variation of the significant wave height $H_{m0}$ in the various experiments. . . . .	33
3.11	Spatial variation of the mean zero-crossing period $T_0$ (Dingemans <i>et al.</i> (1986), top left panel) or $T_{m02}$ (other panels) in the various experiments. . . . .	34
3.12	Mean water-level setup $\bar{\zeta}$ in Boers (1996). . . . .	34
3.13	Depth contours and experimental layout of the Dingemans <i>et al.</i> (1986) experiment (case me35). . . . .	35
3.14	Snapshots of the free surface indicating where the HFA is active. . . . .	36
3.15	Cross-sections of the significant wave height and mean zero crossing period in the Dingemans <i>et al.</i> (1986) experiment. . . . .	37
3.16	Comparison between measured and computed variance density spectra in the Dingemans <i>et al.</i> (1986) experiment. . . . .	38
3.17	Measured and computed wave induced current field for the Dingemans <i>et al.</i> (1986) experiment. . . . .	40
3.18	Measured and computed current direction for the Dingemans <i>et al.</i> (1986) experiment. . . . .	40
3.19	Measured and computed current magnitude for the Dingemans <i>et al.</i> (1986) experiment. . . . .	40

4.1	Layout of the flume experimental setup by Smith (2004). . . . .	52
4.2	Comparison between modeled and observed values of significant wave height. . . . .	56
4.3	Scatter plots of observed versus computed values for the significant wave height, mean period, skewness and asymmetry. . . . .	59
4.4	Comparison between the observed and computed energy density spectra. . . . .	60
4.5	Comparison between the observed and computed energy flux contained in a frequency band around contained in a frequency band around the peak. . . . .	62
4.6	Comparison between the observed and computed normalized energy fluxes at the primary peak and its first and second harmonics. . . . .	63
4.7	The slope of best fit line to the log of the wavenumber spectrum within the Toba and Zakharov range. . . . .	64
4.8	The nonlinear source term computed at two different gauges. . . . .	66
4.9	Probability density functions for the normalized free surface estimated from the observations and from the Monte Carlo simulations. . . . .	68
4.10	Mean of the spectral distribution function of energy dissipation. . . . .	69
4.11	Absolute relative error in the angular frequency, and the resonant mismatch. . . . .	73
5.1	Snapshots of normalized wave variance of the three-packet interference example. . . . .	82
5.2	Cross-sections of normalized wave variance of the three-packet interference example. . . . .	83
5.3	Spectral evolution of the three-packet interference example. . . . .	84
5.4	Plan view of the experimental setup by Vincent and Briggs (1989) including a ray-traced solution for unidirectional monochromatic waves. . . . .	86
5.5	Normalized wave heights along transects across and behind the submerged shoal as considered by Vincent and Briggs (1989). . . . .	87
5.6	Plan view of modeled wave heights for the experimental set-up as considered by Vincent and Briggs (1989). . . . .	88
5.7	Sketch of wave interference geometry on the radius of convergence. . . . .	91
5.8	Contours of normalized wave height behind a semi-infinite breakwater and a breakwater gap. . . . .	92
5.9	Cross-sections of normalized wave height behind a semi-infinite breakwater and a breakwater gap. . . . .	93
6.1	Sketch of a local slope and a least squares fit to $\sigma$ within the predefined coherent zone. . . . .	106
6.2	Plan view of normalized wave heights. . . . .	108
6.3	Normalized wave height along the indicated transects. . . . .	109
6.4	Coupled mode and variance density spectra down wave of the shoal. . . . .	110
6.5	Plan view of the modulus of the normalized covariance function. . . . .	112
6.6	Normalized covariance functions along transects. . . . .	112
6.7	Bathymetry near Scripps and La Jolla canyon, and locations of observation points. . . . .	113

---

6.8	Directional and integrated frequency spectra as observed at the Outer Torres Peynes buoy on the 16 <sup>th</sup> and 30 <sup>th</sup> of November, 2003. . . . .	115
6.9	Normalized wave heights near the NCEX site on 16 November. . . . .	116
6.10	Normalized wave height along the indicated depth contours on 16 November. . . . .	116
6.11	Normalized wave heights near the NCEX site on 30 November. . . . .	119
6.12	Normalized wave height along the indicated depth contours on 30 November. . . . .	119
6.13	Illustration of the four directional sweep method used in the present study. . . . .	124



# Acknowledgements

Being jet-lagged on a Friday afternoon, after returning from a conference, might be considered a small price to pay compared with the fantastic experience gained from a visit to the beautiful island of Hawai'i. However, from the perspective of productivity, during the final months of my thesis – what surely must be the most stressful moment in the life of a PhD student – it is downright inconvenient. That said, somehow it provides for the perfect reflective mindset that is required for writing the acknowledgements.

Looking back on 4<sup>+</sup> years of research, the transition from a somewhat clueless student, who thought he could understand everything, into a just as clueless academic who knows there is always a next level of knowledge to master, has been alternately rewarding, challenging *and* frustrating. During this process, I have managed to stumble on many a pitfall – in research and in life – but was fortunate enough to receive support by many, each of whom in one way or another contributed to help me complete this dissertation.

From my personal perspective I feel that this thesis would not have existed without the tremendous support by Leo Holthuijsen and Tim Janssen. Leo always supported me along my endeavours, even when I managed to stray away from the initial research path. Although this implied we could not always directly cooperate, I profited immensely from the feedback he provided, and from the example he set in scientific rigor and most importantly, scientific integrity – thank you Leo! The contribution by Tim to my scientific development can hardly be overestimated. Although we were mostly separated by the Atlantic Ocean – and the entire continental United States to boot – his support, critical reading, ideas and feedback have been invaluable. I tremendously profited from my short stays in San Francisco, where during a few weeks I would learn more than during the previous few months, and enjoyed meeting up with Anke, Erik, Roos, Pepijn and being viciously greeted by Beans – thank you for everything Tim! To quote your own acknowledgements: “I hope we can have some more of that!”.

Naturally my promoter – Professor Guus Stelling – also played a crucial role in my development. I fondly remember his role during my MSc thesis, the collaboration we had on developing non-hydrostatic version of XBeach (and SWASH), and the many discussions and meetings we had. However, above all, I appreciate the trust and freedom he gave me to pursue my own research path. I am also grateful for the support I received from the staff of the section, and in particular I would like to thank Dr Marcel Zijlema with whom I enjoyed collaborating on SWASH, and who provided welcome feedback on this thesis. Furthermore, I wish to express gratitude to Professor Wim Uijtewaal and Professor Julie Pietrzak for their support.

My co-conspirators in pursuit of a PhD (or otherwise engaged), at either the second/third floor, or those hidden deep within the bowels (i.e. the ‘lab’) of the con-

crete monstrosity that is the civil engineering building, provided for a great working climate over the years. I enjoyed meeting up with you over a coffee, a beer, and – on those rare occasions I skipped working – lunch! Thanks André, Andres, Cynthia, Matthieu, Melike, Miguel, Nicolette, Sierd, Steven, XueXue, Willem and all others whom I worked with! However, those I shared a room with – be it at work or at a hotel – deserve a special mention. Thank you James, I enjoyed travelling all over the world accompanied by a cynical British travel guide; “Gu” and Victor, for raising my spirits while drinking spirits, discussing economic policy and for your interior decorating skills; Dirk, for our constant “foot fight” due to your ridiculously long legs, and our collaboration; and Ocean, for our discussions on anything from Chinese politics, printable folding crafts depicting “Angry Birds” to numerical schemes!

Without doubt, there are many more that deserve to be mentioned here, and to those I inadvertently left out, I apologize. If you let me know, and if there ever will be a second edition, I will surely include you! However, before wrapping up, I want to express my gratitude towards my parents; I cannot even begin to list all the things you have done – and are doing – for me! Nor can I express in full how much I admire you. Moreover, I tremendously admire the way of life that my brother Xander and his partner Sandra share, and the energy and ambition of my sister Marion and her partner Michiel. Most of all I think all of you have been patient and kind to a brother who has his personal quirks – and never checks or answers his mail. It is a privilege to see ones nieces (Iris & Lotte), nephews (Danko & Aram) and children of friends (Teije) being born, and grow up! To Dena, thank you for the good times, and for showing me the wonder that is Iran. To my friends of old, Mirza, Johan, Dirk, Martijn, Simke and Nicole (& partners); thank you for providing the necessary distractions, and for helping me out when the currents of life were going against me.

Finally, despite the stress that accompanies the final days of any large project, these last months my quality of life has improved exponentially, for which the blame squarely lies with Mathilde. Thank you for tremendously enriching my life, you wonderful creature ...



Delft – May, 2014  
Pieter Bart Smit

# List of publications

## JOURNAL ARTICLES

### FIRST AUTHOR

SMIT, P.B., ZIJLEMA, M. and STELLING, G.S., 2013 Depth-induced breaking in a non-hydrostatic nearshore wave model. *Coast. Eng.*, 76, 1–16.

SMIT, P.B. and JANSSEN, T.T., 2013b The Evolution of Inhomogeneous Wave Statistics through a Variable Medium. *J. Phys. Oceanogr.*, 43, 1741–1758.

SMIT, P.B., JANSSEN, T.T., HOLTHUIJSEN, L.H. and SMITH, J.M., 2014b Non-hydrostatic modelling of surf zone wave dynamics. *Coast. Eng.*, 83, 36–48.

### CO-AUTHOR

RIJNSDORP, D.P., SMIT, P.B. and ZIJLEMA, M., 2014c Non-hydrostatic modelling of infragravity waves under laboratory conditions. *Coast. Eng.*, 85, 30–42.

ZIJLEMA, M., STELLING, G.S. and SMIT, P.B., 2011b SWASH: An operational public domain code for simulating wave fields and rapidly varied flows in coastal waters. *Coast. Eng.*, 58 (10), 992–1012

## CONFERENCE PROCEEDINGS, WORKSHOPS AND TALKS

### FIRST AUTHOR

SMIT, P.B. and STELLING, G.S., 2009 Accurate prediction of tsunami propagation in complex bathymetries. In *paper presented at Tsunamis and Geophysical Warnings: Workshop at the Lighthill Institute of Mathematical Science, London, UK, 17 December*.

SMIT, P.B. and JANSSEN, T.T., 2011 Coherent Interference and Diffraction in Random Waves. In *Conference Proceedings, 12th Int. Workshop on Wave Hindcasting and Forecasting, Hawai'i, USA*.

SMIT, P.B., JANSSEN, T.T. and HERBERS, T.H.C., 2012b Topography-induced focusing of random waves. In *Conference Proceedings, 33rd Int. Conf. Coastal Eng, Santander, Spain*.

SMIT, P.B., JANSSEN, T.T. and HERBERS, T.H.C., 2012a Coherent interference in random waves. In *Paper presented at the Ocean Sciences Meeting, Salt Lake City, USA, 20–24 February*.

SMIT, P.B., ZIJLEMA, M. and STELLING, G.S., 2012c Depth-induced Wave Breaking in SWASH. In *paper presented at the 1st International SWASH workshop, Delft, The Netherlands, 24–25 September*.

SMIT, P.B. and JANSSEN, T.T., 2013a Evolution of coherent interference in random waves. In *paper presented at Waves in Shallow Enviroments, Washington, USA, 21–25 April*.

SMIT, P.B., JANSSEN, T.T. and HERBERS, T.H.C., 2014a Refractive focusing of coherent waves. In *Paper presented at the Ocean Sciences Meeting, Honolulu, USA, 23–28 February*.

#### CO-AUTHOR

RIJNSDORP, D.P., SMIT, P.B. and ZIJLEMA, M., 2012 Non-hydrostatic modelling of infragravity waves using SWASH. In *Conference Proceedings, 33rd Int. Conf. Coastal Eng., Santander, Spain*.

DE BAKKER, A., TISSIER, M., RUESSINK, B.G., SMIT, P.B. and HERBERS, T.H.C., 2014 Bispectral evolution over a laboratory beach. In *Paper presented at the NCK Days, Delft, The Netherlands, 27–28 March*.

RIJNSDORP, D.P., SMIT, P.B., RUESSINK, B.G. and ZIJLEMA, M., 2014b Recent experiences with non-hydrostatic modelling of infragravity waves. In *Paper presented at the NCK Days, Delft, The Netherlands, 27–28 March*.

RIJNSDORP, D.P., SMIT, P.B., RUESSINK, B.G. and ZIJLEMA, M., 2014a Modelling of infragravity waves near Egmond aan Zee with a non-hydrostatic wave model. In *34th Int. Conf. Coastal Eng, Seoul, South Korea, 15–20 June (to be presented)*.

SALMON, J., HOLTHUIJSEN, L.H., SMIT, P.B., VAN VLEDDER, G. and ZIJLEMA, M., 2014a Alternative source terms for SWAN in the coastal region. In *To be presented at: 34th Int. Conf. Coastal Eng, Seoul, South Korea, 15–20 June (to be presented)*.

ZIJLEMA, M., STELLING, G.S. and SMIT, P.B., 2011a Simulating nearshore wave transformation with non-hydrostatic wave-flow modelling. In *Conference Proceedings, 12th Int. Workshop on Wave Hindcasting and Forecasting, Hawai'i, USA*.

ZIJLEMA, M., VAN VLEDDER, G.P., HOLTHUIJSEN, L.H., SALMON, J.E. and SMIT, P.B., 2013 Swan and its recent developments. In *Conference Proceedings, 13th Int. Workshop on Wave Hindcasting and Forecasting, Banff, Canada*.

#### SCIENTIFIC REPORTS

SMIT, P.B., 2008 *Non-hydrostatic modelling of large scale tsunamis*. Master's thesis, Delft, University of Technology.

SMIT, P.B., STELLING, G.S., ROELVINK, D., VAN THIEL DE VRIES, J., MCCALL, R., VAN DONGEREN A., ZWINKELS, C. and JACOBS, R., 2009 *XBeach: Non-hydrostatic model*. Tech. rep., Delft University of Technology and Deltares.

# Curriculum vitae

Born on the 17<sup>th</sup> of January, 1983, I grew up in Zoetermeer near the Hague in the Netherlands. Starting in 1995, I received my secondary education (VWO) at the Erasmus College in Zoetermeer, of which I graduated in 2001. After a brief spell at Utrecht University studying Physics (2001-2002), I started my academic education (BSc and MSc) at Delft University of Technology studying Civil Engineering. I graduated in November 2008 at the section of Environmental Fluid Mechanics under the supervision of Prof. Guus Stelling on the thesis entitled “Non-hydrostatic modelling of large scale tsunamis”. Following my graduation, I started as a full-time Ph.D. candidate in 2008 at the TU Delft, during which I also served as a full time lecturer for the graduate course Ocean Waves. The research performed during my doctoral research has been documented in this dissertation, which I defend on the 6<sup>th</sup> of June, 2014. Hereafter I will continue working for two months at the Delft University of Technology, after which I hope to receive a Rubicon grant from the NWO to continue research as a post-doctoral fellow at Stanford University under the guidance of Professor Stephen Monismith.